Labeling approaches for functional analyses of adhesion G protein-coupled receptors

Markierungsverfahren zur funktionellen Analyse von Adhäsions-G-Protein-gekoppelten Rezeptoren

Doctoral thesis for a doctoral degree

at the Graduate School of Life Sciences,

Julius-Maximilians-Universität Würzburg,

Section Neuroscience

submitted by

Steffen Altrichter

from

Stuttgart

Würzburg, 2020

Submitted on:

Members of the Thesis Committee

Chairperson: Prof. Dr. Markus Sauer

Primary Supervisor: Prof. Dr. Tobias Langenhan, D.Phil. (Oxon)

Supervisor (Second): Prof. Dr. Robert J. Kittel

Supervisor (Third): Prof. Dr. Carsten Hoffmann

Supervisor (Fourth): Dr. Jörg Hamann

Date of Public Defence:

Date of Receipt of Certificates:

Affidavit

I hereby confirm that my thesis entitled Labeling approaches for functional analyses of adhesion G protein-coupled receptors is the result of my own work. I did not receive any help or support from commercial consultants. All sources and / or materials applied are listed and specified in the thesis.

Furthermore, I confirm that this thesis has not yet been submitted as part of another examination process neither in identical nor in similar form.

Place, Date Signature

Eidesstattliche Erklärung

Hiermit erkläre ich an Eides statt, die Dissertation Markierungsverfahren zur funktionellen Analyse von Adhäsions-G-Protein-gekoppelten Rezeptoren eigenständig, d.h. insbesondere selbstständig und ohne Hilfe eines kommerziellen Promotionsberaters, angefertigt und keine anderen als die von mir angegebenen Quellen und Hilfsmittel verwendet zu haben.

Ich erkläre außerdem, dass die Dissertation weder in gleicher noch in ähnlicher Form bereits in einem anderen Prüfungsverfahren vorgelegen hat.

Ort, Datum Unterschrift

Danksagung

Als erstes möchte ich mich bei Tobias Langenhan für die Möglichkeit, meine Doktorarbeit unter seiner Leitung anfertigen zu dürfen, bedanken. Ich danke ihm zudem für die exzellente Betreuung, außerordentliche Unterstützung und die vielen Möglichkeiten mich mittels seiner Hilfe weiter zu entwickeln. Vielen lieben Dank Tobias, dass du mir stets mit Rat und Tat zu Seite gestanden hast.

Außerdem gilt mein Dank Robert Kittel, Carsten Hoffmann und Jörg Hamann für die Mitbetreuung meiner Doktorarbeit und den damit verbunden Ratschlägen und Interpretationen meiner Ergebnisse.

Als nächstes bedanke ich mich bei Nicole Scholz. Sie hatte stets ein offenes Ohr bei wissenschaftlichen Problemstellungen und hatte sie auch selbst eine Menge um die Ohren, war sie trotzdem in der gesamten Zeit eine sehr große Hilfe.

Mein Dank gilt auch meinen lieben Kollegen Dmitrij Ljaschenko, Matthias Nieberler, Nadine Ehmann, Ina Brauer, Johanna Irmer, Mareike Hemberger und allen anderen Kollegen aus Würzburger und Leipziger Zeit, welche einen wichtigen Teil zum Gelingen dieser Arbeit beigetragen haben.

Spezieller Dank gilt zudem Maria Oppmann, welche mich in der Würzburger Zeit ohne Wenn und Aber in den Laboralltag eingeführt hat und mir immer mit Rat und Tat zur Seite stand.

Des Weiteren möchte ich mich herzlich bei all den freundlichen Helfern aus anderen Laboren bedanken. Hierbei seien allem voran Gabriela Aust, Gerti Beliu und Nelly Rüttiger genannt ohne deren Hilfe manch ein Experiment nicht möglich gewesen wäre.

Dank gilt auch der deutschen Forschungsgemeinschaft, der Graduate School of Life Sciences und dem Elitenetzwerk Bayern für die (finanzielle) Unterstützung.

Als letztes habe ich mir auf dieser Seite noch Platz aufgehoben für die wichtigsten Personen in meinem Leben – meine Familie. Liebe Sarah, ich danke dir von ganzem Herzen für die Unterstützung während meiner Doktorarbeit. Vielen Dank, dass du ohne zu zögern mit nach Leipzig gekommen bist und ich jeden Tag mit dir Verbringen darf. Vielen Dank. Joris ich danke dir, dass du Sarah und mir jeden Tag aufs Neue ein Lächeln ins Gesicht zauberst.

Contents of this thesis is part of the following manuscripts:

Scholz, N.*, Ehmann, N.*, Sachidanandan, D., Imig, C., Cooper, B.H., Jahn, O., Reim, K., Brose, N., Meyer, J., Lamberty, M., **Altrichter, S.**, Bormann, A., Hallermann, S., Pauli, M., Heckmann, M., Stigloher, C., Langenhan, T.[#], Kittel, R.J.[#], 2019. Complexin cooperates with Bruchpilot to tether synaptic vesicles to the active zone cytomatrix. J Cell Biol 218, 1011–1026. https://doi.org/10.1083/jcb.201806155

Altrichter, S.*, Beliu, G.*, Guixà-González, R.*, Hemberger, M., Brauer, I., Scholz, N., Kuhlemann, A., Pérez-Hernández, G., Hildebrand, P.W.[#], Sauer, M.[#], Langenhan, T.[#] Tethered agonist exposure in intact adhesion GPCRs through intrinsic structural flexibility of the GAIN domain. *In Revision*.

*contributed equally

[#]correspondence

Labeling approaches for functional analyses of adhesion G protein-coupled receptors

Table of Contents

1 Abbreviations

°C	Degree Celsius
7TM	Seven transmembrane
α_{2A}AR	α_{2A}-adrenergic receptor
α-BuTX	α-Bungarotoxin
A1	ADGRA1/GPR123
aGPCR	Adhesion G protein-coupled receptor
AT1	Angiotensin II type 1
B	Backbone
B1	ADGRB1/BAI1
B2	ADGRB2/BAI2
B3	ADGRB3/BAI3
BBS	α-Bungarotoxin binding site
Brp	Bruchpilot
C1	ADGRC1/CELSR1
CFP	Cyan fluorescent protein
Cpx	Complexin
CTF	C-terminal fragment
CUB	Complement C1r/C1s, Uegf, Bmp1
D1	ADGRD1/GPR133
DAPT	N-[N-(3,5-Difluorophenacetyl)-L-alanyl]-S-phenylglycine t-butyl ester
dH_2O	Distilled water
DMEM	Dulbecco's modified eagle medium
DMSO	Dimethyl sulfoxide
DNA	Deoxyribonucleic acid
DPBS	Dulbecco's phosphate-buffered saline
E2	ADGRE2/EMR2
E5	ADGRE5/CD97
ECL	Extracellular loop

ECR	Extracellular region
EDT	1,2-Ethanedithiol
e.g.	*Exempli gratia* (for example)
EGF	Epidermal growth factor
ELISA	Enzyme-linked immunosorbent assay
ER	Endoplasmic reticulum
F1	ADGRF1/GPR110
F5	ADGRF5/GPR116
Fig.	Figure
FlAsH	Fluorescein arsenical hairpin binder
FlAsH-EDT_2	Fluorescein arsenical hairpin binder, bis-EDT adduct
FRET	Förster resonance energy transfer
g	Gram
G1	ADGRG1/GPR56
G2	ADGRG2/GPR64
G3	ADGRG3/GPR97
G5	ADGRG5/GPR114
G6	ADGRG6/GPR126
GAIN	GPCR autoproteolysis-inducing
GFP	Green fluorescent protein
GPCR	G protein-coupled receptor
GPS	GPCR proteolytic site
GRK	GPCR kinase
h	Hour
HRM	Hormone receptor motif
HA	Human influenza hemagglutinin
HEK	Human embryonic kidney
HRP	Horseradish peroxidase
ICL	Intracellular loop

ICR	Intracellular region
I	Insert/Insertion
i.a.	*Inter alia* (among other things)
ID	Identification number
IF	Immunofluorescence
IG	Immunoglobulin
kb	Kilo base pairs
kDa	Kilo Dalton
l	Liter
L	Linker
L1	ADGRL1/Latrophilin 1
L3	ADGRL3/Latrophilin 3
LAS X	Leica Application Suite X
M	Molar
mCit	mCitrine
min	Minute
mTurq	mTurquoise
n	Number of duplicates
N	Number of experiments
NGS	Normal goat serum
NTF	N-terminal fragment
OLF	Olfactomedin-like
PAGE	Polyacrylamide gel electrophoresis
PAR	Protease-activated receptor
PBM	PDZ-binding motif
PBS	Phosphate-buffered saline
PBS-T	PBS + Tween-20
PBT	PBS + Triton X-100
PCR	Polymerase chain reaction

PDZ	PSD-95/discs-large/ZO-1
PFA	Paraformaldehyde
PLA	Proximity ligation assay
PM	Plasma membrane
R	Replacement
ROI	Region of interest
rpm	Rounds per minute
RS_{Coin}	pcDNA3.1-*Mb*PylRS^{F}/tRNA^{M15}
RS_{Lemke}	pcDNA3.1-tRNA^{Pyl}/NESPylRS^{AF}
RT	Room temperature
SDM	Site-directed mutagenesis
SDS	Sodium dodecyl sulfate
SEA	Sea urchin sperm protein, enterokinase, agrin
SEM	Standard error of the mean
SLIC	Sequence- and ligation-independent cloning
SPIEDAC	Strain-promoted inverse electron-demand Diels-Alder cycloaddition
Supp.	Supplementary
TA	Tethered agonist
Tab.	Table
TAG	Amber stop codon
TCO*A	trans-Cyclooct-2-en – L - Lysine
TCS	Thrombin cleavage site
TEV	Tobacco etch virus
TSR	Thrombospondin type 1 repeat
UAA	Unnatural amino acid
VBU	Vibratory urticaria
v/v	Volume of a fluid per total volume of solution (%)
w/v	Weight of a solid per total volume of solution (%)
YFP	Yellow fluorescent protein

2 Summary

The superfamily of G protein-coupled receptors (GPCRs) comprises more than 800 members, which are divided into five families based on phylogenetic analyses (GRAFS classification): Glutamate, Rhodopsin, Adhesion, Frizzled/Taste2 and Secretin. The adhesion G protein-coupled receptor (aGPCR) family forms with 33 homologs in Mammalia the second largest and least investigated family of GPCRs. The general architecture of an aGPCR comprises the GPCR characteristics of an extracellular region (ECR), a seven transmembrane (7TM) domain and an intracellular region (ICR). A special feature of aGPCRs is the extraordinary size of the ECR through which they interact with cellular and matricellular ligands via adhesion motif folds. In addition, the ECR contains a so-called GPCR autoproteolysis-inducing (GAIN) domain, which catalyzes autoproteolytic cleavage of the protein during maturation. This cleavage leads to the formation of an N-terminal (NTF) and a C-terminal fragment (CTF), which build a unit by means of hydrophobic interactions and therefore appear as a heterodimeric receptor at the cell surface.

In the past, it has been shown that the first few amino acids of the CTF act as a tethered agonist (TA) that mediates the activation of the receptor through the interaction with the 7TM domain. However, the molecular mechanism promoting the TA-7TM domain interaction remains elusive. This work reveals a novel molecular mechanism that does not require the dissociation of the NTF-CTF complex to promote release of the TA and thus activation of the aGPCR. The introduction of bioorthogonal labels into receptor-signaling-relevant regions of the TA of various aGPCRs demonstrated that the TA is freely accessible within the intact GAIN domain. This suggests a structural flexibility of the GAIN domain, which allows a receptor activation independent of the NTF-CTF dissociation, as found in cleavage-deficient aGPCR variants. Furthermore, the present study shows that the cellular localization and the conformation of the 7TM domain depends on the activity state of the aGPCR, which in turn indicates that the TA mediates conformational changes through the interaction with the 7TM domain, which ultimately regulates the receptor activity. In addition, biochemical analyses showed that the GAIN domain-mediated autoproteolysis of the human aGPCR CD97 (ADGRE5/E5) promotes further cleavage events within the receptor. This suggests that aGPCRs undergo cleavage cascades, which are initialized by the autoproteolytic reaction of the GAIN domain. Thus, it can be assumed that aGPCRs are subject to additional proteolytic events. Finally, the constitutive internalization of the NTF and the CTF of E5 was demonstrated by various labeling methods. It was possible to label both fragments independently and to follow their subcellular location *in vitro*. In summary, these obtained results contribute to a better understanding about the molecular mechanisms of activity and signaling of aGPCRs.

3 Zusammenfassung

Die Superfamilie der G-Protein-gekoppelten Rezeptoren (GPCRs) umfasst weit mehr als 800 Mitglieder, welche aufgrund von phylogenetischen Analysen in fünf Familien unterteilt werden (GRAFS Klassifizierung): Glutamat, Rhodopsin, Adhäsion, Frizzled/Taste2 und Sekretin. Die Familie der Ädhesions-G-Protein-gekoppelten Rezeptoren (aGPCRs) bildet mit 33 Homologen in Säugetieren die zweitgrößte Familie innerhalb der GPCRs. Die generelle Architektur eines aGPCRs weist die GPCR typischen Merkmale einer extrazellulären Region (ECR), einer sieben Transmembrandomäne (7TM) und einer intrazellulären Region (ICR) auf. Eine Besonderheit stellt hierbei die außergewöhnliche Größe der ECR, welche über vielfältige Domänen mit zellulären und matrixgebundenen Liganden interagieren, dar. Zusätzlich umfasst die ECR eine sogenannte GPCR Autoproteolyse-induzierende (GAIN) Domäne, an welcher während der Proteinreifung eine autoproteolytische Spaltung stattfindet. Diese Spaltung führt zur Entstehung eines N-terminalen (NTF) und C-terminalen Fragmentes (CTF), welche mittels hydrophober Wechselwirkung eine Einheit an der Zelloberfläche und daher einen heterodimeren Rezeptor bilden.

In der Vergangenheit zeigte sich, dass die ersten paar Aminosäuren des CTF als angebundener Agonist (TA) agieren und über die Interaktion mit der 7TM Domäne eine Aktivierung des Rezeptors vermitteln. Der molekulare Mechanismus, welcher die Wechselwirkung zwischen TA und 7TM Domänen fördert, ist jedoch weiterhin unbekannt. Diese Arbeit enthüllt einen neuartigen molekularen Mechanismus, welcher keine Dissoziation des NTF-CTF Komplexes benötigt, um eine Freisetzung des TA und damit eine Aktivierung des aGPCR zu gewährleisten. Mittels der Einbringung von bioorthogonalen Markierungen in rezeptorsignalisierungs-relevante Bereiche des TA von diversen aGPCRs, wurde gezeigt, dass dieser innerhalb der intakten GAIN Domäne freizugänglich vorliegt. Dies lässt auf eine strukturelle Flexibilität der GAIN Domäne schließen, welche eine Rezeptoraktivierung unabhängig von der NTF-CTF Dissoziation erlaubt, wie sie auch bei spaltungsdefizienten aGPCR Varianten vorzufinden ist. Des Weiteren zeigt die vorliegende Arbeit, dass sich die zelluläre Lokalisation und die Konformation der 7TM Domäne abhängig vom Aktivitätszustand des aGPCR ist, was wiederrum daraufhin deutet, dass der TA über die Interaktion mit der 7TM Domäne eine Konformationsänderung vermittelt, welche letztendlich die Rezeptoraktivität reguliert. Zudem zeigten biochemische Analysen, dass neben der GAIN Domänen-vermittelten Autoproteolyse des humanen aGPCRs CD97 (ADGRE5/E5) weitere proteolytische Spaltungen innerhalb des Rezeptors stattfinden. Dies deutet daraufhin, dass aGPCRs Spaltungskaskaden durchlaufen, welche über die autoproteolytischen Reaktion der GAIN Domäne initialisiert werden. Dadurch kann angenommen werden, dass aGPCRs zusätzlichen proteolytischen Ereignissen

unterliegen. Schlussendlich konnte mittels diverser Markierungsverfahren die konstitutive Internalisierung des NTF und des CTF von E5 nachgewiesen werden. Es war möglich beide Fragmente unabhängig voneinander zu markieren und deren subzelluläre Lokalisation *in vitro* zu verfolgen. Zusammenfassend tragen die gewonnen Ergebnisse zu einem besseren Verständnis der zugrundeliegenden molekularen Mechanismen in Bezug auf Aktivität und Signalübertragung von aGPCRs bei.

4 Introduction

4.1 Adhesion class G protein-coupled receptors

G protein-coupled receptors (GPCRs) represent, with approximately 800 members in human, the largest known protein superfamily characterized by the existence of a seven transmembrane (7TM) domain and the interaction with heterotrimeric guanine nucleotide-binding proteins (G proteins) (Fredriksson et al., 2003; Lagerström and Schiöth, 2008). GPCRs are able to bind a variety of ligands, resulting in a conformational change of the receptor and the activation of the 7TM domain-associated G protein (Weis and Kobilka, 2018). Activation leads to the dissociation of the G protein, which enables the regulation of downstream signaling pathways (Weis and Kobilka, 2018). Along this path, GPCRs play an important role in the processing of biological signals, e.g. taste, smell, light, cell metabolism, neurotransmission and immune response (Hu et al., 2017). Furthermore, defects in GPCR functions correlate with a broad spectrum of disease, e.g. cancer, neurodegenerative malfunctions or metabolic disorders, such as obesity or diabetes (Heng et al., 2013). Approximately over 40 % of all clinical drugs target GPCRs, further indicating their relevance for clinical application and research (Heng et al., 2013).

Based on phylogenetic analyses, the GPCR superfamily was subdivided into five families (GRAFS classification): Glutamate, Rhodopsin, Adhesion, Frizzled/Taste2, and Secretin (Fredriksson et al., 2003). Adhesion G protein-coupled receptors (aGPCRs) form with 33 homologs in Mammalia the second largest, however, least investigated family of GPCRs (Langenhan et al., 2013). A hallmark feature of aGPCRs is the large extracellular region (ECR), which contains a pattern of diverse adhesion motif folds. This pattern forms the basis for the categorization of the aGPCRs into nine subfamilies (Hamann et al., 2015) (**Fig. 1A**). In this thesis, I will focus on diverse aGPCR members of different subfamilies, including rat Latrophilin (ADGRL1/L1), *Drosophila* CIRL, human EMR2 (ADGRE2/E2), human CD97 (ADGRE5/E5), mouse GPR116 (ADGRF5/F5) and human BAI3 (ADGRB3/B3) **(Fig. 1B**).

Even though aGPCRs are widely expressed in most organ systems, which conceivably reflects their involvement in a variety of physiological processes (Hamann et al., 2015), their detailed structural and functional aspects are still incompletely understood. Interestingly, the malfunction of aGPCRs correlates with a broad spectrum of human disorders, ranging from bilateral frontoparietal polymicrogyria (Piao et al., 2004), Usher syndrome (Reiners et al., 2005; Weston et al., 2004) and neural tube defects (Allache et al., 2012; Robinson et al., 2012) to vibratory urticaria (Boyden et al., 2016).

Furthermore, aGPCRs are linked to a variety of cancer types (Aust et al., 1997; Lum et al., 2010; Ward et al., 2011), which suggests the importance for a prospective elucidation of unknown mechanisms regarding their structure and function.

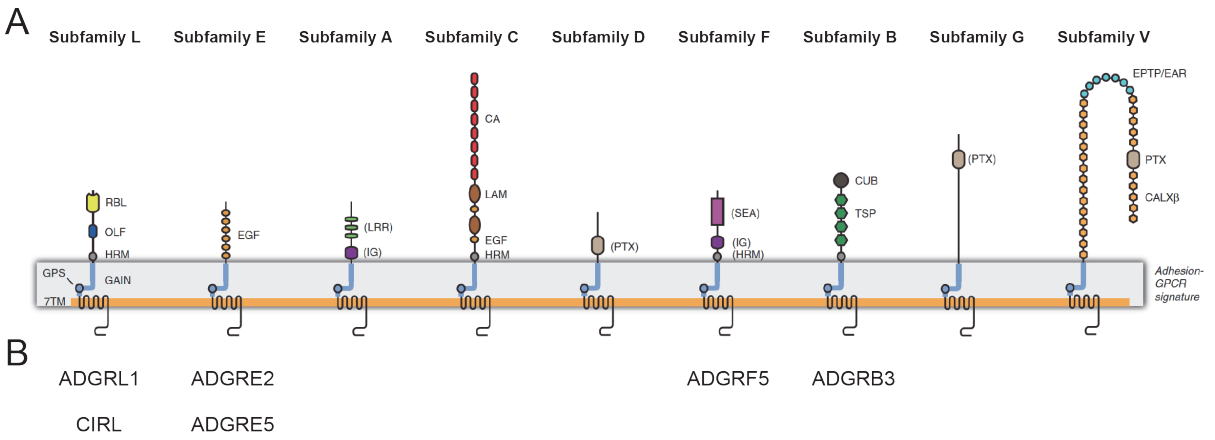

Fig. 1: Adhesion GPCR family.

(A) aGPCRs are subdivided into nine subfamilies based on the unique compositions of the N-terminal domains. Hallmark features of every aGPCRs is the existence of the 7TM domain and the juxtamembrane GAIN domain (except GPR123/ADGRA1/A1), which catalyzes autoproteolysis during protein maturation and ensures the formation of a heterodimer. Most aGPCRs are expressed in vertebrates, in contrast, until now homologs in invertebrates are exclusively found for subfamily L and subfamily C. Adapted from Langenhan et al., 2013. (B) In this thesis investigated aGPCRs members and their subfamily affiliation. L1 and CIRL belong to the subfamily L, E2 and E5 are members of the subfamily E, F5 is characterized as a subfamily F member and B3 is classified as a subfamily B member.

4.2 Structural hallmarks of aGPCRs

Based on their topology, the general architecture of an aGPCR can be subdivided into three parts: an ECR, a 7TM domain and an intracellular region (ICR) (Langenhan et al., 2013) (**Fig. 2**). The 7TM domain forms a barrel-like structure and anchors the receptor to the cell membrane (Nijmeijer et al., 2016). Moreover, the interaction with the G protein occurs at the intracellular face of the 7TM domain (Nijmeijer et al., 2016). The ECR typically includes subfamily-dependent adhesion domains, which are able to recognize and interact with cellular and matricellular ligands (Araç et al., 2016). In addition, the ECR contains a juxtamembrane GPCR autoproteolysis-inducing (GAIN) domain (Araç et al., 2016, 2012). The highly conserved GAIN domain exists in 32 out of the 33 human aGPCRs (absent in A1) (Hamann et al., 2015). Interestingly, the GAIN domain mediates an autocatalytic self-cleavage, first observed for the E5 receptor (Gray et al., 1996). Self-cleavage occurs during protein maturation at the GPCR proteolysis site (GPS), which is closely located to the C-terminal end of the GAIN domain (Nieberler et al., 2016). In addition, the GPS encompasses a cleavage

tripeptide consisting of an histidine, followed by a leucine or isoleucine and ending with a serine or threonine (HL/I↓S/T) (Lin et al., 2010). The autoproteolytic reaction results in the separation of the aGPCR, rendering an N-terminal fragment (NTF) and a C-terminal fragment (CTF) (Gray et al., 1996; Krasnoperov et al., 1997). These two fragments appear as a non-covalently attached heterodimer at the cell membrane (Araç et al., 2012; Gray et al., 1996; Krasnoperov et al., 1997; Lin et al., 2004). However, a minority of aGPCR members are non-cleaved, because of the missing consensus sequence or due to structural hinderance as is the case of B3 (Araç et al., 2012; Langenhan, 2019).

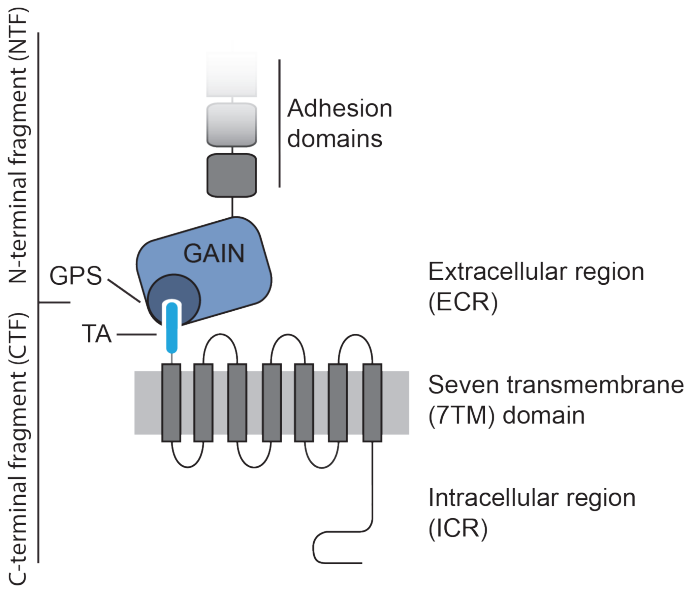

Fig. 2: General molecular structure of aGPCRs.

Topology-based compartmentation of aGPCR architecture implicates a three-partite structure consisting of an ECR, a 7TM domain and an ICR. The ECR contains adhesion domains of different nature, which are characterized by their function in cell-cell and cell-matrix interactions. In addition, the ECR comprises a GAIN domain, which catalyzes the self-cleavage of the receptor at the highly conserved GPS during the protein maturation. Self-cleavage results in the formation of an NTF and a CTF (cleavage-based compartmentation). These two fragments are attached to each other through non-covalently forces mediated by the GAIN domain. Attachment of NTF and CTF ensures the presence of heterodimeric aGPCRs at the cell membrane. The last β-strand of the GAIN domain is separated from the NTF through the autoproteolytic reaction. This β-strand acts as a tethered agonist (TA), which is able to interact with the 7TM domain, resulting in the activation of downstream signaling pathways (see 4.3).

4.3 Mechanisms of aGPCR activation

There are currently several principles that describe the activation of aGPCRs. Previous studies indicated tethered agonism as a possible molecular mechanism able to modulate the activity of aGPCRs. In addition, the solved crystal structures of the L1

and B3 GAIN domains indicated the molecular foundation of this mechanism. The crystal structure of the GAIN domain is composed of a subdomain A consisting of six α-helices and a subdomain B consisting of 13 β-strands (Araç et al., 2012) (**Fig. 3A**). The autoproteolytic reaction occurs between the last two β-strands resulting in the cleavage of the full-length receptor into an NTF and a CTF. The last β-strand of the GAIN domain forms the beginning of the newly appearing CTF. *In vitro* and *in vivo* analyses of aGPCRs indicated that this β-strand acts as a tethered agonist (TA) (Liebscher et al., 2014; Stoveken et al., 2015). The principle behind this observation was based on experiments with engineered aGPCRs containing a deletion of the NTF, which resulted in a high receptor activity (**Fig. 3B**), whereas the deletion of the whole ECR led to an abolished signaling (Hilbig et al., 2018; Liebscher et al., 2014; Paavola et al., 2011; Stoveken et al., 2015). Furthermore, synthetic peptides derived from the TA sequences were able to induce a receptor activation (Liebscher et al., 2014; Stoveken et al., 2015; Wilde et al., 2016). Also using synthetic peptides from other aGPCRs led to an increased activity (Demberg et al., 2017).

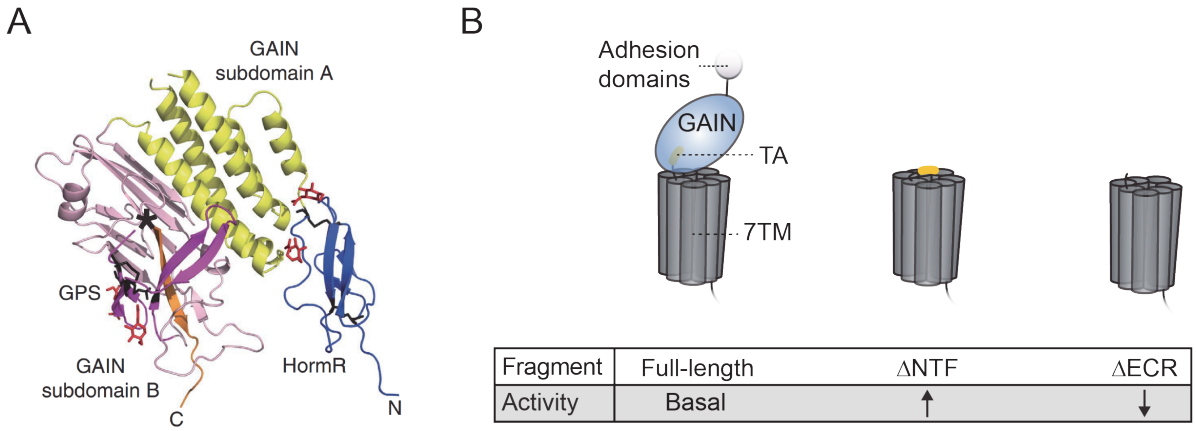

Fig. 3: Tethered agonism of aGPCRs provides a possibility to activate intracellular signaling cascades.

(A) Crystal structure of rat L1 GAIN and hormone receptor motif (HRM) domain. The GAIN domain can be subdivided into a subdomain A consisting of six α-helices and subdomain B consisting of 13 β-strands. Autoproteolytic reaction (asterisk) occurs between the last two β-strands. Furthermore, the crystal structure indicates that the TA is deeply buried inside the remaining GAIN domain. Adapted from Araç et al., 2012**.** (B). Artificial aGPCRs constructs demonstrated the activation of downstream signaling by tethered agonism. Signaling assays revealed a high activity for ΔNTF aGPCRs (exposed TA) compared to a basal activity for full-length receptors (buried TA) and absent activity for ΔECR receptors (no TA).

Interestingly, the crystal structure of the cleaved L1 GAIN domain showed that the TA is deeply buried inside the remaining domain, leading to the question of how the TA is

able to successfully activate the receptor. Current working models have different ideas on how the activation of aGPCRs is mediated through the TA.

The first model, termed dissociation model, describes the separation of the NTF and the CTF, which releases the buried TA (**Fig. 4**). The hydrophobic nature of the TA triggers the interaction with the 7TM domain leading to the stabilization of an active receptor conformation. However, this model is inapplicable for aGPCRs, which naturally display a cleavage-deficiency (Hamann et al., 2015). In addition, the mechanism of tethered agonism was already confirmed for naturally non-cleaved GPR114 (ADGRG5/G5) through *in vitro* signaling assays (Wilde et al., 2016). Furthermore, *in vivo* experiments regarding the receptor activity of invertebrates Latrophilin homologs CIRL and LAT-1 indicated no negative effect due to an abolished self-cleavage (Prömel et al., 2012; Scholz et al., 2017). These findings lead to a second model describing the successful activation of aGPCRs through the TA. This so-called non-dissociation model suggests the interaction of the TA and the 7TM domain upon a conformational change of the GAIN domain without the separation of the heterodimer.

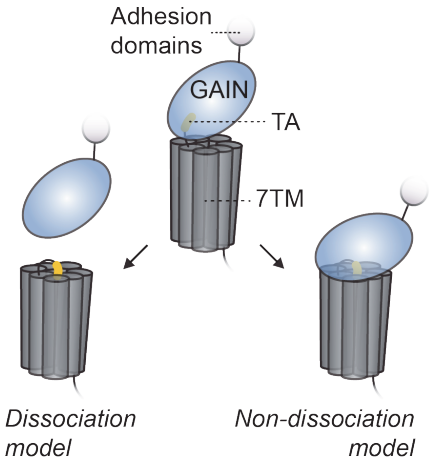

Fig. 4: Possible signaling models for TA-dependent activation of aGPCRs.

Hypothetical models describe the conformational response of an aGPCR due to a mechanical stimulation and/or ligand binding. Stimulation results in a (1) dissociation- or (2) non-dissociation-mediated activation. (1) Separation of NTF and CTF or (2) conformational/ distance change of the GAIN-7TM domain tandem leads to a release of buried TA and subsequent interaction with the 7TM domain.

In addition, the mechanism of a TA-independent activation was observed for GPR56 (ADGRG1/G1) and BAI1 (ADGRB1/B1) (Kishore et al., 2016; Kishore and Hall, 2017; Salzman et al., 2017). B1 lacking the ECR displayed an increased activity in various signaling assays, indicating a receptor activation independent of the TA (Kishore et al.,

2016). However, the activity of G1 ranged from increased to decreased in dependency of the used signaling assay (Kishore et al., 2016). These findings support the idea that the activation of several downstream signaling pathways is TA-independent, whereas others are TA-dependent (Kishore et al., 2016). In addition, the TA-independent signaling of G1 using synthetic ligands interacting with the ECR (Salzman et al., 2017), suggests that the activation mechanisms of aGPCRs are versatile and complex.

Most of the experiments regarding the discovery that aGPCRs are activated by tethered agonism were based on artificially truncated receptor variants lacking the NTF (Liebscher et al., 2014; Stoveken et al., 2015). In contrast, the physiological stimuli (e.g. ligands, force) for the activation of aGPCRs through the release of the TA are still unknown for the majority of aGPCRs. However, previous findings suggested the involvement of aGPCRs in mechanosensation (Scholz et al., 2016). The *Drosophila melanogaster* homolog CIRL is, amongst other neuron populations, expressed in the chordotonal neurons, which offers extero- and proprioceptive functions (Scholz et al., 2017, 2015). *In vivo* data revealed the modulation of ionotropic receptor currents and the downregulation of cAMP levels in sensory neurons upon mechanical stimulation of CIRL, which directly demonstrated the molecular function of CIRL as a potential mechanosensor (Scholz et al., 2017, 2015). Interestingly, the molecular composition of the ECR, which includes a broad spectrum of adhesive folds, implies the involvement of membrane- or matrix-fixed ligands to mediate the mechanical forces into signaling. Hints therefore were observed in the dynamic activation of GPR126 (ADGRG6/G6) through a combination of mechanical forces and the binding of his natural ligand laminin-211 (Petersen et al., 2015).

Furthermore, mechanosensation has also been linked to human disorders. A prominent example is a rare autosomal dominant form of vibratory urticaria (VBU). Affected patients carry E2 receptors with a C492Y mutation within the GAIN domain. This mutation causes dermal hives and increased histamine levels due to enhanced degranulation of mast cells. Symptoms are triggered by vibratory stimulation of the skin. The destabilization of the NTF-CTF heterodimer was hypothesized as the molecular mechanism, leading to an increasing separation (Boyden et al., 2016). Later in this thesis, I will further focus on the investigation of the C492Y mutation in the E2 receptor and its influence on the GAIN domain conformation.

In summary, the experimental data indicate the existence of two different TA-dependent activation models, which are mediated by mechanical stimulation and/or ligand interaction. Furthermore, these models are not mutually exclusive, which leads to the assumption of a context dependent co-existence, e.g. ligand type, type and strength of the mechanical stimuli, and cellular localization of the aGPCR. In addition,

the observation of TA-independent signaling modes implies the versatility of aGPCRs activation mechanisms.

4.4 ADGRE5 as a model aGPCR

E5 belongs to the aGPCR subfamily E, one of the most investigated subfamilies. In 1995, E5 was the first described aGPCR alongside E1 (Baud et al., 1995; Hamann et al., 1995). Already then it was noted that these receptors contain a 7TM domain and several epidermal growth factor (EGF)-like domains at the N-terminus, accordingly the name of this receptor family EGF-7TM was chosen (McKnight and Gordon, 1996). Over the past years, several other members of this family were discovered in vertebrates, leading to presently five members. All members indicate a high similarity in the structural composition of the NTF consisting of 2-5 consecutive EGF-like domains (Krishnan et al., 2016).

4.4.1 Structure of ADGRE5

E5 comprises the common structural features of the aGPCR family: an ECR, a 7TM domain and an ICR. The ECR consists of EGF-like domains and the GAIN domain. Like most aGPCRs, E5 is also cleaved by an autoproteolytic reaction during the protein maturation (Gray et al., 1996). However, the self-cleavage can be inhibited by a single point mutation of the cleavage tripeptide HL↓S either to ALS, HLA or HLG (Hilbig et al., 2018; Hsiao et al., 2011; Yang et al., 2017). Alternative RNA splicing of E5 leads to the existence of three isoforms in humans, differing in their number of EGF domains (Kwakkenbos et al., 2004) (**Fig. 5A**). The EGF domain at the N-terminal end without the ability of calcium-binding is present in all isoforms, whereas the number of remaining calcium-binding EGF domains ranges from 2-4 (Kwakkenbos et al., 2004). Interestingly, E2 shows a high similarity in the arrangement of the NTF and, additionally in the sequence of the EGF domains with a difference of only three amino acids when compared to E5 (Lin et al., 2000). Furthermore, EGF domains are also present in other aGPCRs subfamilies, e.g. CELSRs (Krishnan et al., 2016). A PSD-95/discs-large/ZO-1 (PDZ)-binding motif (PBM) consisting of ASESGI is present at the C-terminal end and is highly phosphorylated after mechanical stimulation, resulting in a disrupted binding to scaffolding proteins and, consequently, a promoted cellular detachment (Hilbig et al., 2018).

In contrast to other members of the aGPCR family, a number of ligands are known for E5 (**Fig. 5B**). The glycosylphosphatidylinositol (GPI)-anchored CD55, which is expressed on most leukocytes, was the first ligand described to bind E5 (Hamann et

al., 1996). Further characterizations of the CD55-E5 interaction revealed the binding of CD55 to the first two EGF domains, whereas the third EGF domain is important for a successful binding (Hamann et al., 1998). Moreover, larger E5 isoforms containing four or five EGF domains showed a reduced binding affinity for CD55 (Hamann et al., 1998). Interestingly, despite the high sequence similarity of the EGF domains of E5 and E2, CD55 binds specifically to E5 (Lin et al., 2001, 2000). Another ligand of E5 is the glycosaminoglycan chondroitin sulfate B, which binds to the EGF4 domain of E5 and E2 (Kwakkenbos et al., 2005). Additionally, a GPI-anchored surface protein named CD90 interacts with the GAIN domain (Wandel et al., 2012). The integrins α5β1 and αvβ3 bind to the RGD motif, which is located near the N-terminal end of the GAIN domain (Wang et al., 2005).

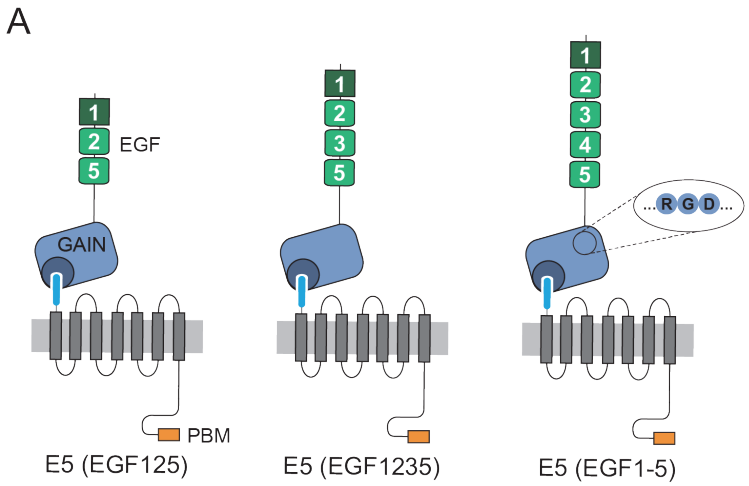

B

Ligand	Interaction
CD55	EGF12
Chondroitin sulfate B	EGF4
CD90	GAIN
α5β1, αvβ3	RGD

Fig. 5: Human E5 comprises three isoforms differing in the number of EGF-like domain repeats and interactions with known ligands.

(A) Schematic illustration of three known E5 isoforms resulting through alternative RNA splicing. The ECR contains one EGF-like domain (dark green) and an isoform-depending number of calcium-binding EGF-like domains (light green). The GAIN domain of E5 includes an RGD motif. A PBM is located at the C-terminal end. (B) Several ligands and their interaction sites are known for E5. CD55 interacts with the EGF1-EGF2 domain tandem, chondroitin sulfate B binds the EGF4 domain, CD90 binds to the GAIN domain, whereas α5β1 and αvβ3 integrins interact with the RGD motif.

4.4.2 Functions of ADGRE5

Native E5 protein is mostly expressed in smooth muscle cells and a variety of cell types of the immune system, e.g. macrophages, dendritic cells, T- and B-cells (Hamann et al., 2016; Jaspars et al., 2001). Based on its expression pattern in different cell types of the immune system and/or the interaction with matricellular ligands (**Fig. 5B**), E5

was found to play a role in immune processes (Lin et al., 2017), angiogenesis (Wang et al., 2005) and cancer (Aust et al., 2016).

The expression and presence of E5 is upregulated at sites of inflammation, indicating its important role in the immune response (Leemans et al., 2004). For example, E5 expression correlates with the lesion stages of multiple sclerosis brain tissue (Visser et al., 2002). In addition, altered expression levels of CD55 suggested the involvement of the CD55-E5 interaction in the inflammatory processes of multiple sclerosis (Visser et al., 2002).

Furthermore, *in vitro* experiments verified the strong binding of α5β1 integrin to the GAIN domain-located RGD motif of E5 (Wang et al., 2005). Interestingly, it is known that an antagonist treatment of α5β1 integrin results in an abolished angiogenesis, which verified its involvement in this process (Kim et al., 2000). In addition, the involvement of E5 in inflammation-dependent angiogenesis through the RGD-mediated α5β1 integrin interaction was observed by *in vivo* assays indicating an increased vascularization after treatment with the recombinant E5 NTF (Wang et al., 2005).

E5 is involved in a broad spectrum of cancer types including thyroid, gastric, pancreatic, esophageal, colorectal, prostate, gall bladder, breast, glioblastoma and leukemia (Aust et al., 2016). Interestingly, the involvement of E5 in cancer often correlates with the presence of the EGF1-EGF2 domain tandem interacting ligand CD55. In pancreatic cancer the expression levels of E5 and CD55 are highly upregulated (He et al., 2015), which was also observable in other cancer types such as primary gallbladder carcinoma (Wu et al., 2012). However, the functional mechanism of this co-expression is still unknown and has to be further analyzed. In addition, experiments regarding E5 expression and signaling in prostate cancer revealed an interaction with $G\alpha_{12/13}$ to increase RhoA levels (Ward et al., 2011).

In summary, the presence and modified expression levels of E5 and other members of the aGPCR family in immune reactions, angiogenesis and cancer point to a prospective pharmacological target in the therapy of related diseases.

4.5 Fluorescent labeling of proteins

In this thesis, I focused on the use of different labeling methods for aGPCRs, which will be introduced in more detail below. In general, fluorescence-based labeling encompasses a broad toolbox of different techniques providing a non-invasive method to analyze biological processes *in vitro* and *in vivo*. The fluorescent labeling of proteins allows the visualization of protein transport and localization, intra- and intermolecular

interactions and conformational changes using specific assays (Toseland, 2013). Depending on the question and the associated experiments, the type of fluorescent labeling technique is more or less suitable for this.

4.5.1 Genetically encoded fluorescent proteins

The most common method for live cell imaging is the direct fusion of genetically encoded fluorescent proteins to the target protein (**Fig. 6A**), which enables a defined stoichiometry. The green fluorescent protein (GFP, ~27 kDa) was discovered and isolated from *Aequorea victoria* (Shimomura et al., 1962). Later, its cDNA was cloned (Prasher et al., 1992) and successfully expressed in pro- and eukaryotic cells being used as a gene expression marker (Chalfie et al., 1994). Over the past years, a library of fluorescent proteins with additional wavelengths, increased photon stability and higher brightness has been discovered (Toseland, 2013). Prominent examples are the cyan fluorescent protein (CFP) and the yellow fluorescent protein (YFP), which based on their physical properties are widely used in Förster resonance energy transfer (FRET) approaches (Bajar et al., 2016). FRET describes the non-radiative energy transfer via dipole-dipole interactions from an excited donor fluorophore to an acceptor fluorophore, resulting in the emission of photons (Förster, 1948). Efficiency of the energy transfer (FRET efficiency) depends on the distance between the donor and the acceptor fluorophores, allowing the use of this technology as a spectroscopic ruler (Stryer, 1978). Typically, FRET occurs between 1-10 nm, which offers an ideal method to investigate intra- and intermolecular interaction, e.g. conformational changes or oligomerization (Bajar et al., 2016). Beside FRET approaches, genetically encoded fluorescent proteins are important for protein counting regarding their provided defined stichometry (Toseland, 2013).

4.5.2 Immunofluorescence staining

Another widely used labeling method is the immunofluorescence (IF) staining using antibodies (**Fig. 6B**). IF staining is a very old technique, which was first described in 1941 for fluorescent β-anthryl-carbamide conjugated to anti-*pneumococcus* strain III serum (Coons et al., 1941). After years of improvements regarding antibody production, fluorescent dyes and microscopy, we are now able to resolve small subcellular structures like single microtubule filaments (~25 nm) using immunofluorescence combined with super-resolution microscopy approaches (Heilemann et al., 2008; van Ooij, 2009). Mostly, IF staining is used with fixed samples. However, antibodies directly conjugated to fluorophores are well suitable for live cell imaging. An advantage of IF labeling is the customized production of specific

antibodies recognizing an epitope within the target protein, while the additional introduction of a tag is not necessary. However, the disadvantage of antibodies is their comparatively large size of ~150 kDa (IgG) and the potentially linked structural hindrance of the target protein. A smaller option are nanobodies, which have a size of ~15 kDa and comprise a single variable domain of heavy-chain-only antibodies mainly from *camelidae* (Mitchell and Colwell, 2018). Even more, small antibody mimics like monobodies (~10 kDa) are an ideal alternative to classical antibodies. In contrast to anti- and nanobodies, the nature of monobodies is derived from the human fibronectin type III domain representing structural homology to the immunoglobulin domain (Koide and Koide, 2006).

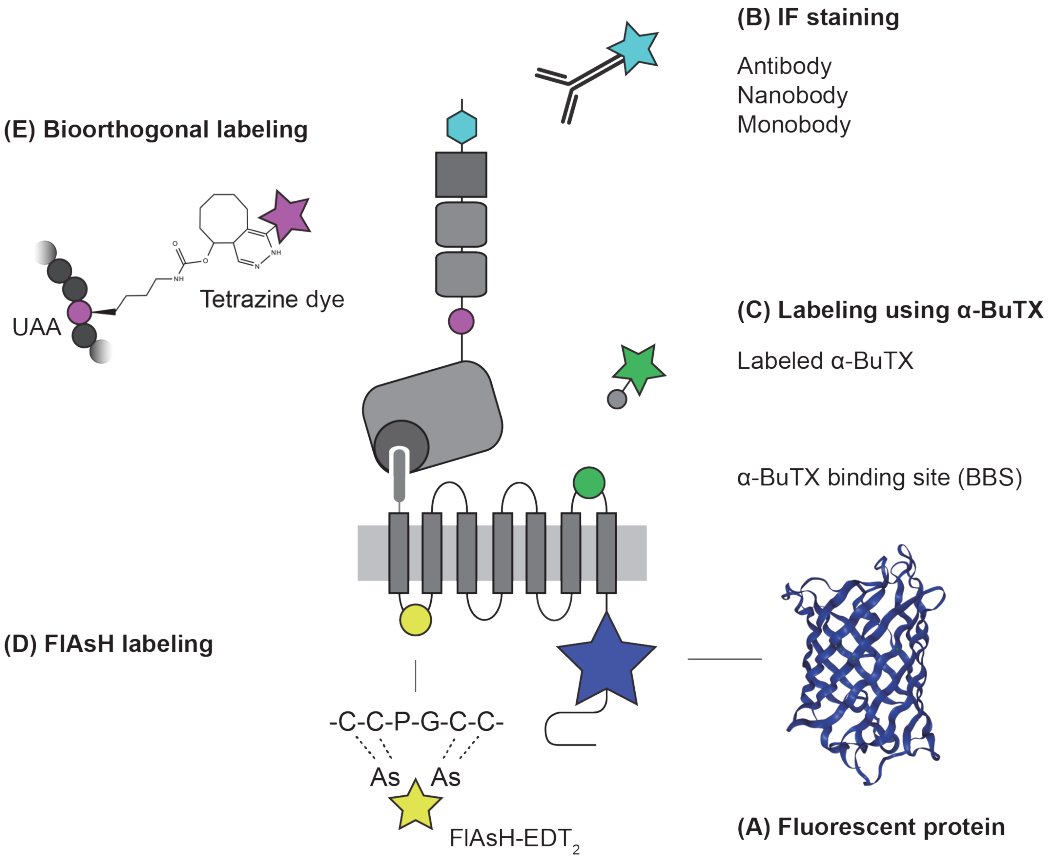

Fig. 6: Overview of common live cell labeling methods.

(A) Labeling using genetically encoded chromophores (e.g. GFP) fused to the target protein. Crystal structure of GFP adapted from Ormö et al., 1996. (B) IF staining using fluorescently labeled antibodies, nanobodies or monobodies (antibody mimics) directed against an antigen. (C) BBS tag fused to the target protein binds irreversibly fluorescently labeled α-BuTX. (D) Labeling of tetracysteine sequences (e.g. CCPGCC) through membrane-permeable FlAsH-EDT_2. (E) Labeling using bioorthogonal click chemistry comprises the incorporation of an UAA and the subsequent labeling of this UAA by a small dye (e.g. tetrazine dye derivatives).

4.5.3 Labeling using fluorescently labeled toxins

The incorporation of peptide tags interacting with toxins provide a further method for the fluorescent labeling of proteins (**Fig. 6C**). Peptides from animal venom are commonly used as therapeutic drugs, insecticides and cosmetics (Pennington et al., 2018). The small size and their high selectivity and affinity set the ideal basis for labeling approaches. A commercially available fluorescently labeled representative toxin is the ~8 kDa small α-Bungarotoxin (α-BuTX), a neurotoxin found in the snake venom of *Bungarus multicinctus* (Chang and Lee, 1963). α-BuTX acts as a competitive antagonist binding with high affinity and specificity to the α-subunit of postsynaptic nicotinic acetylcholine receptors (Nirthanan and Gwee, 2004). Further screens for an optimized α-Bungarotoxin binding site (BBS) using a phage-display peptide library revealed a collection of peptide sequences able to bind α-BuTX (Balass et al., 1997). Finally a 13 amino acid motif, WRYYESSLEPYPD, was found to bind α-BuTX with the highest affinity compared to the previously investigated peptide sequences (Kasher et al., 2001). This peptide sequence has already been successfully used for the visualization of GPCRs (Sergin et al., 2017; Wilkins et al., 2008). The broad spectrum of fluorescently labeled and commercially available α-BuTX variants ensures its use in different fluorescence-based approaches, e.g. FRET analysis. Furthermore, the membrane-impermeability of α-BuTX provides the ability to distinguish between surface and intracellularly located proteins (Hannan et al., 2013).

4.5.4 Fluorescent labeling of tetracysteine motif

A prominent and minimally invasive labeling method provides the binding of fluorescein arsenical hairpin binder, bis-EDT adduct (FlAsH-EDT_2) to a tetracysteine motif (CCXXCC) (Griffin et al., 1998) (**Fig. 6D**). The naturally non-fluorescent FlAsH-EDT_2 has a size of only ~0.7 kDa and becomes fluorescent after binding to the tetracycsteine motif (Griffin et al., 1998). The chemical background to this reaction is the reversible covalent bond between the arsenic compounds of FlAsH-EDT_2 and the thiols groups of the tetracycsteine motif (Griffin et al., 1998) Further analysis on the labeling efficiency of FlAsH demonstrated increased affinities using a hairpin forming CCPGCC motif (Adams et al., 2002). Optimizations of the flanking regions of the tetracysteine motif led to the 12 amino acid motifs, HRWCCPGCCKTF and FLNCCPGCCMEP, which provide a higher fluorescence signal and stronger binding (Martin et al., 2005). Along the yellow fluorescent FlAsH, the red fluorescent ReAsH is prominently used (Adams and Tsien, 2008). The yellow fluorescent nature of FlAsH provides the use for FRET analysis as an acceptor fluorophore in combination with CFP. The advantage of FlAsH over YFP as an acceptor for CFP lies in its reduced size of ~0.7 kDa compared

to 27 kDa providing less structural and functional hindrance and, at the same time, greater FRET signals (Hoffmann et al., 2005).

4.5.5 Fluorescent labeling using bioorthogonal click chemistry

Live cell labeling using bioorthogonal click chemistry represents the currently least space demanding labeling method (~0.5 kDa) used in this thesis (**Fig. 6E**). The basic principle is the specific and spontaneous reaction of non-toxic compounds in aqueous solutions under physiological conditions (Kolb et al., 2001). In detail, the necessary compounds for live cell labeling comprise unnatural amino acids (UAAs) bearing strained alkenes and tetrazine dye derivatives (Nikić et al., 2016, 2015). The incorporation mechanism of these UAA at a specific site within the target protein is ensured by genetic code expansion (Nikić et al., 2016, 2015). A detailed overview of the molecular background of this method will be highlighted later in this work (see 6.3.3). Briefly, the incorporated UAA reacts with a tetrazine dye derivative within several minutes via a strain-promoted inverse electron-demand Diels-Alder cycloaddition (SPIEDAC) (Blackman et al., 2008; Nikić et al., 2015). A variety of tetrazine dye derivatives are available, differing in their spectroscopic properties and cell permeabilities, therefore providing a toolbox for labeling of intra- and extracellular proteins (Beliu et al., 2019).

4.6 Aim of this study

Labeling of proteins using fluorescent proteins or dyes are common approaches to investigate their functional behavior and properties. However, there is a broad spectrum of labeling methods available, differing in sensitivity, specificity and spatial size. Interestingly, the label size and position are crucial to avoid a negative effect on the protein function due to structural hindrance. In the past, fluorescent labeling already helped a better understanding of GPCRs regarding their cellular localization, interaction partners, oligomerization and conformational changes. In prospect, methods with minor effects on the physiological behavior of a receptor, such as FlAsH labeling or the labeling using bioorthogonal click chemistry, will further shed light on this.

Interestingly, most labeling methods have not been utilized for the aGPCRs so far. Reason for this is the extraordinary architecture of aGPCRs, which comprises a variety of N-terminal domains. These domains share physiological functions for the aGPCRs, making it difficult to find suitable labeling positions without hindrance of the receptor. However, the molecular mechanism behind aGPCRs activity and signaling are still

unknown. Therefore, the screening of suitable labeling techniques and their ideal insertion sites within the aGPCR architecture are of great interest to investigate aGPCRs in extensive detail.

Ideally, I will find a set of suitable fluorescence-based labeling methods, which provide the potential for functional and structural analyses of aGPCRs, contributing to improve the general knowledge about this receptor family relating to the cellular localization and the structural mechanism of its activation including the tethered agonism. Additionally, I will investigate the potential existence of alternative cleavage events over than the GAIN domain-mediated cleavage.

5 Materials and Methods

5.1 Solutions

All chemicals and reagents used in this thesis were, if not stated otherwise, purchased from Merck, Sigma-Aldrich or Carl Roth.

Solutions:

10x PBS	74 g NaCl 12.46 g Na_2HPO_4 x $2H_2O$ 4.14 g NaH_2PO_4 x H_20 ad 1 l dH_2O pH 7.4
4 % (w/v) PFA	8 g paraformaldehyde (PFA) in 15 ml dH_2O (55 °C) 10 drops 2 N NaOH 20 ml 10x PBS ad 200 ml dH_2O pH 7.4
x % PBS-T	1x PBS + x % (v/v) Tween-20
x % PBT	1x PBS + x % (v/v) Triton X-100
Running buffer (Western blot)	3.03 g Tris 14.4 g glycine 1.0 g SDS ad 1 l dH_2O
Labeling buffer (FlAsH)	2.4 g HEPES 8.7 g NaCl 1.85 g KCl 2 ml MgCl (1 M) 4 ml $CaCl_2$ (1 M) 1.8 g Glucose ad 1 l dH_2O pH 7.3

Imaging buffer (FlAsH)	2.4 g HEPES 8.12 g NaCl 0.4 g KCl 1 ml MgCl (1 M) 2 ml $CaCl_2$ (1 M) ad 1 l dH_2O pH 7.3
TEV buffer	50 mM Tris 138 mM NaCl 1 mM 1,4-dithiothreitol pH 8.0

5.2 Molecular biology

5.2.1 Polymerase chain reaction-based cloning

Polymerase chain reaction (PCR) is a method used to amplify linearized DNA fragments using oligonucleotide DNA primers (produced by Eurofins Genomics or Microsynth Seqlab).

Inverse PCR was performed using Q5 High-Fidelity DNA polymerase (New England Biolabs) according to manufacturer´s recommendations. Site-directed mutagenesis (SDM) PCR was performed using *Pfu* DNA polymerase (Agilent) or *PfuUltra* High-Fidelity DNA polymerase (Agilent) according to manufacturer´s recommendations. Sequence- and ligation-independent cloning (SLIC) PCR was performed using AccuStar DNA polymerase (Eurogentec) or Q5 High-Fidelity DNA polymerase according to Li and Elledge, 2012.

5.2.2 DNA restriction digest

Type II restriction endonucleases were purchased from New England Biolabs. Digest of plasmid DNA was performed for a minimum duration of 1 h at 37 °C in the provided buffers.

5.2.3 Agarose gel electrophoresis and DNA purification

Linearized DNA fragments resulting from restrictions digests or PCRs were size-dependently separated by gel electrophoresis using an electrophoresis unit. Samples were mixed with loading buffer and loaded on 0.5-2 % (w/v) agarose gels (Biozym

Scientific). To visualize the separated DNA fragments, samples were excited at 600 nm by a diffused light source of the Odyssey Fc Imaging System (Licor). Subsequently, the DNA fragments were extracted from the gel and purified using QIAquick Gel Extraction Kit (Qiagen). All procedures were performed according to manufacturer's manual.

5.2.4 DNA ligation

DNA fragments were ligated at 16 °C overnight using T4 DNA ligase (Roche). The backbone-containing fragment was dephosphorylated using Antarctic phosphatase (Roche).

5.2.5 Transformation into competent bacterial cells

To amplify plasmid DNA, the DNA was transfected into chemically competent XL1-Blue cells of the genotype:

recA1 endA1 gyrA96 thi-1 hsdR17 supE44 relA1 lac [F´ *proAB lacI*^{q}*ZΔM15* Tn*10* (Tet^{r})]

5.2.6 DNA isolation

Plasmid DNA of XL1-Blue cells was isolated using QIAprep Spin Miniprep Kit (Qiagen) or CompactPrep Plasmid Midi Kit (Qiagen). All procedures were carried out according to manufacturer´s recommendations.

5.2.7 DNA sequencing

Plasmid DNA was externally sequenced by Eurofins Genomics or Microsynth Seqlab.

5.2.8 Plasmid and primer list

Detailed information of kindly provided plasmids (**Supp. Tab. 1**), generated plasmids (**Supp. Tab. 2**) and used primers (**Supp. Tab. 3**) are listed in the supplemental information. In this study used receptors based on specific isoforms: *Drosophila* CIRL constructs based on isoform E, human E2 constructs based on EGF1-5 isoform, human E5 constructs based on EGF125 isoform, rat L1 constructs based on isoform CL1AA and human B3 constructs based on isoform A. Constructs only used for cloning are indicated as subclones. Additionally, some constructs were externally synthesized by GenScript (Leiden, Netherlands).

5.3 Cell culture

5.3.1 Maintenance and seeding

Human embryonic kidney 293 cells (HEK-293, RRID:CVCL_0045), HEK-293T cells (RRID:CVCL_0063) and COS-7 cells (RRID:CVCL_0224) were maintained in petri dishes (#664160, Greiner Bio-One) with cell growth medium, which consists of Dulbecco's modified eagle medium (DMEM, #11995065, Gibco) containing 10 % (v/v) fetal bovine serum (#10500, Gibco) and 1 % (v/v) penicillin-streptomycin mixture (#15140122, Gibco). Mammalian cells were incubated in a 5 % CO_2 atmosphere at 37 °C. Cells were grown to a nearly confluent cell layer and then subcultured at a 1:20 (HEK-293, HEK-293T) or 1:10 ratio (COS-7) typically twice a week (Monday and Friday). For imaging experiments cells were seeded before transfection on cover slides in a 24 well plate (#662160, Greiner Bio-One) or directly on a µ-slide 8 well (#80826, ibidi). For ELISA experiments cells were seeded on 96 well plates (#655090 or #655098, Greiner Bio-One). To produce a high protein amount for biochemical analysis (Western blot), cells were seeded on 6 well plates (# 657160, Greiner Bio-One). Prior to seeding the dishes were coated with 0.01 % (w/v) poly-L-Lysine (#P9404, Sigma-Aldrich) for 30-60 min at RT.

5.3.2 Transfection

Mammalian cells were transfected at 60-80 % confluency with the transfection reagent Lipofectamine 2000 (#11668019, Invitrogen) with the suitable 1:1 plasmid/reagent mixture (according to manufacturer´s recommendations) and incubated for at least 24 h at 37 °C and 5 % CO_2. The plasmids encoding for constructs with an amber stop codon (TAG) were mixed in a 1:1 ratio with pcDNA3.1-$tRNA^{Pyl}$/NESPylRS^{AF} plasmid (RS_{Lemke}) (Nikić et al., 2016) or pcDNA3.1-*Mb*PylRS^{F}/$tRNA^{M15}$ plasmid (RS_{Coin}) (Serfling et al., 2018). These plasmids were kindly provided by Edward Lemke and Irene Coin. In addition, the UAA trans-Cyclooct-2-en – L - Lysine (TCO*A, #SC-8008, SiChem) was supplemented in the cell growth medium at a final concentration of 250 µM, diluted 1:4 with 1 M HEPES. After 8 h of incubation, the cell growth medium was exchanged to fresh cell growth medium without added UAA. The cells were incubated for at least 16 h before labeling.

5.3.3 Surface ELISA

HEK-293 or HEK-293T cells were fixed with 4 % (w/v) PFA at RT for 10 min. Next, cells were blocked with 1x PBS containing 5 % (v/v) goat serum (#G6767, Sigma-Aldrich) at RT for 30-60 min. Then, cells were incubated for 1 h at RT with 1:1000

dilution of α-HA-Peroxidase (RRID: AB_390917) in 1x PBS containing 5 % (v/v) goat serum. After at least three washing steps using 1x PBS, the cells were incubated with a substrate solution consisting of 1 mg/ml o-phenylenediamine and 1 µl/ml hydrogen peroxide solved in a 0.05 M citric acid and 0.05 M disodium phosphate solution (pH 5) at RT. The reaction was stopped within 10 min using 2.5 M sulfuric acid. The absorbance of the supernatants was measured at 490 nm using a multimode-reader (GloMax-Multi+, Promega or SpectraMax M, Molecular Devices). Whole cell ELISA was performed using 0.05 % PBT instead of 1x PBS.

5.4 Protein biochemistry

5.4.1 DAPT treatment

Prior to the chemical lyse and following biochemical analysis via Western blot, HEK-293T cells were treated with 10 µM N-[N-(3,5-Difluorophenacetyl)-L-alanyl]-S-phenylglycine t-butyl ester (DAPT, #D5942, Sigma-Aldrich), which was solved in dimethyl sulfoxide (DMSO) and directly added to the transfection mixture. Cells treated with DMSO served as a control. Treated cells were incubated with these mixtures for 1 day at 37 °C and 5 % CO_2.

5.4.2 Thrombin & TEV proteolysis

HEK-293T cells were treated with 7.5 U thrombin protease (#T9326, Sigma-Aldrich) in DMEM for 1 h at 37 °C and 5 % CO_2. Cells treated exclusively with DMEM served as a control. Protein samples were harvested and biochemically analyzed via Western blot.

In a further experiment, HEK-293T cells were treated with 10 µM TEV protease, which was produced in-house, in TEV buffer (see 5.1) for 1 h at 30 °C. Next, cells were washed once with TEV buffer. Cells treated exclusively with TEV buffer served as a control. Protein samples were harvested and biochemically analyzed via Western blot.

5.4.3 Protein harvest

HEK-293T cells were chemically lysed with 200 µl M-PER buffer (#78503, Thermo Scientific) containing 1:100 protease inhibitor (#P8340, Sigma-Aldrich) on an orbital shaker for 5 min at 4 °C. The lysate was collected and centrifuged at 15.200 xg for 5 min at 4 °C. Supernatants were collected and stored at -80 °C.

5.4.4 SDS-PAGE

Supernatants were diluted 4:1 with 4x protein loading buffer (#928-40004, Licor) containing 10 % (v/v) β-mercaptoethanol. Samples were loaded on a Novex 4-12 % Tris-Glycine Mini Gel (Invitrogen) or a Novex 8-16 % Tris-Glycine Mini Gel (Invitrogen), which were applied in a Mini Gel Tank (Invitrogen). Electrophoresis was performed in Running buffer (see 5.1) at RT.

5.4.5 Western blot

Protein bands were transferred from the gel on a nitrocellulose membrane with 0.2 µm pore size (Invitrogen). Transfer was performed in an iBlot 2 Dry Blotting System (Invitrogen). After the transfer, the membrane was incubated with a blocking solution on a shaker for 1 h at RT. Blocking solution consisted of a 1:2 dilution of blocking buffer (#927-40000, Licor) and 1x PBS. Next, the membrane was treated with 1:1000 rabbit-α-HA (RRID:AB_1549585), 1:1000 mouse-α-V5 (RRID:AB_2792973) and 1:5000 mouse-α-E7 (RRID:AB_2315513) diluted in blocking solution containing 0.1 % (v/v) Tween-20 on a shaker overnight at 4 °C. Following at least three washing steps with 0.1 % PBS-T, the membrane was incubated with 1:15000 IRDye 680RD Goat anti-Rabbit IgG (#926-68071, Licor) and 1:15000 IRDye 800CW Goat anti-Mouse IgG (#926-32210, Licor) diluted in blocking solution containing 0.1 % (v/v) Tween-20 on a shaker for 1 h at RT. After the membrane was washed several times with 0.1 % PBS-T, the protein bands were detected by the excitation at 685 nm and 785 nm using a solid-state diode laser of the Odyssey Fc Imaging System (Licor).

5.5 Labeling techniques

5.5.1 Labeling with CellMask Orange

Living HEK-293 cells were stained with 1x CellMask Orange (#C10045, Invitrogen) diluted in 1x PBS for 5 min at RT. Cells were washed three times with 1x PBS before imaging in 1x PBS.

5.5.2 Immunofluorescence staining

HEK-293 and HEK-293T cells were immunolabeled using antibodies listed in **Tab. 1**.

Tab. 1: Antibodies used for IF staining.

Antibody	Dilution	Reference
rat-α-HA	1:500	RRID:AB_390918
mouse-α-V5	1:500	Invitrogen
rabbit-α-ADGRE5	1:200	RRID:AB_1846345
mouse-α-HA-Alexa 488	1:500	RRID:AB_2610624
mouse-α-Calnexin-Alexa 488	1:500	RRID:AB_2662809
goat-α-rat-Alexa 488	1:250	RRID:AB_2534074
goat-α-mouse-Alexa 488	1:250	RRID:AB_2534088
goat-α-rabbit-Alexa 488	1:500	RRID:AB_143165

To label the HA epitope with rat-α-HA or the V5 epitope with mouse-α-V5, the HEK-293 cells were fixed with 4 % (v/v) PFA for 10 min at RT. Next, cells were blocked for 1 h in 0.1 % PBT containing 5 % (v/v) normal goat serum (NGS, RRID:AB_2336983) at RT. Next, samples were incubated with 1:500 rat-α-HA or 1:500 mouse-α-V5 in 0.1 % PBT containing 5 % (v/v) NGS overnight at 4°C. After at least three washing steps using 0.1 % PBT, the samples were incubated for 2 h at RT with 1:250 goat-α-rat-Alexa 488 or 1:250 goat-α-mouse-Alexa 488 in 0.1 % PBT containing 5 % (v/v) NGS. Again, the samples were washed at least three times with 0.1 % PBT and imaged in 1x PBS afterwards.

Live cell immunolabeling of HEK-293T cells with mouse-α-HA-Alexa 488 was performed by the 1:500 dilution of the antibody in cell growth medium. Cells were incubated for 30 min at 37 °C and 5 % CO_2. After labeling, the cells were rinsed once with fresh cell growth medium and either fixed at RT with 4 % (w/v) PFA for 10 min or directly imaged in live cell imaging solution (#A14291DJ, Invitrogen). Fixed cells were imaged in live cell imaging solution too.

The GAIN domain of E5 was labeled using 1:200 rabbit-α-ADGRE5 diluted in cell growth medium for 30 min at 37 °C and 5 % CO_2. After labeling, the cells were rinsed once with cell growth medium and fixed at RT with 4 % (w/v) PFA for 10 min. Fixed cells were blocked with 1x Dulbecco's phosphate-buffered saline (DPBS, #14190144, Gibco) containing 2 % (w/v) bovine serum albumin (#126593, Sigma-Aldrich) at RT for 1 h and labeled with 1:500 goat-α-rabbit-Alexa 488 overnight at 4 °C. Cells were washed three times with 1x DPBS before imaging in live cell imaging solution.

Procedure for dual labeling via IF labeling and bioorthogonal labeling is described in 5.5.5.

5.5.3 Labeling of tetracysteine motif

HEK-293, HEK-293T and COS-7 cells were FlAsH-labeled according to standardized and published protocol (Hoffmann et al., 2010). Briefly, cells were washed twice with Labeling buffer (see 5.1). Next, 1 ml DMSO and 2.1 µl 1,2-ethanedithiol (EDT) were mixed (solution 1). A mixture of 0.5 µl solution 1 and 0.5 µl FlAsH in 1 ml Labeling buffer were added to each well, resulting in 500 nM FlAsH and 12.5 µM EDT per well. Cells were incubated for 1 h at 37°C. After incubation, the cells were washed once with Labeling buffer. Next, 1 ml DMSO and 42 µl EDT were mixed (solution 2). To remove unspecific FlAsH binding, cells were incubated with a mixture of 0.5 µl solution 2 in 1 ml Labeling buffer per well, resulting in 250 nM EDT per well. Cells were incubated for 10 min at 37°C. After incubation, the cells were washed twice with Labeling buffer. Finally, the cells were imaged in Imaging buffer (see 5.1).

5.5.4 Labeling of α-bungarotoxin binding site

HEK-293T cells were incubated with 1:500 α-BuTX-Alexa 488 (#B13422, Invitrogen) in cell growth medium for 30 min at 37 °C and 5 % CO_2. After one washing step using cell growth medium, the cells were either fixed at RT with 4 % (w/v) PFA for 10 min (confocal imaging) or directly imaged in live cell imaging solution (FRET measurements). Fixed cells were imaged in live cell imaging solution too.

5.5.5 Bioorthogonal labeling

For single bioorthogonal labeling of UAAs, the transfected HEK-293T were labeled with 1.5 µM tetrazine dye derivative H-Tet-ATTO 488 (#CLK-010-02, Jena Bioscience), H-Tet-Cy3 (#CLK-014-05, Jena Bioscience) or H-Tet-Cy5 (#CLK-015-05, Jena Bioscience) in cell growth medium for 30 min at 37 °C and 5 % CO_2. After labeling, the cells were directly imaged in live cell imaging solution or washed once with cell growth medium and fixed at RT with 4 % (w/v) PFA for 10 min. Fixed cells were imaged in live cell imaging solution too.

Dual labeling via IF labeling and bioorthogonal labeling was achieved through a co-incubation of 1.5 µM tetrazine dye derivative and antibody for 30 min at 37 °C and 5 % CO_2. After labeling, the cells were rinsed once with cell growth medium and fixed at RT with 4 % (w/v) PFA for 10 min. The fixed cells were imaged in live cell imaging solution.

Optionally, the endoplasmic reticulum (ER) of fixed cells was stained using mouse-α-Calnexin-Alexa 488. Therefore, the fixed cells were permeabilized for 30 min at RT using 0.05 % PBT containing 5 % (v/v) goat serum. Next, cells were incubated for 1 h

at RT with antibody in 0.05 % PBT containing 5 % (v/v) goat serum. After two washing steps using 1x PBS, the cells were imaged in live cell imaging solution.

5.5.6 Proximity ligation assay

The proximity ligation assay (PLA) is already well established for *Drosophila* larvae using the Duolink In Situ Red Kit Mouse/Rabbit (#DUO92101, Sigma-Aldrich) (Wang et al., 2015). I used the PLA to verify the interaction between Complexin (Cpx) and Bruchpilot (Brp) at the active zone of *Drosophila melanogaster*. Therefore, living third-instar *Drosophila* larvae were dissected in ice-cold hemolymph-like solution (Stewart et al., 1994) and fixed for 15 min at RT using 4 % (w/v) PFA afterwards. Next, third-instar larvae were blocked for 1 h in 0.05 % PBT containing 5 % (v/v) NGS. Next, samples were incubated with 1:500 rabbit-α-Cpx (RRID:AB_2568068) and 1:250 mouse-α-Brp (RRID:AB_528108) antibodies overnight at 4°C. After three 10 min washing steps using 0.05 % PBT, the samples were incubated for 2 h at 37 °C with a 1:5 dilution of α-rabbit PLUS (#DUO92002, Sigma-Aldrich) and α-mouse MINUS (#DUO92004, Sigma-Aldrich) PLA probes, which were added to 5 % (v/v) NGS containing blocking solution. 1:250 α-HRP-Alexa 488 antibody (RRID:AB_2338965) was added to the mixture in order to enable visualization of neuronal membranes. Following two 5 min washing steps with Wash buffer A, samples were treated with ligation solution (1:40 dilution of ligase in ligase buffer) for 1 h at 37 °C. Again, samples were washed twice for 2 min with Wash buffer A. Next, the samples were incubated in amplification solution (1:80 dilution of polymerase in amplification buffer) for 2 h at 37 °C. After two 10 min washing steps using Wash buffer B, samples were washed twice in 0.01x Wash buffer B and kept in Vectashield-H1000 (#H-1000, Vector Laboratories) overnight at 4 °C before mounting and imaging.

5.5.7 Cell vibration

HEK-293T cells were seeded on a µ-slide 8 well, which was coated with 0.01 % (w/v) chondroitin sulfate B (#C3788, Sigma-Aldrich) for 60 min at RT. Transfected HEK-293T cells were labeled with 1.5 µM H-Tet-Cy5 in cell growth medium for 20 min at 37 °C on an orbital shaker at 750 rpm. Control cells were labeled without shaking. After labeling, the cells were washed once with growth medium and fixed at RT with 4 % (w/v) PFA for 10 min before imaging in live cell imaging solution.

5.6 Microscopical techniques

5.6.1 Confocal microscopy

Confocal images were obtained with a LSM5 Pascal microscope (63x/1.25 oil objective and 63x/1.0 water objective, Zeiss) or SP8 micoscope (63x/1.3 glycerol objective and 63x/1.2 water objective, Leica). Single plane images on the LSM5 Pascal were acquired with suitable excitation settings for the respective fluorophore (mTurquoise: diode with 405 nm; EGFP/mVenus/Alexa 488: argon laser with 488 nm; CellMask Orange: helium-neon laser with 543 nm). Images were adjusted for brightness and contrast using Fiji (RRID:SCR_002285).

Single plane images on the SP8 were acquired with suitable settings for the respective fluorophore (mTurquoise: diode with 405 nm or 442 nm; ATTO 488/Alexa 488: argon laser with 488 nm or 496 nm; Cy3/FlAsH/mCitrine: argon laser with 514 nm; mRFP: diode-pumped solid state laser with 561 nm; Cy5: helium-neon laser with 633 nm). Same imaging settings were chosen when receptor variants were compared. Images were adjusted for brightness and contrast using Fiji.

5.6.2 FRET measurements using acceptor photobleaching

Living HEK-293T cells expressing potential FRET sensors were confocally imaged in live cell imaging solution using a SP8 microscope (63x/1.3 glycerol objective). Exemplary intensity curves of mTurquoise and mCitrine were obtained by time-lapse microscopy. The $FRET_{Efficiency}$ was calculated by acceptor bleaching method using FRET AB mode of the Leica Application Suite X (LAS X, RRID:SCR_013673). The acceptor fluorophore was bleached in a region of interest (ROI). The ROI included one transfected HEK-293T cell. Intensity of the donor fluorophore was measured before ($Donor_{Pre}$) and after the bleaching ($Donor_{Post}$).

The Efficiency of intramolecular FRET was quantified as

$$FRET_{Efficiency} = \frac{Donor_{post} - Donor_{pre}}{Donor_{post}}$$

The Efficiency of intermolecular FRET was quantified as

$$FRET_{Efficiency} = \frac{Donor_{corrected\ post} - Donor_{pre}}{Donor_{corrected\ post}}$$

The intensity of $Donor_{Post}$ was corrected by the difference of $Donor_{Post}$ and $Donor_{Pre}$ of the receptor variant containing a single mCitrine (R^{mCit}). The difference was averaged by the number of analyzed cells (n).

$$Donor_{corrected\ post} = Donor_{post} - \frac{1}{n}\sum_{i=1}^{n}(Donor_{post}(R^{mCit}))_i - (Donor_{pre}(R^{mCit}))_i$$

5.6.3 Quantification of imaging data

Quantifications were based on single plane images with an optimized resolution (calculated by LAS X) at a zoom level of 0.75. The intensity of H-Tet-Cy5 signal was measured without accumulation or averaging using the hybrid photodetector of the SP8 microscope (63x/1.3 glycerol objective), which returns linear measurements of single photon counts. Single photon counts of ROIs were calculated with LAS X based on the raw 8-bit images. ROIs were defined as HEK-293T cell patches expressing labeled receptors within the focus level and with intact membrane. ROIs were manually outlined. The sum of all photons above the background noise were calculated and divided through the number of labeled cells within the ROI. Cells transfected with empty vector (EV) served as a negative control to calculate the background noise. The number of labeled cells were manually counted.

5.7 Statistics

ELISA experiments were performed with indicated number of duplicates (n) and each experiment was independently repeated by indicated number (N). Individual measurements were normalized to the empty vector (EV) and the indicated control construct. Normalized datasets with $N \geq 2$ were checked for their Gaussian distribution; depending on the result datasets from individual receptor variants were compared via an unpaired t test or Mann-Whitney test.

Quantification of bioorthogonal H-Tet-Cy5 labels was calculated based on indicated number of images or cells per experiment (n). The experiment was independently repeated by indicated number (N). Individual data points were normalized to the EV and the indicated control construct. Normalized datasets with $N \geq 2$ were tested for normal distribution and depending on the result compared via an unpaired t test or Mann-Whitney test.

Analyses were performed using Prism 7 (RRID:SCR_002798). All graphs show the mean and standard error of the mean (SEM) of normalized datasets.

6 Results

6.1 Introduction of the used receptor nomenclature

In order to better understand which receptor variants have been studied and which changes have been made to the receptor layout, a short nomenclature was introduced (**Fig. 7**).

(1) E5	Short nomenclature of the investigated aGPCR member - CD97/ADGRE5
(2) $E5^{H>A}$	Mutation of the receptor - Mutation of Histine to Alanine within the cleavage tripeptide of E5
(3) mTurq-E5	Fusion of a small protein or tag to the NTF - mTurquoise in the NTF of E5
(4) $E5\text{-}TAG^{ECL1}$	Fusion of a small protein or tag to the CTF - Amber stop codon in the CTF, more presicely in the ECL1 of E5

Fig. 7: Explanation of the introduced nomenclature used in this study to describe receptor variants.

6.2 Selection of a model aGPCR

The aim of this chapter was the identification of a member of the aGPCR family serving as a model receptor to study aGPCR signal transduction using well established and innovative fluorescence-based labeling techniques *in vitro*. The main characteristics of the sought model receptor are its high expression and successful membrane trafficking to the plasma membrane of mammalian cell lines like the human kidney cell lines HEK-293, HEK-293T or the monkey kidney cell line COS-7. These cell lines are commonly used in combination with fluorescence-based approaches because of their high transfection efficiency and reliable protein biosynthesis. In the first step of my thesis, I tested the expression of diverse aGPCRs using fluorescence microscopy and ELISA. All investigated receptor variants in this study were extended with an N-terminal HA tag following the signal peptide (if not stated otherwise), which was used for expression analysis by ELISA using a monoclonal HRP-coupled antibody directed against the HA epitope.

6.2.1 Expression studies of ADGRE5, ADGRF5 and CIRL

Protein expression levels and the cellular localization of three aGPCR members were analyzed: *Drosophila* CIRL, mouse F5 and human E5. Advantages of these aGPCRs regarding functional analyses are the existence of binding partners and the direct evidence of coupling several downstream signaling pathways (Langenhan, 2019). Furthermore, experimental data suggest that these aGPCR members are associated with mechanosensation (Bridges et al., 2013; Hilbig et al., 2018; Scholz et al., 2015). Consequently, we consider them to represent ideal model receptors to analyze the complex activation mechanisms of the aGPCR family.

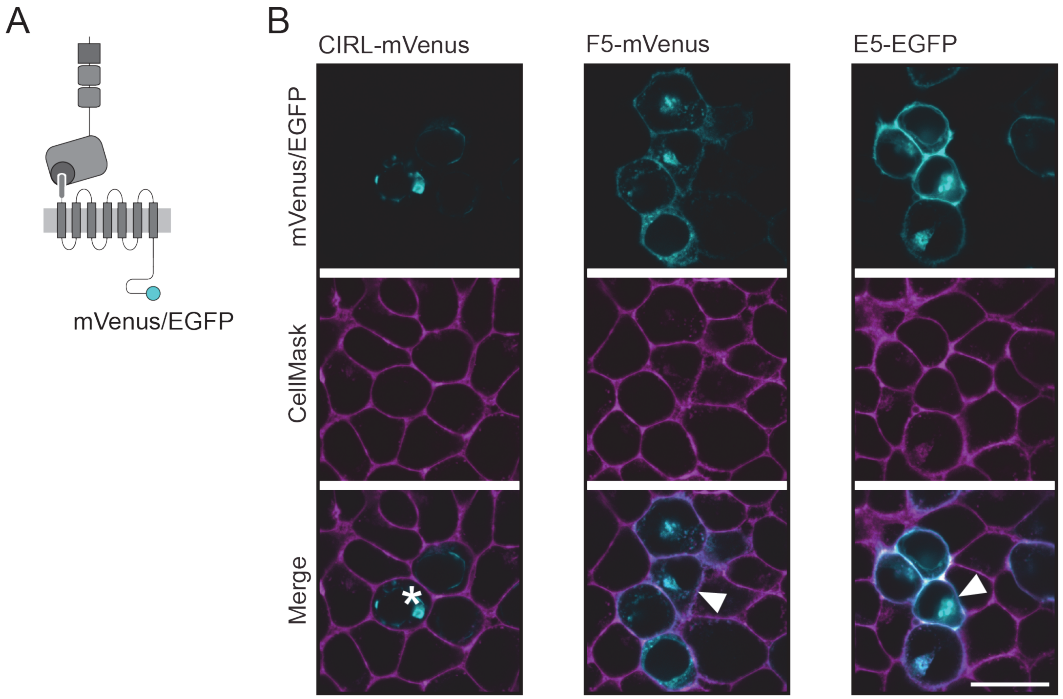

Fig. 8: F5 and E5 are successfully delivered to the plasma membrane of mammalian cells.

(A) Schematic illustration of the aGPCR structure indicates the position of the C-terminally fused mVenus or EGFP. (B) Live cell imaging of HEK-293 cells expressing CIRL-mVenus, F5-mVenus and E5-EGFP (cyan) on a confocal level. The plasma membrane was stained with CellMask Orange (magenta). The merged image reveals surface delivery of F5 and E5 (white arrow), whereas CIRL is not transported to the plasma membrane (white asterisk). Scale bar 20 µm.

In a first setup, I transfected these aGPCR constructs into HEK-293 cells. To visualize the receptor localization within HEK-293 cells, the genetically encoded chromophores mVenus or EGFP were fused to the C-terminal end of the receptors (**Fig. 8A**). I determined the cellular localization of the fusion proteins using confocal microscopy (**Fig. 8B**). Confocal images showed expression of all three aGPCRs in HEK-293 cells.

In addition, a clear visualization of the HEK-293 plasma membrane was ensured using the membrane stain CellMask Orange as a co-marker to analyze the successful cell surface delivery. Overlap between the fluorescence signal of the fusion proteins and the membrane stain revealed a successfully surface delivery of F5 and E5. In contrast, no proper plasma membrane trafficking was observable for CIRL. However, using a different labeling strategy (bioorthogonal labeling, see 6.3.3) showed that a small amount of CIRL was also present at the plasma membrane of HEK-293T cells (**Supp. Fig. 1**).

To further verify the microscopy data, I quantified the surface expression and whole cell expression of CIRL, F5 and E5 by ELISA. The analyzed aGPCRs were cloned in two different mammalian expression vectors (pcDps and pHL-sec), hence for the ELISA experiments the receptors were subdivided into two groups.

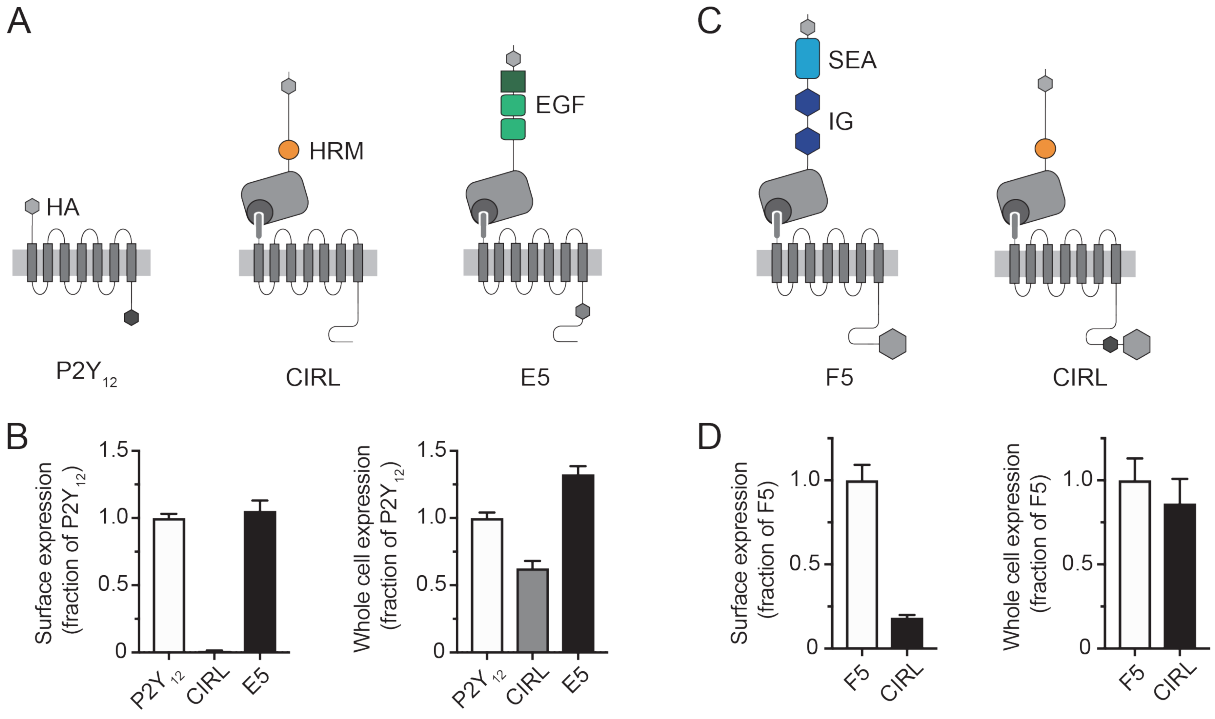

Fig. 9: Quantified expression levels verify the surface delivery of F5 and E5.

(A) Schematic illustrations of $P2Y_{12}$, CIRL and E5 in a pcDps vector backbone. Receptor specific domains (HRM = hormone receptor motif; EGF = epidermal growth factor) are highlighted. (B) Quantification of surface and whole cell expression levels of $P2Y_{12}$, CIRL and E5 in HEK-293 cells by ELISA. Dataset normalized to the expression level of $P2Y_{12}$. Data are shown as mean ± SEM (N = 1, n = 6). (C) Schematic illustrations of F5 and CIRL in a pHL-sec vector backbone. Receptor specific domains (SEA = sea urchin sperm protein, enterokinase, agrin; IG = immunoglobulin) are highlighted. (D) Quantification of surface and whole cell expression levels of F5 and CIRL in HEK-293 cells by ELISA. Dataset normalized to the expression level of F5. Data are shown as mean ± SEM (N = 1, n = 6).

In the first experiment, CIRL and E5 were compared with the human $P2Y_{12}$ receptor, a member of the GPCR superfamily (class A), which is involved in platelet aggregation, thrombosis and hemostasis regulation (Cattaneo, 2015) (**Fig. 9A**). $P2Y_{12}$ served as a positive control for this experimental setup (Liebscher et al., 2014; Mogha et al., 2013). The evaluation of the ELISA data demonstrated that the surface expression of $P2Y_{12}$ and E5 were on a comparable level (**Fig. 9B**). In contrast, no surface expression of CIRL was detectable. However, whole cell expression analyses showed that the general synthesis of these three receptors in HEK-293 cells occurred.

In a second experiment, I compared the expression levels of CIRL and F5 (**Fig. 9C**). Quantified data indicated surface expression of F5 and CIRL (**Fig. 9D**). The CIRL expression was sharply reduced to ~18 % compared to F5. In contrast, ELISA analyses of the whole cell expression displayed the synthesis of these aGPCRs on a similar level in HEK-293 cells.

6.2.2 Chimeric and cleavage-deficient CIRL variants show impaired surface delivery

Chimeric receptor variants of CIRL were designed to further investigate the insufficient surface expression using ELISA. In addition, I analyzed the potential effect of GAIN domain cleavage-deficiency on the membrane trafficking of CIRL.

Currently, no signal peptide of CIRL is known, which could be the reason for its impaired membrane trafficking. However, *in vivo* experiments with *CIRL*^{Rescue} animals showed a proper receptor function compared to wildtype animals, suggesting that the membrane delivery is unimpaired (Scholz et al., 2017, 2015). Consequently, heterologous expression of a *Drosophila* protein in a mammalian cell line may be causing insufficient surface delivery due to problems with protein synthesis and/or surface delivery machinery. Interestingly, the plasma membrane localization of several aGPCRs could be improved by the fusion of the $P2Y_{12}$ N-terminus (Bohnekamp and Schöneberg, 2011; Hilbig et al., 2018; Liebscher et al., 2014), therefore I fused the N-terminus of $P2Y_{12}$ to the CTF of CIRL with/without the TA sequence (**Fig. 10A**). I expressed these chimeric receptor variants in HEK-293 cells and analyzed the surface expression. While the evaluation of the ELISA data demonstrated surface expression of the positive control $P2Y_{12}$, no surface delivery was observable for CIRL (**Fig. 10B**). In contrast, chimeric receptor variants $P2Y_{12}$-CIRL$^{\Delta TA}$ and $P2Y_{12}$-CIRL displayed a slightly increased localization of 3-6 % compared to $P2Y_{12}$ at the plasma membrane suggesting that the $P2Y_{12}$ N-terminus is also able to improve the surface expression of CIRL *in vitro*.

Next, I investigated the correlation between the surface expression and GAIN domain-mediated cleavage of CIRL. A potential separation of the NTF and CTF of the native receptor or during protein maturation through internal or external factors could lead to a loss of the HA-tagged NTF, consequently this would be associated with a reduced or undetectable surface delivery. Furthermore, studies indicated contrary results regarding the influence of the GAIN domain-mediated cleavage on the surface expression, ranging from normal to no delivery (Bohnekamp and Schöneberg, 2011; Krasnoperov et al., 2002). For this purpose, I abolished the autoproteolysis reaction of CIRL through mutations of the cleavage tripeptide HL↓T either to ALT or to HLA (Scholz et al., 2017). Then, I transfected cleavable CIRL, cleavage-deficient CIRL$^{H>A}$ and CIRL$^{T>A}$ constructs into HEK-293 cells and subsequently quantified their surface expression. ELISA data displayed no enhanced surface delivery of the cleavage-deficient CIRL variants, indicating that the surface delivery is independent of the self-cleavage (**Fig. 10C**).

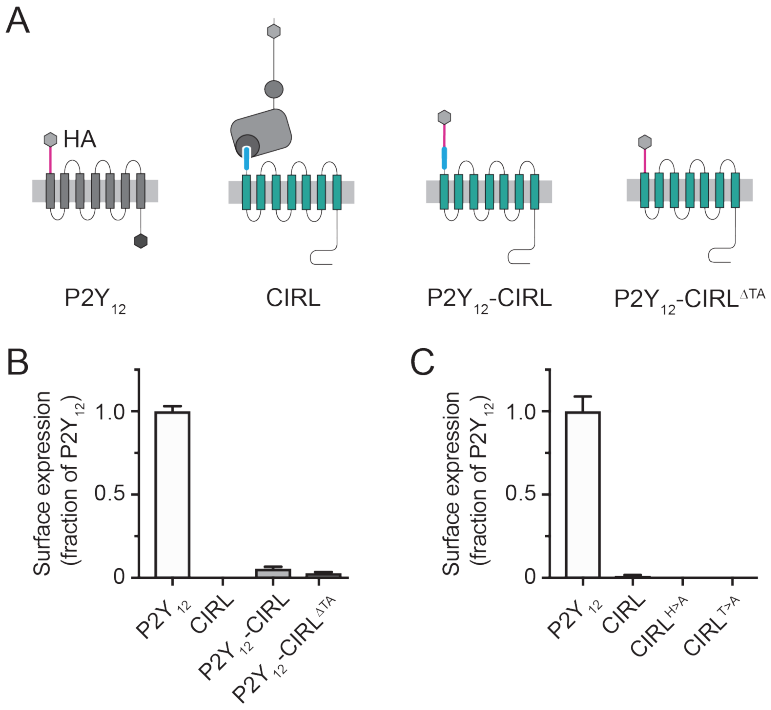

Fig. 10: Chimeric P2Y$_{12}$-CIRL and cleavage-deficient CIRL variants show insufficient surface expression.

(A) Schematic illustration of P2Y$_{12}$, CIRL and chimeric P2Y$_{12}$-CIRL, P2Y$_{12}$-CIRL$^{\Delta TA}$ variants. Chimeric P2Y$_{12}$-CIRL variants consists of a P2Y$_{12}$ N-terminus (magenta) fused to the CIRL CTF (green) with/without the TA (cyan). (B) Quantification of surface expression levels of P2Y$_{12}$, CIRL and chimeric receptors in HEK-293 cells by ELISA. Dataset normalized to the expression level of P2Y$_{12}$. Data are shown as mean ± SEM (N = 1, n = 6). (C) Quantification of surface expression levels of P2Y$_{12}$, cleavable CIRL, cleavage-deficient CIRL$^{H>A}$ and CIRL$^{T>A}$ variants in HEK-293 cells by ELISA. Dataset normalized to the expression level of P2Y$_{12}$. Data are shown as mean ± SEM (N = 1, n = 6).

6.2.3 ADGRE5 as a model aGPCR

Previous experiments showed abundant surface delivery of the human E5 receptor compared to CIRL and F5 in mammalian cells (see 6.2.1). Therefore, I chose this receptor as a model aGPCR to investigate the molecular mechanisms of its activity by fluorescence-based approaches. Hence, I continued with a thorough characterization of the expression and visualization behavior of this receptor *in vitro*.

First, I analyzed the influence of the autoproteolysis reaction on the surface expression of E5 by ELISA as previously described. For this purpose, I inhibited the natural cleavage of E5 through mutations of the cleavage tripeptide HL↓S either to ALS or to HLA (Hilbig et al., 2018; Hsiao et al., 2011) (**Fig. 11A**). To quantify surface expression levels in dependency of the autoproteolysis, I transfected cleavable E5, cleavage-deficient $E5^{H>A}$ and $E5^{S>A}$ constructs into HEK-293T cells. ELISA data revealed a cleavage-independent surface delivery of E5 (**Fig. 11B**). However, expression levels of E5 and $E5^{H>A}$ were comparable, whereas the surface delivery of $E5^{S>A}$ was slightly increased.

Additionally, I focused on the RGD motif, which is located in the GAIN domain of E5 and is necessary for the interaction with integrins (Hamann et al., 1995; Wang et al., 2005) (**Fig. 11A**). There is a known genetic polymorphism of the RGD motif to a QGD motif. Consequently, I investigated whether the QGD motif has a significant impact on the surface expression of E5 by ELISA. To this end, $E5^{Q283}$ and $E5^{R283}$ constructs were transfected into HEK-293 cells. Quantified surface expression levels of both variants were indistinguishable from each other, indicating no negative influence on a proper membrane trafficking by the RGD or QGD motifs (**Fig. 11C**).

Finally, the E5 layout was genetically expanded by an N-terminal HA epitope, which was already utilized for the ELISAs, and a C-terminal V5 epitope (**Fig. 12A**). These epitopes are useful for the separate detection of the NTF and the CTF. To test the labeling through both epitope tags, I expressed E5 in HEK-293 cells and performed IF stainings afterwards. Confocal imaging of permeabilized cells indicated a specific staining of the NTF and the CTF compared to control cells lacking transgenetically expressed E5 (**Fig. 12B**). Furthermore, images showed intracellular and surface localization of NTF and CTF.

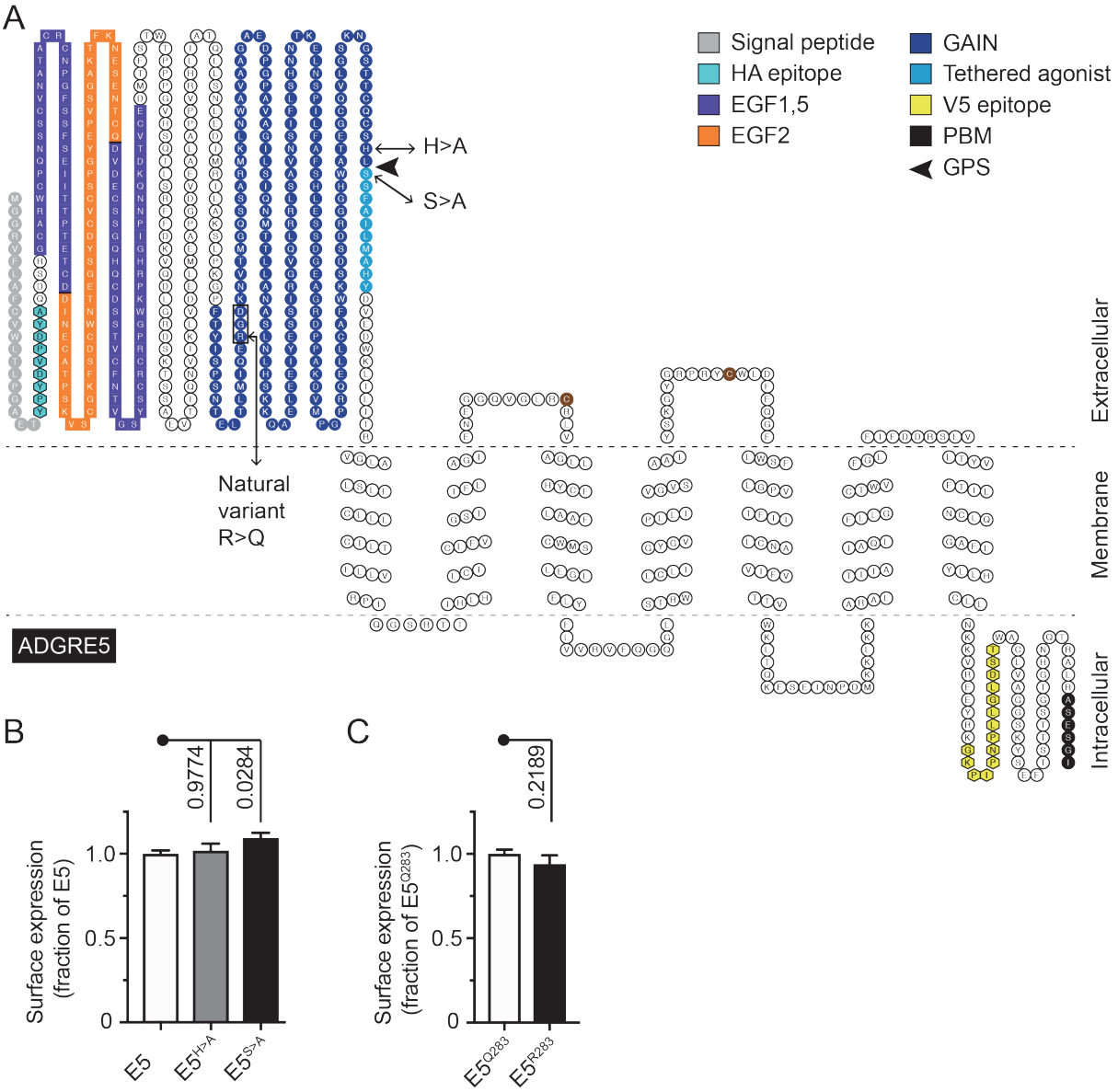

Fig. 11: Surface expression of E5 is independent of the autoproteolytic cleavage and the integrin-binding motif.

(A) Schematic structure and amino acid sequence of the human E5 receptor used in this thesis. The amino acid sequence indicates mutated positions (H>A, S>A), which prevent the self-cleavage. Furthermore, the RGD motif and the position of the natural R>Q variant is indicated. (B) Quantification of surface expression levels of cleavable E5, cleavage-deficient $E5^{H>A}$ and $E5^{S>A}$ variants in HEK-293T cells by ELISA. Dataset normalized to the expression level of E5. Data are shown as mean ± SEM (N = 3, n = 4). (C) Quantification of surface expression levels of $E5^{Q283}$ and $E5^{R283}$ in HEK-293 cells by ELISA. Dataset normalized to the expression level of $E5^{Q283}$. Data are shown as mean ± SEM (N = 2, n = 6).

Additionally, I was able to directly demonstrate the antibody-induced internalization of the E5 receptor by IF staining of the N-terminal HA epitope. HEK-293T cells expressing E5 were fixed prior to an IF staining for 30 min (non-permeabilized, t = 0 min). Confocal images displayed an exclusive surface localization of E5 (**Fig. 12C**). In contrast, HEK-

293T cells expressing E5 receptors, which were immunostained for 30 min prior to the fixation (non-permeabilized, t = 30 min), showed internalized E5 receptors in vesicular structures. In 6.3.4, I will further focus on this observation.

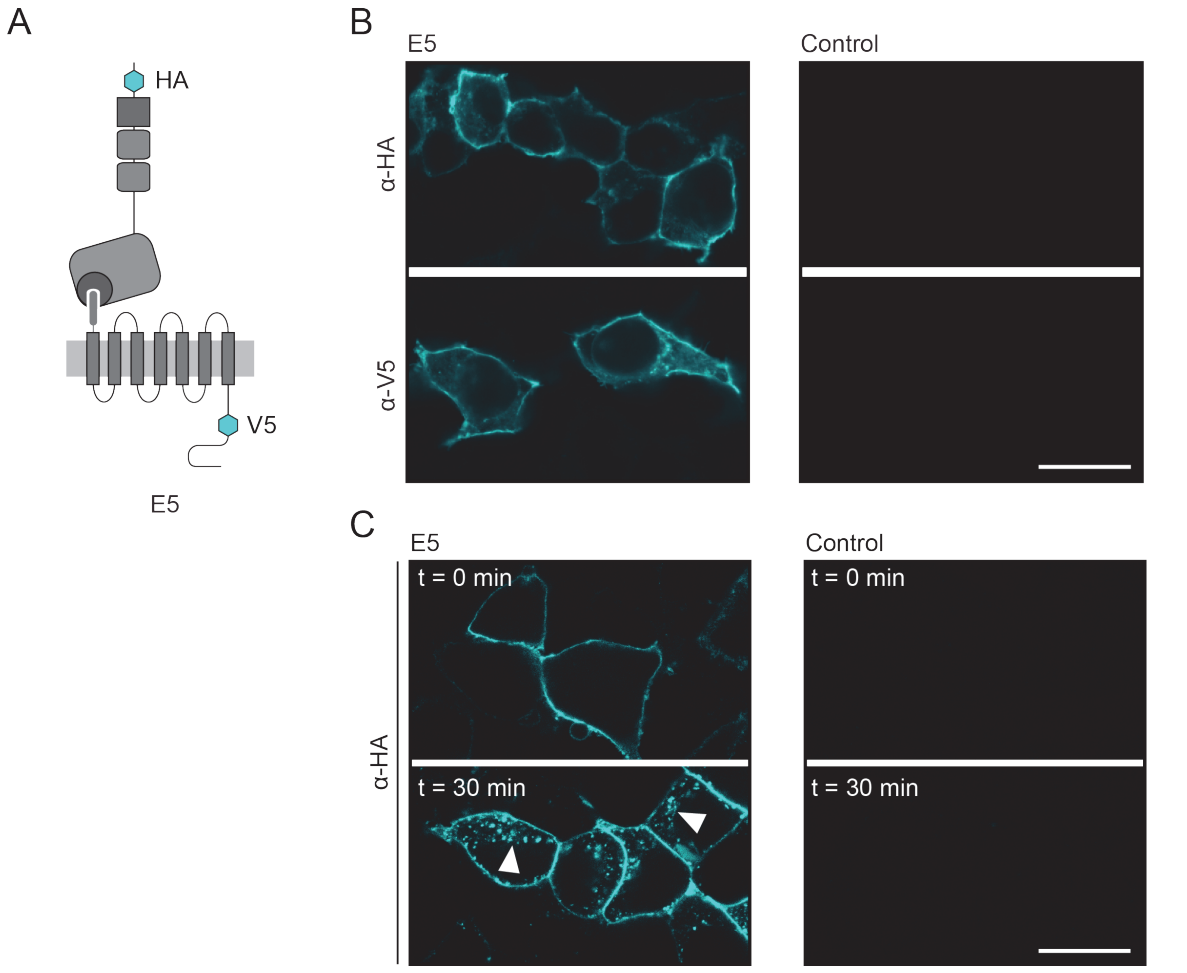

Fig. 12: Separate visualization of NTF and CTF indicates the internalization of E5.

(A) Schematic illustration of E5 displays the position of the N-terminal HA epitope and C-terminal V5 epitope. (B) Confocal images of HEK-293 cells expressing E5 and control cells (only treated with transfection reagent). Images display a specific IF staining of the HA epitope and V5 epitope of E5. (C) Confocal images of HEK-293T cells expressing E5 and control cells (only treated with transfection reagent). The IF staining of fixed cells (t = 0 min) compared to living cells (t = 30 min) by α-HA-Alexa 488 indicates the internalization of E5 (white arrow). Scale bars 20 µm.

In summary, the experimental data demonstrated the efficient *in vitro* expression and visualization of the aGPCRs CIRL, F5 and E5 by fluorescence-based microscopy and ELISA approaches. Plasma membrane trafficking was shown for F5 and E5 receptors. The attempt to guide CIRL to the plasma membrane by the fusion of the $P2Y_{12}$ N-terminus to CIRL was successful, but its surface expression was significantly

decreased compared to $P2Y_{12}$. Furthermore, the inhibition of the CIRL cleavage at the GPS had no positive effect on the surface delivery in HEK-293 cells. Therefore, I decided to focus on E5 as a model receptor for further analyses regarding the molecular mechanisms of the aGPCR activity. The surface delivery of E5 was independent of the GAIN domain-mediated proteolysis. In addition, E5 receptors containing the natural variant QGD instead of the RGD motif within the GAIN domain showed an unimpaired surface expression. Furthermore, I established IF staining of E5 NTF and CTF. In this context, I was able to demonstrate that the immunostaining of the N-terminal HA epitope enabled the direct visualization of internalized E5 *in vitro*.

6.3 Fluorescent labeling of ADGRE5 *in vitro*

In this chapter the goal was to establish fluorescent labeling methods for *in vitro* aGPCR visualization. In addition, the desired fluorescent labeling strategies will be the foundation for the generation of optical aGPCR sensors to further analyze the molecular mechanism of aGPCR function, e.g. of conformational changes in response to a receptor stimulation using FRET. To create optically tractable sensor proteins, I focused on a broad spectrum of live cell labeling techniques such as genetically encoded chromophores, IF staining, FlAsH labeling, α-BuTX labeling and bioorthogonal labeling. The previously characterized E5 receptor served as a model aGPCR due to its high expression levels in mammalian cells (see 6.2.1).

6.3.1 Labeling of tetracysteine-tagged ADGRE5 by FlAsH-EDT_2

First, I focused on a minimal space demanding labeling technique based on a permeable fluorescein derivative named FlAsH-EDT_2 (~0.7 kDa). This naturally non-fluorescent substance becomes fluorescent after binding to a motif containing a tetracysteine sequence (Griffin et al., 1998). In the past, FlAsH labeling in combination with CFP was successfully employed to determine conformational changes of GPCRs with minor hindrance of the receptors structure and function (Hoffmann et al., 2005). Therefore, the transfer of FlAsH labeling to aGPCRs in view to its use for functional analyses was of great interest. The successful procedure of FlAsH labeling was conducted in collaboration with Nelly Rüttiger (Institute of Molecular Cell Biology at the University Hospital of Jena).

To compare the FlAsH labeling efficiency for its potential use in prospective FRET approaches, I expanded the E5 receptor layout by a genetically encoded CFP variant mTurquoise. To avoid negative effects on the receptor folding and based on previous aGPCR engineering approaches (Prömel et al., 2012; Scholz et al., 2017), mTurquoise

was inserted into an unstructured linker region between the EGF5 and GAIN domains in the NTF of E5. mTurquoise is characterized by a high quantum yield and long fluorescence lifetime (Goedhart et al., 2010).

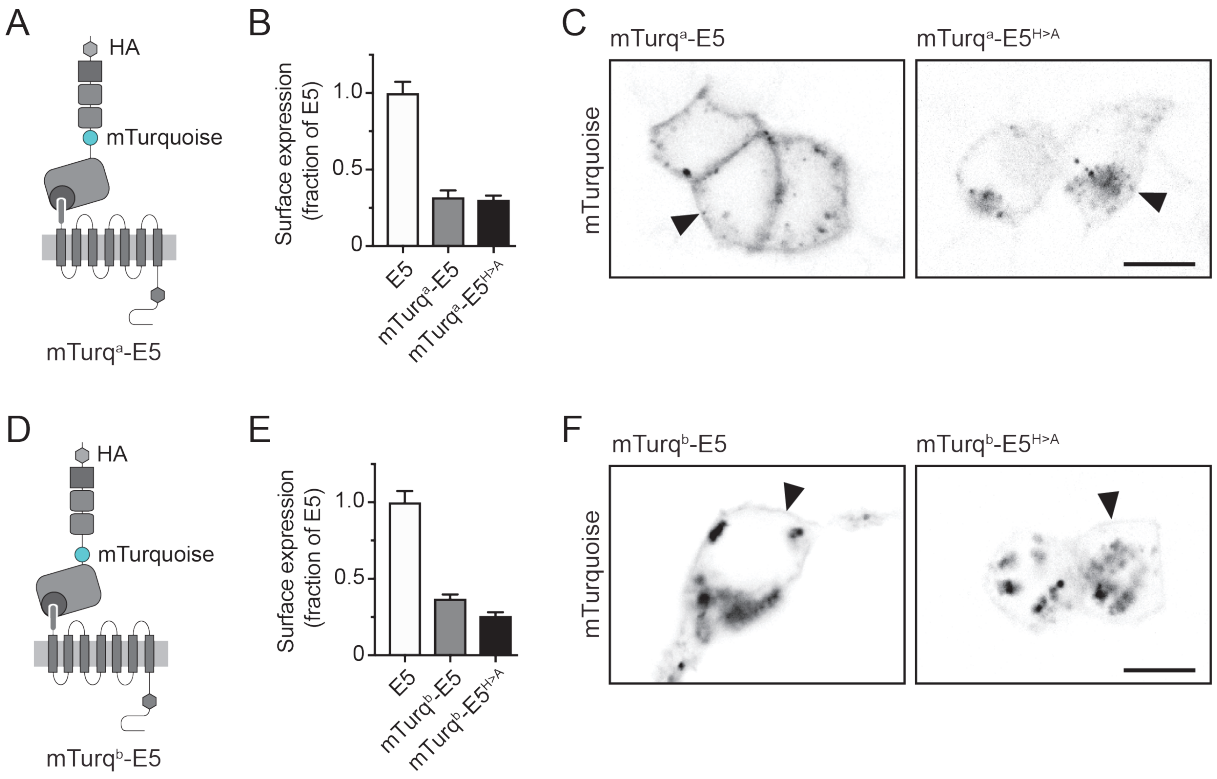

Fig. 13: mTurquoise inserted into the NTF offers the direct visualization of E5 in living cells.

(A) Schematic illustration of E5 indicates the position of mTurquoise within the NTF close to the EGF5 domain (mTurq^{a}). (B) Quantification of surface expression levels of cleavable mTurq^{a}-E5 and cleavage-deficient mTurq^{a}-E5$^{H>A}$ compared to E5 in HEK-293 cells by ELISA. Dataset normalized to the expression level of E5. Data are shown as mean ± SEM (N = 1, n = 6). (C) Confocal images of HEK-293 cells expressing cleavable mTurq^{a}-E5 and cleavage-deficient mTurq^{a}-E5$^{H>A}$ indicate the presence of the receptors at the plasma membrane (black arrow). (D) Schematic illustration of E5 indicates the position of mTurquoise within the NTF close to the GAIN domain (mTurq^{b}). (E) Quantification of surface expression levels of cleavable mTurq^{b}-E5 and cleavage-deficient mTurq^{b}-E5$^{H>A}$ compared to E5 in HEK-293 cells by ELISA. Dataset normalized to the expression level of E5. Data are shown as mean ± SEM (N = 1, n = 6). (F) Confocal images of HEK-293 cells expressing cleavable mTurq^{b}-E5 and cleavage-deficient mTurq^{b}-E5$^{H>A}$ indicate the presence of the receptors at the plasma membrane (black arrow). Scale bars 10 µm.

mTurquoise was integrated at two different positions between the EGF5 and GAIN domains of cleavable E5 and cleavage-deficient E5$^{H>A}$, in one case closer to the EGF5 domain (mTurq^{a}) (**Fig. 13A**), in the other closer to the GAIN domain (mTurq^{b}) (**Fig. 13D**). I analyzed the potential effect of the fused mTurquoise on the surface

delivery of E5 by ELISA. For this purpose, I transfected these E5 constructs into HEK-293 cells. ELISA data showed an indistinguishable surface delivery of 30-32 % of the mTurq^{a}-E5 variants compared to the E5 fraction, suggesting that the incorporation of mTurquoise into the EGF5-GAIN domain linker region led to a decreased surface expression (**Fig. 13B**). However, the GAIN domain-mediated cleavage had no negative effect.

Moreover, confocal imaging confirmed the surface expression of mTurq^{a}-E5 variants (**Fig. 13C**). Fluorescence signals appeared inside and weakly at the plasma membrane of HEK-293 cells. Interestingly, the surface delivery was independent of the mTurquoise position within the linker region of the EGF5 and GAIN domains, which was indicated by comparable results rendered by ELISA (**Fig. 13E**) and confocal imaging (**Fig. 13F**) of the mTurq^{b}-E5 variants.

Previously, I had inserted mTurquoise into the NTF of E5. Consequently, the next step was the additional insertion of a tetracysteine motif for further labeling approaches by FlAsH-EDT$_2$. I inserted the modified tetracysteine motif, ESQCCPGCCARS, which had previously allowed a successful FlAsH labeling of the A_{2A}-adenosine receptor (Hoffmann et al., 2010). Based on the experience of GPCR FlAsH labeling approaches, I decided to integrate the tetracysteine motif into the 3rd intracellular loop (ICL3) of E5 (Hoffmann et al., 2010, 2005) (**Fig. 14A**).

First, I compared the FlAsH labeling of cleavable (mTurq^{a}-E5-FlAsH) and cleavage-deficient dually tagged E5 (mTurq^{a}-E5$^{H>A}$-FlAsH) using confocal imaging. Cleavage-deficient constructs served as a control, to test whether the FlAsH labeling procedure led to a separation between the NTF and the CTF. I expressed the FlAsH-tagged E5 variants and a positive control in HEK-293 cells and labeled them with FlAsH-EDT$_2$ afterwards. Confocal imaging indicated no prominent FlAsH labeling neither of cleaved mTurq^{a}-E5-FlAsH nor of non-cleaved mTurq^{a}-E5$^{H>A}$-FlAsH (**Fig. 14B**). Additionally, the mTurquoise signal revealed the vesicular aggregation of E5 inside the cells, which further indicated an insufficient surface delivery. However, the E5-FlAsH construct without mTurquoise also showed a missing FlAsH labeling, assuming that the presence of an N-terminal mTurquoise per se was not the reason for an insufficient labeling. The α_{2A}-adrenergic receptor (α_{2A}AR) served as a positive control for a successful FlAsH labeling (Hoffmann et al., 2005). Imaging of α_{2A}AR showed mTurquoise and FlAsH signal at the plasma membrane.

In addition, I observed an impaired surface localization of FlAsH-labeled mTurq-E5 variants without the tetracysteine motif by confocal imaging. This suggested a possible negative effect on the aGPCR localization due to the FlAsH labeling procedure in HEK-293 cells (**Fig. 14C**).

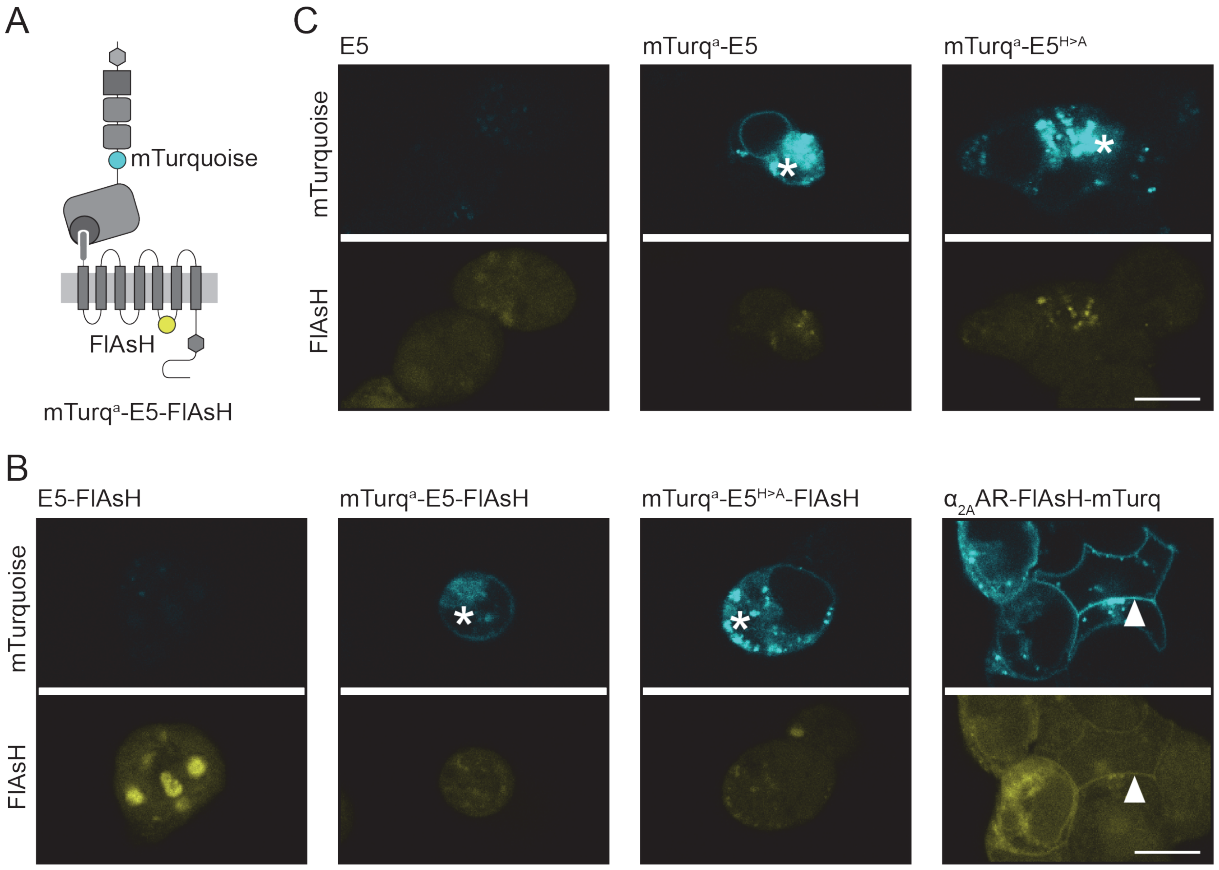

Fig. 14: FlAsH labeling of E5 demonstrates no distinct fluorescence signal.

(A) Schematic illustration of E5 containing an mTurquoise within the NTF close to the EGF5 domain (mTurq^{a}) and a tetracysteine motif (FlAsH tag) within the ICL3. (B) Confocal images of HEK-293 cells expressing E5-FlAsH constructs with and without NTF-fused mTurquoise (cyan) indicate no successful FlAsH labeling (yellow) compared to the positive control (α_{2A}AR-FlAsH-mTurq). mTurquoise signals demonstrate the vesicular aggregation of E5 inside the cells (white asterisk). α_{2A}AR shows mTurquoise and FlAsH signal at the plasma membrane (white arrow). (C) Confocal images of HEK-293 cells expressing E5 constructs without FlAsH tag suggest an impaired surface localization due to the FlAsH labeling procedure. E5 forms vesicular aggregates inside the cells (white asterisk). Scale bars 10 µm.

Since the FlAsH labeling approaches in HEK-293 cells were unsuccessful, I decided to focus on additional mammalian cell lines, HEK-293T and COS-7, to increase the surface expression and the number of labeled receptors at the membrane. To this end, I expressed cleavable mTurq^{a}-E5-FlAsH **(Fig. 15A**) and cleavage-deficient mTurq-E5$^{H>A}$-FlAsH (**Fig. 15C**) in HEK-293, HEK-293T and COS-7 cells. At first, the surface expression was analyzed without FlAsH labeling by confocal microscopy. Fluorescence signals of the NTF-fused mTurquoise showed no evidence for an improved surface delivery neither of cleaved E5 (**Fig. 15B**) nor of non-cleaved E5 (**Fig. 15D**) in HEK-293T and COS-7 compared to HEK-293.

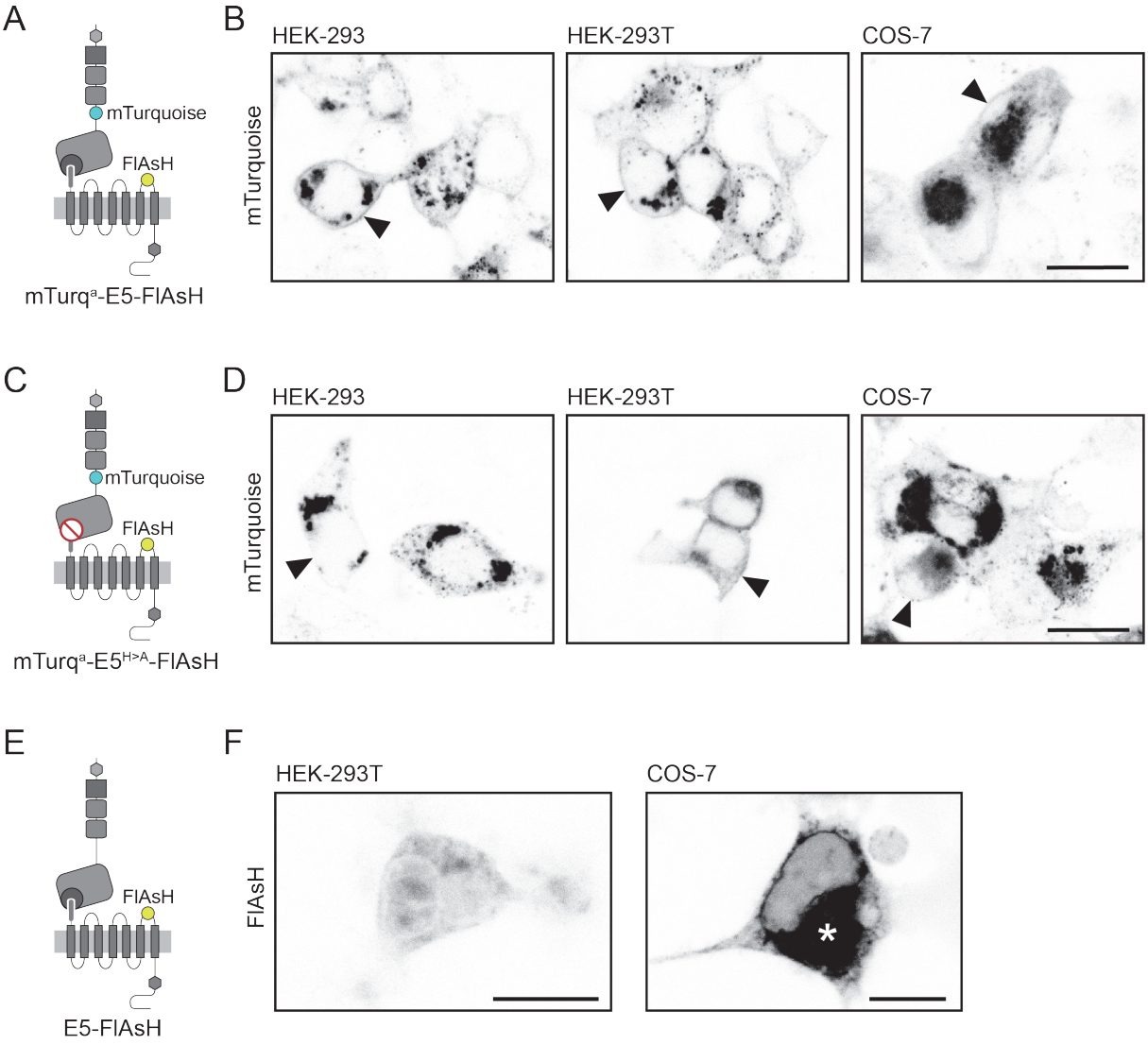

Fig. 15: Tetracysteine-tagged E5 shows an absent FlAsH signal at the plasma membrane in different mammalian cell lines.

(A) Schematic illustration of the cleavable mTurq^{a}-E5-FlAsH construct. (B) Confocal images of mammalian cell lines (HEK-293, HEK-293T and COS-7) expressing mTurq^{a}-E5-FlAsH without FlAsH labeling. mTurquoise signal indicates surface expression in the tested cell lines (black arrow). (C) Schematic illustration of the cleavage-deficient mTurq^{a}-E5$^{H>A}$-FlAsH construct. (D) Confocal images of mammalian cell lines (HEK-293, HEK-293T and COS-7) expressing mTurq^{a}-E5$^{H>A}$-FlAsH without FlAsH labeling. mTurquoise signal indicates surface expression in the tested cell lines (black arrow). (E) Schematic illustration of the E5-FlAsH construct. (F) Confocal images of FlAsH-labeled HEK-293T and COS-7 cells expressing E5-FlAsH indicate an absent FlAsH label at the plasma membrane. FlAsH signal is detectable in the intracellular space of COS-7 cells (white asterisk). Scale bars (B,D) 20 µm, (F) 10 µm.

Then, I tested the FlAsH labeling in combination with HEK-293T and COS-7 cells. To this end, I transfected the E5-FlAsH construct (**Fig. 15E**) into these cell lines, labeled them with FlAsH-EDT$_2$ and analyzed the fluorescence signals afterwards. FlAsH signals were not detectable at the cell surface in any of the tested cell lines (**Fig. 15F**).

However, a strong FlAsH signal was observable in the intracellular space of COS-7 cells.

In sum, these findings suggested that the FlAsH method under the tested conditions is not applicable to aGPCRs labeling approaches including the subsequent usage for optical sensors.

6.3.2 Labeling of BBS-tagged ADGRE5 by α-BuTX

In my own hands, the successful fluorescent labeling of aGPCR CTF in non-permeabilized living cells was a great challenge. Neither live cell IF staining of tagged ECLs was fruitful (data not shown) nor the use of alternative methods like the FlAsH labeling of tetracysteine-tagged ICL3 (see 6.3.1).

In search of alternative minimal invasive fluorescent labeling methods, the labeling of a BBS tag using membrane-impermeable α-BuTX (~8 kDa) appeared to be an appropriate approach. α-BuTX was initially discovered in the snake venom of *Bungarus multicinctus* (Chang and Lee, 1963). In the past, a variety of synthetic peptides were discovered, which indicated a high binding affinity for α-BuTX. One of these high affinity peptides consists of the amino acid sequence WRYYESSLEPYPD (Kasher et al., 2001). To test the labeling of aGPCRs with fluorescently labeled α-BuTX, I inserted the BBS sequence mentioned above into the ECLs of E5. The insertion (I) of the BBS tag was either placed into the center of the ECL with (I+R) or without replacement (I-R) of an amino acid fragment of the loop corresponding in size to the length of the BBS tag **(Fig. 16A**). In addition, in some receptor variants I increased the flexibility of the BBS tag by fusion with a GGGGS linker (L) on both N- and C- termini, which has already been successfully used for other proteins (Zhao et al., 2008).

At first, the surface delivery of E5 in dependency of the fused BBS tag into the 1st (ECL1), 2nd (ECL2) or 3rd ECL (ECL3) was quantified (**Fig. 16B**). For that purpose, I transfected BBS-containing E5 constructs into HEK-293T cells and analyzed the surface expression by ELISA. Quantified data of E5-BBS^{ECL1} variants revealed a surface delivery of at least ~68 % of E5 fraction (**Fig. 16C**). Additionally, the ELISA data of E5-BBS^{ECL2} variants demonstrated at least ~63 % surface expression compared to E5 (**Fig. 16D**). The last panel demonstrated the surface delivery of E5-BBS^{ECL3} variants (**Fig. 16E**). Quantified expression levels were not less than ~65 % of E5 fraction. All collected ELISA data taken together, revealed a sufficient surface delivery of all tested E5-BBS^{ECLX} variants, which differed depending on the BBS tag position within the ECLs. The highest surface expression of 88-93 % was shown in the

case of E5-BBS$^{ECLX/I-R-L}$ variants containing an inserted (without replacement) linker-free BBS tag.

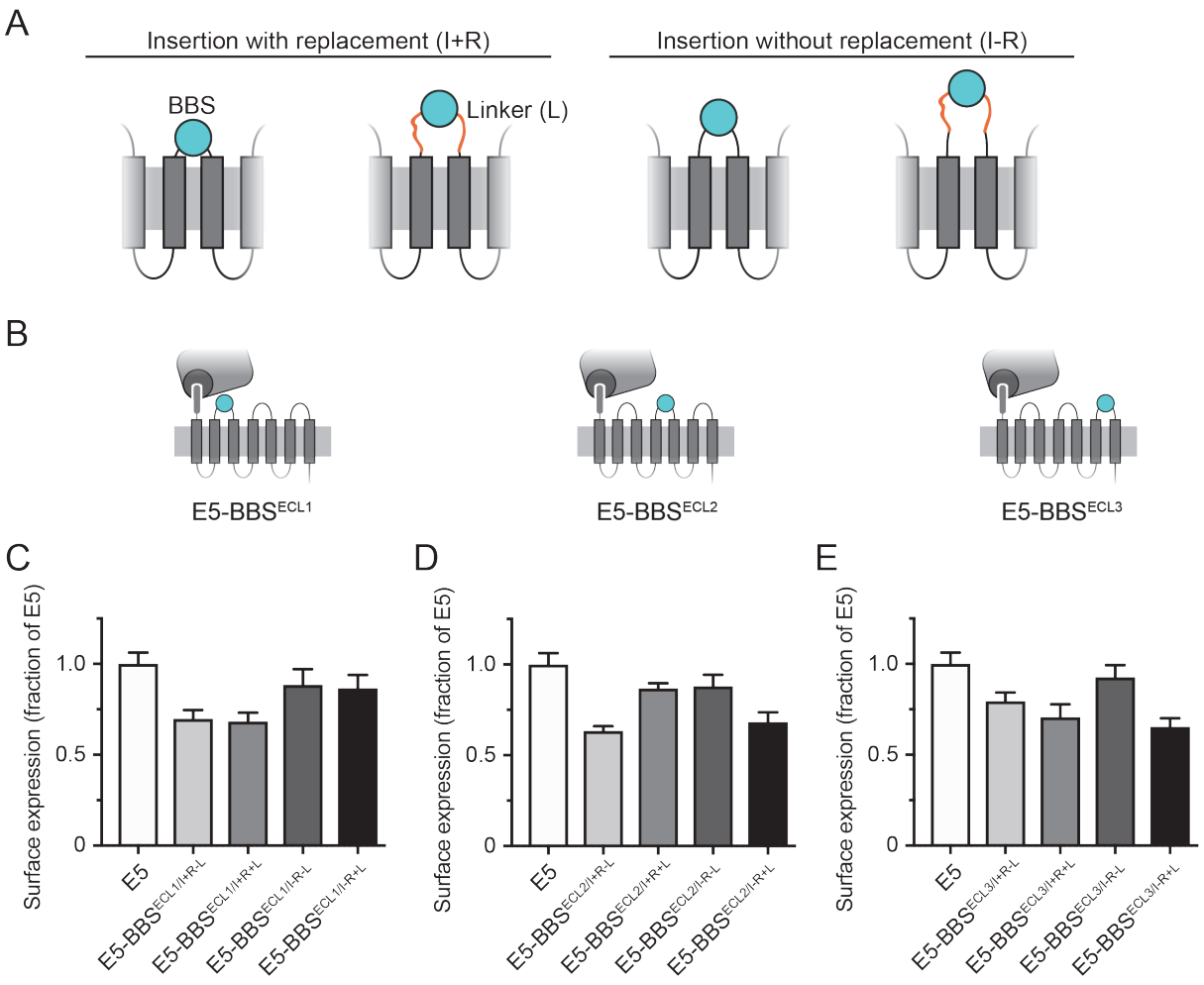

Fig. 16: E5 constructs containing a BBS tag in the ECL are expressed at the plasma membrane.

(A) Schematic illustration of different BBS tag incorporation strategies. The BBS tag is inserted with or without the replacement (I+R or I-R) of the corresponding amino acid sequence. In addition, the BBS tag is expanded with or without N- and C-terminal GGGGS linkers (L). (B) Different BBS tag incorporation strategies are conducted for ECL1, ECL2 and ECL3 of E5. (C,D,E) Quantification of surface expression levels of E5 variants containing a BBS tag in (C) ECL1, (D) ECL2 or (E) ECL3 compared to E5 in HEK-293T cells by ELISA. Dataset normalized to the expression level of E5. Data are shown as mean ± SEM (N = 1, n = 4).

Previous ELISA data indicated surface delivery of all tested E5-BBS^{ECLX} variants. Therefore, I decided to transfect all variants into HEK-293T cells to further benchmark the accessibility and beneficial usage of the BBS for fluorescence microscopy. To this end, I labeled living cells expressing BBS-expanded E5 receptors with α-BuTX-Alexa 488. Prior to confocal imaging, cells were fixed to prevent any further change of

fluorescence signals. Images demonstrated a prominent labeling of most E5-BBS^{ECLX} variants at the plasma membrane, with the exception of E5-BBS$^{ECLX/I+R-L}$ variants (**Fig. 17**). Interestingly, the presence of a linker (E5-BBS$^{ECLX/I+R+L}$) led to weak fluorescence signals for the ECL1 and ECL3 positions, and to a stronger signal for the ECL2 position. E5-BBS$^{ECLX/I-R-L}$ variants indicated a labeling only for the ECL1 and ECL2 variants, while no fluorescence signal was detectable in the case of the ECL3 variant. The brightest signals were detectable for E5-BBS$^{ECLX/I-R+L}$ variants, suggesting that the expanded size of the ECL by the insertion without replacement and the bilateral linker improved the accessibility of the BBS tag. Additionally, I observed the internalization of all labeled E5-BBS^{ECLX} variants, which indicated that fluorescently labeled α-BuTX could be generally suitable to study receptor internalization.

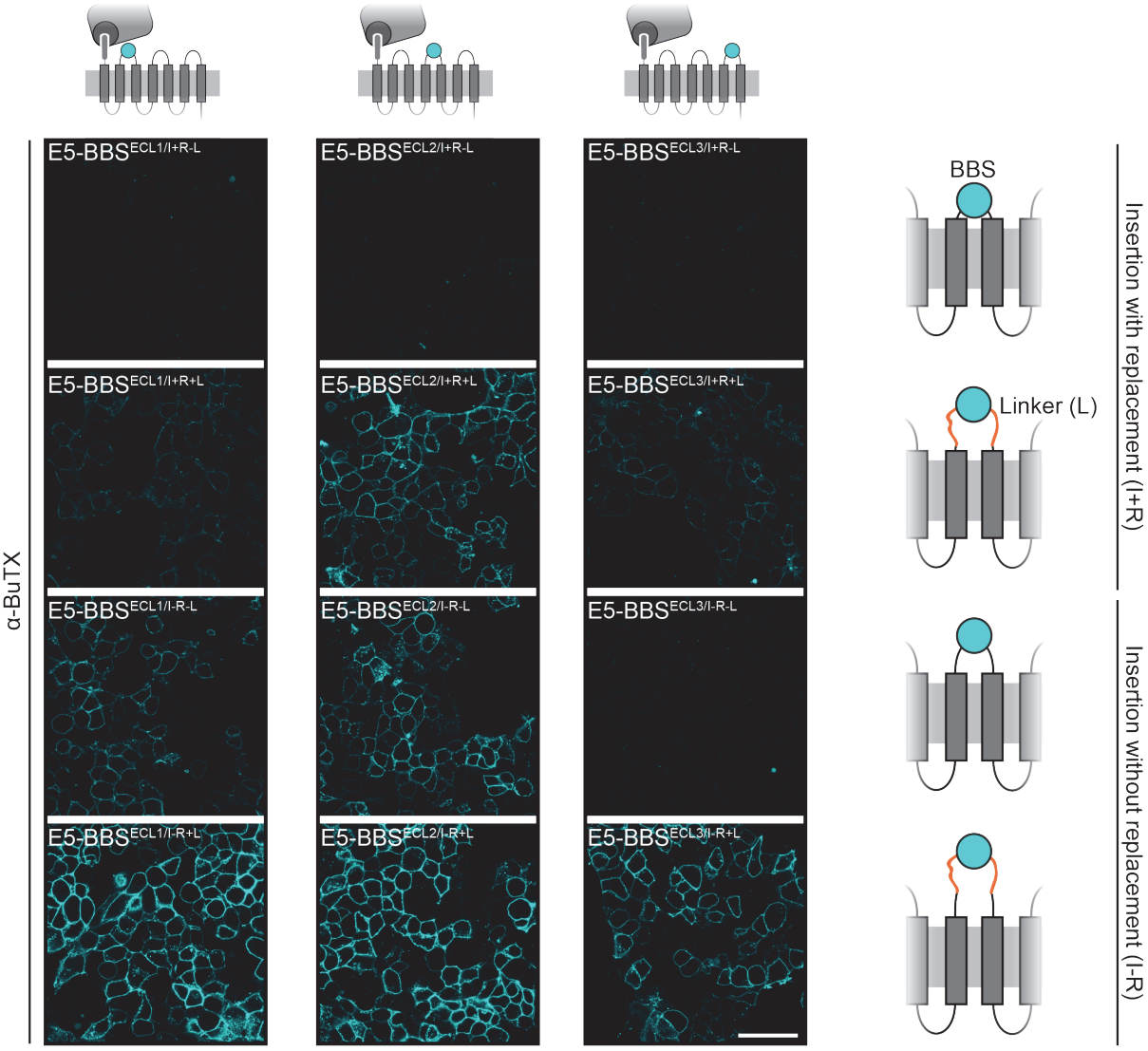

Fig. 17: Fluorescent labeling of the BBS tag in the ECL of E5 shows efficiency differences depending on position and insertion strategy.

Confocal images of HEK-293T cells expressing E5 constructs containing a BBS tag in the ECL1 (left panel), ECL2 (middle panel) or ECL3 (right panel). Panels indicate from top to bottom different BBS tag insertion strategies. The BBS tag is integrated in the ECL via insertion with or without replacement (I+R or I-R) of the corresponding amino acid sequence. In addition, the BBS tag is expanded with or without N- and C-terminal GGGGS linkers (L). BBS tags were labeled with α-BuTX-Alexa 488. Images indicate highest fluorescence signals in case of E5-BBS$^{ECLX/I-R+L}$ variants. Scale bar 50 µm.

In the last part of this section, I investigated the potential use of α-BuTX in combination with a genetically encoded chromophore for dual labeling of aGPCRs to serve as part of an optical conformation sensor (e.g. FRET sensor) to shed light on the structural mechanisms underlying aGPCR activation. Previously, I inserted mTurquoise into the unstructured linker region between the EGF5 and GAIN domains of E5, which led to a decreased surface expression (see 6.3.1). Interestingly, mTurquoise and the EGF5 domain share a comparable size. Consequently, the replacement of the EGF5 domain by mTurquoise was chosen to avoid a negative impact on the E5 surface expression through an excessive elongation of the receptor's ECR by the mTurquoise addition.

To quantify the surface expression of newly generated mTurq-E5 (**Fig. 18C**), the construct was transfected into HEK-293T cells and then the surface expression analyzed by ELISA. Quantified ELISA data showed the expression of mTurq-E5 at the plasma membrane and, interestingly, demonstrated no significant differences compared to E5 (**Fig. 18A**). Moreover, confocal imaging of HEK-293T cells expressing mTurq-E5 verified receptor synthesis and surface delivery (**Fig. 18B**).

Previous experiments indicated a high surface expression and best labeling result of E5-BBS$^{ECLX/I-R+L}$ variants. For this purpose, I combined these constructs with the mTurq-E5 construct, which resulted in mTurq-E5-BBS$^{ECLX/I-R+L}$ variants (**Fig. 18C**). In collaboration with Mareike Hemberger, I investigated the surface expression of these variants by ELISA. Quantified data demonstrated a surface delivery of at least ~72 % compared to E5 (**Fig. 18D**). In addition, confocal imaging of mTurq-E5-BBS$^{ECLX/I-R+L}$ variants showed fluorescence signals of mTurquoise and α-BuTX-Alexa 488 at the plasma membrane (data not shown).

Fluorescently labeled α-BuTX in combination with a BBS tag proved a useful strategy for aGPCR labeling. The experiments indicated an effective labeling of BBS-tagged ECL1, ECL2 and ECL3 of E5. Furthermore, α-BuTX labeling was suitable for dual-tagging of E5 in combination with mTurquoise, which provided a potential usage for the functional analysis of aGPCR activity, e.g. by FRET experiments (see 6.4.1).

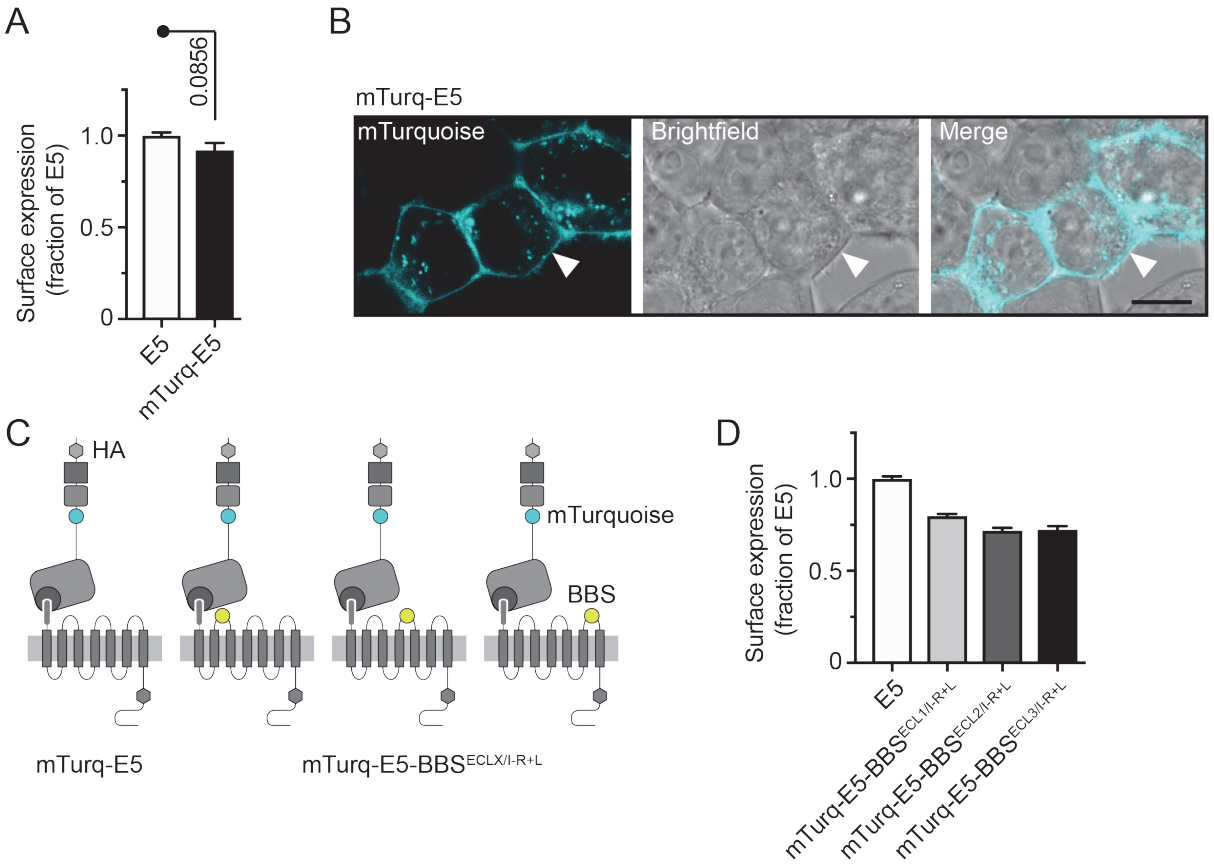

Fig. 18: mTurquoise- and BBS-tagged E5 sensor shows a proper surface delivery.

(A) Quantification of surface expression levels of mTurq-E5 compared to E5 in HEK-293T cells by ELISA. Dataset normalized to the expression level of E5. Data are shown as mean ± SEM (N = 3, n = 4). (B) Confocal images of HEK-293 cells expressing mTurq-E5 display distinct fluorescence signals at the plasma membrane (white arrow). (C) Schematic illustration of E5 indicates the position of a fused mTurquoise within the NTF and a BBS tag within the ECL. The BBS tag is integrated in the ECL via the insertion without replacement (I-R) of the corresponding amino acid sequence. In addition, the BBS tag is expanded with N- and C-terminal GGGGS linkers (L). (D) Quantification of surface expression levels of E5-BBS$^{ECLX/I-R+L}$ variants compared to E5 in HEK-293T cells by ELISA (performed by Mareike Hemberger). Dataset normalized to the expression level of E5. Data are shown as mean ± SEM (N = 1, n = 12). Scale bar 10 µm.

6.3.3 Labeling of ADGRE5 by bioorthogonal click chemistry

Live cell labeling by bioorthogonal click chemistry represents the least space demanding method (0.5-2 kDa) at the moment (Nikić et al., 2015). The basic principle is the site-specific incorporation of UAAs by genetic code expansion of the amber stop codon (TAG) using a modified pyrrolysine RS/tRNA (Pyl^{RS}/tRNA^{Pyl}) pair of *Methanosarcina* (Nikić et al., 2016, 2015) (**Fig. 19A**). The modified RS loads the UAA to the modified tRNA, which recognizes the amber stop codon of the mRNA. Finally, this leads to the successful incorporation of the UAA. In this thesis, I used the UAA

TCO*A, which reacts via SPIEDAC with the tetrazine group of functionalized organic fluorophores (Blackman et al., 2008; Nikić et al., 2015) (**Fig. 19B**).

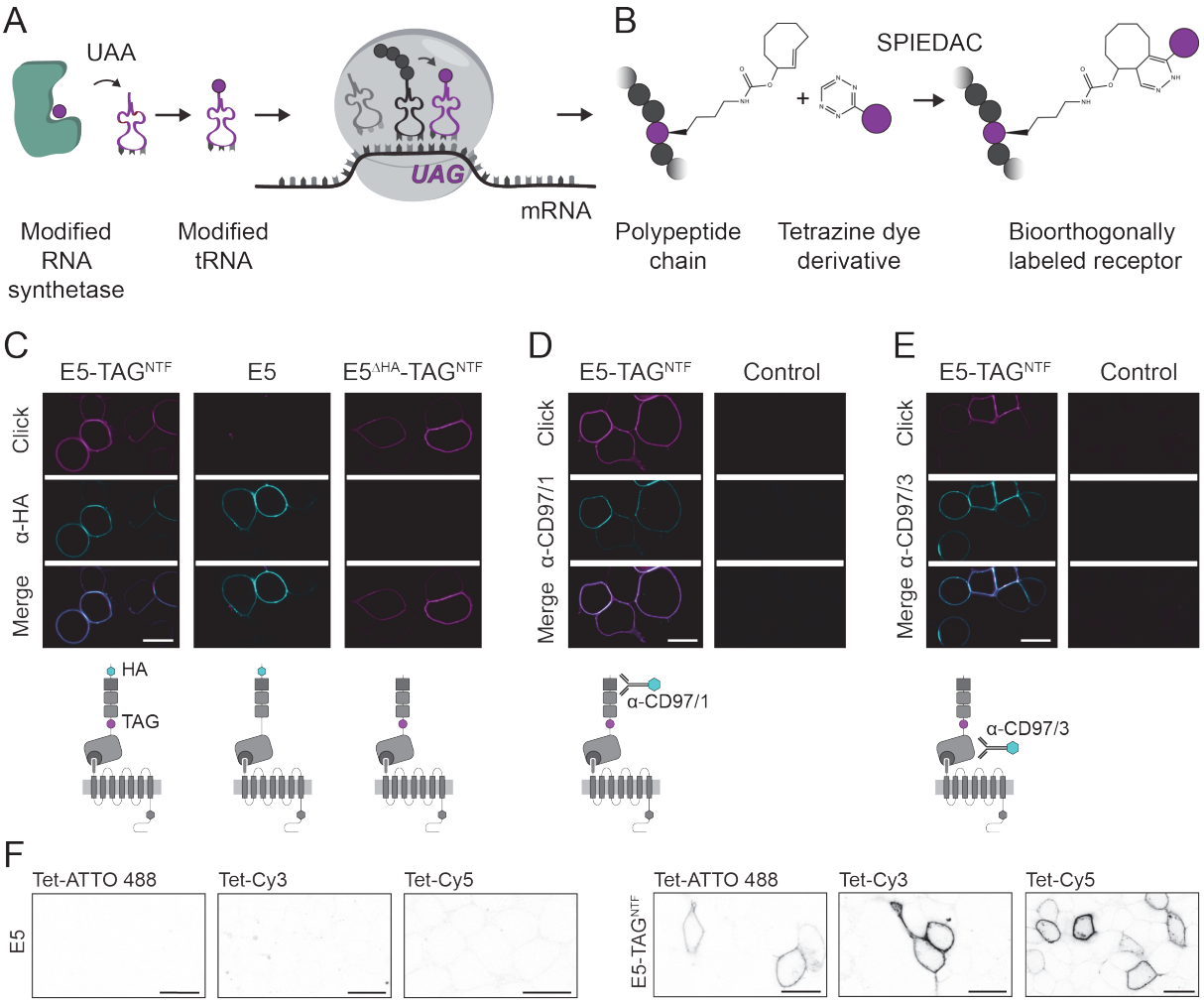

Fig. 19: Bioorthogonal click chemistry provides a minimally invasive, rapid and specific method to label aGPCRs.

(A,B) Schematic illustration of the general principle behind bioorthogonal click chemistry. (A) The host genetic machinery is expanded by the introduction of a modified RS and modified tRNA, which is able to interact with amber stop codons. This enables the incorporation of UAAs into the protein sequence during the protein translation. (B) The UAA reacts via a SPIEDAC reaction with the tetrazine group of a functionalized organic fluorophore. (C) Confocal images of HEK-293T cells expressing E5-TAG^{NTF} reveal a specific bioorthogonal labeling with H-Tet-Cy5 (magenta) and IF staining using α-HA-Alexa 488 (cyan) of E5 compared to the control constructs E5 and E5$^{\Delta HA}$-TAG^{NTF}. (D,E) Confocal images of HEK-293T cells expressing E5-TAG^{NTF} reveal a specific (D) bioorthogonal labeling with H-Tet-Cy5 (magenta) and IF staining using α-CD97/1-Alexa 532 (cyan), or (E) bioorthogonal labeling with Me-Tet-ATTO 488 (magenta) and IF staining using α-CD97/3-Alexa 647 (cyan). (F) Confocal images of HEK-293T cells expressing E5-TAG^{NTF} demonstrate a specific bioorthogonal labeling with H-Tet-ATTO 488, H-Tet-Cy3 and H-Tet-Cy5 compared to untagged E5. (C,D,E) performed by Gerti Beliu. Used Pyl^{RS}/tRNA^{Pyl} system: RS$_{Lemke}$. Scale bars 20 µm.

To adapt and characterize this method, the E5 receptor was bestowed with an amber stop codon in the unstructured linker region between the EGF5 and GAIN domains. In a first experiment, in collaboration with Gerti Beliu (Department of Biotechnology and Biophysics at the University of Würzburg), I analyzed the specificity of the bioorthogonal labeling compared to IF labeling of the HA epitope. Therefore, we separately expressed E5-TAG^{NTF} (both tags) and the control variants E5 (HA tag only) and E5$^{\Delta HA}$-TAG^{NTF} (bioorthogonal tag only) in HEK-293T cells. All variants were co-expressed with the Pyl^{RS}/tRNA^{Pyl} system in the presence of UAAs. E5 variants were labeled with the membrane-impermeable H-Tet-Cy5 and α-HA-Alexa 488. Confocal imaging confirmed the specificity of bioorthogonal and IF labeling (**Fig. 19C**).

Additionally, we used two monoclonal antibodies, CD97/1 and CD97/3, to compare the labeling specificity and efficiency of bioorthogonal labeling with standard immunolabels for E5. CD97/1 recognizes the EGF1 domain of E5 (Eichler et al., 1994) and CD97/3 is directed against the GAIN domain of E5 (Hamann et al., 2000). Confocal images displayed a complete overlap of bioorthogonal labels and fluorescently labeled antibodies, which indicated that the labels are present in the same target protein (**Fig. 19D,E**). Furthermore, this approach demonstrated that the bioorthogonal click chemistry matches conventional IF methods for aGPCRs. In addition, I demonstrated the specific bioorthogonal labeling of E5-TAG^{NTF} compared to untagged E5 for additional tetrazine dye derivatives H-Tet-ATTO 488 and H-Tet-Cy3 (**Fig. 19F**).

To further optimize the bioorthogonal labeling of the E5 receptor, I tested the efficiency of the UAA incorporation into the NTF in dependency of two different Pyl^{RS}/tRNA^{Pyl} systems by Western blot, ELISA and confocal microscopy. I compared the previously published and well-characterized Pyl^{RS}/tRNA^{Pyl} systems: pcDNA3.1-tRNA^{Pyl}/NESPylRS^{AF} (RS$_{Lemke}$) (Nikić et al., 2016) and pcDNA3.1-*Mb*PylRS^{F}/tRNA^{M15} (RS$_{Coin}$) (Serfling et al., 2018).

First, I transfected cleavage-deficient E5$^{S>A}$ and E5$^{S>A}$-TAG^{NTF} constructs into HEK-293T cells and analyzed cell lysates by Western blot. Cleavage-deficient variants provided the opportunity to analyze exclusively full-length receptors. Protein fractions were detected using antibodies directed against the N-terminal HA epitope and the C-terminal V5 epitope **(Fig. 20A**). Western blot analysis of E5$^{S>A}$ demonstrated the appearance of full-length E5 in the α-HA- and α-V5-representing channel between the 75 kDa and 100 kDa marker band (**Fig. 20B**), which fits to the predicted size of 84.2 kDa (**Fig. 20C**). Interestingly, the protein expression level of full-length E5$^{S>A}$-TAG^{NTF} was noticeably increased in combination with the RS$_{Coin}$ system (**Fig. 20B**). Furthermore, I observed the formation of two lower bands between 25 kDa and 37 kDa when using the α-HA antibody. These bands may indicate the formation of truncated NTFs compared to the predicted NTF size of 48.5 kDa (**Fig. 20C**).

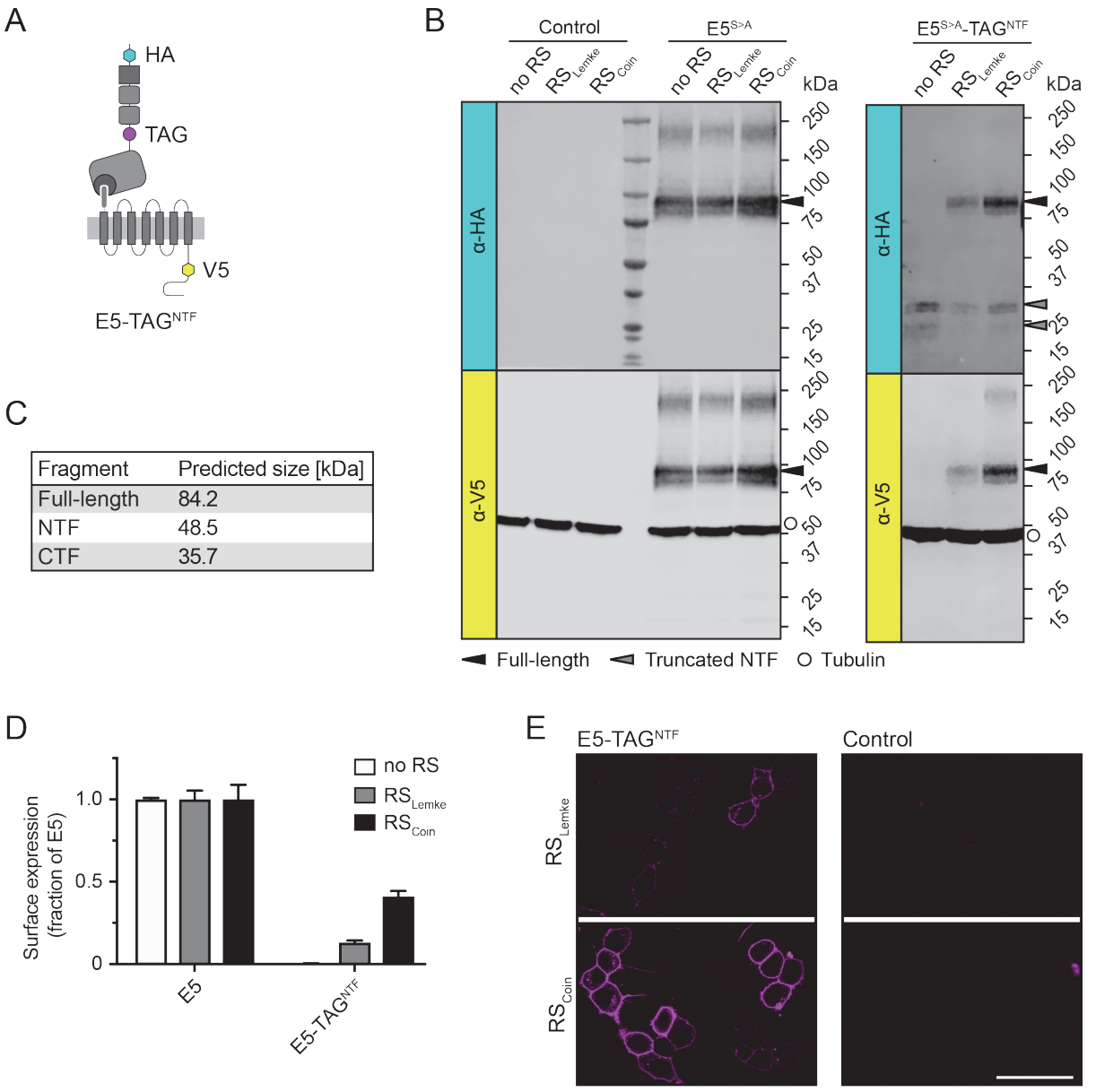

Fig. 20: Benchmarking of the UAA incorporation in E5 using two different Pyl^{RS}/tRNA^{Pyl} systems (RS$_{Lemke}$ and RS$_{Coin}$).

(A) Schematic illustration of E5-TAG^{NTF} expanded by an N-terminal HA epitope, a C-terminal V5 epitope and an amber stop codon (TAG) within the linker region between EGF5 and GAIN domains. (B) Western blot analyses of non-cleaved E5$^{S>A}$ and E5$^{S>A}$-TAG^{NTF} transfected into HEK-293T cells compared to control cells (only transfected with EV) using α-HA and α-V5 antibodies. Detection of β-tubulin serves as an internal loading control. (C) Predicted E5 fragment sizes of full-length receptor, NTF and CTF based on their amino acid sequence. (D) Quantification of surface expression levels of E5-TAG^{NTF} compared to E5 in HEK-293T cells by ELISA. Dataset normalized to the expression level of E5. Data are shown as mean ± SEM (N = 1, n = 4). (E) Confocal images of HEK-293T cells expressing H-Tet-Cy5-labeled E5-TAG^{NTF} compared to control cells (only transfected with the respective Pyl$^{RS/}$tRNA^{Py} system). Scale bar 50 µm.

Additionally, I investigated the influence of RS_{Lemke} and RS_{Coin} systems on the surface expression of E5. To this end, I expressed E5-TAG^{NTF} in HEK-293T cells and determined the surface delivery compared to E5 using pre-described ELISA. Quantified surface expression levels showed an increased expression from 13 % to 41 % for the RS_{Coin} system compared to the RS_{Lemke} system (**Fig. 20D**). ELISA data additionally showed the absence of truncated E5-TAG^{NTF} at the plasma membrane when cells were transfected without an extra RS system.

Finally, I investigated the influence of the RS_{Lemke} and RS_{Coin} system on the efficiency of the bioorthogonal labeling. To this end, E5-TAG^{NTF} were expressed in HEK-293T cells and confocally imaged after labeling with H-Tet-Cy5. Microscopic images showed an increased fluorescence signal for E5-TAG^{NTF} in combination with the RS_{Coin} system (**Fig. 20E**). In addition, the confocal imaging of control cells indicated that both Pyl^{RS}/$tRNA^{Pyl}$ systems permitted a specific bioorthogonal labeling.

6.3.4 Bioorthogonal and IF labeling of ADGRE5 indicates co-residence of NTF and CTF at the plasma membrane

Useful features of bioorthogonal click chemistry in cells are the temporal and spatial separation between UAA incorporation and the reaction with the tetrazine dye derivative. If the UAA is located in the ECR of the target protein and if membrane-impermeable dyes are employed, bioorthogonal labeling occurs only at proteins located in the plasma membrane. This comprises an alternative method for surface-exclusive aGPCR visualization besides the use of IF staining and α-BuTX labeling. I tested this assumption with the already characterized mTurq-E5 variant (see 6.3.2), which contains an NTF-fused mTurquoise instead of the EGF5 domain. Since genetically encoded fluorophores like mTurquoise are readily detectable upon folding in the ER, this obscures exclusive plasma membrane labeling. For this purpose, I combined mTurq-E5 with bioorthogonal labels within the extracellular loops of the 7TM domain representing the CTF label. These generated mTurq-E5-TAG^{ECLX} variants displayed an ideal model to demonstrate the surface-exclusive labeling of E5 using bioorthogonal click chemistry compared to genetically encoded fluorophores.

In a first experiment, I tested the bioorthogonal labeling of the ECL3 of E5. To do so, I transfected mTurq-E5-TAG^{ECL3} (**Fig. 21A**) and control constructs (E5, mTurq-E5) into HEK-293T cells and labeled these with H-Tet-Cy5 afterwards. Confocal imaging revealed the effective labeling of mTurq-E5-TAG^{ECL3} compared to the control constructs without bioorthogonal label (**Fig. 21B**). In addition, dually labeled mTurq-E5-TAG^{ECL3} demonstrated the co-residence of the NTF (mTurquoise) and the CTF (bioorthogonal label) at the cell surface. Furthermore, I observed a large fraction of

mTurquoise signal in intracellular locations, e.g. vesicular and perinuclear cisternal structures, which likely corresponded to newly synthesized receptors in the ER. The fluorescence signal of the bioorthogonal labeling was mainly detectable on the cell surface, only a few intracellular fluorescent vesicles were present. Interestingly, these constitutively internalized vesicles included mTurquoise signals, which indicated the internalization of E5 as a full-length heterodimer. Internalized vesicles did not correlate with the ER, which was stained with α-Calnexin-Alexa 488 antibodies.

In addition, the bioorthogonal labeling of mTurq-E5-TAG^{ECL3} was successfully accomplished with H-Tet-Cy3, which once again confirmed the surface expression and internalization of E5 as a heterodimeric receptor (**Fig. 21C**). In contrast, the bioorthogonal labeling of mTurq-E5-TAG^{ECL3} using H-Tet-ATTO 488 was not successful due to absent fluorescent signals.

In addition, I repeated the experiment also for mTurq-E5-TAG^{ECL1} and mTurq-E5-TAG^{ECL2} variants, and compared the results with the already established mTurq-E5-TAG^{ECL3} (**Fig. 22A**). I transfected these constructs into HEK-293T cells. This time, I combined mTurquoise and bioorthogonal labeling of the ECL with IF staining of the N-terminal HA tag to visualize E5 by confocal imaging. This way, both receptor tags become exposed to their respective label, the α-HA-Alexa 488 (NTF) and H-Tet-Cy5 (CTF), only upon presentation of E5 at the plasma membrane. Moreover, this allows a clear demonstration of the internalization of E5 as a heterodimer without background signals (mTurquoise) of newly synthesized receptors. Confocal images of transfected cells allowed for a clear distinction between the NTF and the CTF for all three E5 variants (**Fig. 22B**). In contrast, the mTurquoise signal scattered widely inside cells, which represents internalized receptors and large amounts of newly synthesized receptors.

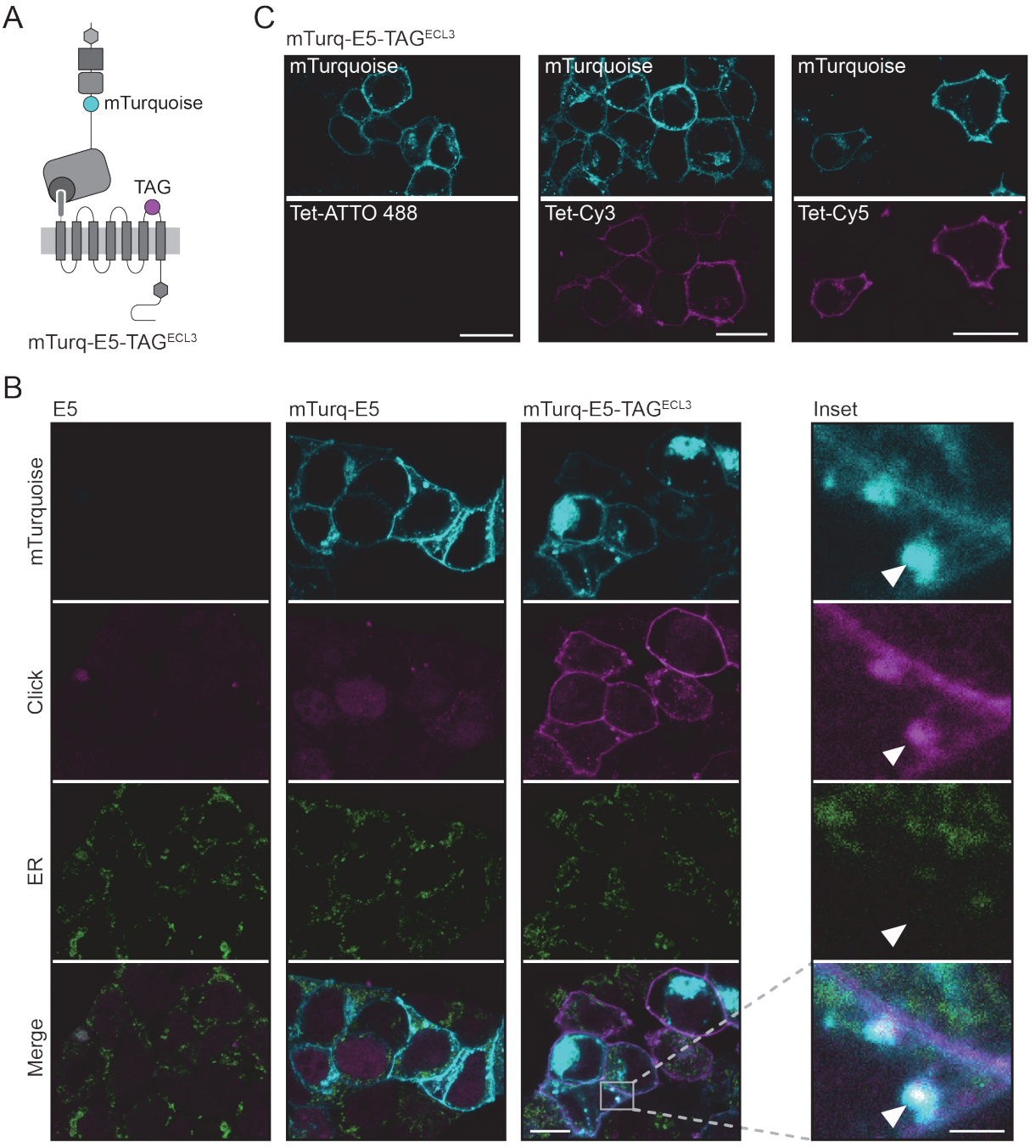

Fig. 21: Dually labeled mTuq-E5-TAG^{ECL3} demonstrate the surface expression and internalization of E5 as a heterodimeric receptor.

(A) Schematic illustration of mTurq-E5-TAG^{ECL3} expanded by an NTF-fused mTurquoise (instead of EGF5 domain) and an amber stop codon (TAG) within the ECL3. (B) Confocal images of HEK-293T expressing E5, singly labeled mTurq-E5 and dually labeled mTurq-E5-TAG^{ECL3}. Cells are labeled with H-Tet-Cy5 (magenta) and an ER marker (α-Calnexin-Alexa 488, green). mTurquoise signals (cyan) are only detectable for the mTurq-fused E5 variants. Dually labeled mTurq-E5-TAG^{ECL3} shows fluorescence signals of the NTF-fused mTurquoise and the CTF-fused bioorthogonal label. The inset reveals the surface expression and internalization of mTurq-E5-TAG^{ECL3} as a heterodimeric receptor (white arrow). (C) Confocal images of HEK-293T expressing mTurq-E5-TAG^{ECL3} demonstrate the labeling and co-residence of NTF (mTurquoise, cyan) and CTF using H-Tet-Cy3 or H-Tet-Cy5 (magenta). The

labeling with H-Tet-ATTO 488 shows no fluorescence signals. Used $Pyl^{RS/}tRNA^{Pyl}$ system: (B) RS_{Coin}, (C) RS_{Lemke}. Scale bars (B) 10 µm, 2 µm (inset), (C) 20 µm.

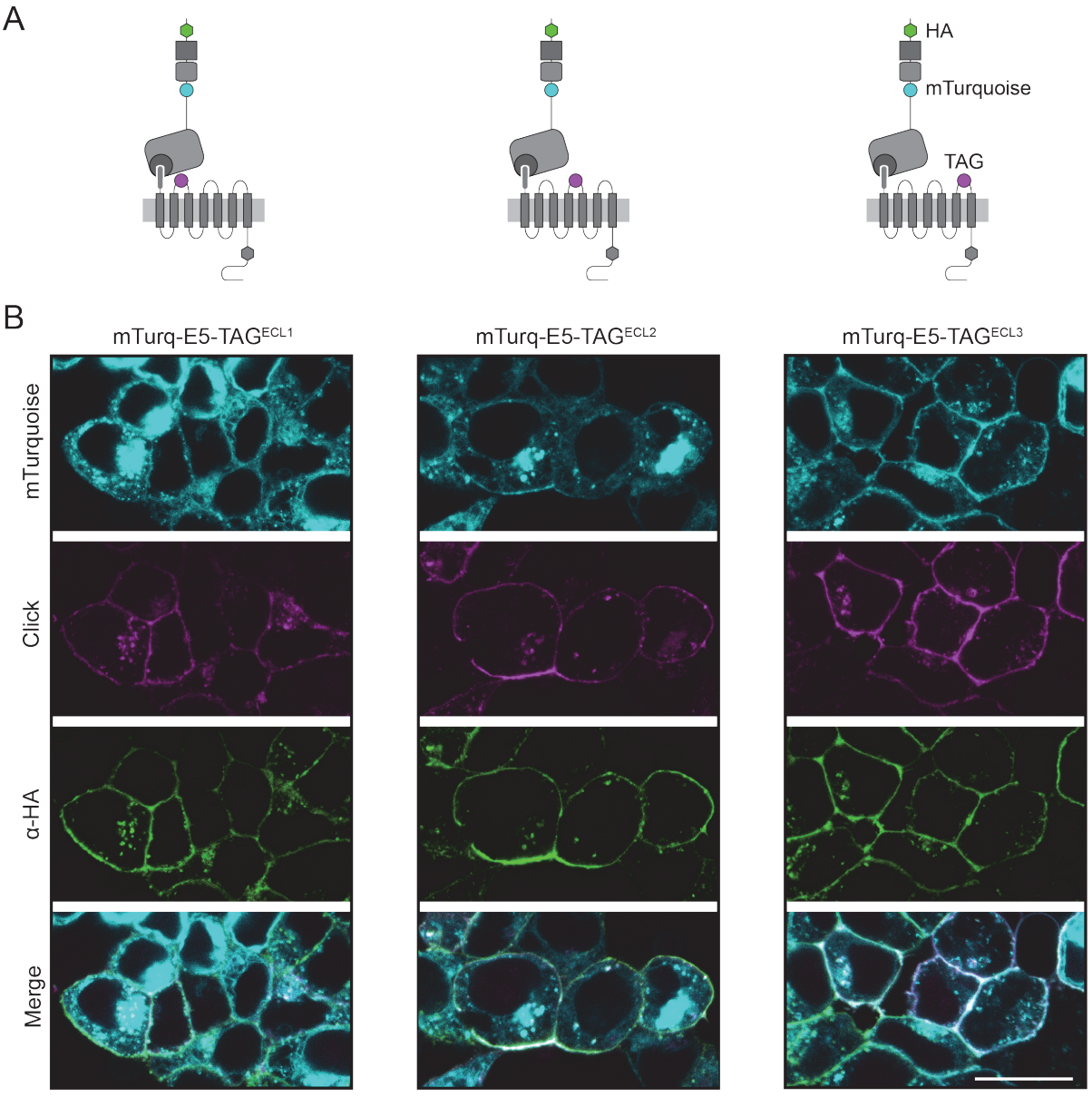

Fig. 22: Bioorthogonal and IF labeling of mTurq-E5-TAG^{ECLX} variants shows co-residence of NTF and CTF at the plasma membrane and in the internalized vesicles.

(A) Schematic illustration of E5 variants represents tag positions: an N-terminal HA epitope, an mTurquoise instead of the EGF5 domain and an amber stop codon (TAG) within the ECL1 (left panel), ECL2 (middle panel) or ECL3 (right panel). (B) Confocal images of HEK-293T expressing mTurq-E5-TAG^{ECL1}, mTurq-E5-TAG^{ECL2} and mTurq-E5-TAG^{ECL3}. Cells are bioorthogonally labeled with H-Tet-Cy5 (magenta) and IF-labeled using α-HA-Alexa 488 (green). IF label (NTF) and bioorthogonal label (CTF) verify the co-residence of NTF and CTF at the plasma membrane and the internalization of E5 as a heterodimer. NTF-fused mTurquoise (cyan) displays large intracellular fractions of newly synthesized E5 receptors. Used $Pyl^{RS/}tRNA^{Pyl}$ system: RS_{Coin}. Scale bar 20 µm.

6.3.5 Differential effects of GPS mutations on ADGRE5 surface residence

In previous experiments, I demonstrated that the abolition of the self-cleavage in E5 has no impact on the surface delivery (see 6.2.3). However, the effect of the bioorthogonal labeling on the autoproteolysis reaction of E5 is still unknown. Therefore, I utilized a set of cleavage-deficient E5 variants to study how the abolition of the GAIN domain-mediated autoproteolysis impacts on the protein expression and surface delivery of bioorthogonally labeled E5.

First, I expressed $E5^{H>A}$-TAG^{NTF} and $E5^{S>A}$-TAG^{NTF} containing an N-terminal bioorthogonal label in HEK-293T cells and subsequently analyzed protein fractions by Western blot using an antibody directed against the N-terminal HA epitope together with an antibody directed against the C-terminal V5 epitope (**Fig. 23A**). Cleavage-deficient variants provided the opportunity to analyze exclusively full-length receptors. Western blot analyses revealed the same band pattern compared to the previous analysis of $E5^{S>A}$-TAG^{NTF} (see 6.3.3). The band pattern using α-HA and α-V5 antibodies verified the appearance of full-length E5, which has a predicted size of 84.2 kDa (**Fig. 23B**), between the 75 kDa and 100 kDa marker bands (**Fig. 23C**). Furthermore, I observed the formation of two lower bands between 25 kDa and 37 kDa in the α-HA-representing channel. These bands may indicate the formation of truncated NTFs compared to the predicted full-length NTF size of 48.5 kDa (**Fig. 23B**). Interestingly, protein band intensities indicated that the expression level of $E5^{S>A}$-TAG^{NTF} was increased compared to $E5^{H>A}$-TAG^{NTF}.

Next, I quantified the surface expression of cleavage-deficient $E5^{H>A}$-TAG^{NTF} and $E5^{S>A}$-TAG^{NTF} compared to cleavable E5-TAG^{NTF} by the pre-described ELISA. Quantified data showed an indistinguishable surface delivery for E5-TAG^{NTF} and $E5^{S>A}$-TAG^{NTF} (**Fig. 23D**). In contrast, $E5^{H>A}$-TAG^{NTF} was significantly reduced to ~37 % compared to E5-TAG^{NTF}. I confirmed this observation by bioorthogonal H-Tet-Cy5 labeling of these $E5^{X}$-TAG^{NTF} variants. Confocal imaging of E5-TAG^{NTF} and $E5^{S>A}$-TAG^{NTF} showed a stronger fluorescence signal compared to $E5^{H>A}$-TAG^{NTF} (**Fig. 23E**).

To measure this finding, I quantified the H-Tet-Cy5 signals based on fluorescence images, which were generated by a hybrid photodetector. The hybrid photodetector returns linear measurements of single photon counts, which allows for the direct readout of fluorescence signals of the different E5 variants and, thus, quantification of the respective receptor label. Also, these measurements confirmed that the $E5^{H>A}$-TAG^{NTF} variant was expressed at a lower level at the cell surface (**Fig. 23F**). All in all, the experimental data demonstrated that ELISA and bioorthogonal labeling are both reliable and comparable means for the quantification of the NTF amount at the plasma membrane.

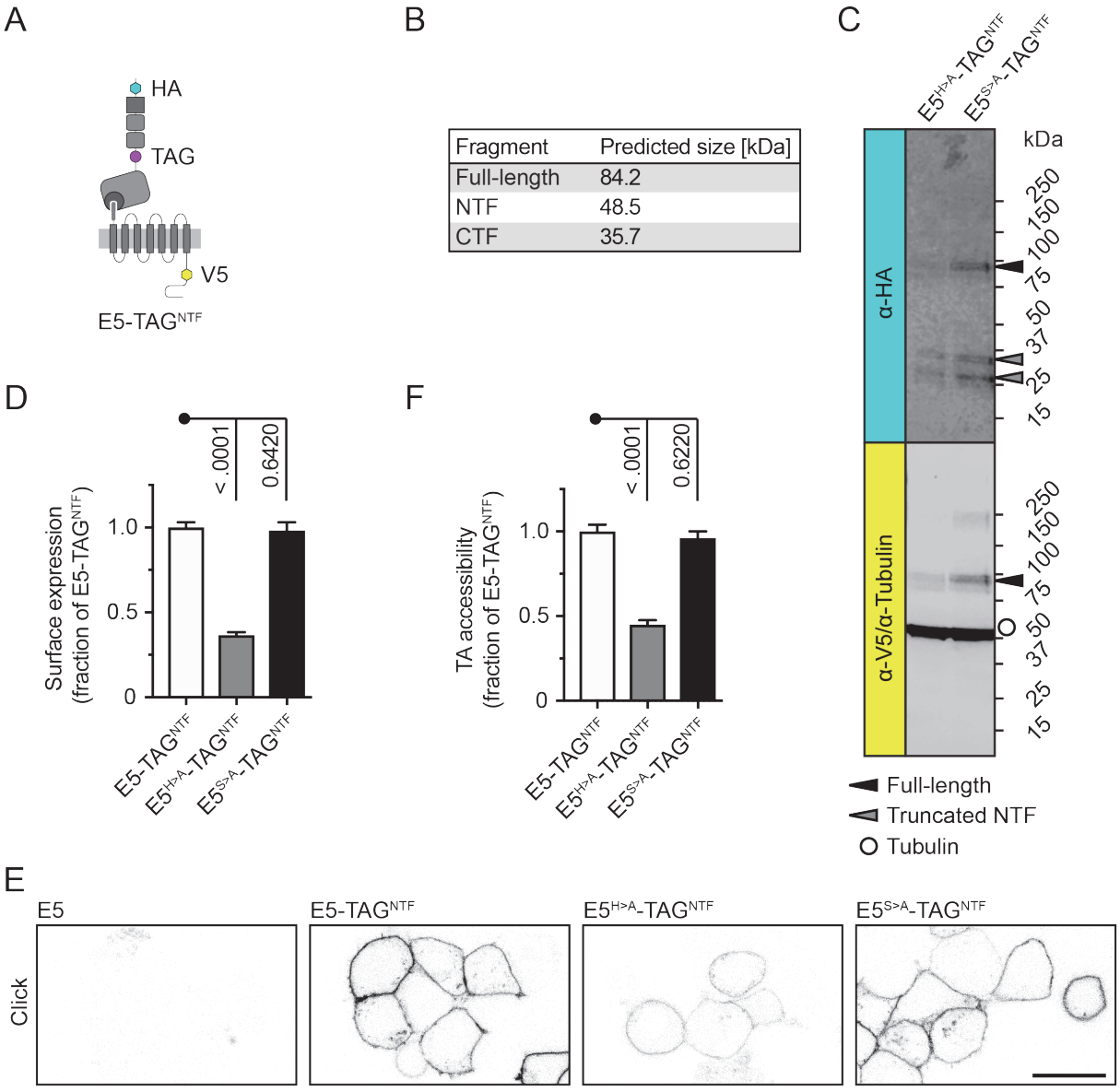

Fig. 23: Bioorthogonal label in the NTF of E5 offers a reliable quantification of surface expression and labeling.

(A) Schematic illustration of E5-TAG^{NTF} expanded by an N-terminal HA epitope, a C-terminal V5 epitope and an amber stop codon (TAG) within the linker region between EGF5 and GAIN domains. (B) Predicted E5 fragment sizes of full-length receptor, NTF and CTF based on their amino acid sequence. (C) Western blot analysis of cleavage-deficient E5$^{H>A}$-TAG^{NTF} and E5$^{S>A}$-TAG^{NTF} transfected into HEK-293T cells using α-HA and α-V5 antibodies. Detection of β-tubulin serves as an internal loading control. (D) Quantification of surface expression levels of HEK-293T cells expressing E5^{X}-TAG^{NTF} variants by ELISA. Dataset normalized to the expression level of E5-TAG^{NTF}. Data are shown as mean ± SEM (N = 2, n = 8). (E) Confocal images of HEK-293T cells expressing E5^{X}-TAG^{NTF} variants. Untagged E5 serves as labeling control. Cells were labeled with H-Tet-Cy5. (F) Quantification of the bioorthogonal label intensity of HEK-293T cells expressing E5^{X}-TAG^{NTF} variants. Dataset normalized to the fluorescence signal intensity of E5-TAG^{NTF}. Data are shown as mean ± SEM (N = 2, n ≥ 10). Used Pyl^{RS}/tRNA^{Pyl} system: RS$_{Coin}$. Scale bar 20 µm.

Next, I moved the bioorthogonal label from the NTF to the CTF by the integration of an amber stop codon in ECL1, ECL2 or ECL3. To test whether this represents a reliable method to quantify the NTF and the CTF separately, I employed the same procedures as for the E5^{X}-TAG^{NTF} receptor variants before.

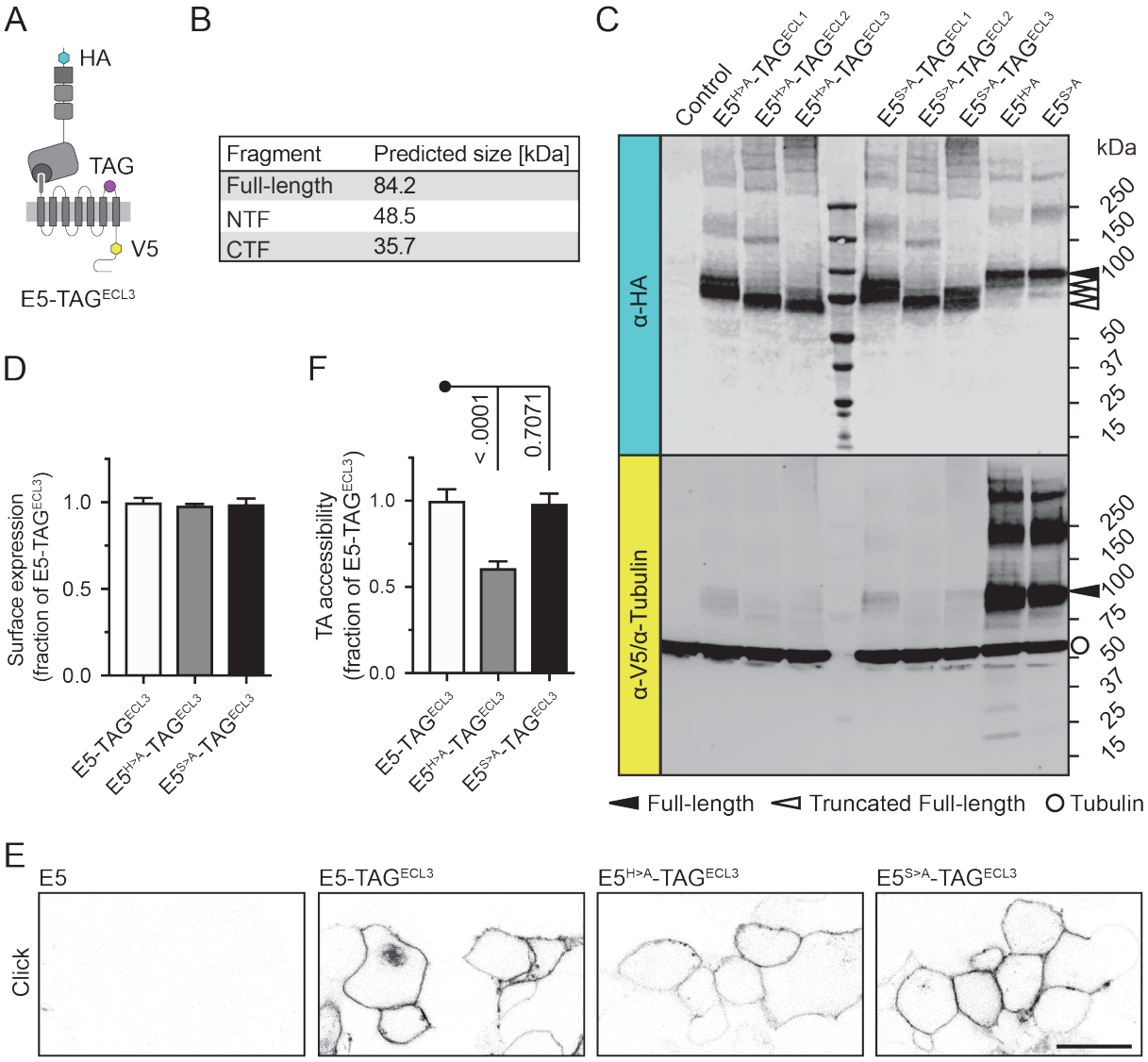

Fig. 24: Bioorthogonal labels in ECLs of E5 lead to the surface expression of truncated unlabeled receptors.

(A) Schematic illustration of E5-TAG^{ECL3} expanded by an N-terminal HA epitope, a C-terminal V5 epitope and an amber stop codon (TAG) within the ECL3. (B) Predicted E5 fragment sizes of full-length receptor, NTF and CTF based on their amino acid sequence. (C) Western blot analysis of cleavage-deficient E5$^{H>A}$, E5$^{S>A}$, E5$^{H>A}$-TAG^{ECLX} and E5$^{S>A}$-TAG^{ECLX} variants transfected into HEK-293T cells compared to control cells (only transfected with the Pyl^{RS}/tRNA^{Pyl} system) using α-HA and α-V5 antibodies. Detection of β-tubulin serves as an internal loading control. (D) Quantification of surface expression levels of HEK-293T cells expressing E5^{X}-TAG^{ECL3} variants by ELISA. Dataset normalized to the expression level of E5-TAG^{NTF}. Data are shown as mean ± SEM (N = 1, n = 12). (E) Confocal images of HEK-293T cells expressing E5^{X}-TAG^{ECL3} variants. Untagged E5 serves as labeling control. Cells were

labeled with H-Tet-Cy5. (F) Quantification of the bioorthogonal label intensity of HEK-293T cells expressing $E5^{X}$-TAG^{ECL3} variants. Dataset normalized to the fluorescence signal intensity of E5-TAG^{ECL3}. Data are shown as mean ± SEM (N = 3, n = 48). Used Pyl^{RS}/$tRNA^{Pyl}$ system: RS_{Coin}. Scale bar 20 µm.

First, I analyzed the protein amount of $E5^{H>A}$-TAG^{ECLX} and $E5^{S>A}$-TAG^{ECLX} by Western blot analysis using an antibody directed against the N-terminal HA epitope together with an antibody directed against the C-terminal V5 epitope (**Fig. 24A**). The band pattern of cleavage-deficient $E5^{H>A}$ and $E5^{S>A}$ demonstrated that the full-length E5 appears near the 100 kDa marker band (**Fig. 24C**), which fits to the predicted size of 84.2 kDa (**Fig. 24B**). Interestingly, I noted that the incorporation of UAAs led to the production of a majority of truncated receptors, which were shortened in accordance with the bioorthogonal label position, and to an almost complete loss of the full-length receptor based on missing C-terminal receptor fragments (**Fig. 24C**).

In contrast, surface expression analyses revealed an unimpaired surface expression for $E5^{H>A}$-TAG^{ECL3} and $E5^{S>A}$-TAG^{ECL3} compared to E5-TAG^{ECL3} (**Fig. 24D**). However, confocal imaging of bioorthogonally labeled $E5^{X}$-TAG^{ECL3} variants using H-Tet-Cy5, showed a stronger fluorescence signal for E5-TAG^{ECL3} and $E5^{S>A}$-TAG^{ECL3} at the cell surface, whereas the label intensity of $E5^{H>A}$-TAG^{ECL3} was reduced (**Fig. 24E**).

The signal quantification of bioorthogonal labels, which only represent full-length but not truncated receptors due to the missing UAAs, confirmed that E5-TAG^{ECL3} and $E5^{S>A}$-TAG^{ECL3} are expressed at similar levels, while the delivery of $E5^{H>A}$-TAG^{ECL3} to the cell surface is reduced (**Fig. 24F**).

In summary, the experimental data of this section demonstrated the successful incorporation of bioorthogonal labels into the receptor layout of E5. However, the efficiency of the label depended on the used Pyl^{RS}/$tRNA^{Pyl}$ system. Furthermore, I showed that a combination of bioorthogonal labeling using membrane-impermeable tetrazine dye derivatives and IF staining using specific antibodies allowed a surface exclusive visualization of E5. In addition, I demonstrated the spontaneous internalization of the NTF and the CTF of E5 in mammalian cells.

Importantly, experimental data revealed that the position of the bioorthogonal label is crucial for the reliability of quantitative analyses such as ELISA and fluorescent label quantifications: The incorporation of a bioorthogonal label into E5 resulted in the formation of full-length and truncated proteins depending on the efficiency of the UAA insertion. In case of the insertion of the UAA in the receptor before the first TM helix truncated receptor parts were possibly secreted and therefore not present at the plasma membrane. Consequently, only full-length UAA-labeled E5 molecules existed at the cell surface, allowing for reliable quantification of the membrane-bound labeled

receptor population through NTF and CTF tags. In contrast, I demonstrated that the incorporation of UAAs C-terminal to the first TM helix of E5 led to the formation of full-length (UAA-labeled) but also truncated (not UAA-labeled) receptors both containing the full or only parts of the 7TM domain anchored to the cell membrane. In this case, the quantification of E5 based on an independent NTF label (in this case an HA tag) assayed a mixed population of full-length and shortened receptors rendering surface amount quantification approaches of the NTF moot through overestimating its abundance, while quantification of a CTF label conceivably still reflected the correct amount of membrane-resident full-length receptors. See the summary of these conclusions in **Fig. 25**.

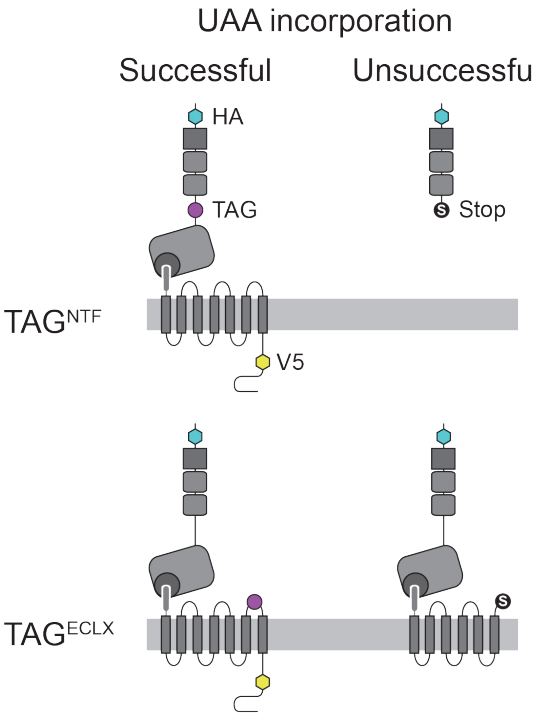

Location of bioorthogonal label	Quantification of N-terminal tag	Quantification of C-terminal tag
NTF	Reliable	Reliable
CTF	Unreliable	Reliable

Fig. 25: Position of the UAA incorporation is essential for the reliability of stoichiometric quantification analyses of NTF and CTF.

The incorporation of a bioorthogonal label into the NTF of E5 results in the formation of full-length proteins and truncated NTFs depending on the success of the UAA insertion. Truncated NTFs are secreted and therefore not present at the plasma membrane. Consequently, only full-length E5 exists at the cell surface, which allows a reliable quantification of NTF and CTF. In contrast, the incorporation of a bioorthogonal label into the CTF of E5 leads to the formation of full-length and truncated CTFs both containing parts of the 7TM domain. Remaining fragments of the 7TM domain allow a surface delivery of truncated CTFs. Consequently, the quantification of E5 NTF returns an overestimation since full-length and truncated E5 receptors are present at the plasma membrane. However, the quantification of bioorthogonal labels or other tags in the CTF are likely correct because these tags are only present in full-length receptors.

6.3.6 Labeling of ADGRE5 through the fusion to genetically encoded chromophores

The fusion of genetically encoded chromophores to a target protein provides one of the most used labeling techniques. An advantage of this method is the defined stoichiometry between chromophore and protein, which ensures protein counting and provides an easier interpretation of FRET data.

In this thesis, I combined and compared the NTF-fused genetically encoded chromophore mTurquoise with CTF-located FlAsH (see 6.3.1), BuTX (see 6.3.2) and bioorthogonal labeling (see 6.3.4). In addition, the combination of the cyan fluorescent protein mTurquoise with α-BuTX or bioorthogonal labels provided a potential use in FRET experiments to analyze conformational changes within the GAIN-7TM tandem in relation to the aGPCR activity (see 6.4.1). Interestingly, mTurquoise negatively influenced the surface expression depending on its exact position within the NTF of E5. The surface delivery was strongly impaired when mTurquoise was inserted into the linker region between the EGF5 and GAIN domains (see 6.3.1), whereas the replacement of the EGF5 domain by mTurquoise had a minor impact on the surface delivery (see 6.3.2). Furthermore, I used the cyan fluorescent protein mTurquoise and the yellow fluorescent protein mCitrine to create an intracellularly tagged E5 FRET sensor, allowing the analysis of conformational changes within the 7TM domain (see 6.4.2). Fused chromophores had no effect on the surface expression of the FRET sensor.

Summing up, in this chapter I transferred and established a panel of live cell labeling methods for aGPCRs on the example of the E5 receptor. I screened these labeling methods for their potential use for functional analyses. The most important characteristics are listed in **Tab. 2**.

Tab. 2: Characteristics of used labeling methods for E5.

Labeling method	Size (kDa)	Permeability	Surface expression (label position)	Procedure time (min)
Fluorescent protein	~27	directly fused to E5	unimpaired (CTF-fused, NTF-fused instead of EGF5 domain) impaired (NTF-fused between EGF5 and GAIN domains)	0
IF staining	~150	impermeable	unimpaired	30-60
α-BuTX labeling	~8	impermeable	slightly impaired (ECL1, ECL2, ECL3)	30-60

Labeling method	Size (kDa)	Permeability	Surface expression (label position)	Procedure time (min)
FlAsH labeling	~0.7	permeable	no surface expression (ICL3)	120-180
Bioorthogonal labeling	0.5-2	permeable*/ impermeable	< 50 % using RS_{Coin} (NTF) unreliable due to truncation (CTF)	10-30

*only impermeable dyes were used in this study

6.4 Functional analysis of aGPCRs via distance measurements

Previously, several members of the aGPCR family were found to function in mechanical contexts (Scholz et al., 2016). In addition, experimental data indicated an involvement of aGPCRs in mechanosensation (Petersen et al., 2015; Scholz et al., 2017, 2015). This leads to the assumption that mechanical forces are able to regulate aGPCR signaling. Presently, it is still unknown how this receptor family converts a mechanical stimulation into signaling and whether the presence of a ligand is necessary to transmit the mechanical forces onto the receptor protein. However, previous experiments showed an activation of downstream signaling pathways after the TA exposure and subsequent interaction with the 7TM domain, indicating a TA-dependent aGPCR activation (Liebscher et al., 2014; Stoveken et al., 2015). Furthermore, cell based assays demonstrated that the TA-dependent aGPCR activation is mediated by mechanical forces (cell shaking) or the combination with a ligand (Petersen et al., 2015; Wilde et al., 2016). However, molecular mechanisms of the TA release are still ill-defined. Currently, there are two models discussed among the aGPCR community. The dissociation model suggests that the NTF removal uncaps the TA, which subsequently engages with the 7TM domain to stabilize an active receptor conformation. In contrast, the non-dissociation model entails a TA-dependent receptor activation through conformational changes of the GAIN and the 7TM domain, resulting in a TA-7TM domain interaction. In this chapter I focused on the elucidation of molecular mechanisms of aGPCR activation using the previously established labeling methods and optical sensors.

6.4.1 Extracellular distance measurements within the GAIN-7TM domain tandem of ADGRE5

In this section, I focused on the molecular investigation of the dissociation and non-dissociation model of aGPCR activation (**Fig. 26**). A FRET approach provides a suitable tool to determine structural changes allowing distance measurements within

10 nm between a donor and acceptor fluorophore. To measure distance changes within the NTF-CTF heterodimer, more precisely between the GAIN domain and the 7TM domain, I used previously designed dually tagged E5 sensors. Hypothetically, the dissociation would correlate with a lower or, respectively, complete loss of FRET signal due to the increasing distance between donor and acceptor. In contrast, the non-dissociation model would predict a lower or higher FRET efficiency depending on the conformational change within the GAIN-7TM domain tandem. Since a low FRET signal could occur in both models, it should be possible to distinguish between the two models by switching off the cleavage.

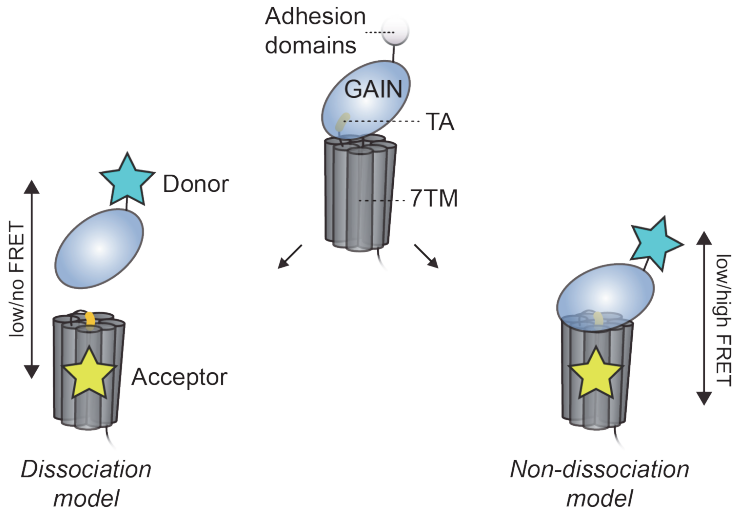

Fig. 26: Possible signaling models for a TA-dependent activation of aGPCRs and their expected FRET efficiencies.

Hypothetical models describe the conformational response of an aGPCR due to a mechanical stimulation and/or ligand binding. Stimulation results in a (1) dissociation-mediated or (2) non-dissociation-mediated activation. (1) Separation of NTF and CTF or (2) conformational/ distance change of the GAIN-7TM domain tandem leads to a release of the buried TA and subsequent interaction with the 7TM domain. The NTF-CTF separation correlates with low or, respectively, no FRET signal due to the increasing distance between donor (NTF-located) and acceptor (ECL-located), whereas conformational changes of the GAIN-7TM domain tandem correlate with a lower or higher FRET signal depending on spatial orientation of donor and acceptor.

In the first experiment, in collaboration with Mareike Hemberger, I focused on the E5 receptor tagged with an mTurquoise instead of the EGF5 domain and a BBS tag within the ECL. Previous experiments indicated a high surface expression and best labeling result of E5-BBS$^{ECLX/I-R+L}$ variants (see 6.3.2). For this purpose, I combined these constructs with the mTurq-E5 construct, which resulted in mTurq-E5-BBS$^{ECLX/I-R+L}$ variants. We expressed mTurq-E5-BBS$^{ECL3/I-R+L}$ (**Fig. 27A**) in HEK-293T cells. The BBS tag was labeled with Alexa 488 conjugated α-BuTX. The spectral properties of

mTurquoise (donor) and Alexa 488 (acceptor) theoretically ensured the energy transfer between these fluorophores allowing FRET analyses (**Fig. 27B**). The efficiency of the energy transfer was quantified via the acceptor bleaching method. To this end, confocal images were captured before and after the bleaching of the acceptor (Alexa 488) within a defined ROI (**Fig. 27C**). Fluorescence intensities within the ROI before and after bleaching revealed no FRET efficiency and therefore no further usage of this sensor for extracellular distance measurements (**Fig. 27D**).

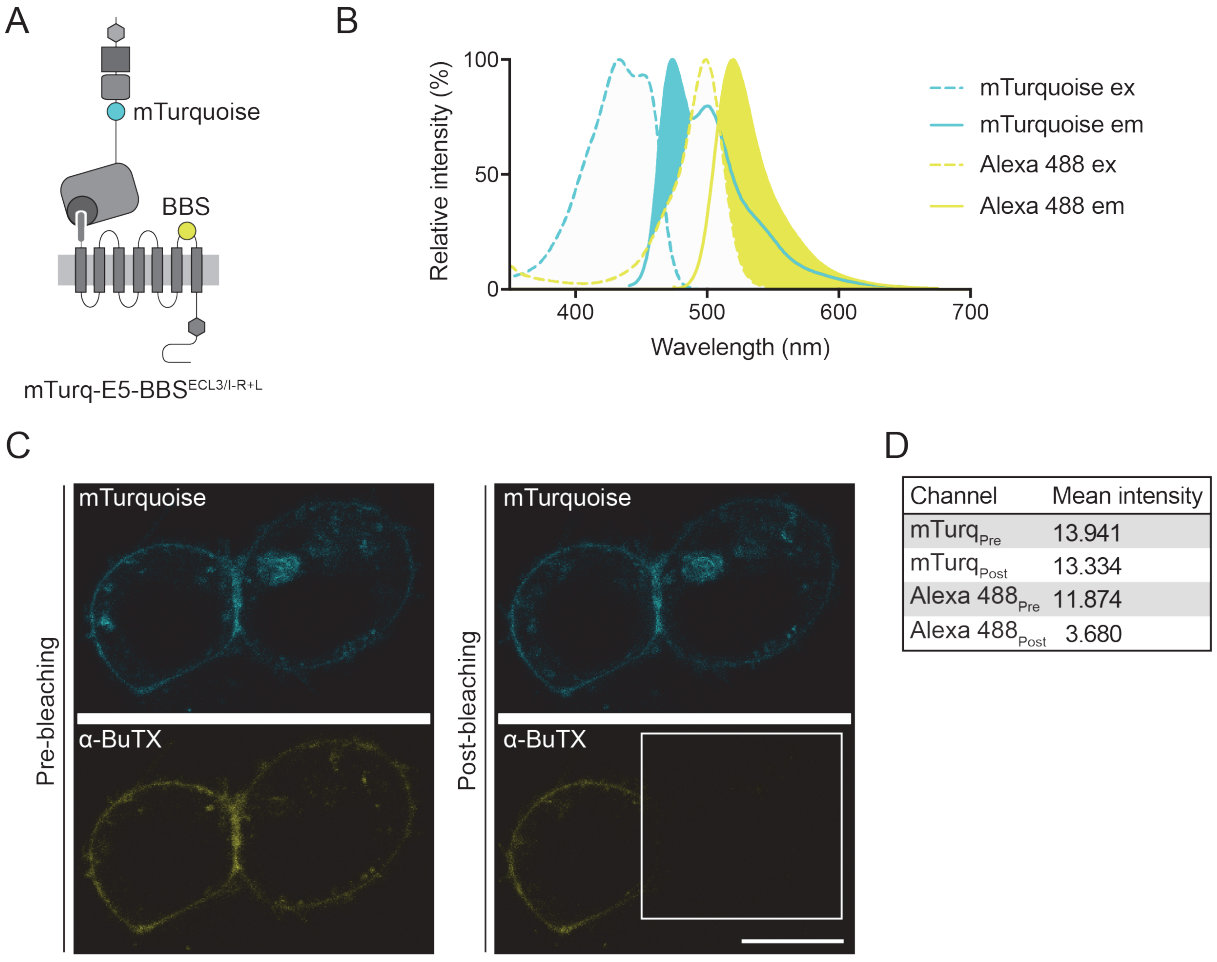

Fig. 27: mTurquoise- and BBS-tagged E5 sensor shows no FRET efficiency in an unstimulated situation.

(A) Schematic illustration of mTurq-E5-BBS$^{ECL3/I-R+L}$ expanded by an NTF-fused mTurquoise (instead of the EGF5 domain) and a BBS tag within the ECL3. (B) Excitation (ex) and emission (em) spectra of mTurquoise and Alexa 488 indicate the theoretical energy transfer between these fluorophores. (C) Confocal images of HEK-293T cells expressing mTurq-E5-BBS$^{ECL3/I-R+L}$. BBS tags are labeled with α-BuTX-Alexa 488. Images show mTurquoise (cyan) and Alexa 488 (yellow) channels pre- and post-bleaching of the acceptor. White box indicates the bleached ROI (experiment performed by Mareike Hemberger). (D) Measured mean intensities of mTurquoise and Alexa 488 before and after acceptor bleaching within the ROI. Scale bar 10 µm.

mTurq-E5-BBS$^{ECLX/I-R+L}$ variants containing a BBS tag within the ECL1 or ECL2 exhibited a similar result, indicating that the absent FRET signal was independent of the BBS tag position (data not shown).

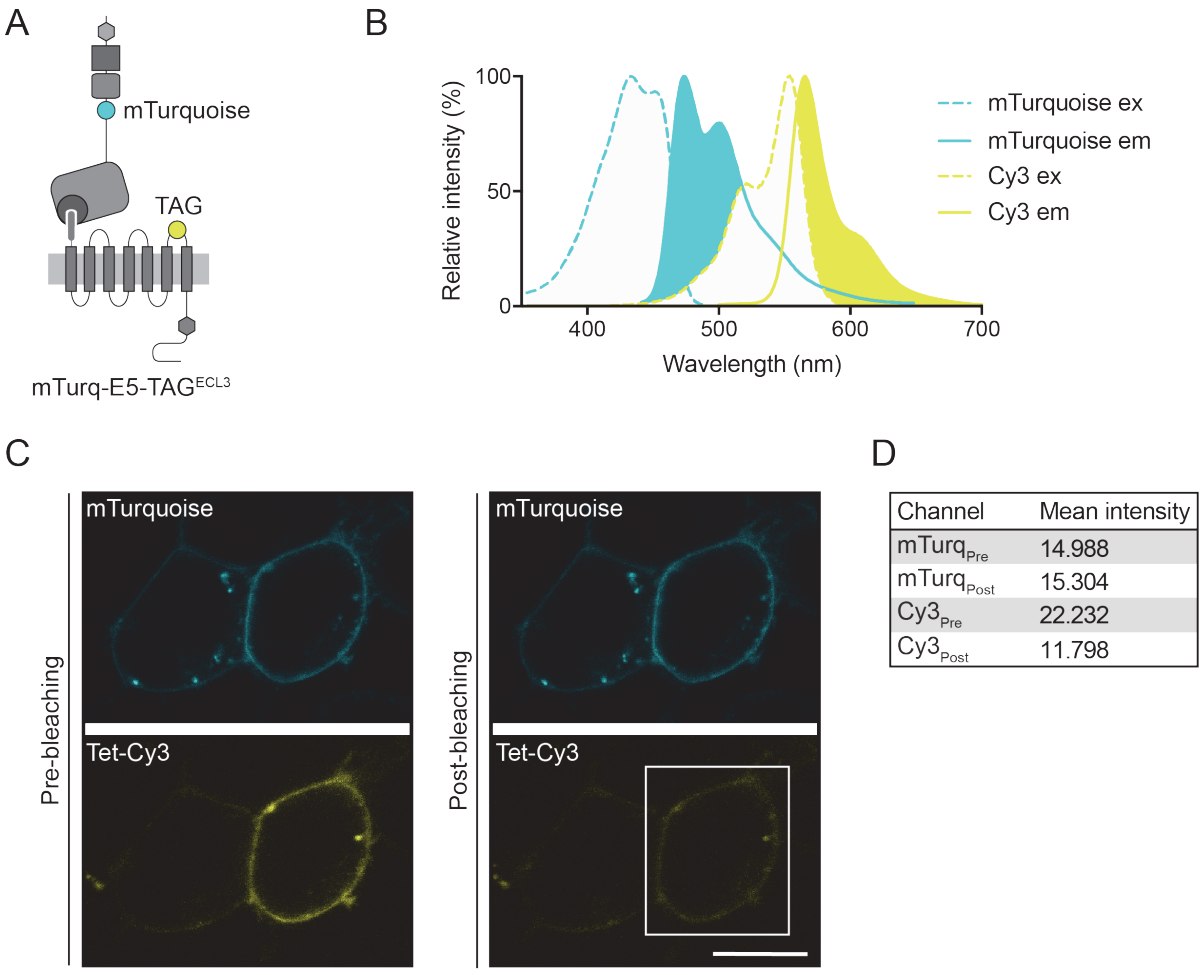

Channel	Mean intensity
$mTurq_{Pre}$	14.988
$mTurq_{Post}$	15.304
$Cy3_{Pre}$	22.232
$Cy3_{Post}$	11.798

Fig. 28: mTurquoise- and TAG-tagged E5 sensor shows no FRET efficiency in an unstimulated situation.

(A) Schematic illustration of mTurq-E5-TAG^{ECL3} expanded by an NTF-fused mTurquoise (instead of the EGF5 domain) and an amber stop codon within the ECL3. (B) Excitation (ex) and emission (em) spectra of mTurquoise and Cy3 indicate the theoretical energy transfer between these fluorophores. (C) Confocal images of HEK-293T cells expressing mTurq-E5-TAG^{ECL3}. UAAs are labeled with H-Tet-Cy3. Images show mTurquoise (cyan) and Cy3 (yellow) channels pre- and post-bleaching of the acceptor. White box indicates the bleached ROI. (D) Measured mean intensities of mTurquoise and Cy3 before and after acceptor bleaching within the ROI. Used Pyl^{RS}/tRNA^{Pyl} system: RS_{Lemke}. Scale bar 10 µm.

Next, I tested the prospective use of an E5 sensor tagged with an mTurquoise instead of the EGF5 domain and a bioorthogonal label within the ECL. For this purpose, I expressed mTurq-E5-TAG^{ECL3} (**Fig. 28A**) in HEK-293T cells. In this experiment, the UAA was labeled with the acceptor-representing fluorophore H-Tet-Cy3, which is a

suitable partner for the energy transfer with mTurquoise (**Fig. 28B**). The FRET efficiency was quantified using the acceptor bleaching method. Confocal images were captured before and after the bleaching of the acceptor (Cy3) within a ROI (**Fig. 28C**). Fluorescence intensities within the ROI before and after bleaching revealed no sufficient energy transfer (**Fig. 28D**). Therefore, I decided to further test other tetrazine dye derivatives.

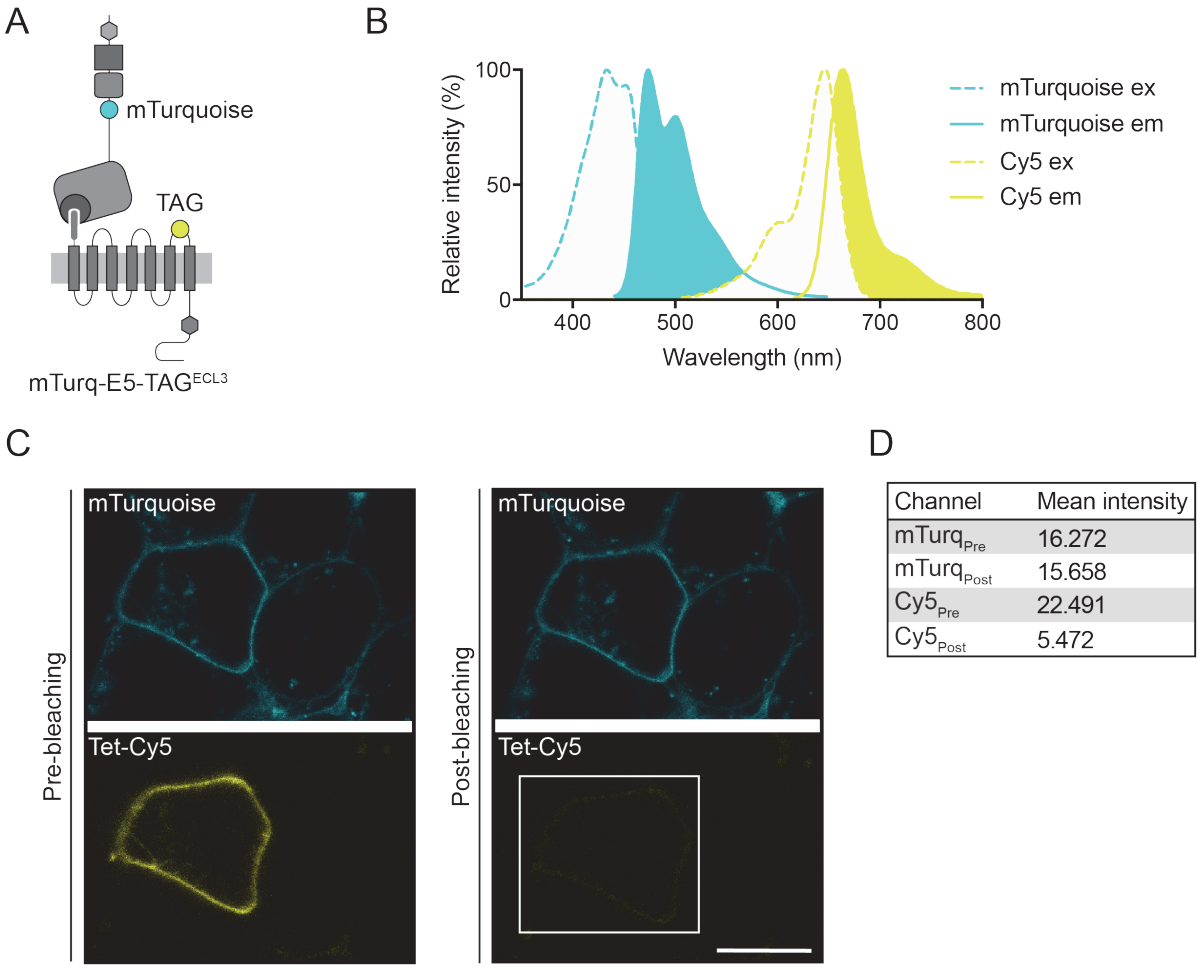

Channel	Mean intensity
$mTurq_{Pre}$	16.272
$mTurq_{Post}$	15.658
$Cy5_{Pre}$	22.491
$Cy5_{Post}$	5.472

Fig. 29: mTurquoise- and TAG-tagged E5 sensor shows no FRET efficiency in an unstimulated situation.

(A) Schematic illustration of mTurq-E5-TAG^{ECL3} expanded by an NTF-fused mTurquoise (instead of the EGF5 domain) and an amber stop codon within the ECL3. (B) Excitation (ex) and emission (em) spectra of mTurquoise and Cy5 indicate the theoretical energy transfer between these fluorophores. (C) Confocal images of HEK-293T cells expressing mTurq-E5-TAG^{ECL3}. UAAs are labeled with H-Tet-Cy5. Images show mTurquoise (cyan) and Cy5 (yellow) channels pre- and post-bleaching of the acceptor. White box indicates the bleached ROI. (D) Measured mean intensities of mTurquoise and Cy5 before and after acceptor bleaching within the ROI. Used Pyl^{RS}/tRNA^{Pyl} system: RS_{Lemke}. Scale bar 10 µm.

Previously, I showed that the labeling of mTurq-E5-TAG^{ECL3} with H-Tet-ATTO 488 was not possible, so I tried H-Tet-Cy5 as an acceptor fluorophore, which had shown the best labeling results before (see. 6.3.4). Again, I transfected the mTurq-E5-TAG^{ECL3} construct (**Fig. 29A**) into HEK-293T cells and labeled with H-Tet-Cy5, which is a suitable partner for the energy transfer with mTurquoise (**Fig. 29B**). The FRET efficiency was quantified using the acceptor bleaching method. Confocal images were captured before and after the bleaching of the acceptor (Cy5) within a ROI (**Fig. 29C**). Also, in this context, no energy transfer was observable (**Fig. 29D**).

mTurq-E5-TAG^{ECLX} variants expanded by bioorthogonal labels within ECL1 or ECL2, showed similar results for H-Tet-Cy3 and H-Tet-Cy5 labeling, indicating that the absent FRET signal was independent of used tetrazine dye derivatives and bioorthogonal label positions (data not shown).

In summary, extracellularly tagged E5 variants were not suitable to determine distance changes within the GAIN-7TM domain tandem by FRET analyses. Reasons for this could be an inappropriate distance and/or the relative orientation between the donor and acceptor fluorophore. To address and overcome this problem, the future sensor designs will have to ensure a close proximity between the donor and acceptor fluorophore. The insertion of a label into the GAIN domain could be a possibility to decrease the distance, however, the labeling method used should not impair the integrity of the GAIN domain. The experimental data in this study suggested that the bioorthogonal labeling of the TA, a part of the GAIN domain, had no effect on its integrity (see 6.5.1) and, therefore, allowing its potential use in future E5 FRET sensors. Another possibility to approximate donor and acceptor is the use of suitable linkers. In addition, such linkers could also help to improve the relative orientation of the fluorophores.

6.4.2 Intramolecular distance measurements within the 7TM domain of ADGRE5

It is well known that the activation of GPCRs leads to a conformational change of the 7TM domain, which results in an activation and dissociation of the G protein and the regulation of a variety of signaling cascades (Weis and Kobilka, 2018). To investigate whether the activation of aGPCRs correlates with a conformational change within the 7TM domain, I engineered a FRET sensor layout, which was successfully used for class A GPCRs in the past (Hoffmann et al., 2005; Jensen et al., 2009; Vilardaga et al., 2003). This FRET sensor layout encompassed an mTurquoise inserted into the ICL3 and an mCitrine fused to the ICR of the E5 receptor (**Fig. 30A**). The spectral properties of mTurquoise (donor) and mCitrine (acceptor) ensure a successful energy transfer (**Fig. 30B**). To test the functionality of this sensor for FRET experiments, I

expressed the sensor (E5-mTurq-mCit) in HEK-293T cells and bleached the mCitrine over 60 seconds. Confocal images before and after bleaching proved the energy transfer and functionality of the FRET sensor (**Fig. 30C**). Additionally, I plotted the fluorescence intensities of the donor and the acceptor over time (**Fig. 30D**). The acceptor bleaching led to a decrease of the mCitrine signal, while at the same time the mTurquoise signal was increased.

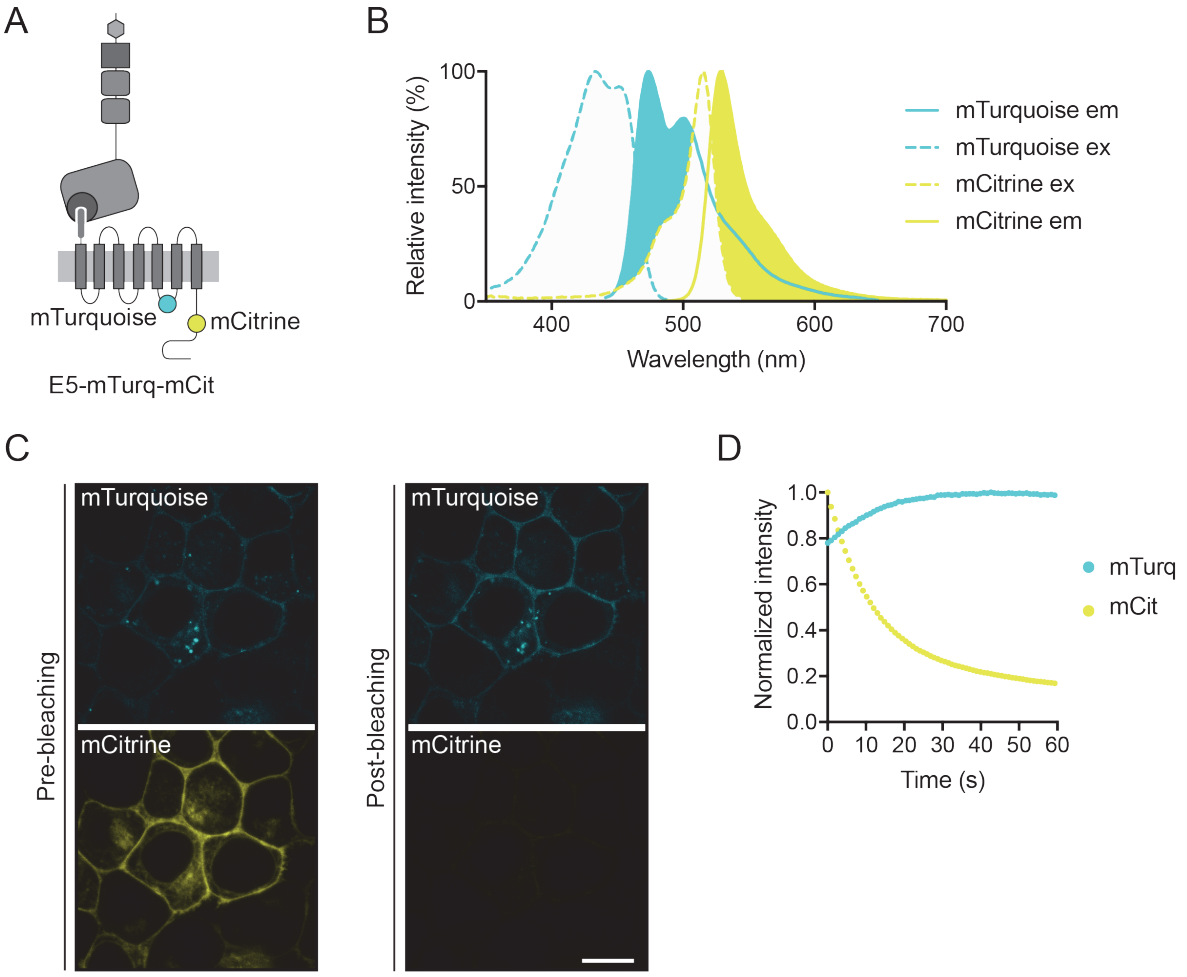

Fig. 30: mTurquoise- and mCitrine-tagged E5 sensor shows FRET efficiency in an unstimulated situation.

(A) Schematic illustration of E5-mTurq-mCit expanded by an ICL3-fused mTurquoise and an ICR-fused mCitrine. (B) Excitation (ex) and emission (em) spectra of mTurquoise and mCitrine indicate the theoretical energy transfer between these fluorophores. (C) Confocal images of HEK-293T cells expressing E5-mTurq-mCit. Images show mTurquoise (cyan) and mCitrine (yellow) channels pre- and post-bleaching of the acceptor. (D) Normalized fluorescence intensities of mTurquoise and mCitrine over a bleaching period of 60s. Scale bar 10 µm.

The next step was to discover whether the E5 FRET sensor could be used to quantify conformational changes of the 7TM domain depending on the activity state. *In vitro*

signaling assays suggested a basal activity for full-length aGPCRs, high activity for receptors lacking the NTF and an abolished activity for receptors with the deletion of the entire ECR (Hilbig et al., 2018; Liebscher et al., 2014; Stoveken et al., 2015) (see 4.3). To test whether these principal signaling states correlate with conformational states of the 7TM domain, I combined the FRET sensor layout either with E5 variants lacking the NTF ($E5^{\Delta NTF}$-mTurq-mCit) or the ECR ($E5^{\Delta ECR}$-mTurq-mCit) and compared them with cleavable and cleavage-deficient full-length E5 variants (**Fig. 31A**).

First, in collaboration with Mareike Hemberger, I analyzed the surface expression of the generated E5 FRET sensors. For this purpose, the FRET constructs were transfected into HEK-293T cells and subsequently the surface expression quantified by the pre-described ELISA. ELISA data showed an unimpaired surface delivery for cleavable and cleavage-deficient (H>A) full-length E5-mTurq-mCit compared to E5 (**Fig. 31B**). Only the cleavage-deficient (S>A) variant showed a slightly reduced expression. Interestingly, both truncated E5 sensors revealed a significantly reduced expression at the plasma membrane, which was slightly higher than the EV control.

Next, the FRET efficiencies of these E5 variants were quantified by acceptor bleaching in living HEK-293T cells. Independent of the cleavage, the full-length E5 sensors showed similar efficiencies (**Fig. 31C**). The FRET efficiencies of E5 variants lacking the NTF (~65 %) or the ECR (~86 %) differed significantly compared with each other and with full-length E5. This resulted in E5, $E5^{\Delta NTF}$ and $E5^{\Delta ECR}$ assuming different conformational states of the 7TM domain, which correlates with different metabotropic activity levels of the respective receptor layouts. An additional explanation could be that differences in subcellular locations of these E5 variants lead to the different FRET efficiencies.

It has been shown for aGPCRs that missense mutations within the TA can abolish the metabotropic activity without affecting surface expression levels (Liebscher et al., 2014; Stoveken et al., 2015). We tested the relationship between the TA mutations and conformational changes of the 7TM domain with regard to the receptor activity using FRET. For this purpose, I mutated the TA of full-length E5 and $E5^{\Delta NTF}$ at position +3 (F>A) and +7 (M>A) (**Fig. 32A**) and subsequently transfected these E5 constructs into HEK-293T. The surface expression determination using ELISA and the quantification of FRET efficiencies by acceptor bleaching were performed in collaboration with Mareike Hemberger. ELISA data revealed an impaired surface delivery for TA-mutated $E5^{F>A}$-mTurq-mCit and $E5^{M>A}$-mTurq-mCit variants (**Fig. 32B**). In detail, the surface expression was reduced to ~64 % and ~72 % respectively compared to E5. However, both mutations in full-length E5 showed a similar expression compared to each other. Truncated E5 sensors demonstrated a

significantly reduced surface delivery to the plasma membrane, which was still above the EV control, independent of the TA mutations.

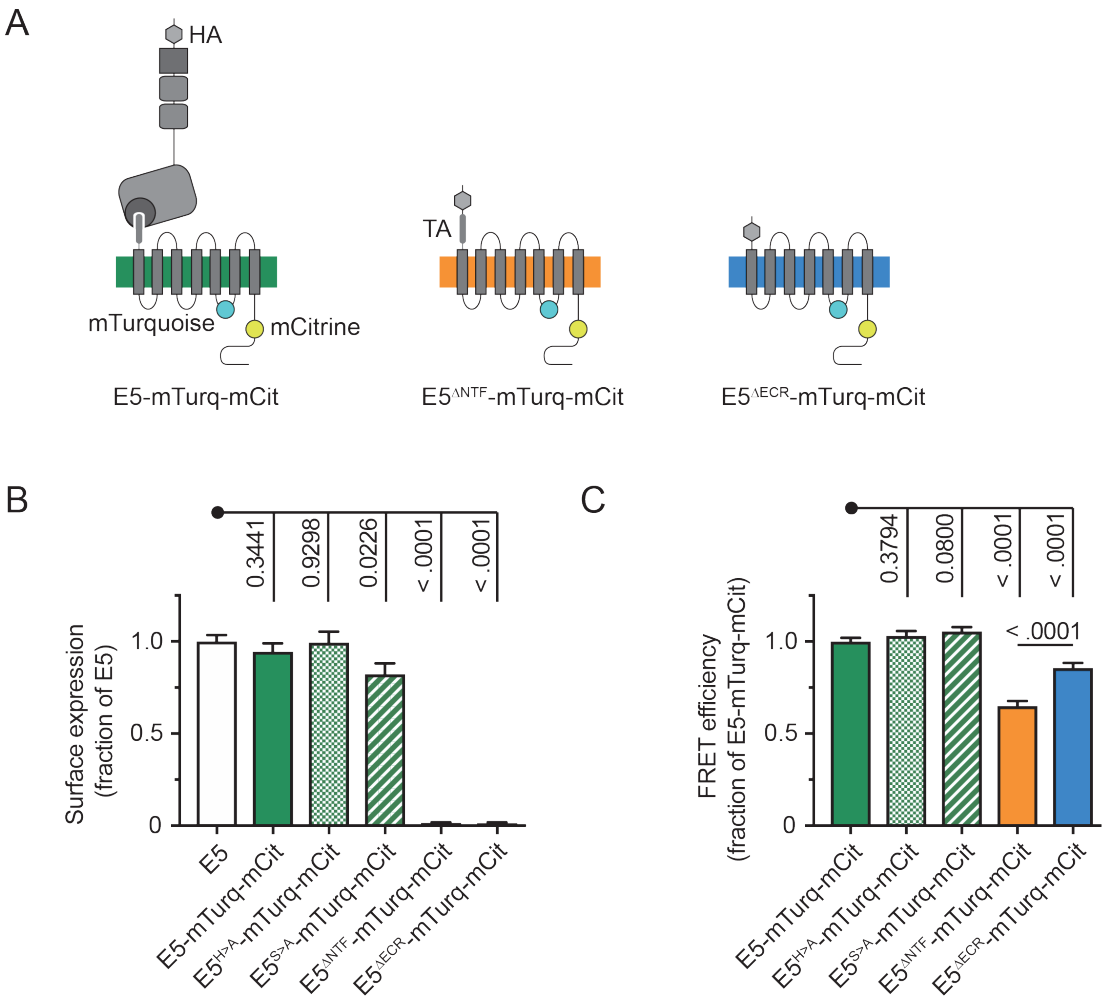

Fig. 31: Full-length and truncated E5 variants differ in their surface expression and 7TM domain conformation.

(A) Schematic illustration of full-length (green), ΔNTF (orange) and ΔECR (blue) FRET sensors of E5. (B) Quantification of surface expression levels of cleavable and cleavage-deficient full-length (green), ΔNTF (orange) and ΔECR (blue) FRET sensors of E5 compared to E5 in HEK-293T cells by ELISA. Dataset normalized to the expression level of E5. Data are shown as mean ± SEM (N = 2, n = 4). (C) Quantification of FRET efficiency levels of cleavable and cleavage-deficient full-length (green), ΔNTF (orange) and ΔECR (blue) E5 FRET sensors in HEK-293T cells by acceptor bleaching. Dataset normalized to the FRET efficiency level of E5-mTurq-mCit. Data are shown as mean ± SEM (N = 4, n ≥ 10). (B,C) performed by Mareike Hemberger.

FRET efficiencies of these E5 variants were quantified by acceptor bleaching. Both full-length E5 variants with mutated TA showed significantly reduced FRET efficiencies on a similar level of 77-83 % compared to unmutated E5-mTurq-mCit (**Fig. 32C**).

Interestingly, the FRET efficiencies were at a similar level as the efficiency of the E5$^{\Delta ECR}$ sensor suggesting a comparable 7TM domain conformation and likely similar receptor activity (**Fig. 31C**). FRET efficiencies of all E5$^{\Delta NTF}$ variants were at a similar level of 64-68 % compared to the unmutated E5-mTurq-mCit (**Fig. 32C**). In this case the TA mutation had no effect on the FRET efficiency and thus on the conformation of the 7TM domain. Reasons for this needs to be investigated in the future.

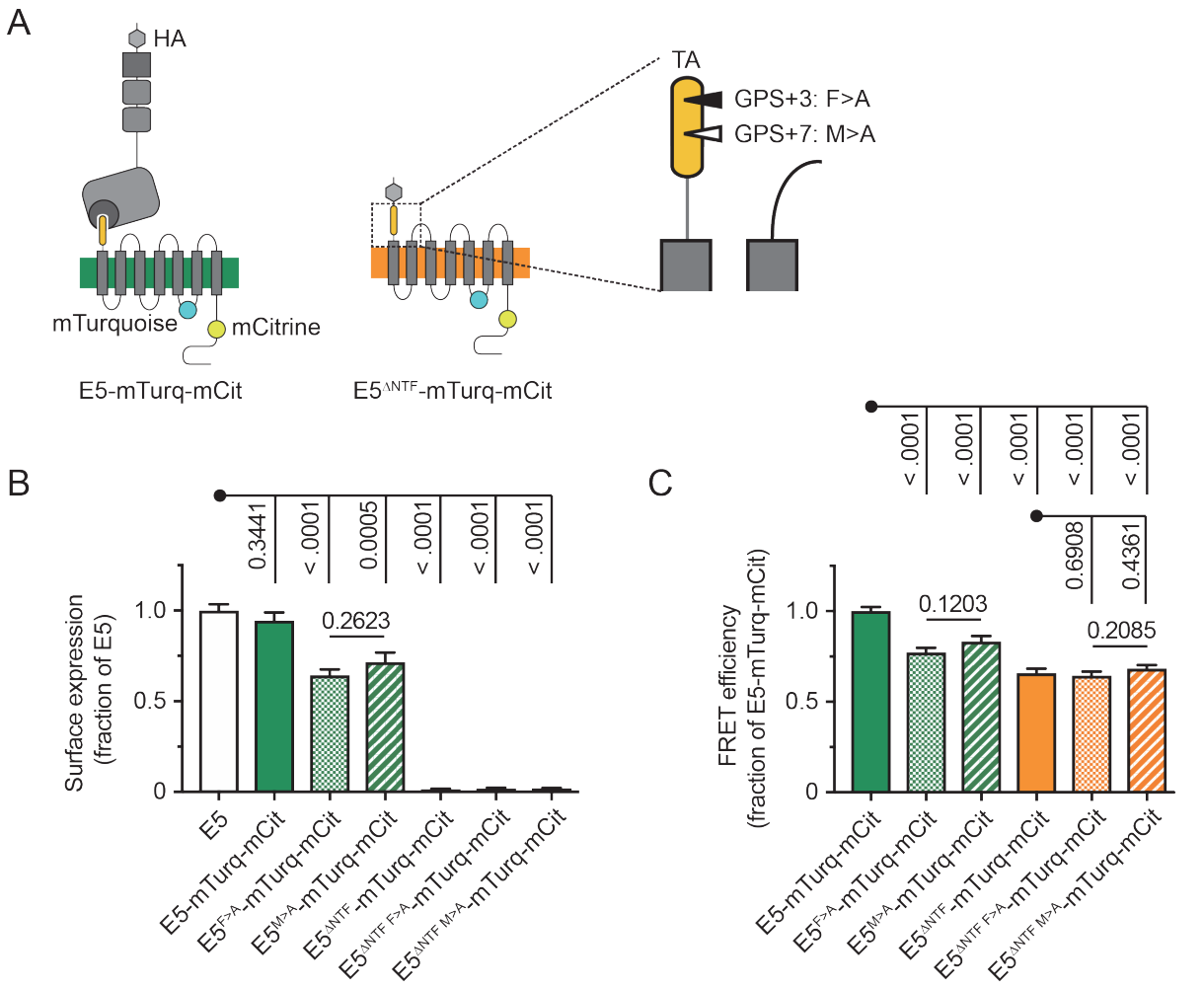

Fig. 32: Influence of a mutated TA on the surface expression and 7TM domain conformation of full-length and ΔNTF E5 variants.

(A) Schematic illustration of full-length (green) and ΔNTF (orange) FRET sensors of E5. Mutation within the TA at position +3 and +7 is highlighted. (B) Quantification of surface expression levels of cleavable and cleavage-deficient full-length (green) and ΔNTF (orange) FRET sensors of E5 in dependency of the TA mutation compared to E5 in HEK-293T cells by ELISA. Dataset normalized to the expression level of E5. Data are shown as mean ± SEM (N = 2, n = 4). (C) Quantification of FRET efficiency levels of cleavable and cleavage-deficient full-length (green) and ΔNTF (orange) FRET sensors of E5 in dependency of the TA mutation in HEK-293T cells by acceptor bleaching. Dataset normalized to the FRET efficiency level of E5-mTurq-mCit. Data are shown as mean ± SEM (N = 2-4, n ≥ 12). (B,C) performed by Mareike Hemberger.

6.4.3 Intermolecular distance measurements of ADGRE5

To further analyze and interpret the previous FRET data, we tested whether the measured FRET efficiencies were exclusively the result of intramolecular FRET or were influenced by intermolecular FRET events, such as dimerization/oligomerization. To this end, I cloned single chromophore constructs of full-length E5, E5$^{\Delta NTF}$ and E5$^{\Delta ECR}$ containing either an mTurquoise or an mCitrine (**Fig. 33A**). In collaboration with Mareike Hemberger, these constructs were singly transfected or co-transfected in HEK-293T cells and compared to the respective dually tagged E5 sensor. The surface expression, determined by ELISA, indicated an unimpaired expression of E5-mTurq-mCit and E5-mTurq compared to E5 (**Fig. 33B**). Only E5-mCit showed a slightly decreased surface expression.

FRET efficiencies of these E5 variants were quantified by acceptor bleaching in living HEK-293T cells. Calculated values were corrected for the absolute intensity differences of the mTurquoise channel since cells expressing only E5-mCit showed FRET events also in the absence of mTurquoise. The FRET efficiency of co-expressed E5-mTurq and E5-mCit was at ~15 % compared to ~45 % of E5-mTurq-mCit (**Fig. 33C**). This indicated the presence of intermolecular FRET events in addition to intramolecular FRET signals.

The same experiments were repeated for the E5$^{\Delta NTF}$ FRET sensor. ELISA data demonstrated a slightly increased surface expression for variants containing either an mTurquoise or an mCitrine compared to E5$^{\Delta NTF}$-mTurquoise-mCitrine (**Fig. 33D**). However, the expression level was still significantly reduced compared to E5.

The corrected FRET efficiency of HEK-293T cells co-expressing E5$^{\Delta NTF}$-mTurq and E5$^{\Delta NTF}$-mCit was at ~19 % compared to ~29 % of E5$^{\Delta NTF}$-mTurq-mCit, which also indicated the presence of intermolecular FRET events in this set of measurements (**Fig. 33E**).

Finally, we conducted the same experiments for the E5$^{\Delta ECR}$ FRET sensor. The surface expression quantified by ELISA was slightly increased for variants containing only one chromophore, either an mTurquoise or an mCitrine, compared to dually tagged E5$^{\Delta ECR}$-mTurquoise-mCitrine (**Fig. 33F**). However, the expression level was still significantly reduced compared to E5.

The corrected FRET efficiency of co-expressed E5$^{\Delta ECR}$-mTurq and E5$^{\Delta ECR}$-mCit was at ~10 % compared to ~37 % of E5$^{\Delta ECR}$-mTurq-mCit, again indicating the presence of intermolecular FRET events (**Fig. 33G**).

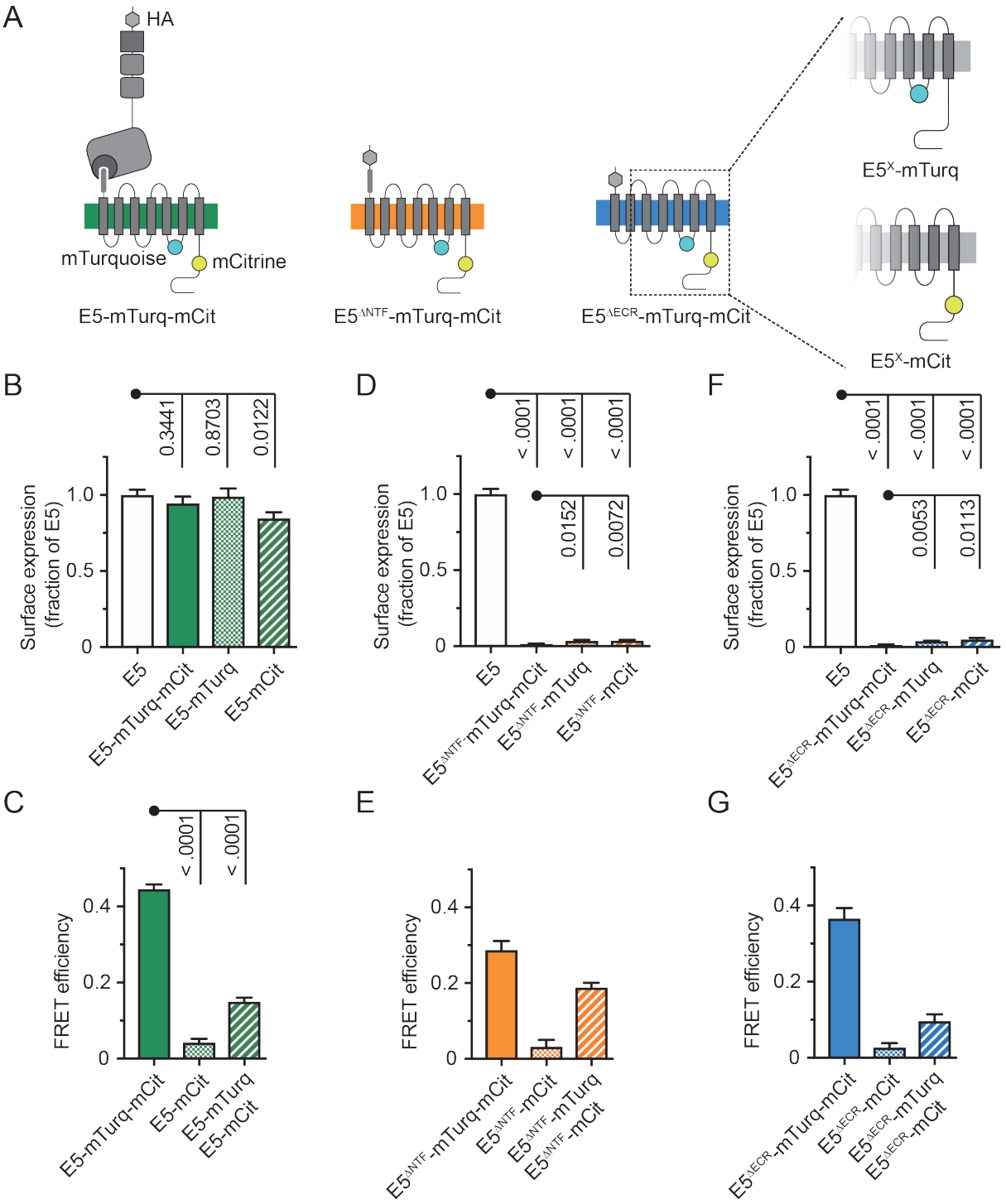

Fig. 33: FRET analyses of singly tagged E5 variants demonstrate intermolecular interactions for full-length and truncated E5 variants.

(A) Schematic illustration of full-length (green), ΔNTF (orange) and ΔECR (blue) FRET sensors of E5 and their respective singly tagged variants. (B,D,F) Quantification of surface expression levels of singly and dually tagged (B) full-length, (D) ΔNTF and (F) ΔECR E5 variants compared to E5 in HEK-293T cells by ELISA. Datasets normalized to the expression level of E5. Data are shown as mean ± SEM (N = 2, n = 4). (C,E,G) Quantification of FRET efficiency levels of singly and dually tagged (C) full-length, (E) ΔNTF and (G) ΔECR E5 in HEK-293T cells by acceptor bleaching. Intermolecular FRET is analyzed via co-expression of E5-mTurq and E5-mCit. Datasets were corrected for absolute intensity differences of the mTurquoise channel.

Data are shown as mean ± SEM ((C) N = 4, n ≥ 10, (E,G) N = 1, n = 10). (B,C,D,E,F,G) performed by Mareike Hemberger.

Altogether, the intramolecular FRET analyses indicated that the deletion of the NTF or the ECR resulted in a conformational change of the 7TM domain. Furthermore, we observed the existence of intermolecular FRET events with proximity differences depending on the extent of the ECR truncation of E5, suggesting the formation of oligomeric E5 fractions *in vitro*.

6.4.4 Proximity ligation assay as an alternative tool to probe molecular interactions/distances

In the last part of this chapter, I introduce the proximity ligation assay (PLA) - a technique to analyze molecular interactions besides FRET approaches. PLA allows the *in situ* detection of intra- or intermolecular interactions on a highly specific and sensitive level within 40 nm or less (Söderberg et al., 2006). Specificity and sensitivity are guaranteed by the binding of two antibodies from different species on the target protein/proteins. Secondary antibodies containing oligonucleotides bind to the previous antibodies. Briefly, the oligonucleotides are ligated by connector oligonucleotides if they are in close proximity to each other. Amplification leads to the formation of a long DNA strand, which builds the template for hybridization of fluorescently labeled oligonucleotides.

Based on the additional long-time research experience of the laboratory with presynaptic active zones in *Drosophila melanogaster*, we decided to use this model as a starting point for the establishment of the PLA. Previous experiments focused on the identification of binding partners of the active zone protein Bruchpilot (Brp). Brp is an essential and critical component for an intact active zone assembly and physiological neurotransmitter release in *Drosophila melanogaster* (Kittel, 2006; Wagh et al., 2006). At the active zone, the Brp molecules are assembled in filamentous oligomers (Fouquet et al., 2009). These oligomers are orientated with the N-terminus to Ca^{2+} channels of the presynaptic plasma membrane and the C-terminus to the cytoplasm (Ehmann et al., 2014; Fouquet et al., 2009). The C-terminal part of Brp tethers synaptic vesicles to the presynaptic plasma membrane, resulting in the release of neurotransmitters and subsequent activation of postsynaptic receptors. To better understand the process of synaptic transmission, the identification of novel molecular interaction partners of Brp involved in the tethering of synaptic vesicles is crucial.

Genetic and functional analyses revealed Complexin (Cpx), a high affinity binding partner of the presynaptic SNARE complex and regulator of synaptic vesicle

exocytosis, as a vesicular interaction partner of Brp (Ishizuka et al., 1995; McMahon et al., 1995). However, coimmunoprecipitation and photoaffinity labeling indicated no evidence for the binding of Brp and Cpx suggesting that both interact indirectly with each other (Scholz et al., 2019). In this context, the PLA seemed to be an applicable tool to confirm the close localization between Cpx and Brp at the active zone cytomatrix of *Drosophila melanogaster*. Therefore, I dissected living third-instar *Drosophila* larvae and performed a PLA using α-Brp and α-Cpx antibodies. Maximal projections of confocal images indicated the location of Brp and Cpx within ~40 nm in the larval axons (**Fig. 34A**) and neuromuscular junction (NMJ) (**Fig. 34B**). These results are an additional evidence for the cooperation of Cpx and Brp at the active zone besides other genetic and functional analyses (Scholz et al., 2019). Furthermore, I demonstrated the functionality and specificity of the PLA *in vivo*.

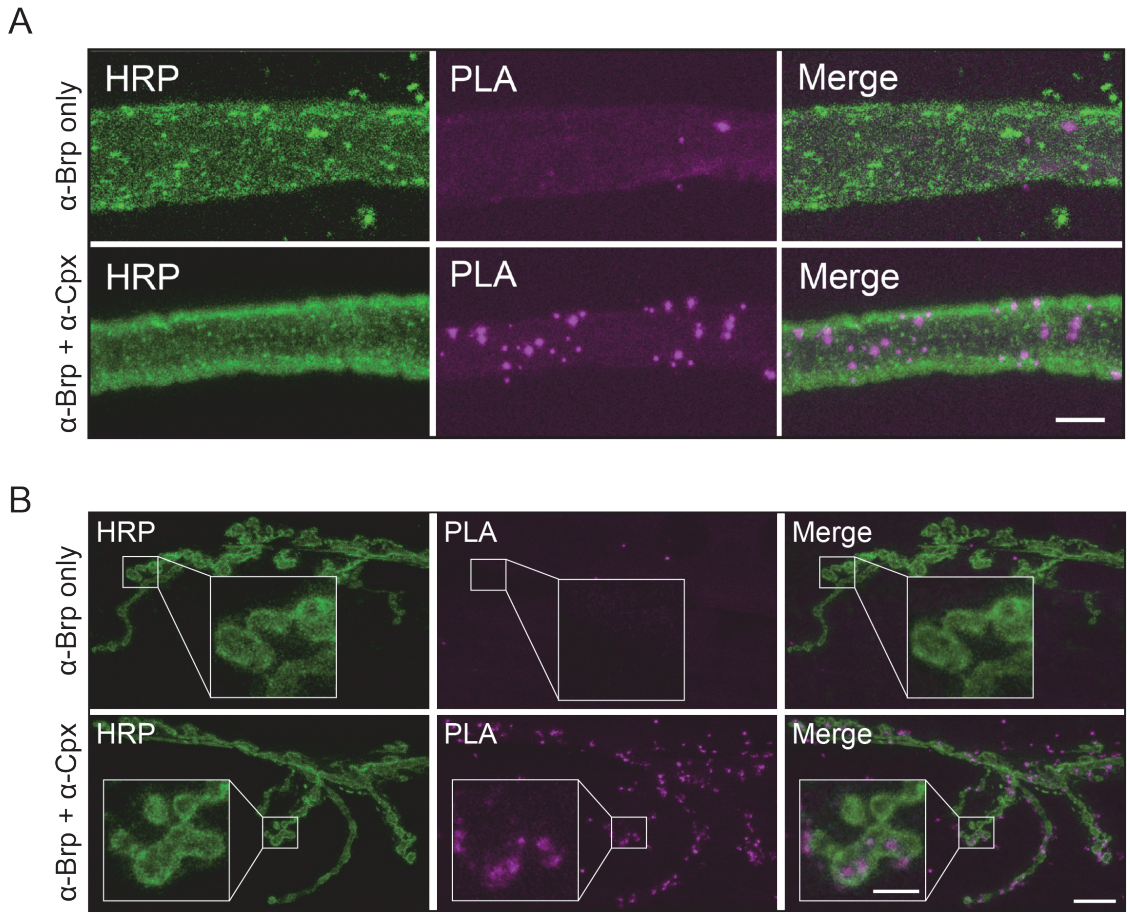

Fig. 34: Brp and Cpx are located in close proximity to each other at the active zone.

(A) Maximal projection of confocal images indicates the localization of Brp and Cpx within ~40 nm in larval axons of *Drosophila melanogaster* by PLA. (B) Maximal projection of confocal images indicates the localization of Brp and Cpx within ~40 nm in NMJs of *Drosophila melanogaster* by PLA. Scale bars (A) 5 µm, (B) 10 µm, 3 µm (inset). Adapted from Scholz et al., 2019.

In prospective view, the PLA appears a suitable means to identify and investigate novel interaction partners for members of the aGPCR family. At the moment only for a minority of aGPCRs the binding partners are known (Langenhan, 2019). Further binding partner identification could thus help to elucidate physiological activation mechanisms, signal transduction or yet unknown functions of aGPCRs.

In sum, in this chapter I screened a panel of extracellularly tagged E5 variants for their potential ability to investigate conformational changes within the GAIN-7TM domain tandem by FRET. Conceptually, this was undertaken to investigate the molecular mechanism of aGPCR activation depending on mechanical forces and/or ligand interaction. So far, the tested FRET sensors suffer from the lack of signal. I also investigated a classically used GPCR FRET sensor layout comprising a fluorophore in the ICL and another one in the ICR (Hlavackova et al., 2012; Hoffmann et al., 2005; Vilardaga et al., 2003). This setup allowed for the analysis of conformational changes within the 7TM domain in response to stimulation. I transferred this layout to the E5 receptor through the fusion of mTurquoise in the ICL3 and mCitrine in the ICR. To validate the functionality of these FRET sensors, I designed constitutively active and inactive receptor variants by truncation of the NTF and the ECR. Previous publications showed that the NTF truncation led to a TA release and an activation of the receptor, whereas the truncation of the remaining TA resulted in an abolished activity (Hilbig et al., 2018; Liebscher et al., 2014; Stoveken et al., 2015). Interestingly, I verified with the constitutively active $E5^{\Delta NTF}$ and inactive $E5^{\Delta ECR}$ receptor variants that FRET signals change possibly due to a conformational change of the 7TM domain, showing the functionality of this aGPCR FRET sensor layout. In addition, I observed no conformational changes in dependency of GAIN domain-mediated proteolysis. Furthermore, mutation of the TA, which in other aGPCRs correlated with an abolished receptor activity (Liebscher et al., 2014; Stoveken et al., 2015), evoked homonymous differences in FRET states of the E5 receptor. Interestingly, mutations of the TA of $E5^{\Delta NTF}$ had no effect on the 7TM domain conformation as reported through FRET measurements. Additionally, the presence of intermolecular FRET signals suggested the oligomerization of E5 in transient transfected cells. I also established an alternative method to investigate protein interactions using a PLA to allow for the detection of molecular interactions within the range of 40 nm or less (Söderberg et al., 2006). Using this method, I was able to confirm the close location of the active zone members Brp and Cpx in larval axons and NMJs suggesting the cooperation of these proteins. In terms of the aGPCR family, this method could be used to discover further interaction/binding partners helping for a better understanding of fundamental receptor mechanisms. At the moment only a limited number of extra- and intracellular binding

partner for half of the aGPCRs are known (Langenhan, 2019), therefore the PLA represents an ideal technique to address this knowledge gap.

6.5 Demonstration of tethered agonist exposure by bioorthogonal labeling

The past years showed that the activation mechanism of aGPCRs are more complex and differing i.a. in the involvement of the TA and external stimuli. Regarding the involvement of the TA, two models for a TA-dependent aGPCR activation are discussed, the dissociation and non-dissociation model (see 4.3). A variety of published results support the non-dissociation model, but the molecular mechanism on how the TA, which is deeply buried inside the GAIN domain, is able to interact with the 7TM domain and therefore regulates the receptor activity is still unknown. Compounding this issue is the fact that the molecular structure of the GAIN-7TM domain tandem of an aGPCR at atomic resolution is not available yet, which would certainly help to further investigate the signaling mechanism of this receptor family. Therefore, the goal of my study was to investigate potential molecular mechanisms of the TA-7TM domain interaction within the intact GAIN domain. A possible mechanism could be a conformational flexibility of the GAIN domain, which allows an interaction of the TA with the 7TM domain even in a non-dissociated situation.

6.5.1 Tethered agonist is accessible in full-length aGPCRs

To investigate the conformational flexibility of the GAIN domain and, in particular of the TA, the accessibility of the TA was directly tested by bioorthogonal labeling. To this end, I introduced an UAA into the highly conserved TA region of the E5 receptor, comprising the first eight amino acids (Liebscher and Schöneberg, 2016). The exact position within the TA core region was selected by an amino acid sequence alignment with TA sequences of aGPCRs, which were experimentally characterized and/or from which crystal structures of the GAIN domain are available. The alignment revealed a high conservation at position +3 and +6 within the TA sequence across different aGPCRs (**Fig. 35A**). As a control, I used position +15, which is located in the linker region between the GAIN domain and the 7TM domain and, therefore, likely irrelevant for the tethered agonism of the E5 receptor (Hilbig et al., 2018).

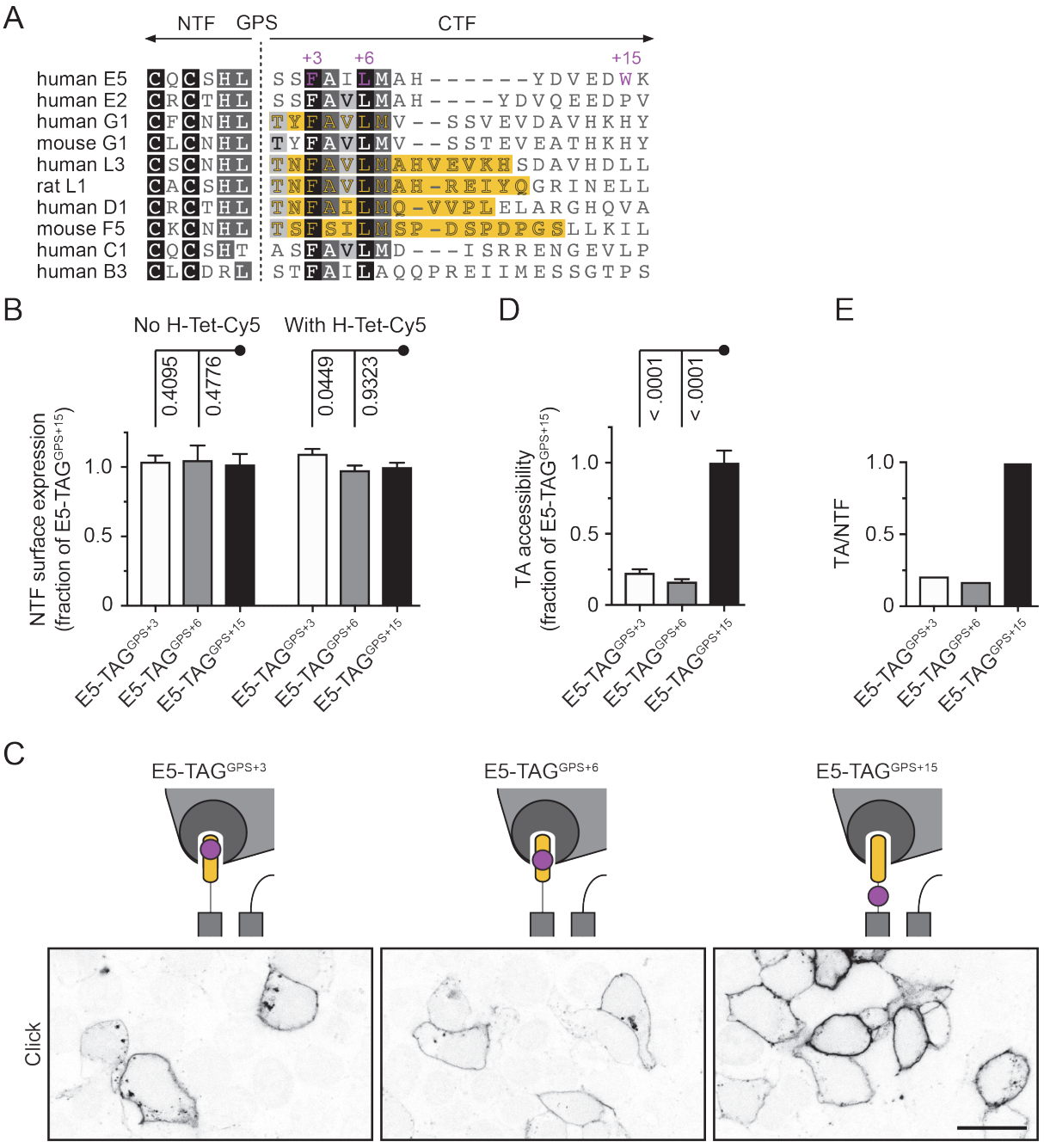

Fig. 35: Bioorthogonal labeling confirms the TA accessibility to the solvent within the intact GAIN domain of E5.

(A) Amino acid sequence alignment of exemplary aGPCR regions containing the GPS and TA regions. Alignment indicates the sequence of experimentally confirmed TAs (yellow) (Brown et al., 2017; Liebscher et al., 2014; Müller et al., 2015; Stoveken et al., 2015) and label positions in the TA and TA-7TM linker region (magenta), residue numbering with respect to GPS is indicated above the alignment. (B) Quantification of surface expression levels of HEK-293T cells expressing E5 variants with/without the addition of H-Tet-Cy5 by ELISA. Variants containing bioorthogonal labels at position +3 and +6 of the TA and in the TA-7TM linker region at position +15. Datasets normalized to the expression level of E5-TAG^{GPS+15}. Data are shown as mean ± SEM (N = 3, n = 4). (C) Confocal images of HEK-293T cells expressing E5-TAG^{GPS+X} variants. Cells were labeled with H-Tet-Cy5. (D) Quantification of bioorthogonal label of HEK-293T cells expressing E5-TAG^{GPS+X} variants. Dataset normalized to the fluorescence

signal intensity of E5-TAG^{GPS+15}. Data are shown as mean ± SEM (N = 3, n = 20). (E) Ratio of TA to NTF confirms the TA accessibility. Used Pyl^{RS}/tRNA^{Pyl} system: RS$_{Coin}$. Scale bar 20 µm.

First, I tested whether the incorporation of UAAs within the TA had an influence on the membrane trafficking of E5-TAG^{GPS+X} variants. I transfected E5-TAG^{GPS+3} and E5-TAG^{GPS+6} constructs into HEK-293T cells and quantified the surface expression compared to the control construct E5-TAG^{GPS+15} by the pre-described ELISA. To further analyze whether the incorporation of the tetrazine dye derivative disrupts the heterodimeric receptor structure, I quantified its surface expression level with and without the addition of H-Tet-Cy5. ELISA data revealed indistinguishable expression levels of all E5-TAG^{GPS+X} variants, indicating that the H-Tet-Cy5 addition had no effect on the NTF-CTF interaction (**Fig. 35B**).

Next, I analyzed the accessibility of TA using confocal imaging. To do so, E5-TAG^{GPS+X} variants were expressed in HEK-293T cells and bioorthogonally labeled with H-Tet-Cy5. Interestingly, the confocal images indicated a weaker but distinct bioorthogonal labeling of E5-TAG^{GPS+3} and E5-TAG^{GPS+6} compared to the control construct E5-TAG^{GPS+15} (**Fig. 35C**). This suggested a better accessibility of E5-TAG^{GPS+15} for the bioorthogonal label. To quantify this observation, I measured photon counts of the bioorthogonal labels of the different E5-TAG^{GPS+X} variants. The fluorescence signal quantification revealed a ~4 times lower labeling of E5-TAG^{GPS+3} and E5-TAG^{GPS+6} compared to the control construct E5-TAG^{GPS+15} (**Fig. 35D**). These findings were confirmed after normalizing bioorthogonal labeling to the surface expression of all receptor layouts (**Fig. 35E**).

To verify the obtained results, I additionally compared the surface expression of E5-TAG^{GPS+X} with E5-TAG^{NTF} and E5 in HEK-293T cells. The ELISA data demonstrated an already described decreasing effect on the surface expression by the introduction of UAAs within the E5 receptor layout (**Fig. 36A**, see 6.3.3). However, the E5-TAG^{GPS+X} variants showed slightly increased surface expression levels compared to the E5-TAG^{NTF} variant. Expression of all tested E5 variants were independent of the addition or omission of tetrazine dye derivates.

Additionally, I controlled the GAIN domain integrity depending on the UAA incorporation. For this purpose, I expressed the three E5-TAG^{GPS+X} variants, E5-TAG^{NTF} and E5 in HEK-293T cells and labeled non-fixed cells with a polyclonal α-ADGRE5 antibody directed against the GAIN domain afterwards. I observed indistinguishable differences of the labeling efficiency between the UAA insertion within the GAIN domain or the TA-7TM linker region (**Fig. 36B**). Additionally, the fluorescence signals of confocal images correlated with surface expression levels.

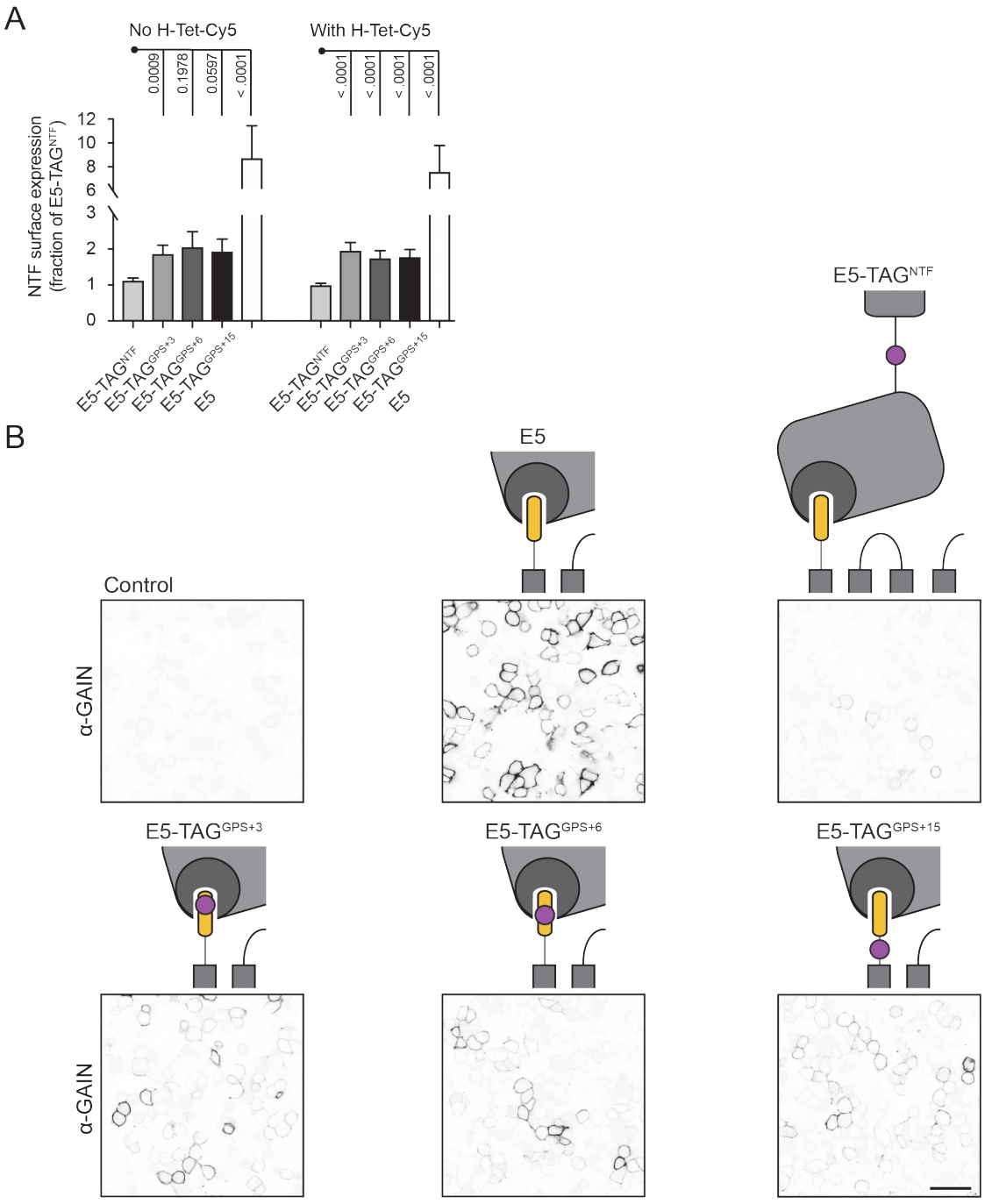

Fig. 36: Bioorthogonally labeled E5-TAG^{GPS+X} does not impede receptor trafficking and GAIN domain formation.

(A) Quantification of surface expression levels of HEK-293T cells expressing E5 variants with/without the addition of H-Tet-Cy5 by ELISA. Variants are expanded by bioorthogonal labels at position +3, +6 of the TA or in the TA-7TM linker region at position +15. Control constructs E5-TAG^{NTF} and E5. Datasets normalized to the expression level of E5-TAG^{NTF}. Data are shown as mean ± SEM (N = 3, n = 4). (B) Confocal images of HEK-293T cells expressing E5 variants (indicated above). Untagged E5 serves as positive control and control cells expressing EV as negative control. Cells were labeled using α-ADGRE5 antibody. Used Pyl^{RS}/tRNA^{Pyl} system: RS$_{Coin}$. Scale bar 50 µm.

All results together suggested that the GAIN domain formation is unimpeded despite of the UAA incorporation.

To test the generality of the TA accessibility across the aGPCR family, I generated L1, B3 and G1 variants containing homologous amber stop codons at positions +3, +6 and within the linker region between the GAIN and 7TM domains.

First, I analyzed the TA accessibility of the L1 receptor (L1 receptor layout: **Supp. Fig. 3**). To do so, I quantified whether the incorporation of UAAs within the TA had any influence on the membrane trafficking of L1-TAG^{GPS+X} variants. Therefore, I expressed L1-TAG^{GPS+3}, L1-TAG^{GPS+6} in HEK-293T cells and analyzed the surface expression compared to the control variant L1-TAG^{GPS+15} by ELISA. In contrast to the E5 receptor, the ELISA data of L1 showed a significantly reduced surface delivery of L1 variants with a tagged TA compared to L1-TAG^{GPS+15}, which ranged from ~41 % (L1-TAG^{GPS+3}) to ~21 % (L1-TAG^{GPS+6}) (**Fig. 37A**).

Next, I analyzed the TA accessibility using confocal microscopy. Images indicated a weaker but distinct bioorthogonal labeling of HEK-293T cells expressing L1-TAG^{GPS+3} and L1-TAG^{GPS+6} compared to L1-TAG^{GPS+15} (**Fig. 37B**). This finding demonstrated a better accessibility of L1-TAG^{GPS+15} for tetrazine dye derivatives. In contrast, the untagged L1 receptor showed no fluorescence signals, which confirmed the specificity of the bioorthogonal labeling for the L1 receptor. To quantify the labeling efficiency, I measured the photon counts of bioorthogonal labels in relation to the position within the L1 receptor. This quantification revealed a similar result as for the E5 receptor. In detail, the labeling of L1-TAG^{GPS+3} and L1-TAG^{GPS+6} was ~4 times lower compared to the control construct L1-TAG^{GPS+15} (**Fig. 37C**). However, the ratio between bioorthogonal labels and surface expression levels indicated a ~75 % labeling accessibility of the TA compared to TA-7TM linker region (**Fig. 37D**).

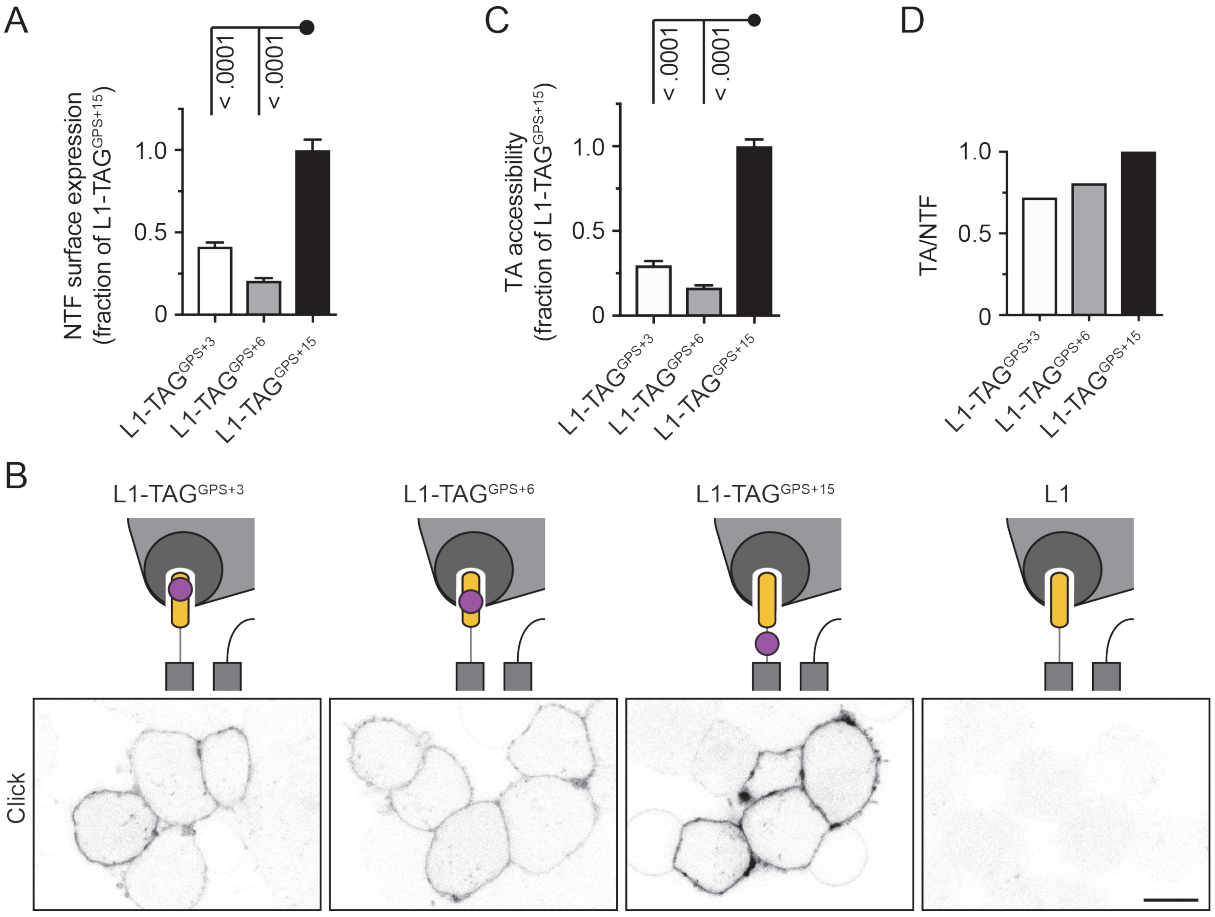

Fig. 37: Bioorthogonal labeling confirms the TA accessibility to the solvent within the intact GAIN domain of L1.

(A) Quantification of surface expression levels of HEK-293T cells expressing L1 variants by ELISA. Variants are expanded by bioorthogonal labels at position +3, +6 of the TA or in the TA-7TM linker region at position +15. Dataset normalized to the expression level of L1-TAG^{GPS+15}. Data are shown as mean ± SEM (N = 3, n = 4). (B) Confocal images of HEK-293T cells expressing L1 variants (indicated above). Untagged L1 serves as labeling control. Cells were labeled with H-Tet-Cy5. (C) Quantification of bioorthogonal label of HEK-293T cells expressing L1-TAG^{GPS+X}. Dataset normalized to the fluorescence signal intensity of L1-TAG^{GPS+15}. Data are shown as mean ± SEM (N = 3, n = 20). (D) Ratio of TA to NTF confirms the TA accessibility. Used Pyl^{RS}/tRNA^{Pyl} system: RS$_{Coin}$. Scale bar 10 µm.

Next, I analyzed the TA accessibility of the B3 receptor (B1 receptor layout: **Supp. Fig. 4**). Again, I quantified whether the incorporation of UAAs within the TA had any influence on the membrane trafficking of B3-TAG^{GPS+X} variants. For this purpose, I expressed B3-TAG^{GPS+3}, B3-TAG^{GPS+6} in HEK-293T cells and analyzed the surface expression compared to the control variant B3-TAG^{GPS+15} by ELISA. The quantified data of B3 variants showed an indistinguishable surface expression, which was consistent with the data of the E5 receptor (**Fig. 38A**).

Next, I analyzed the TA accessibility using confocal microscopy. Images showed a weaker but distinct bioorthogonal labeling of HEK-293T cells expressing B3-TAG^{GPS+3}

and B3-TAG^{GPS+6} compared to B3-TAG^{GPS+15} (**Fig. 38B**). The fluorescence signals showed an increased accessibility of the UAA for the B3-TAG^{GPS+15} variant. In contrast, B3 without amber stop codon showed no fluorescence signal, which verified the specificity of bioorthogonal labeling for the B3 receptor. The labeling efficiency was quantified by measuring the photon counts of bioorthogonal labels in relation to the position within the B3 receptor. The quantification revealed a ~4 times lower fluorescence signal of B3-TAG^{GPS+3} and an approximately half reduced signal of B3-TAG^{GPS+6} compared to B3-TAG^{GPS+15} (**Fig. 38C**). I confirmed these findings through the ratio between bioorthogonal labels and surface expression levels (**Fig. 38D**).

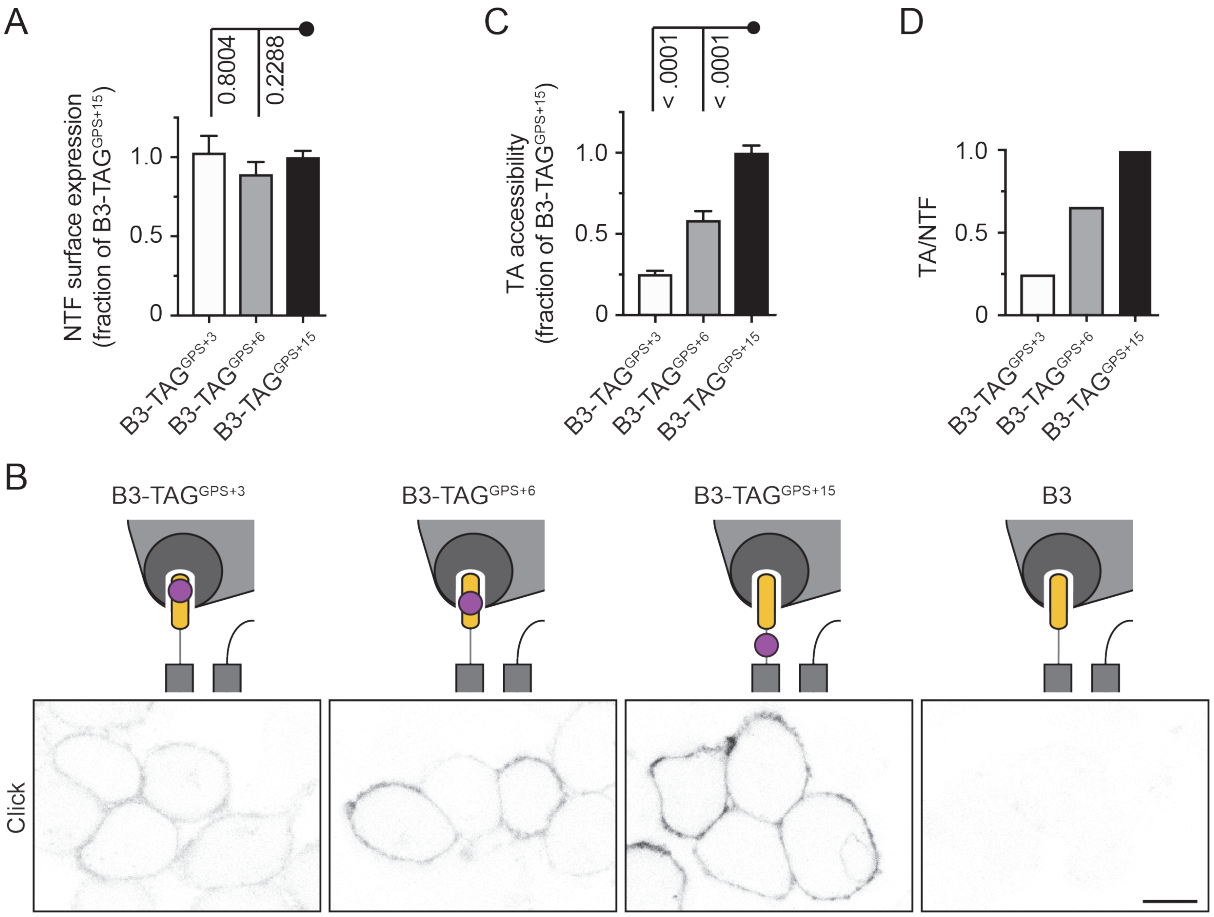

Fig. 38: Bioorthogonal labeling confirms the TA accessibility to the solvent within the intact GAIN domain of B3.

(A) Quantification of surface expression levels of HEK-293T cells expressing B3 variants by ELISA. Variants are expanded by bioorthogonal labels at position +3, +6 of the TA or in the TA-7TM linker region at position +15. Dataset normalized to the expression level of B3-TAG^{GPS+15}. Data are shown as mean ± SEM (N = 3, n = 4). (B) Confocal images of HEK-293T cells expressing B3 variants (indicated above). Untagged B3 serves as labeling control. Cells were labeled with H-Tet-Cy5. (C) Quantification of bioorthogonal label of HEK-293T cells expressing B3-TAG^{GPS+X}. Dataset normalized to the fluorescence signal intensity of B3-TAG^{GPS+15}. Data are shown as mean ± SEM (N = 3, n = 20). (D) Ratio of TA to NTF confirms the TA accessibility. Used Pyl^{RS}/tRNA^{Pyl} system: RS$_{Coin}$. Scale bar 10 µm.

In a last experiment, I also tested the TA accessibility of G1. HEK-293T cells expressing G1-TAG^{GPS+3}, G1-TAG^{GPS+6} and control variants G1-TAG^{GPS+18}, G1-TAG^{NTF} were bioorthogonally labeled with H-Tet-Cy5 and subsequently confocally imaged. In this case, I also demonstrated the TA accessibility using bioorthogonal labeling. However, the weak intensity of the fluorescence signals of the bioorthogonal labels allowed no deeper quantification (**Supp. Fig. 2**).

Summarizing, I showed for three aGPCRs from different subfamilies the generality of TA accessibility by the incorporation of bioorthogonal labels within the TA core region. This leads to the assumption that the TA and the GAIN domain in general are highly flexible. Furthermore, the experimental data demonstrated that the bioorthogonal labeling had no impact on the GAIN domain integrity, suggesting a prospective use for the direct labeling of entire domains.

6.5.2 A vibratory urticaria mutation in ADGRE2 GAIN domain does not increase tethered agonist accessibility

Previous experiments regarding the TA accessibility formed the basis to investigate the effect of a human missense mutation in the GAIN domain of E2, which leads to a rare autosomal dominant form of VBU. The affected patients carry a C492Y mutation within the GAIN domain of E2 receptors (E2 receptor layout: **Supp. Fig. 5**). This mutation causes dermal hives and increased histamine levels due to enhanced degranulation of mast cells. The symptoms are triggered by vibratory stimulation of the skin (Boyden et al., 2016). The suggested molecular mechanism of this disease is the destabilization of the NTF-CTF heterodimer of E2^{C492Y} based on the reduction of non-covalent binding forces within the cleaved GAIN domain. Therefore, I assumed that the decreased affinity within the NTF-CTF heterodimer is caused or at least accompanied by a higher flexibility of the GAIN domain, subsequently resulting in an increased exposure of the TA of E2, which should be detectable by bioorthogonal labeling. To test this assumption, I integrated amber stop codons within the TA at position +3, +6 and +17 of E2 and E2^{C492Y}. I transfected these constructs into HEK-293T cells and quantified the surface expression by ELISA. Surface expression levels of E2 tagged at position +3 and +6 were ~25 % decreased compared to E2-TAG^{GPS+17} **(Fig. 39A**).

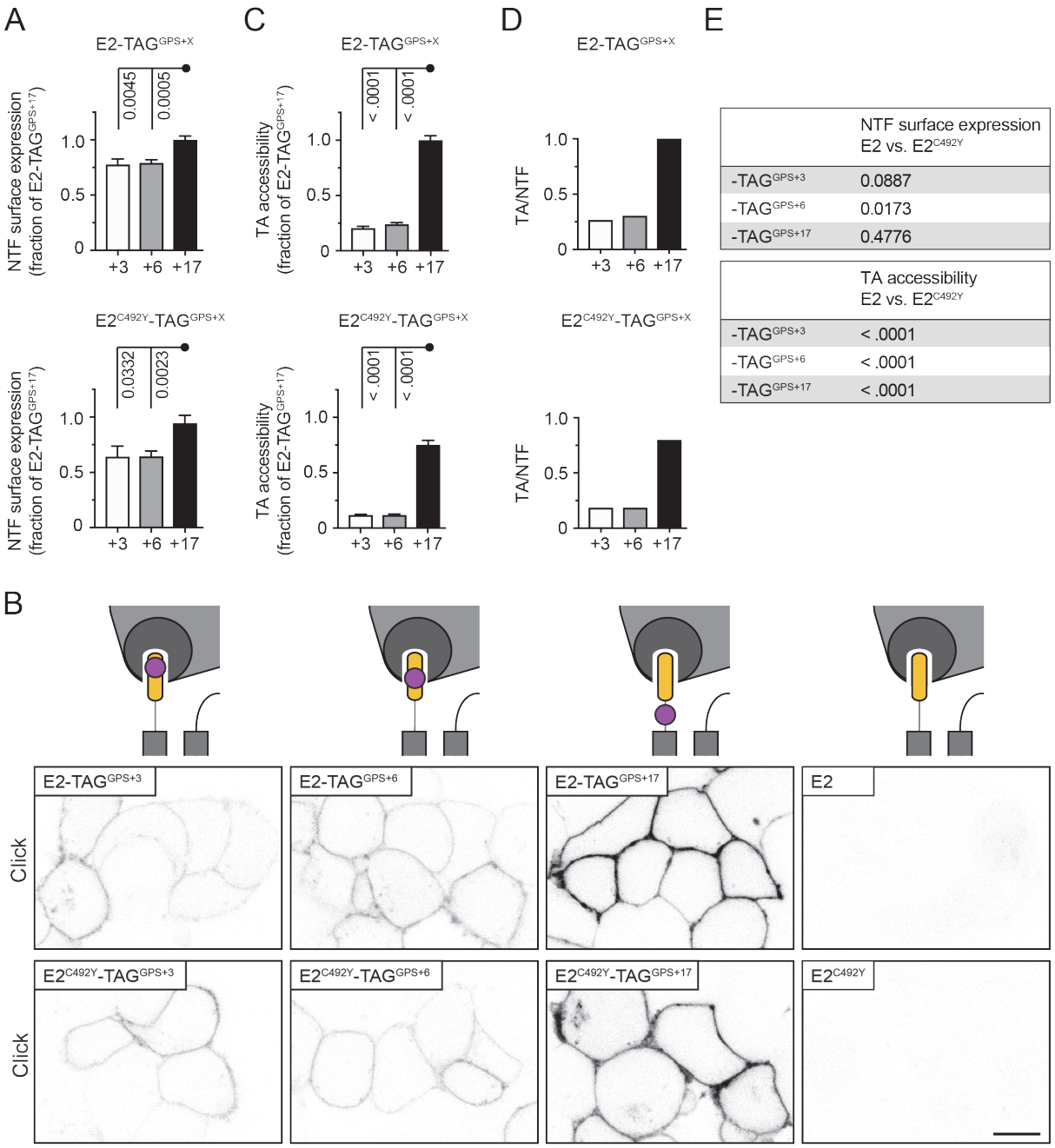

Fig. 39: Bioorthogonal labeling confirms the TA accessibility to the solvent within the intact GAIN domain of E2.

(A) Quantification of surface expression levels of HEK-293T cells expressing E2 and E2^{C492Y} variants by ELISA. Variants are expanded by bioorthogonal labels at position +3, +6 of the TA or in the TA-7TM linker region at position +17. Datasets normalized to the expression level of E5-TAG^{GPS+17}. Data are shown as mean ± SEM (N = 3, n = 4). (B) Confocal images of HEK-293T cells expressing E2-TAG^{GPS+X} and E2^{C492Y}-TAG^{GPS+X} variants. Untagged E2 and E2^{C492Y} serve as labeling controls. Cells were labeled with H-Tet-Cy5. (C) Quantification of bioorthogonal label of HEK-293T cells expressing E2 and E2^{C492Y} variants. Datasets normalized to the fluorescence signal intensity of E5-TAG^{GPS+17}. Data are shown as mean ± SEM (N = 3, n = 20). (D) Ratio of TA to NTF confirms the TA accessibility. (E) Comparison of surface expression and TA accessibility between E2-TAG^{GPS+X} and E2^{C492Y}-TAG^{GPS+X} variants shows no increased TA accessibility due to the mutation. Used Pyl^{RS}/tRNA^{Pyl} system: RS$_{Coin}$. Scale bar 10 µm.

The $E2^{C492Y}$ variants showed similar results with a surface delivery decrease of ~30 % compared to $E2^{C492Y}$-TAG^{GPS+17}. Interestingly, a significant difference between the E2 and $E2^{C492Y}$ variants was only observable at the position +6 (**Fig. 39E**). The surface expression was slightly decreased for $E2^{C492Y}$-TAG^{+6} compared to E2-TAG^{+6}.

Next, I investigated the TA accessibility by bioorthogonal labeling on a confocal level. E2 and $E2^{C492Y}$ constructs were transfected into HEK-293T cells and subsequently labeled with H-Tet-Cy5. Images showed a weaker but distinct bioorthogonal labeling at position +3 and +6 of E2 and $E2^{C492Y}$ compared to the control construct (position +17). These findings indicated a better accessibility at the position +17 (**Fig. 39B**). To quantify these observations, I measured photon counts of the bioorthogonal labels for the E2 and $E2^{C492Y}$ variants. The signal quantification revealed a ~4 times lower labeling of E2-TAG^{GPS+3} and E2-TAG^{GPS+6} compared to the control construct E2-TAG^{GPS+15} and ~6 times lower labeling of $E2^{C492Y}$-TAG^{GPS+3} and $E2^{C492Y}$-TAG^{GPS+6} compared to the control construct $E2^{C492Y}$-TAG^{GPS+15} (**Fig. 39C**). These findings were confirmed by the ratio between bioorthogonal labels and surface expression levels for all receptor layouts (**Fig. 39D**). Interestingly, the TA of $E2^{C492Y}$ variants was even less accessible compared to their non-mutated counterparts contradicting the model that suggests a decreased affinity between the NTF and the CTF in the presence of the mutation (**Fig. 39E**).

As the TA accessibility of $E2^{C492Y}$ in an unstimulated situation was unaffected, I combined mechanical stimulation and bioorthogonal labeling. To this end, I expressed the bioorthogonally (un)tagged E2 and $E2^{C492Y}$ variants in HEK-293T cells and applied a mechanical stimulation through shaking at 750 rpm during the labeling period. I chose this form of mechanical stimulation because it already led to a destabilization of the E2 heterodimer in mast cells (Boyden et al., 2016). To evaluate the effect of the mechanical stimulation on the TA accessibility, I compared unstimulated cells (**Fig. 40A**) with stimulated cells (**Fig. 40B**). Interestingly, the confocal images indicated no obvious impact on the TA accessibility caused by a mechanical stimulation, which suggested that the C492Y mutation in VBU patients is not involved in causing in the activation of E2 through the GAIN domain destabilization.

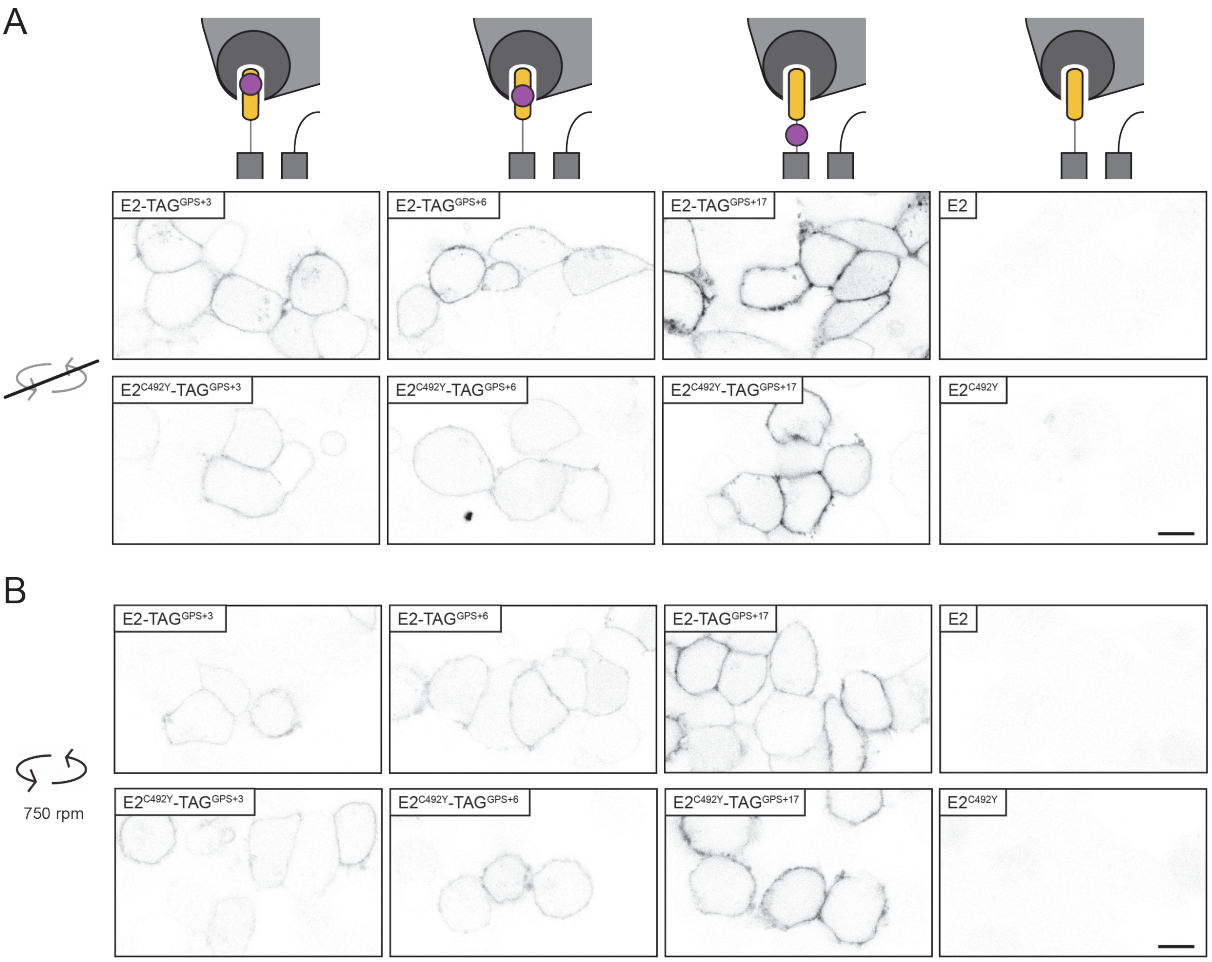

Fig. 40: Mechanical stimulation has no impact on the TA accessibility of E2 and E2^{C492Y}.

(A,B) Confocal images of HEK-293T cells expressing E2 and E2^{C492Y} variants. Variants are expanded by bioorthogonal labels at position +3, +6 of the TA or in the TA-7TM linker region at position +17. Untagged E2 and E2^{C492Y} serve as labeling controls. Cells were labeled with H-Tet-Cy5 for 20 min without shaking (A) and with shaking at 750 rpm (B). Used Pyl^{RS}/tRNA^{Pyl} system: RS$_{Coin}$. Scale bars 10 µm.

In summary, this chapter combines the bioorthogonal labeling with the functional analysis of aGPCRs. The sequential labeling of different positions within the highly conserved TA sequence demonstrated the general accessibility and flexibility of this region. These findings were comparable for a panel of aGPCRs: E5, L1, B3 and E2.

Furthermore, I investigated the effect of a human missense mutation in the GAIN domain of E2, which leads to a rare autosomal dominant form of VBU (Boyden et al., 2016). Hypothetically, this C492Y mutation leads to a destabilization of the NTF-CTF heterodimer and thus to an increased accessibility of the TA (Boyden et al., 2016). Interestingly, the TA of E2^{C492Y} was slightly but significantly less accessible compared to their non-mutated counterparts. These findings suggested that the mechanical stimulation through shaking the cells prior to or during labeling did not impact the TA

accessibility indicating that the C492Y change in VBU patients is not causing the exposure of the TA through the GAIN domain destabilization and subsequent receptor activation.

6.6 Natural and artificial cleavage of ADGRE5

The GAIN domain represents a hallmark feature of the aGPCR family. The main function of this domain is the autoproteolysis during the receptor maturation at the GPS leading to the receptor separation into an NTF and a CTF (Gray et al., 1996; Krasnoperov et al., 1997). Furthermore, the GAIN domain mediates the non-covalent attachment of NTF and CTF resulting in the formation of a heterodimeric aGPCR layout (Araç et al., 2012; Gray et al., 1996; Krasnoperov et al., 1997; Lin et al., 2004). Apart from the autoproteolytic cleavage at the GAIN domain, different aGPCRs undergo additional cleavage reactions, e.g. the autoproteolytic cleavage at the SEA domain of GPR110 (ADGRF1/F1) and F5 receptors or the protease-mediated cleavage by furin at the N-terminus of BAI2 (ADGRB2/B2), F5 and G6 receptors (Fukuzawa and Hirose, 2006; Moriguchi et al., 2004; Nieberler et al., 2016; Okajima et al., 2010). Additional cleavage events of the E5 receptor are currently unknown so I investigated the possibility of further cleavage sites of E5. Moreover, I was interested in the engineering of an inducible E5 cleavage and its impact on the NTF-CTF formation. The last part of this chapter is devoted to the elucidation of potential amphipathic α-helices in the GAIN domain of E5, which may function as 7TM domain independent membrane-anchors of the NTF.

6.6.1 Additional proteolytic processing steps of ADGRE5 are dependent on GAIN domain proteolysis

Additional autoproteolytic and protease-mediated cleavage reactions of aGPCRs have been described in the past. Besides aGPCRs, other members of the GPCR superfamily are cleaved through proteases to ensure their proper biological function. Of particular interest are polycystin-1 and Notch receptors, which are cleaved by several other proteases, e.g. γ-secretases (Merrick et al., 2012; Nieberler et al., 2016; van Tetering and Vooijs, 2011). Interestingly, also the ECR of polycystein-1 contains a GAIN domain, which catalyzes the self-cleavage of the receptor resulting in the formation of a non-covalently attached NTF-CTF heterodimer (Merrick et al., 2014; Trudel et al., 2016).

In the past, I observed a variety of unexpected CTF bands of E5 in Western blot analyses. These bands differed in size and further indicated the presence of additional

cleavage sites in the CTF of E5, similar to the γ-secretase cleavage of polycystin-1 or Notch. Consequently, this could suggest a number of further biological functions of E5. For this purpose, I investigated the presence of potential γ-secretase cleavage sites by the inhibition of this enzyme using DAPT (Dovey et al., 2009).

Consequently, I transfected cleavable and cleavage-deficient E5 constructs into HEK-293T cells. The E5 layout was expanded by an N-terminal HA epitope and a C-terminal V5 epitope allowing the separate detection of the NTF and the CTF by Western blot analysis (**Fig. 41A**). To avoid the potential cleavage by γ-secretases, the cells were treated with the γ-secretase inhibitor DAPT for 1 day after transfection. Interestingly, the Western blot analysis of DAPT-treated and -untreated cells demonstrated no differences in the band pattern (**Fig. 41B**). Cleavable E5 in contrast to cleavage-deficient $E^{H>A}$ and $E5^{S>A}$ showed a prominent band above 50 kDa in the α-HA-representing channel, which could indicate the NTF, since this band size fits approximately with its predicted size of 48.5 kDa (**Fig. 41C**). A possible reason for the wide appearance of the band could be the glycosylation of the NTF. The cleavage-deficient E5 variants indicated a distinct band between 75 kDa and 100 kDa using the α-HA and α-V5 antibody (**Fig. 41B**). This band correlated with the predicted full-length receptor size of 84.2 kDa (**Fig. 41C**). Additionally, I detected a prominent band at 75 kDa in the α-HA- and α-V5-representing channel of cleaved and non-cleaved E5 (**Fig. 41B**). This band may represent the non-cleaved, non-glycosylated E5 pro-protein. Moreover, the formation of E5 oligomers under reducing conditions were indicated by several bands above 150 kDa. Based on the amino acid sequence I calculated a size of 35.7 kDa for the CTF (**Fig. 41C**). Interestingly, the Western blot of cleaved E5 showed three bands using the α-V5 antibody, one at 25 kDa, another one slightly above 37 kDa and a weaker band between 50 kDa and 75 kDa (**Fig. 41B**). The presence of three instead of one band below the full-length receptor suggested the existence of alternative cleavage sites within the E5 receptor. Assuming that the band above 37 kDa corresponds to the CTF, the larger band could indicate a cleavage in the NTF and the smaller band a cleavage in the CTF of E5. Furthermore, the Western blot analysis demonstrated that these bands appeared independently of the DAPT treatment, which refuted that the additional cleavage events are mediated by γ-secretases.

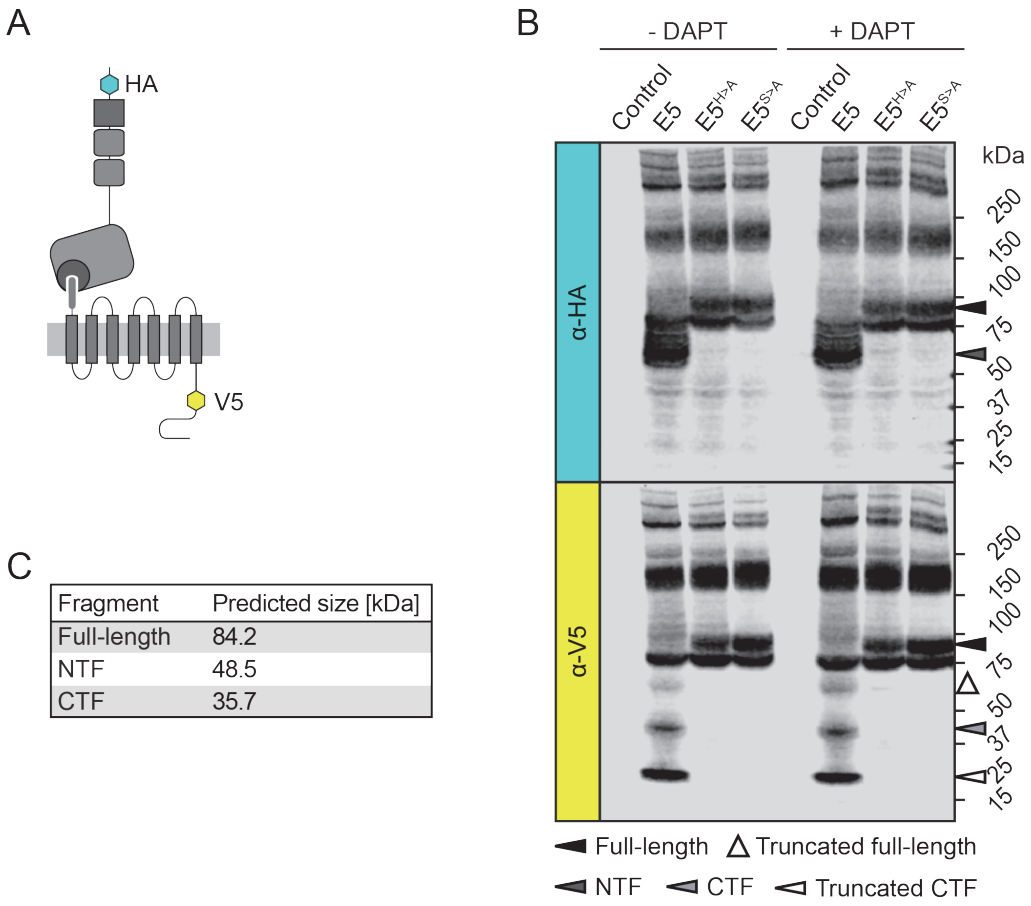

C

Fragment	Predicted size [kDa]
Full-length	84.2
NTF	48.5
CTF	35.7

Fig. 41: GAIN domain-mediated cleavage of E5 controls additional cleavage events within the receptor structure

(A) Schematic illustration of E5 receptor expanded by an N-terminal HA epitope and a C-terminal V5 epitope. (B) Western blot analysis of cleaved E5 and non-cleaved $E5^{H>A}$, $E5^{S>A}$ compared to control cells (only transfected with EV) using α-HA and α-V5 antibodies. Constructs were transfected into HEK-293T cells and treated with and without DAPT for 1 d before protein harvest. (C) Predicted E5 fragment sizes of full-length receptor, NTF and CTF based on their amino acid sequence.

6.6.2 Artificial cleavage of ADGRE5 through thrombin and TEV protease

Previous Western blot analysis using an α-V5 antibody demonstrated the existence of three bands appearing only for cleavable E5 receptors. Assuming that one of these bands represents the CTF, the origin of the other two bands is still unclear. The lowest band could indicate the additional processing of the CTF. To investigate whether this process is controlled by an initial cleavage event of the full-length receptor resulting in a cleavage cascade comparable to the Notch receptors (Blaumueller et al., 1997; Brou et al., 2000; Mumm et al., 2000; van Tetering and Vooijs, 2011), I engineered cleavage inducible E5 variants. The artificial cleavage was ensured by the integration of a thrombin or TEV cleavage site in the linker region between the TA and the 7TM domain of the cleavage-deficient $E5^{H>A}$ variant.

First, I utilized a thrombin cleavage site (TCS) for the E5 receptor. Interestingly, the thrombin cleavage of an aGPCR was already established for the E2 receptor. His-Hsien Lin's lab generated a chimeric E2-PAR1 receptor consisting of E2 ECR and full-length PAR1 (Huang et al., 2018, 2012). The PAR1 receptor contains a natural TCS allowing the inducible release of the E2 ECR (Huang et al., 2018, 2012). However, I inserted exclusively the TCS-corresponding amino acid sequence in the TA-7TM linker region of full-length $E5^{H>A}$ to ensure the functional receptor layout (**Fig. 42A**). Furthermore, I expanded $E5^{H>A}$ by an amber stop codon in the NTF for the additional visualization of the receptor using bioorthogonal labeling and by an N-terminal HA epitope and a C-terminal V5 epitope ($E5^{H>A}$-TAG^{NTF}-TCS). The effect of the inserted TCS on the surface expression was investigated by confocal imaging. For this purpose, I expressed $E5^{H>A}$-TAG^{NTF} and $E5^{H>A}$-TAG^{NTF}-TCS in HEK-293T cells. The non-permeabilized cells were simultaneously labeled through bioorthogonal labeling with H-Tet-Cy5 and IF staining with α-HA-Alexa 488. Both labeling techniques verified the localization of $E5^{H>A}$-TAG^{NTF} and $E5^{H>A}$-TAG^{NTF}-TCS at the plasma membrane (**Fig. 42B**). Additionally, the images demonstrated no obvious impact on the surface delivery of $E5^{H>A}$-TAG^{NTF}-TCS due to the TCS in the TA-TM7 linker region compared to $E5^{H>A}$-TAG^{NTF}.

Next, I analyzed the consequences of the artificial cleavage by thrombin on the fragmentation of E5. Therefore, HEK-293T cells expressing $E5^{H>A}$-TAG^{NTF} and $E5^{H>A}$-TAG^{NTF}-TCS were treated with or without thrombin protease followed by protein harvest and Western blot analysis. The analysis of $E5^{H>A}$-TAG^{NTF} and $E5^{H>A}$-TAG^{NTF}-TCS verified the appearance of the full-length receptor, which has a predicted size of 84.2 kDa (**Fig. 42D**), between the 75 kDa and 100 kDa marker band (**Fig. 42C**). Furthermore, I observed for both variants the appearance of two low-weight bands between 25 kDa and 37 kDa in the α-HA-representing channel, which I already detected in previous experiments of $E5^{X>A}$-TAG^{NTF} (see 6.3.3 and 6.3.5). These bands may indicate the formation of truncated NTF compared to the predicted NTF size of 48.5 kDa (**Fig. 42D**). Regarding the thrombin-induced cleavage, the $E5^{H>A}$-TAG^{NTF}-TCS variant showed no band at the predicted CTF size of 35.7 kDa (**Fig 42C,D**). In addition, no band lower than the full-length-representing band was detectable in the α-V5-representing channel (**Fig. 42C**). In summary, the artificial E5 cleavage at the TCS within the TA-7TM region by thrombin could not be demonstrated.

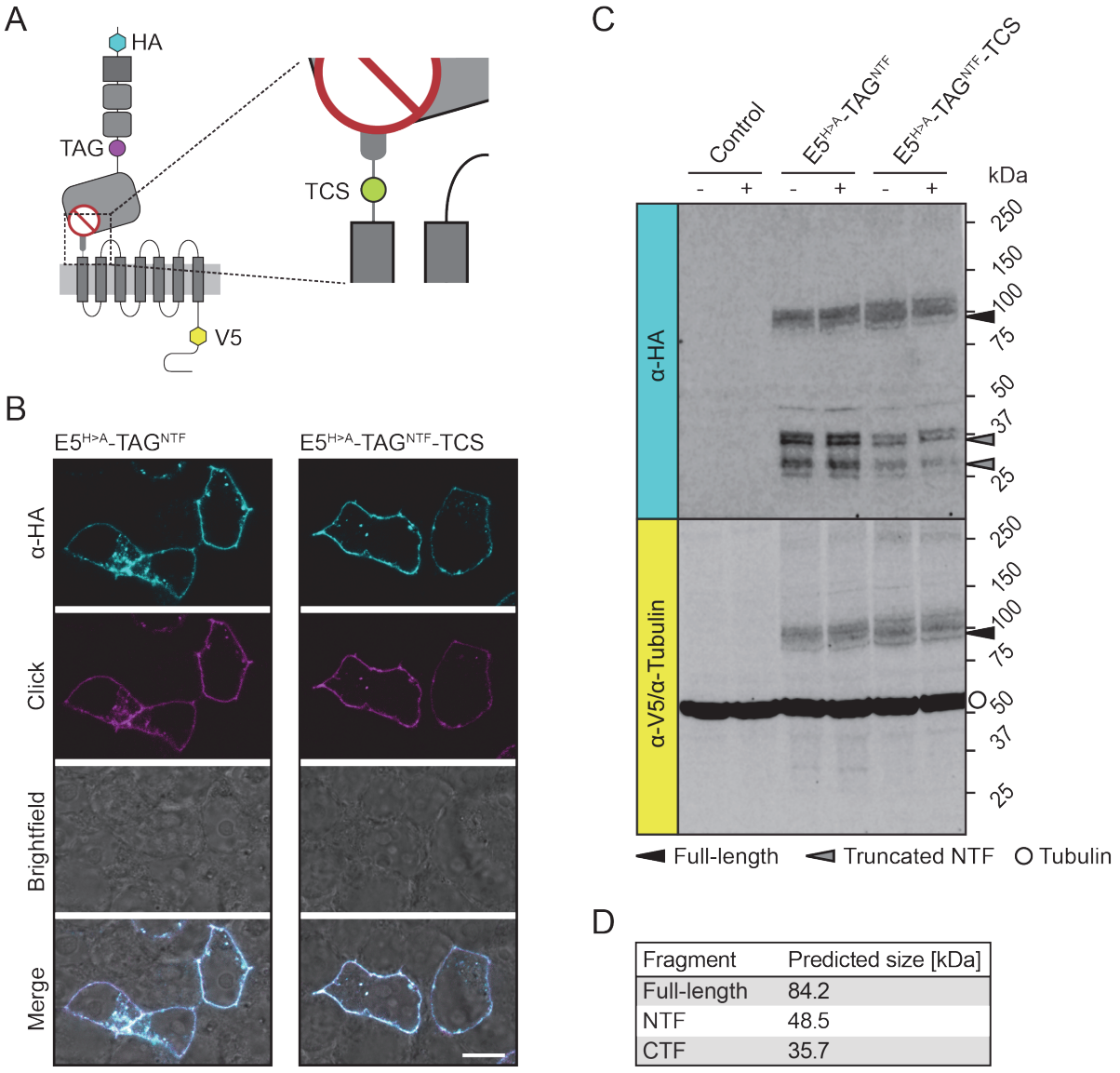

Fig. 42: Thrombin cleavage of GPS-cleavage-deficient E5 could not be demonstrated.

(A) Schematic illustration of cleavage-deficient E5$^{H>A}$-TAG^{NTF}-TCS expanded by an N-terminal HA epitope, a C-terminal V5 epitope, an amber stop codon within linker region between EGF5 and GAIN domains, and a TCS within the TA-7TM linker region. (B) Confocal images of HEK-293T expressing E5$^{H>A}$-TAG^{NTF} and E5$^{H>A}$-TAG^{NTF}-TCS. Cells are IF-labeled using α-HA-Alexa 488 (cyan) and bioorthogonally labeled using H-Tet-Cy5 (magenta). (C) Western blot analysis of cleavage-deficient E5$^{H>A}$-TAG^{NTF}, E5$^{H>A}$-TAG^{NTF}-TCS compared to control cells (only transfected with Pyl^{RS}/tRNA^{Pyl}) using α-HA and α-V5 antibodies. Constructs were transfected into HEK-293T cells and treated with and without thrombin protease for 1 h prior to protein harvest. Detection of β-tubulin serves as an internal loading control. (D) Predicted E5 fragment sizes of full-length receptor, NTF and CTF based on their amino acid sequence. Used Pyl^{RS}/tRNA^{Pyl} system: RS$_{Coin}$. Scale bar 10 µm.

An alternative method for a protease-induced cleavage of E5 is the use of a TEV cleavage site and respective protease. Previous experiments indicated a reduced E5 surface expression through the presence of a bioorthogonal label in the NTF (see

6.3.3). Therefore, I decided to incorporate the TEV cleavage site in the cleavage-deficient $E5^{H>A}$ containing an N-terminal HA tag and a C-terminal V5 tag without the addition of an amber stop codon (**Fig. 43A**). Moreover, I increased the potential flexibility and exposure of the TEV cleavage site by flanking it with GGGGS linkers, which had previously also increased the accessibility of BBS tags within the ECLs of E5 (see 6.3.2).

First, in collaboration with Mareike Hemberger, I analyzed whether the engineered $E5^{H>A}$-TEV^{Linker} variant was still transported to the plasma membrane. For this purpose, E5, $E5^{H>A}$ and $E5^{H>A}$-TEV^{Linker} were expressed in HEK-293T cells and subsequent the surface expression was quantified by ELISA. The quantification data indicated a surface expression of ~86 % for $E5^{H>A}$-TEV^{Linker} compared to E5 (**Fig. 43B**). Also, the cleavage deficiency had no negative effect on the surface delivery, as earlier determined in this thesis (see 6.2.3).

As a next step, we tested the TEV cleavage and its impact on the fragmentation of E5. HEK-293T cells expressing $E5^{H>A}$ and $E5^{H>A}$-TEV^{Linker} were treated with or without TEV protease, followed by protein harvest and Western blot analysis. The analysis of $E5^{H>A}$ and $E5^{H>A}$-TEV^{Linker} confirmed the appearance of the full-length receptor, which has a predicted size of 84.2 kDa (**Fig. 43D**), between the 75 kDa and 100 kDa marker band (**Fig. 43C**). Furthermore, a prominent band at 75 kDa was present in both the α-HA- and α-V5-representing channel of $E5^{H>A}$ and $E5^{H>A}$-TEV^{Linker}. This band may represent the non-cleaved, non-glycosylated E5 pro-protein, which already appeared in previous experiments (see 6.6.1). Moreover, the formation of E5 oligomers under reducing conditions was indicated by a prominent band above 150 kDa. Regarding the TEV-induced cleavage, the $E5^{H>A}$-TEV^{Linker} variant treated with TEV showed a distinct band at 25 kDa in the α-V-representing channel, which is slightly smaller compared to the calculated CTF size of 35.7 kDa (**Fig. 43C,D**). The appearance of this band correlates with the disappearance of the full-length E5 representing band. Furthermore, TEV-treated $E5^{H>A}$-TEV^{Linker} showed a distinct band between 50 kDa and 75 kDa, which represents the NTF even indicated previously (see 6.6.1). Interestingly, the artificial cleavage seems to have an influence on the NTF bands fraction and thus possibly on the glycosylation compared to the natural cleavage (see 6.6.1).

In summary, the cleavage of $E5^{H>A}$-TEV^{Linker} by the TEV protease at an artificial TEV cleavage site within the TA-7TM region by TEV protease could be demonstrated. Intriguingly, such artificial proteolytic processing of E5 can replace naturally occurring GAIN domain cleavage in the control of subsequent fragmentation of the receptor, likely due to secondary cleavage events executed by other, yet unbeknown, proteases.

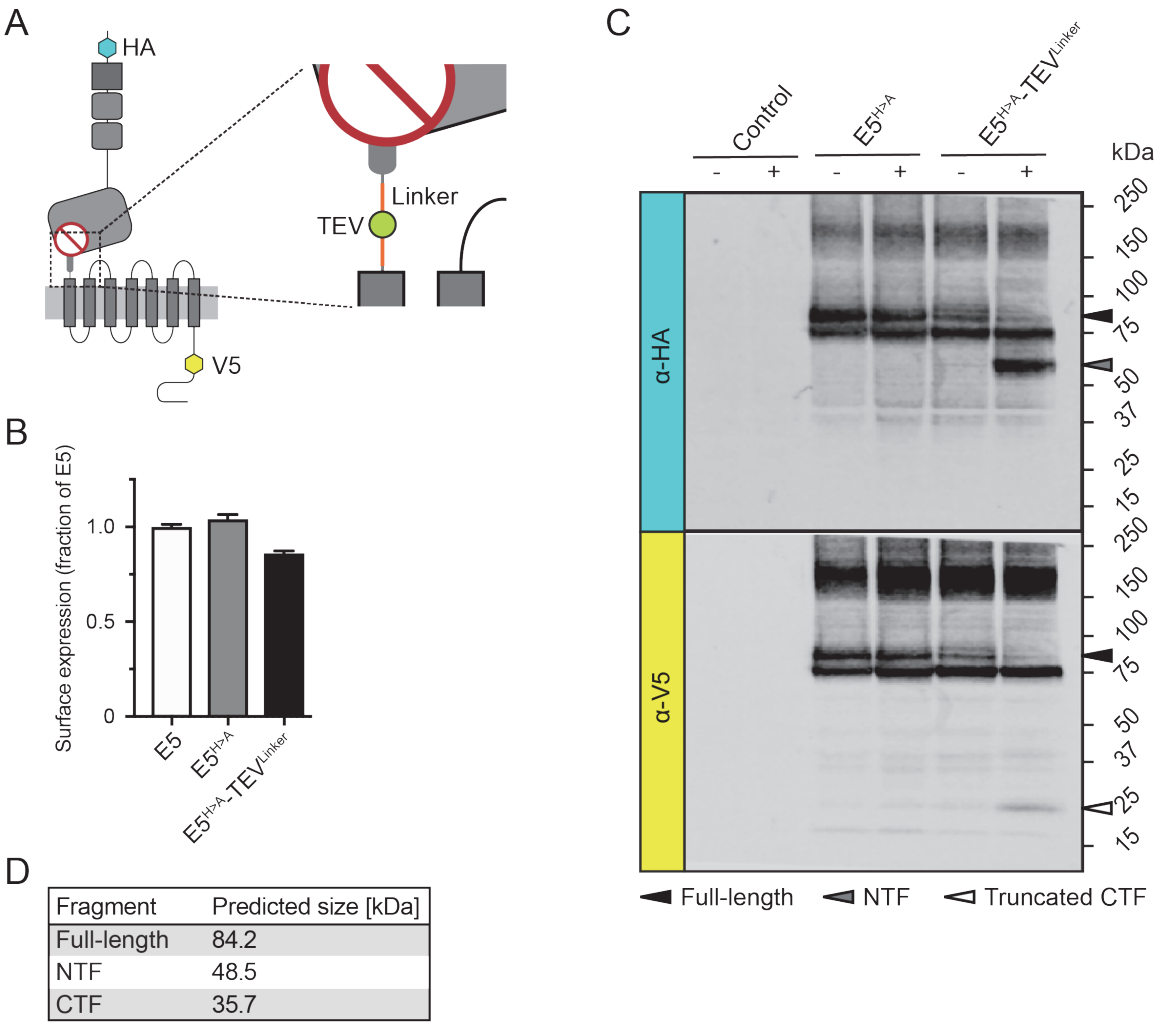

D

Fragment	Predicted size [kDa]
Full-length	84.2
NTF	48.5
CTF	35.7

Fig. 43: Proteolytic cleavage by TEV protease of the GPS-cleavage-deficient E5 is feasible and governs secondary receptor fragmentation.

(A) Schematic illustration of cleavage-deficient $E5^{H>A}$-TEV^{Linker} expanded by an N-terminal HA epitope, a C-terminal V5 epitope and a TEV cleavage site within the TA-7TM linker region. (B) Quantification of surface expression levels of HEK-293T cells expressing $E5^{H>A}$ and $E5^{H>A}$-TEV^{Linker} compared to E5. Dataset normalized to expression level of E5. Data are shown as mean ± SEM (N = 1, n = 12). (C) Western blot analysis of cleavage-deficient $E5^{H>A}$, $E5^{H>A}$-TEV^{Linker} compared to control cells (only transfected with EV) using α-HA and α-V5 antibodies. Constructs were transfected into HEK-293T cells and treated with and without TEV protease for 1 h prior to protein harvest. (D) Predicted E5 fragment sizes of full-length receptor, NTF and CTF based on their amino acid sequence. (B,C) performed by Mareike Hemberger.

6.6.3 Amphipathicity of the GAIN domain of ADGRE5

A basic property of aGPCRs is the autoproteolytic cleavage, which leads to the formation of a NTF-CTF heterodimer (Araç et al., 2012; Gray et al., 1996; Krasnoperov et al., 1997; Lin et al., 2004). However, studies of L1 and E2 also showed that a minority of the NTF localize separately from the CTF at the plasma membrane (Huang et al., 2012; Volynski et al., 2004). Further investigations revealed the existence of an

amphipathic α-helix in the GAIN domain of E2 anchoring the receptor to the membrane. Amphipathic helices provide the NTF the ability of membrane-anchoring independently of the CTF. In addition, the existence of similar amphipathic helices was also predicted in E5, B2, E4, and L2 (Huang et al., 2018).

Therefore, I decided to further investigate the actual presence of an amphipathic helix in E5 using a fluorescence-based approach. Theoretically, the amphipathic helix should give the NTF of cleaved E5 receptors the ability to localize independently of the CTF at other cells, including non-transfected cells. In contrast, cleavage-deficient E5 receptors should not show this behavior due to the lacking heterodimeric appearance.

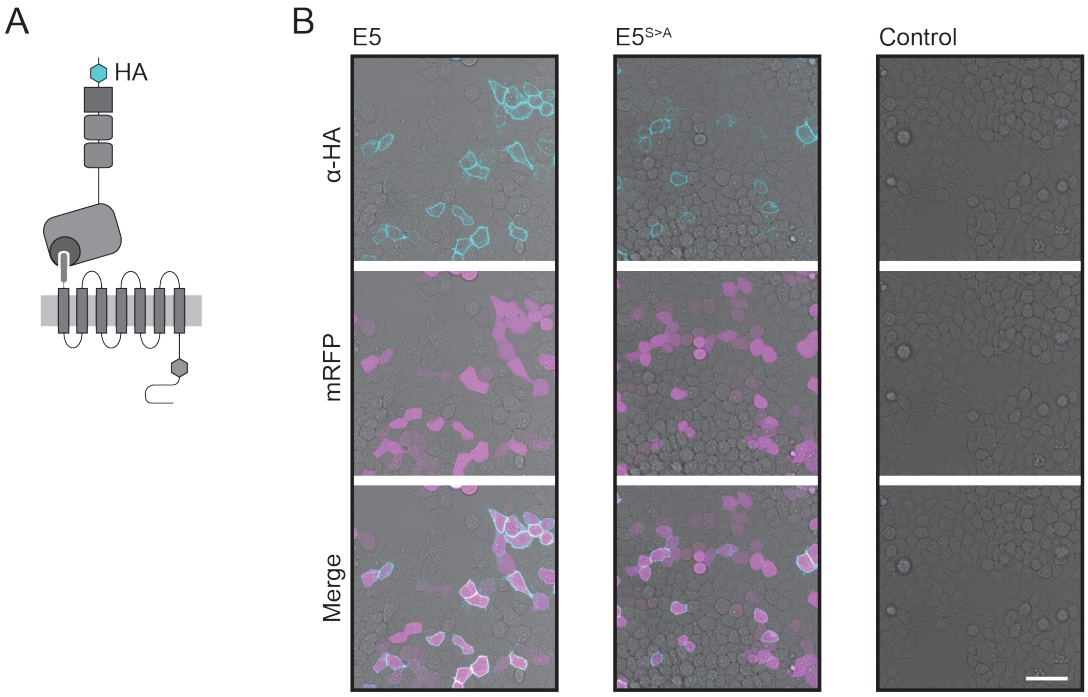

Fig. 44: Fluorescence microscopy shows no evidence for the existent of a membrane-anchoring helix in the GAIN domain of E5.

(A) Schematic illustration of E5 expanded by an N-terminal HA epitope. (B) Confocal images of unfixed HEK-293T cells co-expressing cleaved E5 or non-cleaved $E5^{S>A}$ together with soluble mRFP (magenta). E5 variants were stained using α-HA-Alexa 488 (cyan). Non-transfected cells serve as labeling controls. Merge shows no NTF localization on non-transfected cells. Scale bar 50 µm.

To test this, I expressed cleavable E5 and cleavage-deficient $E5^{S>A}$ containing an N-terminal HA tag in HEK-293T cells (**Fig. 44A**). Non-transfected HEK-293T cells served as a negative control. To visualize cells expressing E5, I co-transfected cells with a plasmid coding for a soluble mRFP. Additionally, the NTFs of E5 were IF stained with α-HA-Alexa 488. The confocal images of living cells indicated the presence of NTFs

only at the plasma membranes of transfected cells, which refuted the existence of a membrane-anchoring helix in the GAIN domain of E5 receptors (**Fig. 44B**).

To sum up, this chapter investigated the possibility of alternative cleavage sites within the E5 receptor based on Western blot analyses, which revealed the formation of truncated NTF and CTF fragments exclusively for cleavable E5 receptors. The incubation with DAPT excluded an γ-secretase-mediated cleavage of E5. Also, an artificial cleavage at an inserted TCS in the linker region of TA and 7TM domain was not successful. However, a TEV cleavage site with N-terminal and C-terminal linkers at the same position was cleavable by TEV proteases. Interestingly, the artificial cleavage using TEV resulted in the additional processing of the CTF. In the last experiment, I explored the existence of an amphipathic α-helix within the GAIN domain of E5, which may be able to anchor the NTF to the plasma membrane independently of the CTF. No evidence for this could be established.

7 Discussion

7.1 Tethered agonist exposure demonstrates the intrinsic structural flexibility of the intact GAIN domain

The GAIN domain, which mediates an autocatalytic self-cleavage during aGPCR maturation, represents a functional and structural hallmark of this receptor family. (Gray et al., 1996; Nieberler et al., 2016). aGPCR self-cleavage leads to the formation of a non-covalently attached heterodimer comprising an NTF and a CTF (Gray et al., 1996; Krasnoperov et al., 1997). So far, experimental data indicated that the first 7-18 amino acids of the CTF acts as a TA, which is able to trigger the activity of an aGPCR through its interaction with the 7TM domain (Liebscher et al., 2014; Liebscher and Schöneberg, 2016; Stoveken et al., 2015; Wilde et al., 2016). Interestingly, two models of TA-dependent aGPCR activation have been discussed for aGPCRs. The first model, termed dissociation model, describes the separation of the NTF from the CTF, which leads to the release of the TA followed by its interaction with the 7TM domain. In the second model, termed non-dissociation model, the interaction of the TA and the 7TM domain is catalyzed through a conformational change of the GAIN domain without the separation of the heterodimer. The physiological stimuli mediating the TA-7TM domain interaction are still unknown or ill-defined for a variety of aGPCRs. However, previous findings revealed the involvement of aGPCRs in mechanosensation, indicating that mechanical forces and/or ligands are able to promote receptor activation (Langenhan, 2019; Petersen et al., 2015; Scholz et al., 2016, 2015).

Interestingly, the GAIN domain crystal structures of the L1 and B3 receptors showed that the TA is deeply buried inside the domain (Araç et al., 2012). This circumstance indicated that the TA is unavailable for interactions with the 7TM domain and thus unable to mediate a receptor stimulation into downstream signaling at a first glance. However, this stands in contrast with different results, which have addressed aGPCR structure and activation. First, aGPCRs such as G5 are activated through the TA, although they are not autoproteolytically cleaved due to the missing consensus cleavage tripeptide sequence (Wilde et al., 2016). Second, the basal activity of cleavable aGPCRs such as GPR133 (ADGRD1/D1), G6 and E5 is maintained even if the autoproteolysis is abolished through mutations of the cleavage tripeptide suggesting a TA-7TM domain interaction (Hilbig et al., 2018; Liebscher et al., 2014). Third, *in vivo* experiments of *Caenorhabditis elegans* LAT-1 and *Drosophila melanogaster* CIRL showed that the aGPCR self-cleavage is dispensable for a proper receptor function (Prömel et al., 2012; Scholz et al., 2017). Furthermore, *in vivo* experiments of CIRL indicated that the mutation of the GPS compromising the first

amino acid of the TA led to an abolition of the GAIN domain-mediated autoproteolysis and the receptor function at the same time (Scholz et al., 2017). Summing up, this set of published experiments supports the non-dissociation model suggesting that the TA of cleavage-deficient aGPCRs is able to interact with the 7TM domain and therefore activate the receptor regardless of its autoproteolysis (see 4.3). However, the molecular mechanism behind the non-dissociation is still unknown at the moment.

I confirmed the TA accessibility in full-length L1, B3, G1, E2 and E5 receptors by bioorthogonal labeling of conserved +3 and +6 positions within their TAs *in vitro*. Interestingly, these *in vitro* approaches revealed an effective labeling of the hydrophobic +3 - +6 stretch within the TA under unstimulated conditions, which further demonstrated that even these positions are becoming exposed, indicating that also the hydrophobic stretch is able to engage with the 7TM domain. Currently, the exact stimuli leading to an activation of aGPCRs are largely ill-defined, therefore approaches were performed in an unstimulated situation. Hypothetically, the stimulation with ligands or mechanical forces could promote a stronger opening of the GAIN domain, leading to an additional exposure of the TA.

Interestingly, concomitant molecular dynamic simulations of the GAIN domain in collaboration with Peter Hildebrand's lab discovered the opening of two flaps, which may provide accessibility of the TA to the solvent (data not shown) (Altrichter et al., unpublished). In detail, these molecular dynamic simulation experiments showed that the polar residues (+1, +2, +7) of the TA core region are exposed in the intact GAIN domain, whereas the hydrophobic residues (+3 - +6) are initially shielded from the polar environment (data not shown) (Altrichter et al., unpublished). Consequently, this opening event within the intact GAIN domain may represent a possible molecular mechanism explaining the non-dissociation model. The molecular dynamic simulations were based on crystal structures of L1, B3 and G1 GAIN domains (Araç et al., 2012; Salzman et al., 2016) and homology models of E2 and E5 GAIN domains, indicating that the TA accessibility is a general structural feature of this receptor family (Altrichter et al., unpublished). Furthermore, these experiments demonstrated the extraordinary flexibility of the GAIN domain (Altrichter et al., unpublished).

Interestingly, protease-activated receptors (PARs), class A GPCR members, are also activated by the exposure of a TA through proteolytic processing of their ECR by a thrombin cleavage (Vu et al., 1991). The crystal structure of PAR1 revealed an orthosteric binding site using the irreversible antagonist, voraxapar, which binds to the extracellular surface and therefore prevents the TA binding (Zhang et al., 2012). The molecular dynamic simulation and bioorthogonal labeling demonstrated the conformational flexibility of the GAIN domain suggesting a model, in which its open conformation exposes the TA, mediating its interaction with the extracellular loops of

the 7TM domain, similar to the PAR1 receptor (**Fig. 45**). The complete opening of the GAIN domain would require extensive structural rearrangements within the GAIN domain, which may affect the non-covalent interactions that anchor the TA inside the domain. These rearrangements could stepwise increase the TA exposure and recognition by the 7TM domain in dependency of the stimulation intensity. In this context, the degree of TA exposure could correlate with the intensity of the signal transduction. Furthermore, this includes transition steps from a pre-bound to a fully 7TM domain-bound TA as previously suggested (Demberg et al., 2015; Liebscher and Schöneberg, 2016).

Also, I investigated the effect of a human missense mutation in the GAIN domain of E2, which leads to a rare autosomal dominant form of VBU. Hypothetically, this C492Y mutation leads to a destabilization of the NTF-CTF heterodimer and thus to an increased accessibility of the TA (Boyden et al., 2016). The mechanical stimulation through shaking the cells prior to or during labeling did not impact the TA accessibility, indicating that the C492Y mutation in VBU patients is not causing the exposure of the TA through the GAIN domain destabilization and subsequent receptor activation. This experiment suggests that beside TA-dependent signaling aGPCRs may undergo further signaling mechanisms without the involvement of the TA in 7TM domain activation. These TA-independent mechanisms may comprise the direct interaction of the GAIN domain or other extracellular domains with the 7TM domain, inducing conformational changes and consequently downstream signaling (Kishore et al., 2016; Kishore and Hall, 2017; Salzman et al., 2017).

In summary, this set of experiments demonstrates an until now unknown mechanism of spontaneous TA exposure, which potentially modulates downstream signaling. Prospective investigations including crystallography or cryogenic electron microscopy of the GAIN-7TM domain tandem are required to further detail their conformational relationship. Approaches like these may solve the exact interaction sites between the TA and the 7TM domain and thus discover suitable targeting regions. Furthermore, pharmacological targeting sites within the GAIN-7TM domain tandem may be revealed, allowing a possible strategy to influence the TA-dependent aGPCR signaling and potentially allows the therapy of related diseases. In addition, experiments performed in this study demonstrated that the bioorthogonal labeling technique is useful to label hardly accessible positions within intact domains like the GAIN domain, therefore providing an ideal tool to replace larger fluorescent tags like genetically encoded chromophores.

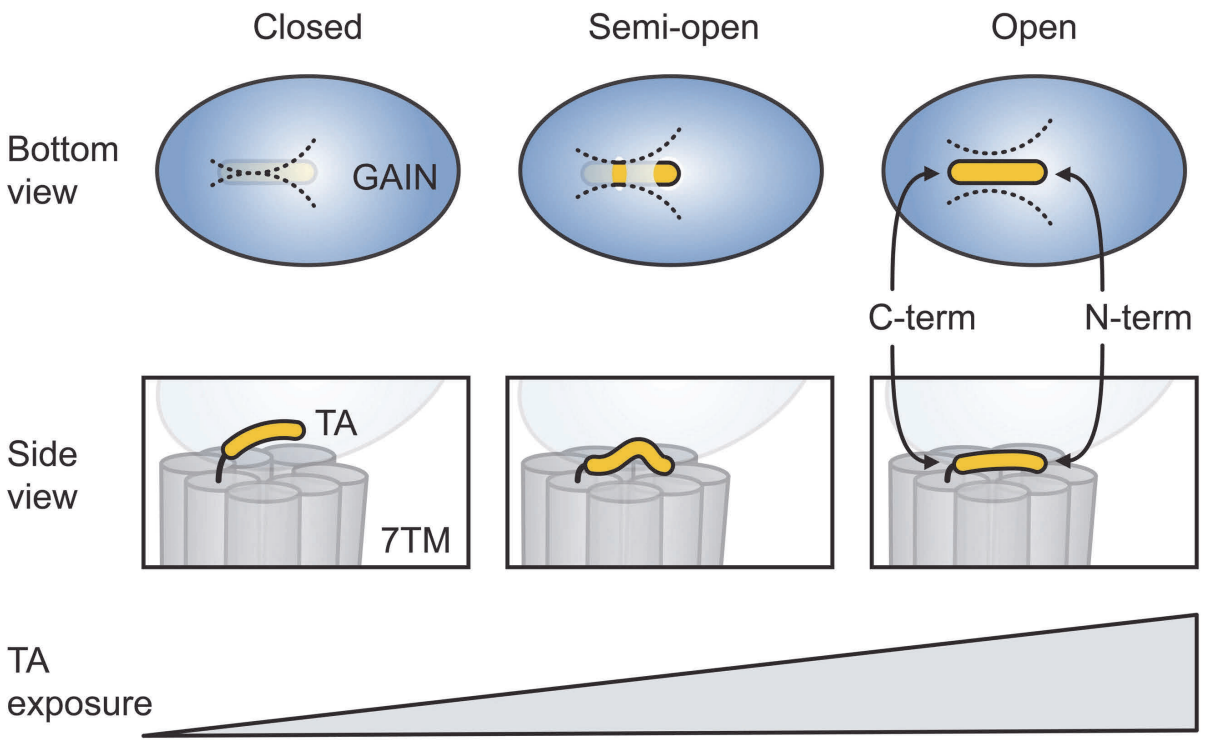

Fig. 45: Model of the structural rearrangements promoting the TA exposure in the intact GAIN domain.

Stimulation of the aGPCR by ligands and/or mechanical forces leads to the opening of two flaps (dashed lines) in the surface of the intact, non-dissociated GAIN domain. The opening stepwise increases the TA exposure and its recognition by the 7TM domain proportionally to the stimulation intensity. Consequently, the TA-7TM domain interaction promotes receptor signaling. The closed and semi-open states of the GAIN domain were observed in crystal structures, molecular homology models and molecular dynamic simulations by Peter Hildebrand's lab. The open state, which would allow the interaction between the entire TA region and the 7TM domain, is speculative. However, bioorthogonal labeling results obtained from this study indicate that a larger region of the TA is exposed to the solvent. Adapted from Altrichter et al., unpublished.

7.2 TA-induced structural changes of the ADGRE5 7TM domain

Molecular dynamic stimulations already demonstrated an opening within the GAIN domain, which may allow the release of the TA and its subsequent interaction with the 7TM domain to stabilize the receptor in an active conformation (Altrichter et al., unpublished). This suggests that the 7TM domain undergoes structural rearrangement mediated by the TA, resulting in the signal transduction through downstream signaling proteins (e.g. G-proteins, β-arrestins). However, experimental evidence for the 7TM domain rearrangements is still missing. A compounding factor is that no solved crystal structure of the 7TM domain is available for the aGPCR family; in contrast, at least one crystal structure was published for other families of the GPCR superfamily (Isberg et al., 2015; Nijmeijer et al., 2016). Crystal structures of proteins provide one way to solve

domain conformations depending on the activity status at atomic resolution allowing, in combination with molecular dynamic stimulation, the detailed investigation of structural rearrangements within the 7TM domain including ECLs, ICLs and transmembrane α-helices (Latorraca et al., 2017). However, another prominent method to determine conformational changes *in vitro* and *in vivo* is FRET. This method allows the measurement of distance changes within the 7TM domain of various GPCR members upon ligand binding (Hoffmann et al., 2005; Nakanishi et al., 2006; Vilardaga et al., 2003; Ziegler et al., 2011). The first functional GPCR FRET sensors were designed for the class A α_{2A}AR, and the class B parathyroid hormone receptor (Vilardaga et al., 2003). Over the recent years more and more FRET sensors were established for further class A and B members, but also for class C GPCRs like the metabotropic glutamate receptor 1 (Hlavackova et al., 2012; Stumpf and Hoffmann, 2016). These sensors helped to analyze the ligand-induced structural changes of the 7TM domain and thus provide a more accurate picture of the functional mechanism and signal transduction of these receptors.

However, FRET sensors capable of investigating structural rearrangements of the aGPCR family are still missing. Additionally, the ill-defined physiological stimuli of aGPCRs constitute an aggravating factor to determine rearrangements upon receptor activation. In order to effectively test whether the 7TM domain of aGPCRs is involved in signal transduction, I used to my advantage the fact that the deletion of the NTF leads to constitutively active receptors ($E5^{\Delta NTF}$) and that the deletion of the CTF leads to constitutively inactive receptors ($E5^{\Delta ECR}$) (Hilbig et al., 2018; Liebscher et al., 2014; Stoveken et al., 2015) (see 4.3). I generated FRET sensors for the E5 receptor based on the previously described GPCR sensor layouts comprising fluorophores in the ICL3 and the ICR (Hoffmann et al., 2005; Jensen et al., 2009; Vilardaga et al., 2003). I demonstrated activity-dependent distance changes within the 7TM domain of E5 by *in vitro* FRET analyses. These distance changes were independent of the receptor self-cleavage. In contrast, mutations of the TA core region, which abolished the metabotropic receptor activity of several aGPCRs (Liebscher et al., 2014; Stoveken et al., 2015), affected the 7TM domain conformation of full-length E5, whereas the conformation of $E5^{\Delta NTF}$ was unaffected. In detail, the FRET efficiency of full-length E5 was reduced to a comparable level of $E5^{\Delta ECR}$, indicating that E5 adopts an inactive receptor conformation upon TA mutation. This set of experiments suggests that the 7TM conformation of E5 differs in dependency of the activation state. In detail, the 7TM domain adopts at least three different conformations – basal, active and inactive conformation. This is comparable to FRET analyses of GPCRs treated either with an agonist or an inverse agonist leading to an receptor activation or inactivation respectively (Hoffmann et al., 2009; Vilardaga et al., 2005). Recent studies suggested

that GPCRs appear to exist in multiple inactive and active conformations, which are probably mediated by the binding of diverse (inverse) agonists (Gurevich and Gurevich, 2017; Manglik et al., 2015). This could also explain the conformational differences between full-length E5 and $E5^{\Delta NTF}$ upon identical mutations of the TA suggesting that both receptors adopt different inactive conformations.

Furthermore, I demonstrated that the cellular localization differs between full-length E5, $E5^{\Delta NTF}$ and $E5^{\Delta ECR}$. Full-length E5 was localized in the cell surface and in intracellular vesicles, whereas the truncated E5 variants were exclusively intracellularly located. Also the NTF/ECR deletion of G6 and D1 generated constitutively active/inactive receptor variants, which exhibited an impaired surface delivery (Liebscher et al., 2014). The authors rescued the surface delivery by the fusion of the $P2Y_{12}$ N-terminus to the N-terminal end of the aGPCR, which still preserved the constitutive activity/inactivity of the receptor (Liebscher et al., 2014). Intriguingly, constitutive receptor activity associated with intracellular localization was observed for several GPCRs (Hendrik Schmidt et al., 2019; Jacobsen et al., 2017; Trivedi and Bhattacharyya, 2012). One example represents the angiotensin II type 1 receptor (AT1), which is a critical mediator in blood pressure control and sodium homeostasis (Miserey-Lenkei et al., 2002). Constitutively active AT1s, genetically engineered by single point mutations within the 7TM domain or the ICR, were mostly located in intracellular vesicles (Miserey-Lenkei et al., 2002). The incubation with the inverse agonist losartan promoted the translocation of constitutively active AT1 to the plasma membrane indicating its constitutively internalization and recycling (Miserey-Lenkei et al., 2002). In this context, I also demonstrated the constitutive internalization of full-length E5 by several labeling approaches, suggesting that constitutively active E5 and AT1 might experience similar intracellular localization and signaling mechanisms. Additionally, a variety of GPCRs undergo internalization after agonist-induced activation at the plasma membrane, resulting in internalization and signaling from intracellular compartments like endosomes or the Golgi system (Calebiro et al., 2010, 2009; Godbole et al., 2017; Irannejad et al., 2013). This represents further evidence that GPCRs are able to perform signaling from intracellular compartments. In contrast, reasons for the predominantly intracellular localization of the constitutively inactive $E5^{\Delta ECR}$ remains elusive for the moment. Speculatively, the deletion of the ECR could affect the receptors conformation in a manner that no proper surface delivery via the translocation machinery is possible.

Another important mechanism regarding the modulation of receptor signaling represents dimerization. The formation of dimers and higher order oligomers between identical (homo-) or different (hetero-oligomerization) proteins occurs in a variety of cytosolic and cell surface receptors (Bain et al., 2007; Lohse, 2010). Oligomerization

of GPCRs is associated with ligand recognition, receptor activation, signal transduction and trafficking (Lohse, 2010). The underlying mechanisms and appearance of dimerization/oligomerization events in regard to the aGPCR family represents a poorly investigated field. Only few experimental data, e.g. the dimerization of the *Caenorhabditis elegans* LAT-1, are available. Intermolecular complementation assays demonstrated that the RBL domain is necessary for the cross-activation between two LAT-1 receptors (Prömel et al., 2012). Consequently, this study demonstrated that the RBL domain mediates the interaction of LAT-1 receptors, resulting in functional dimers *in vivo* (Prömel et al., 2012). In this thesis, intermolecular FRET analyses showed the oligomerization of another aGPCR member, the E5 receptor. In detail, FRET analyses of basal active and constitutively active/inactive E5 variants revealed diverse effects on the distance between the receptors in relation to their activity, meaning that the distance of inactive receptors was wider in contrast to active receptors, which showed the closest proximity, whereas the basal active receptor was to be classified in between (**Fig. 46**). However, also activity-dependent arrangements of the 7TM domains to each other could lead to different FRET signals. Furthermore, it is probably important that the investigated E5 variants showed different cellular localizations, which could also have an effect on the oligomerization. These FRET analyses further suggested, that the E5 oligomerization is mediated via the 7TM domain. Interestingly, oligomerization mediated by the 7TM domain was also observed for another member of the subfamily E, the E2 receptor (Davies et al., 2007). The authors described the oligomerization of E2 as an autoproteolysis-independent mechanism (Davies et al., 2007). Western blot analyses of E5 showed multiple bands above the full-length receptor, indicating oligomeric E5 complexes. Interestingly, these complexes appear also under reducing conditions, suggesting strong non-covalent forces between the E5 proteins. Furthermore, oligomeric E5 bands appeared independently of the GAIN domain-mediated cleavage, which further arises the question for the physiological function of the autoproteolysis.

In conclusion, the obtained FRET results in this thesis indicate an activity- and localization-dependent structural rearrangement of the E5 7TM domain and an oligomerization of E5 (**Fig. 46**). This allows for speculations about the mechanisms of aGPCR signaling. Basal active E5 is transported to the plasma membrane, where it slightly interacts with further E5 receptors. The activation through the TA results in a rapid internalization and stronger interaction between the E5 receptors, which stabilizes the active receptor conformation. Additionally, these events promote conformational changes of the 7TM domain, which lead to the activation of downstream signaling partners. Next, the desensitization is mediated by the dissociation of the E5 receptors and the conformational change of their 7TM domain,

preventing further interactions with signaling partners. Finally, E5 may be transported to the lysosome, resulting in receptor degradation, or transported back to the plasma membrane. This speculative signaling life cycle based on experimental data of constitutively active/inactive E5 variants, which allow the simplified investigation of fundamental aGPCR signaling mechanisms. However, prospective analyses could be performed exclusively with full-length aGPCRs and physiological relevant stimuli to further elucidate the complex molecular mechanisms of aGPCR signaling. In addition, the combination of FRET assays and signaling assays are of great interest to simultaneously analyze the relation between structural rearrangements and activity of aGPCRs.

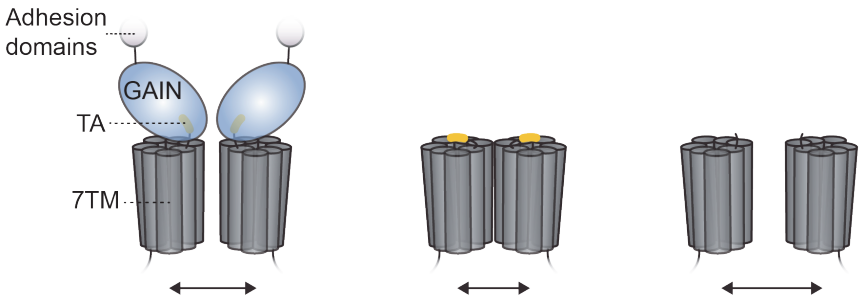

Fragment	Full-length	ΔNTF	ΔECR
Activity	Basal	↑	↓
Localization	PM/Intracellular	Intracellular	Intracellular

Fig. 46: Potential activity- and/or cellular localization-dependent oligomerization modes of E5.

The formation of oligomeric E5 complexes depends on the activity status and/or the cellular localization of the receptors. Full-length E5 localizes at the plasma membrane (PM) and in intracellular vesicles, and shows a basal activity. The deletion of the NTF leads to an increased activity and a closer receptor distance, whereas the deletion of the CTF leads to a decreased activity and a wider receptor distance. Additionally, these deletions result into an exclusively intracellular receptor localization. Original data of depicted E5 signaling assay results are published in Hilbig et al., 2018.

7.3 Natural and artificial receptor cleavages control secondary proteolytic processing of ADGRE5

This thesis already highlights the biological importance of the GAIN domain and its TA for the activation and signal transduction of aGPCRs. I demonstrated that the TA is able to interact with the 7TM domain independent of the NTF-CTF dissociation. Additionally, I showed that the cleavage deficiency of the GAIN domain had no influence on the 7TM domain conformation. Altogether, this suggests that the GAIN

domain-mediated self-cleavage is likely irrelevant for the aGPCR signal transduction. Also *in vitro* and *in vivo* experiments showed that the receptors function was not affected by non-functional autoproteolysis (Hilbig et al., 2018; Liebscher et al., 2014; Prömel et al., 2012; Scholz et al., 2017). In addition, several aGPCRs remain uncleaved due to the absent GPS motif and are still fully functional (Langenhan, 2019; Wilde et al., 2016). Consequently, this raises the question of the physiological role of the GAIN domain-mediated cleavage.

Surprisingly, Western blot analysis of E5 performed in this thesis revealed an unexpected band pattern, comprising additional bands apart from the expected full-length receptor, NTF and CTF corresponding bands. The band pattern suggests the existence of a cleavage site in the NTF above the GAIN domain and another cleavage site in the CTF, more precisely in the 7TM domain (**Fig. 47A**). Interestingly, the additional observed bands disappeared in cleavage-deficient E5 variants, indicating that the autoproteolysis initializes additional cleavage events within the receptor and, thus, suggests a potential new and still unknown biochemical processing and physiological function. However, the nature of the cleavage sites and its protease(s) remains not known. In this context, additional NTF- and CTF-located cleavage sites beside the GAIN domain are already known for several aGPCRs (**Fig. 47B**). The subfamily F members, F1 and F5, undergo an autoproteolytic reaction at the SEA domain, which is located in the NTF above the GAIN domain (Abe et al., 2002; Lum et al., 2010). The resulting fragments of the SEA domain-mediated cleavage remain non-covalently attached to each other similar to the fragments of the GAIN domain-mediated autoproteolysis (Levitin et al., 2005). However, in the case of the SEA domain, the remaining N-terminal fragment represents a proEGF2 region, which is additionally cleaved by furin, a serine protease (Fukuzawa and Hirose, 2006). This cleavage converts the fragment to a EGF2 domain, which remains associated to the F5 receptor forming a heterotrimer (Fukuzawa and Hirose, 2006). Similar furin-mediated cleavage events within the NTF were also observed for B1, B2 and G6 (Cork et al., 2012; Moriguchi et al., 2004; Okajima et al., 2010). In the case of B1, the cleavage occurs in two steps: furin protease activates the matrix metalloproteinase-14, which finally cleaves between the thrombospondin type-1 repeats (Cork et al., 2012). Another example is the furin-mediated cleavage of L1 and L2, which occurs at the TA-7TM domain linker region for a minor fraction of receptors (Krasnoperov et al., 2009). The cleavage of several aGPCRs by furin allows for speculations about the existence of a furin cleavage site within the E5 sequence. For this purpose, the use of furin specific inhibitors could elucidate whether E5 is cleaved by furin or not. However, a prediction algorithm for furin cleavage sites showed no hit for E5 at the moment (Duckert et al., 2004).

CTF-located cleavage sites are already known for polycystin-1, an eleven transmembrane-spanning protein, which is involved in autosomal dominant polycystic kidney disease (Igarashi, 2002). This molecule shares structural characteristics with aGPCRs including an extraordinarily large ECR containing a GAIN domain, hallmark feature of the aGPCR family (Merrick et al., 2014). In contrast to E5, the polycystin-1 CTF is cleaved by a γ-secretase regardless of its autoproteolysis (Merrick et al., 2014; Woodward et al., 2010) (**Fig. 47B**). Mechanical stimulation triggers the further processing (Chauvet et al., 2004; Low et al., 2006; Merrick et al., 2014). The Notch receptor is another example for transmembrane domain cleavage. This single transmembrane receptor undergoes a cleavage cascade (**Fig. 47B**), including S1 cleavage by a furin protease in the Golgi system, resulting in the formation of a heterodimeric receptor (Blaumueller et al., 1997). Ligand binding catalyzes a metalloprotease-mediated cleavage at the S2 site (Brou et al., 2000). The resulting CTF is additionally cleaved by a γ-secretase at the S3 site, which promotes the translocation of the intracellular fragment to the nucleus (van Tetering and Vooijs, 2011). In this study, I also tested whether the E5 CTF is additionally processed by a γ-secretase. To this end, I specifically inhibited γ-secretases using DAPT, which was already successfully applied for the Notch receptor (Dovey et al., 2009; Geling, 2002). DAPT treatment showed no impact on the Western blot band pattern, indicating no involvement of a γ-secretase in the CTF cleavage of E5. Consequently, the nature of the CTF-located cleavage sites is still unknown, so the use of additional specific protease inhibitors could help to further solve this puzzle.

Interestingly, the further E5 processing, which is initialized by the autoproteolytic cleavage of the GAIN domain, can also be mimicked by artificial cleavage within the TA-7TM linker region, suggesting that the formation of the heterodimeric receptor layout is necessary for additional cleavage events. This allows for the speculation that the proteolytic separation of E5 leads to conformational changes promoting the accessibility of additional cleavage sites.

In summary, Western blot analyses indicate unknown cleavage events within the NTF and the CTF of E5. However, experimental data in this thesis allow no statement about the nature and sequence of the additional cleavage sites within the E5 receptor, which thus, remain unknown at the moment. With the purpose of elucidating the exact position of cleavage sites and their origin, the purification of the fragments and their subsequent analysis by Edman degradation, which allows the sequencing of amino acid sequences from the N-terminal end (Edman, 1949), could be performed. Furthermore, the subcellular localization, interaction partners and functional relevance of these E5 fragments are still unknown. In this context, detailed analyses could

elucidate these questions, contributing to a better understanding of their overall function.

A

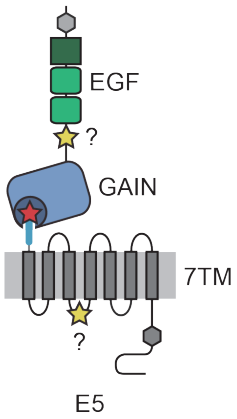

Fragment	Predicted size [kDa]
Full-length	84.2
NTF	48.5
CTF	35.7

B

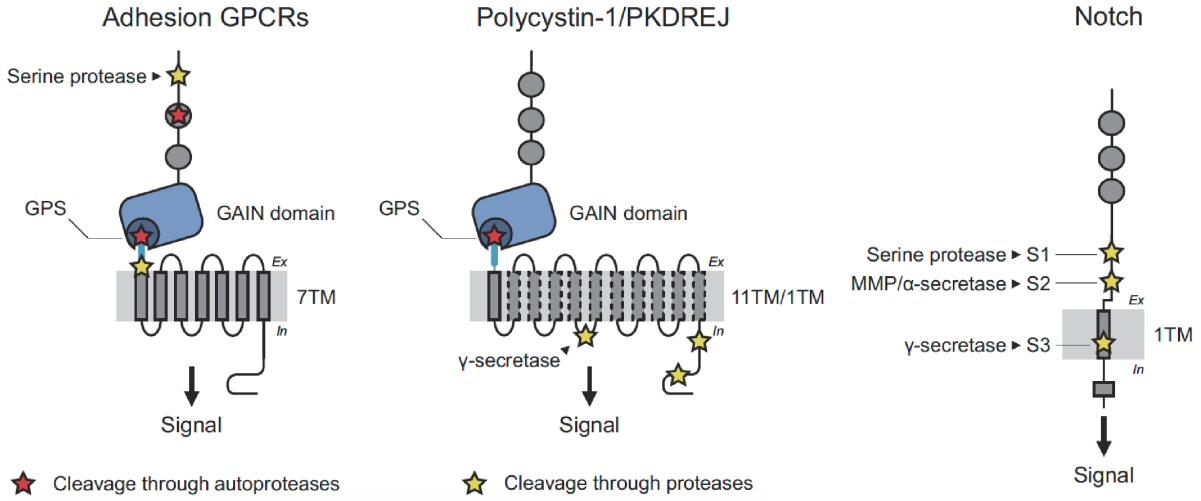

Fig. 47: Theoretical processing of E5 in comparison to known cleavage events of transmembrane receptors.

(A) Schematic illustration of potential additional cleavage sites within E5. Predicted E5 fragment sizes of full-length receptor, NTF and CTF based on their amino acid sequence. (B) Schematic illustration of known autoproteolytic cleavage and proteases-mediated cleavage events within aGPCRs in comparison to polycystin-1 and Notch receptor. Adapted from Nieberler et al., 2016.

7.4 Internalization modes of ADGRE5

The process of internalization represents the least investigated and ill-defined mechanism of the aGPCR family. In contrast, it is well understood that the stimulation by ligands results in the arrestin-dependent internalization of many members of the GPCR superfamily (**Fig. 48**). In detail, receptor stimulation leads to the release of G-proteins, promoting the phosphorylation of intracellular receptor regions by GPCR

kinases (GRKs). The association of phosphorylated receptors with β-arrestin mediates the desensitization and clustering of GPCRs in clathrin-coated pits. Finally, the receptors are internalized via the clathrin-dependent endocytic machinery and transported to early endosomes, where the dephosphorylation and the ligand dissociation occurs. The internalized GPCRs are either delivered to lysosomes resulting in their degradation or they are recycled and transported back to the plasma membrane (Irannejad and von Zastrow, 2014; Lohse and Hoffmann, 2014) .

Interestingly, recent studies demonstrate that β-arrestins function as scaffolds and adapters that modulate mitogen-activated protein kinases, including c-Jun N-terminal kinases and extracellular-regulated kinases, consequently regulating their related pathways (Miller and Lefkowitz, 2001).

The recruitment of β-arrestins was only observed for few aGPCRs, namely: B1, B2, G1, GPR64 (ADGRG2/G2) and GPR97 (ADGRG3/G3) (Kishore et al., 2016; Langenhan, 2019; Southern et al., 2013; Zhang et al., 2018). Furthermore, co-immunoprecipitation analyses revealed the direct interaction between E5 and β-arrestin 1, suggesting that also E5 undergoes arrestin-dependent internalization (Yin et al., 2018). In this case, the receptor internalization was triggered by the stimulation with soluble CD55, resulting in an extensive phosphorylation by GRKs (Yin et al., 2018). In contrast, I demonstrated that full-length E5 internalized independently of a specific stimulation through ligands and/or mechanical forces. This ligand-independent internalization, also known as constitutive internalization, has been observed for several other members of the GPCR superfamily (Hendrik Schmidt et al., 2019; Jacobsen et al., 2017; Trivedi and Bhattacharyya, 2012). Intriguingly, this process mediates the degradation and recycling of GPCRs similar to the ligand-induced internalization, however, the physiological function of the constitutive internalization remains elusive at the moment (Hendrik Schmidt et al., 2019; Scarselli and Donaldson, 2009). Interestingly, the ligand-dependent E5 internalization was observed in human hepatocarcinoma cell line SMMC-7721 (Yin et al., 2018), whereas I determined the ligand-independent internalization of E5 in HEK-293T cells, suggesting that the type of internalization depends on the cellular background. Similar mechanisms were already described for the melanocortin-4 receptor, which is ligand-dependent internalized in HEK-293 cells and ligand-independent in N2A and GT1-7 cells (Gao et al., 2003; Mohammad et al., 2007)

It remains unknown whether the constitutive internalization of E5 occurs by β-arrestin-dependent or -independent mechanisms. However, both mechanisms have already been observed for GPCRs. The mechanism of β-arrestin-dependent constitutive internalization has been described for the α_{1a}-adrenergic receptor (Morris et al., 2004).

In contrast, the constitutive internalization of chemokine receptor US28 occurred independently of β-arrestin recruitment (Fraile-Ramos et al., 2003). In this regard, already established FRET sensors could help to elucidate a relationship between β-arrestin and aGPCR (Krasel et al., 2005; Nuber et al., 2016).

In conclusion, published data and experimental data of this study indicate that E5 undergoes ligand-dependent and -independent internalization events, which may promote desensitization, degradation, recycling and intracellular signaling modes. The appearance of intracellular signaling modes were already demonstrated in this study by extensive FRET analyses. However, the mechanisms of E5 internalization are still elusive. For this purpose, prospective analyses will deal with the scientific question whether ligand-dependent and -independent internalization occur simultaneously or are specifically triggered by different effectors such as cell type, receptor activity or interaction partners. Additionally, functional and subcellular location differences between these internalization types represent another point to investigate in detail. The combination of established labeling techniques and pre-described signaling assays (Hilbig et al., 2018; Liebscher et al., 2014; Nazarko et al., 2018) will certainly contribute to elucidate the complex internalization mechanisms of aGPCRs.

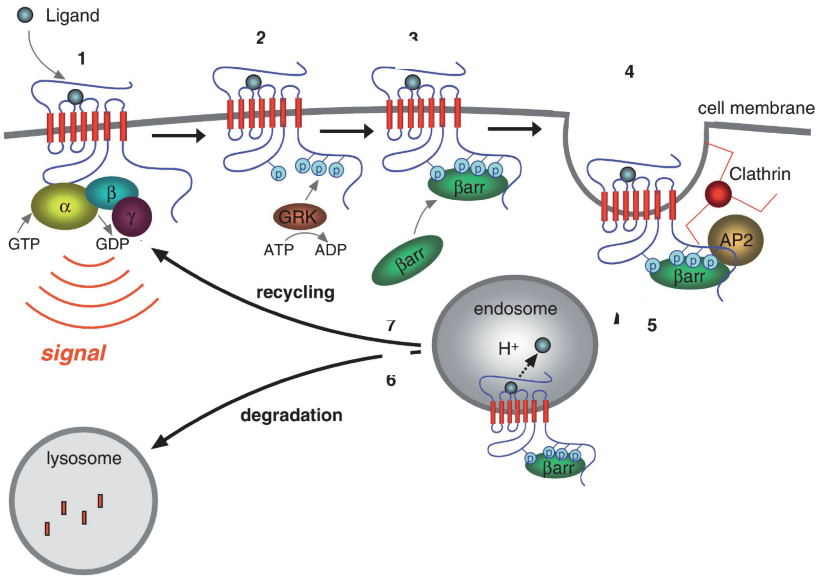

Fig. 48: β-arrestin-dependent signaling life cycle of GPCRs.

Receptor stimulation leads to the release of G-proteins, followed by phosphorylation of the intracellular receptor region through GPCR kinases (GRK). Next, the phosphorylated receptors interact with β-arrestin, mediating the desensitization and clustering of GPCRs in clathrin-coated pits. The receptors are internalized via the clathrin-dependent endocytic machinery, followed by their transport to early endosomes, where the dephosphorylation and the ligand dissociation occurs. Finally, the internalized GPCRs are either delivered to lysosomes resulting in their degradation or they are recycled and transported back to the plasma membrane. Adapted from Irannejad and von Zastrow, 2014.

8 References

Abe, J., Fukuzawa, T., Hirose, S., 2002. Cleavage of Ig-Hepta at a “SEA” Module and at a Conserved G Protein-coupled Receptor Proteolytic Site. J. Biol. Chem. 277, 23391–23398. https://doi.org/10.1074/jbc.M110877200

Adams, S.R., Campbell, R.E., Gross, L.A., Martin, B.R., Walkup, G.K., Yao, Y., Llopis, J., Tsien, R.Y., 2002. New Biarsenical Ligands and Tetracysteine Motifs for Protein Labeling in Vitro and in Vivo: Synthesis and Biological Applications. J. Am. Chem. Soc. 124, 6063–6076. https://doi.org/10.1021/ja017687n

Adams, S.R., Tsien, R.Y., 2008. Preparation of the membrane-permeant biarsenicals FlAsH-EDT2 and ReAsH-EDT2 for fluorescent labeling of tetracysteine-tagged proteins. Nat Protoc 3, 1527–1534. https://doi.org/10.1038/nprot.2008.144

Allache, R., De Marco, P., Merello, E., Capra, V., Kibar, Z., 2012. Role of the planar cell polarity gene CELSR1 in neural tube defects and caudal agenesis. Birth Defects Res. Part A Clin. Mol. Teratol. 94, 176–181. https://doi.org/10.1002/bdra.23002

Altrichter, S., Beliu, G., Guixà-González, R., Hemberger, M., Brauer, I., Scholz, N., Kuhlemann, A., Pérez-Hernández, G., Hildebrand, P.W., Sauer, M., Langenhan, T., unpublished. Tethered agonist exposure in intact adhesion GPCRs through intrinsic structural flexibility of the GAIN domain. In Revision.

Araç, D., Boucard, A.A., Bolliger, M.F., Nguyen, J., Soltis, S.M., Südhof, T.C., Brunger, A.T., 2012. A novel evolutionarily conserved domain of cell-adhesion GPCRs mediates autoproteolysis. EMBO J. 31, 1364–1378. https://doi.org/10.1038/emboj.2012.26

Araç, D., Sträter, N., Seiradake, E., 2016. Understanding the Structural Basis of Adhesion GPCR Functions, in: Langenhan, T., Schöneberg, T. (Eds.), Adhesion G Protein-Coupled Receptors. Springer International Publishing, Cham, pp. 67–82. https://doi.org/10.1007/978-3-319-41523-9_4

Aust, G., Eichler, W., Laue, S., Lehmann, I., Heldin, N.E., Lotz, O., Scherbaum, W.A., Dralle, H., Hoang-Vu, C., 1997. CD97: a dedifferentiation marker in human thyroid carcinomas. Cancer Res. 57, 1798–1806.

Aust, G., Zhu, D., Van Meir, E.G., Xu, L., 2016. Adhesion GPCRs in Tumorigenesis, in: Langenhan, T., Schöneberg, T. (Eds.), Adhesion G Protein-Coupled Receptors. Springer International Publishing, Cham, pp. 369–396. https://doi.org/10.1007/978-3-319-41523-9_17

Bain, D.L., Heneghan, A.F., Connaghan-Jones, K.D., Miura, M.T., 2007. Nuclear Receptor Structure: Implications for Function. Annu. Rev. Physiol. 69, 201–220. https://doi.org/10.1146/annurev.physiol.69.031905.160308

Bajar, B.T., Wang, E.S., Zhang, S., Lin, M.Z., Chu, J., 2016. A Guide to Fluorescent

Protein FRET Pairs. Sensors (Basel, Switzerland) 16. https://doi.org/10.3390/s16091488

Balass, M., Katchalski-Katzir, E., Fuchs, S., 1997. The -bungarotoxin binding site on the nicotinic acetylcholine receptor: Analysis using a phage-epitope library. Proceedings of the National Academy of Sciences 94, 6054–6058. https://doi.org/10.1073/pnas.94.12.6054

Baud, V., Chissoe, S.L., Viegas-Péquignot, E., Diriong, S., N'Guyen, V.C., Roe, B.A., Lipinski, M., 1995. EMR1, an unusual member in the family of hormone receptors with seven transmembrane segments. Genomics 26, 334–344.

Beliu, G., Kurz, A.J., Kuhlemann, A.C., Behringer-Pliess, L., Meub, M., Wolf, N., Seibel, J., Shi, Z.-D., Schnermann, M., Grimm, J.B., Lavis, L.D., Doose, S., Sauer, M., 2019. Bioorthogonal labeling with tetrazine-dyes for super-resolution microscopy. Commun Biol 2, 261. https://doi.org/10.1038/s42003-019-0518-z

Blackman, M.L., Royzen, M., Fox, J.M., 2008. Tetrazine Ligation: Fast Bioconjugation Based on Inverse-Electron-Demand Diels−Alder Reactivity. J. Am. Chem. Soc. 130, 13518–13519. https://doi.org/10.1021/ja8053805

Blaumueller, C.M., Qi, H., Zagouras, P., Artavanis-Tsakonas, S., 1997. Intracellular Cleavage of Notch Leads to a Heterodimeric Receptor on the Plasma Membrane. Cell 90, 281–291. https://doi.org/10.1016/S0092-8674(00)80336-0

Bohnekamp, J., Schöneberg, T., 2011. Cell Adhesion Receptor GPR133 Couples to G_s Protein. J. Biol. Chem. 286, 41912–41916. https://doi.org/10.1074/jbc.C111.265934

Boyden, S.E., Desai, A., Cruse, G., Young, M.L., Bolan, H.C., Scott, L.M., Eisch, A.R., Long, R.D., Lee, C.-C.R., Satorius, C.L., Pakstis, A.J., Olivera, A., Mullikin, J.C., Chouery, E., Mégarbané, A., Medlej-Hashim, M., Kidd, K.K., Kastner, D.L., Metcalfe, D.D., Komarow, H.D., 2016. Vibratory Urticaria Associated with a Missense Variant in ADGRE2. N. Engl. J. Med. 374, 656–663. https://doi.org/10.1056/NEJMoa1500611

Bridges, J.P., Ludwig, M.-G., Mueller, M., Kinzel, B., Sato, A., Xu, Y., Whitsett, J.A., Ikegami, M., 2013. Orphan G Protein–Coupled Receptor GPR116 Regulates Pulmonary Surfactant Pool Size. Am J Respir Cell Mol Biol 49, 348–357. https://doi.org/10.1165/rcmb.2012-0439OC

Brou, C., Logeat, F., Gupta, N., Bessia, C., LeBail, O., Doedens, J.R., Cumano, A., Roux, P., Black, R.A., Israël, A., 2000. A novel proteolytic cleavage involved in Notch signaling: the role of the disintegrin-metalloprotease TACE. Mol. Cell 5, 207–216.

Brown, K., Filuta, A., Ludwig, M.-G., Seuwen, K., Jaros, J., Vidal, S., Arora, K., Naren, A.P., Kandasamy, K., Parthasarathi, K., Offermanns, S., Mason, R.J., Miller, W.E., Whitsett, J.A., Bridges, J.P., 2017. Epithelial Gpr116 regulates pulmonary alveolar homeostasis via Gq/11 signaling. JCI Insight 2.

https://doi.org/10.1172/jci.insight.93700

Calebiro, D., Nikolaev, V.O., Gagliani, M.C., de Filippis, T., Dees, C., Tacchetti, C., Persani, L., Lohse, M.J., 2009. Persistent cAMP-Signals Triggered by Internalized G-Protein–Coupled Receptors. PLoS Biol 7, e1000172. https://doi.org/10.1371/journal.pbio.1000172

Calebiro, D., Nikolaev, V.O., Persani, L., Lohse, M.J., 2010. Signaling by internalized G-protein-coupled receptors. Trends in Pharmacological Sciences 31, 221–228. https://doi.org/10.1016/j.tips.2010.02.002

Cattaneo, M., 2015. P2Y12 receptors: structure and function. J. Thromb. Haemost. 13 Suppl 1, S10-16. https://doi.org/10.1111/jth.12952

Chalfie, M., Tu, Y., Euskirchen, G., Ward, W.W., Prasher, D.C., 1994. Green fluorescent protein as a marker for gene expression. Science 263, 802–805. https://doi.org/10.1126/science.8303295

Chang, C.C., Lee, C.Y., 1963. ISOLATION OF NEUROTOXINS FROM THE VENOM OF BUNGARUS MULTICINCTUS AND THEIR MODES OF NEUROMUSCULAR BLOCKING ACTION. Arch Int Pharmacodyn Ther 144, 241–257.

Chauvet, V., Tian, X., Husson, H., Grimm, D.H., Wang, T., Hieseberger, T., Igarashi, P., Bennett, A.M., Ibraghimov-Beskrovnaya, O., Somlo, S., Caplan, M.J., 2004. Mechanical stimuli induce cleavage and nuclear translocation of the polycystin-1 C terminus. J. Clin. Invest. 114, 1433–1443. https://doi.org/10.1172/JCI21753

Coons, A.H., Creech, H.J., Jones, R.N., 1941. Immunological Properties of an Antibody Containing a Fluorescent Group. Experimental Biology and Medicine 47, 200–202. https://doi.org/10.3181/00379727-47-13084P

Cork, S.M., Kaur, B., Devi, N.S., Cooper, L., Saltz, J.H., Sandberg, E.M., Kaluz, S., Van Meir, E.G., 2012. A proprotein convertase/MMP-14 proteolytic cascade releases a novel 40 kDa vasculostatin from tumor suppressor BAI1. Oncogene 31, 5144–5152. https://doi.org/10.1038/onc.2012.1

Davies, J.Q., Chang, G.-W., Yona, S., Gordon, S., Stacey, M., Lin, H.-H., 2007. The Role of Receptor Oligomerization in Modulating the Expression and Function of Leukocyte Adhesion-G Protein-coupled Receptors. J. Biol. Chem. 282, 27343–27353. https://doi.org/10.1074/jbc.M704096200

Demberg, L.M., Rothemund, S., Schöneberg, T., Liebscher, I., 2015. Identification of the tethered peptide agonist of the adhesion G protein-coupled receptor GPR64/ADGRG2. Biochemical and Biophysical Research Communications 464, 743–747. https://doi.org/10.1016/j.bbrc.2015.07.020

Demberg, L.M., Winkler, J., Wilde, C., Simon, K.-U., Schön, J., Rothemund, S., Schöneberg, T., Prömel, S., Liebscher, I., 2017. Activation of Adhesion G Protein-

coupled Receptors: AGONIST SPECIFICITY OF STACHEL SEQUENCE-DERIVED PEPTIDES. J. Biol. Chem. 292, 4383–4394. https://doi.org/10.1074/jbc.M116.763656

Dovey, H.F., John, V., Anderson, J.P., Chen, L.Z., De Saint Andrieu, P., Fang, L.Y., Freedman, S.B., Folmer, B., Goldbach, E., Holsztynska, E.J., Hu, K.L., Johnson-Wood, K.L., Kennedy, S.L., Kholodenko, D., Knops, J.E., Latimer, L.H., Lee, M., Liao, Z., Lieberburg, I.M., Motter, R.N., Mutter, L.C., Nietz, J., Quinn, K.P., Sacchi, K.L., Seubert, P.A., Shopp, G.M., Thorsett, E.D., Tung, J.S., Wu, J., Yang, S., Yin, C.T., Schenk, D.B., May, P.C., Altstiel, L.D., Bender, M.H., Boggs, L.N., Britton, T.C., Clemens, J.C., Czilli, D.L., Dieckman-McGinty, D.K., Droste, J.J., Fuson, K.S., Gitter, B.D., Hyslop, P.A., Johnstone, E.M., Li, W.-Y., Little, S.P., Mabry, T.E., Miller, F.D., Ni, B., Nissen, J.S., Porter, W.J., Potts, B.D., Reel, J.K., Stephenson, D., Su, Y., Shipley, L.A., Whitesitt, C.A., Yin, T., Audia, J.E., 2009. Functional gamma-secretase inhibitors reduce beta-amyloid peptide levels in brain: γ-secretase inhibitors reduce Aβ levels in PDAPP mouse brain. Journal of Neurochemistry 76, 173–181. https://doi.org/10.1046/j.1471-4159.2001.00012.x

Duckert, P., Brunak, S., Blom, N., 2004. Prediction of proprotein convertase cleavage sites. Protein Engineering, Design and Selection 17, 107–112. https://doi.org/10.1093/protein/gzh013

Edman, P., 1949. A method for the determination of amino acid sequence in peptides. Arch Biochem 22, 475.

Ehmann, N., van de Linde, S., Alon, A., Ljaschenko, D., Keung, X.Z., Holm, T., Rings, A., DiAntonio, A., Hallermann, S., Ashery, U., Heckmann, M., Sauer, M., Kittel, R.J., 2014. Quantitative super-resolution imaging of Bruchpilot distinguishes active zone states. Nat Commun 5, 4650. https://doi.org/10.1038/ncomms5650

Eichler, W., Aust, G., Hamann, D., 1994. Characterization of an early activation-dependent antigen on lymphocytes defined by the monoclonal antibody BL-Ac(F2). Scand. J. Immunol. 39, 111–115. https://doi.org/10.1111/j.1365-3083.1994.tb03348.x

Förster, T., 1948. Zwischenmolekulare Energiewanderung und Fluoreszenz. Annalen der Physik 437, 55–75. https://doi.org/10.1002/andp.19484370105

Fouquet, W., Owald, D., Wichmann, C., Mertel, S., Depner, H., Dyba, M., Hallermann, S., Kittel, R.J., Eimer, S., Sigrist, S.J., 2009. Maturation of active zone assembly by *Drosophila* Bruchpilot. J Cell Biol 186, 129–145. https://doi.org/10.1083/jcb.200812150

Fraile-Ramos, A., Kohout, T.A., Waldhoer, M., Marsh, M., 2003. Endocytosis of the Viral Chemokine Receptor US28 Does Not Require Beta-Arrestins But Is Dependent on the Clathrin-Mediated Pathway. Traffic 4, 243–253. https://doi.org/10.1034/j.1600-0854.2003.00079.x

Fredriksson, R., Lagerström, M.C., Lundin, L.-G., Schiöth, H.B., 2003. The G-protein-coupled receptors in the human genome form five main families. Phylogenetic

analysis, paralogon groups, and fingerprints. Mol. Pharmacol. 63, 1256–1272. https://doi.org/10.1124/mol.63.6.1256

Fukuzawa, T., Hirose, S., 2006. Multiple Processing of Ig-Hepta/GPR116, a G Protein–Coupled Receptor with Immunoglobulin (Ig)-Like Repeats, and Generation of EGF2-Like Fragment. The Journal of Biochemistry 140, 445–452. https://doi.org/10.1093/jb/mvj170

Gao, Z., Lei, D., Welch, J., Le, K., Lin, J., Leng, S., Duhl, D., 2003. Agonist-Dependent Internalization of the Human Melanocortin-4 Receptors in Human Embryonic Kidney 293 Cells. J Pharmacol Exp Ther 307, 870–877. https://doi.org/10.1124/jpet.103.055525

Geling, A., 2002. A gamma-secretase inhibitor blocks Notch signaling in vivo and causes a severe neurogenic phenotype in zebrafish. EMBO Reports 3, 688–694. https://doi.org/10.1093/embo-reports/kvf124

Godbole, A., Lyga, S., Lohse, M.J., Calebiro, D., 2017. Internalized TSH receptors en route to the TGN induce local Gs-protein signaling and gene transcription. Nat Commun 8, 443. https://doi.org/10.1038/s41467-017-00357-2

Goedhart, J., van Weeren, L., Hink, M.A., Vischer, N.O.E., Jalink, K., Gadella Jr, T.W.J., 2010. Bright cyan fluorescent protein variants identified by fluorescence lifetime screening. Nature Methods 7, 137–139. https://doi.org/10.1038/nmeth.1415

Gray, J.X., Haino, M., Roth, M.J., Maguire, J.E., Jensen, P.N., Yarme, A., Stetler-Stevenson, M.A., Siebenlist, U., Kelly, K., 1996. CD97 is a processed, seven-transmembrane, heterodimeric receptor associated with inflammation. J. Immunol. 157, 5438–5447.

Griffin, B.A., Adams, S.R., Tsien, R.Y., 1998. Specific covalent labeling of recombinant protein molecules inside live cells. Science 281, 269–272. https://doi.org/10.1126/science.281.5374.269

Gurevich, V., Gurevich, E., 2017. Molecular Mechanisms of GPCR Signaling: A Structural Perspective. IJMS 18, 2519. https://doi.org/10.3390/ijms18122519

Hamann, J., Aust, G., Araç, D., Engel, F.B., Formstone, C., Fredriksson, R., Hall, R.A., Harty, B.L., Kirchhoff, C., Knapp, B., Krishnan, A., Liebscher, I., Lin, H.-H., Martinelli, D.C., Monk, K.R., Peeters, M.C., Piao, X., Prömel, S., Schöneberg, T., Schwartz, T.W., Singer, K., Stacey, M., Ushkaryov, Y.A., Vallon, M., Wolfrum, U., Wright, M.W., Xu, L., Langenhan, T., Schiöth, H.B., 2015. International Union of Basic and Clinical Pharmacology. XCIV. Adhesion G protein-coupled receptors. Pharmacol. Rev. 67, 338–367. https://doi.org/10.1124/pr.114.009647

Hamann, J., Eichler, W., Hamann, D., Kerstens, H.M., Poddighe, P.J., Hoovers, J.M., Hartmann, E., Strauss, M., van Lier, R.A., 1995. Expression cloning and chromosomal

mapping of the leukocyte activation antigen CD97, a new seven-span transmembrane molecule of the secretion receptor superfamily with an unusual extracellular domain. J. Immunol. 155, 1942–1950.

Hamann, J., Hsiao, C.-C., Lee, C.S., Ravichandran, K.S., Lin, H.-H., 2016. Adhesion GPCRs as Modulators of Immune Cell Function, in: Langenhan, T., Schöneberg, T. (Eds.), Adhesion G Protein-Coupled Receptors. Springer International Publishing, Cham, pp. 329–350. https://doi.org/10.1007/978-3-319-41523-9_15

Hamann, J., Kwakkenbos, M., Lier, R. van, 2000. Characterization of EGF-TM7 family members by novel monoclonal antibodies. Tissue Antigens 55.

Hamann, J., Stortelers, C., Kiss-Toth, E., Vogel, B., Eichler, W., van Lier, R.A., 1998. Characterization of the CD55 (DAF)-binding site on the seven-span transmembrane receptor CD97. Eur. J. Immunol. 28, 1701–1707. https://doi.org/10.1002/(SICI)1521-4141(199805)28:05<1701::AID-IMMU1701>3.0.CO;2-2

Hamann, J., Vogel, B., van Schijndel, G.M., van Lier, R.A., 1996. The seven-span transmembrane receptor CD97 has a cellular ligand (CD55, DAF). J. Exp. Med. 184, 1185–1189. https://doi.org/10.1084/jem.184.3.1185

Hannan, S., Wilkins, M.E., Thomas, P., Smart, T.G., 2013. Tracking Cell Surface Mobility of GPCRs Using α-Bungarotoxin-Linked Fluorophores, in: Methods in Enzymology. Elsevier, pp. 109–129. https://doi.org/10.1016/B978-0-12-391862-8.00006-5

He, Z., Wu, H., Jiao, Y., Zheng, J., 2015. Expression and prognostic value of CD97 and its ligand CD55 in pancreatic cancer. Oncology Letters 9, 793–797. https://doi.org/10.3892/ol.2014.2751

Heilemann, M., van de Linde, S., Schüttpelz, M., Kasper, R., Seefeldt, B., Mukherjee, A., Tinnefeld, P., Sauer, M., 2008. Subdiffraction-Resolution Fluorescence Imaging with Conventional Fluorescent Probes. Angew. Chem. Int. Ed. 47, 6172–6176. https://doi.org/10.1002/anie.200802376

Hendrik Schmidt, J., Perslev, M., Bukowski, L., Stoklund, M., Herborg, F., Herlo, R., Lindegaard Madsen, K., 2019. Constitutive internalization across therapeutically targeted GPCRs correlates with constitutive activity. Basic Clin Pharmacol Toxicol bcpt.13274. https://doi.org/10.1111/bcpt.13274

Heng, B.C., Aubel, D., Fussenegger, M., 2013. An overview of the diverse roles of G-protein coupled receptors (GPCRs) in the pathophysiology of various human diseases. Biotechnology Advances 31, 1676–1694. https://doi.org/10.1016/j.biotechadv.2013.08.017

Hilbig, D., Sittig, D., Hoffmann, F., Rothemund, S., Warmt, E., Quaas, M., Stürmer, J., Seiler, L., Liebscher, I., Hoang, N.A., Käs, J.A., Banks, L., Aust, G., 2018. Mechano-

Dependent Phosphorylation of the PDZ-Binding Motif of CD97/ADGRE5 Modulates Cellular Detachment. Cell Rep 24, 1986–1995. https://doi.org/10.1016/j.celrep.2018.07.071

Hlavackova, V., Zabel, U., Frankova, D., Batz, J., Hoffmann, C., Prezeau, L., Pin, J.-P., Blahos, J., Lohse, M.J., 2012. Sequential Inter- and Intrasubunit Rearrangements During Activation of Dimeric Metabotropic Glutamate Receptor 1. Science Signaling 5, ra59–ra59. https://doi.org/10.1126/scisignal.2002720

Hoffmann, C., Gaietta, G., Bünemann, M., Adams, S.R., Oberdorff-Maass, S., Behr, B., Vilardaga, J.-P., Tsien, R.Y., Ellisman, M.H., Lohse, M.J., 2005. A FlAsH-based FRET approach to determine G protein-coupled receptor activation in living cells. Nat. Methods 2, 171–176. https://doi.org/10.1038/nmeth742

Hoffmann, C., Gaietta, G., Zürn, A., Adams, S.R., Terrillon, S., Ellisman, M.H., Tsien, R.Y., Lohse, M.J., 2010. Fluorescent labeling of tetracysteine-tagged proteins in intact cells. Nat Protoc 5, 1666–1677. https://doi.org/10.1038/nprot.2010.129

Hoffmann, C., Zürn, A., Bünemann, M., Lohse, M.J., 2009. Conformational changes in G-protein-coupled receptors-the quest for functionally selective conformations is open: Methods to detect conformational changes in GPCRs. British Journal of Pharmacology 153, S358–S366. https://doi.org/10.1038/sj.bjp.0707615

Hsiao, C.-C., Chen, H.-Y., Chang, G.-W., Lin, H.-H., 2011. GPS autoproteolysis is required for CD97 to up-regulate the expression of N-cadherin that promotes homotypic cell-cell aggregation. FEBS Lett. 585, 313–318. https://doi.org/10.1016/j.febslet.2010.12.005

Hu, G.-M., Mai, T.-L., Chen, C.-M., 2017. Visualizing the GPCR Network: Classification and Evolution. Sci Rep 7, 1–15. https://doi.org/10.1038/s41598-017-15707-9

Huang, Y.-S., Chiang, N.-Y., Chang, G.-W., Lin, H.-H., 2018. Membrane-association of EMR2/ADGRE2-NTF is regulated by site-specific N-glycosylation. Sci Rep 8, 4532. https://doi.org/10.1038/s41598-018-22849-x

Huang, Y.-S., Chiang, N.-Y., Hu, C.-H., Hsiao, C.-C., Cheng, K.-F., Tsai, W.-P., Yona, S., Stacey, M., Gordon, S., Chang, G.-W., Lin, H.-H., 2012. Activation of myeloid cell-specific adhesion class G protein-coupled receptor EMR2 via ligation-induced translocation and interaction of receptor subunits in lipid raft microdomains. Mol. Cell. Biol. 32, 1408–1420. https://doi.org/10.1128/MCB.06557-11

Igarashi, P., 2002. Genetics and Pathogenesis of Polycystic Kidney Disease. Journal of the American Society of Nephrology 13, 2384–2398. https://doi.org/10.1097/01.ASN.0000028643.17901.42

Irannejad, R., Tomshine, J.C., Tomshine, J.R., Chevalier, M., Mahoney, J.P., Steyaert, J., Rasmussen, S.G.F., Sunahara, R.K., El-Samad, H., Huang, B., von Zastrow, M.,

2013. Conformational biosensors reveal GPCR signalling from endosomes. Nature 495, 534–538. https://doi.org/10.1038/nature12000

Irannejad, R., von Zastrow, M., 2014. GPCR signaling along the endocytic pathway. Current Opinion in Cell Biology 27, 109–116. https://doi.org/10.1016/j.ceb.2013.10.003

Isberg, V., de Graaf, C., Bortolato, A., Cherezov, V., Katritch, V., Marshall, F.H., Mordalski, S., Pin, J.-P., Stevens, R.C., Vriend, G., Gloriam, D.E., 2015. Generic GPCR residue numbers – aligning topology maps while minding the gaps. Trends in Pharmacological Sciences 36, 22–31. https://doi.org/10.1016/j.tips.2014.11.001

Ishizuka, T., Saisu, H., Odani, S., Abe, T., 1995. Synaphin: A Protein Associated with the Docking/Fusion Complex in Presynaptic Terminals. Biochemical and Biophysical Research Communications 213, 1107–1114. https://doi.org/10.1006/bbrc.1995.2241

Jacobsen, S.E., Ammendrup-Johnsen, I., Jansen, A.M., Gether, U., Madsen, K.L., Bräuner-Osborne, H., 2017. The GPRC6A receptor displays constitutive internalization and sorting to the slow recycling pathway. J. Biol. Chem. 292, 6910–6926. https://doi.org/10.1074/jbc.M116.762385

Jaspars, L.H., Vos, W., Aust, G., van Lier, R.A.W., Hamann, J., 2001. Tissue distribution of the human CD97 EGF-TM7 receptor. Tissue Antigens 57, 325–331. https://doi.org/10.1034/j.1399-0039.2001.057004325.x

Jensen, J.B., Lyssand, J.S., Hague, C., Hille, B., 2009. Fluorescence changes reveal kinetic steps of muscarinic receptor–mediated modulation of phosphoinositides and Kv7.2/7.3 K^+ channels. J Gen Physiol 133, 347–359. https://doi.org/10.1085/jgp.200810075

Kasher, R., Balass, M., Scherf, T., Fridkin, M., Fuchs, S., Katchalski-Katzir, E., 2001. Design and synthesis of peptides that bind α-bungarotoxin with high affinity. Chemistry & Biology 8, 147–155. https://doi.org/10.1016/S1074-5521(00)90063-2

Kim, S., Bell, K., Mousa, S.A., Varner, J.A., 2000. Regulation of Angiogenesis in Vivo by Ligation of Integrin α5β1 with the Central Cell-Binding Domain of Fibronectin. The American Journal of Pathology 156, 1345–1362. https://doi.org/10.1016/S0002-9440(10)65005-5

Kishore, A., Hall, R.A., 2017. Disease-associated extracellular loop mutations in the adhesion G protein-coupled receptor G1 (ADGRG1; GPR56) differentially regulate downstream signaling. J. Biol. Chem. 292, 9711–9720. https://doi.org/10.1074/jbc.M117.780551

Kishore, A., Purcell, R.H., Nassiri-Toosi, Z., Hall, R.A., 2016. Stalk-dependent and Stalk-independent Signaling by the Adhesion G Protein-coupled Receptors GPR56 (ADGRG1) and BAI1 (ADGRB1). J. Biol. Chem. 291, 3385–3394. https://doi.org/10.1074/jbc.M115.689349

Kittel, R.J., 2006. Bruchpilot Promotes Active Zone Assembly, Ca2+ Channel Clustering, and Vesicle Release. Science 312, 1051–1054. https://doi.org/10.1126/science.1126308

Koide, A., Koide, S., 2006. Monobodies: Antibody Mimics Based on the Scaffold of the Fibronectin Type III Domain, in: Protein Engineering Protocols. Humana Press, New Jersey, pp. 95–110. https://doi.org/10.1385/1-59745-187-8:95

Kolb, H.C., Finn, M.G., Sharpless, K.B., 2001. Click Chemistry: Diverse Chemical Function from a Few Good Reactions. Angew. Chem. Int. Ed. Engl. 40, 2004–2021.

Krasel, C., Bunemann, M., Lorenz, K., Lohse, M.J., 2005. -Arrestin Binding to the 2-Adrenergic Receptor Requires Both Receptor Phosphorylation and Receptor Activation. Journal of Biological Chemistry 280, 9528–9535. https://doi.org/10.1074/jbc.M413078200

Krasnoperov, V., Deyev, I.E., Serova, O.V., Xu, C., Lu, Y., Buryanovsky, L., Gabibov, A.G., Neubert, T.A., Petrenko, A.G., 2009. Dissociation of the Subunits of the Calcium-Independent Receptor of α-Latrotoxin as a Result of Two-Step Proteolysis †. Biochemistry 48, 3230–3238. https://doi.org/10.1021/bi802163p

Krasnoperov, V., Lu, Y., Buryanovsky, L., Neubert, T.A., Ichtchenko, K., Petrenko, A.G., 2002. Post-translational Proteolytic Processing of the Calcium-independent Receptor of α-Latrotoxin (CIRL), a Natural Chimera of the Cell Adhesion Protein and the G Protein-coupled Receptor: ROLE OF THE G PROTEIN-COUPLED RECEPTOR PROTEOLYSIS SITE (GPS) MOTIF. J. Biol. Chem. 277, 46518–46526. https://doi.org/10.1074/jbc.M206415200

Krasnoperov, V.G., Bittner, M.A., Beavis, R., Kuang, Y., Salnikow, K.V., Chepurny, O.G., Little, A.R., Plotnikov, A.N., Wu, D., Holz, R.W., Petrenko, A.G., 1997. α-Latrotoxin Stimulates Exocytosis by the Interaction with a Neuronal G-Protein-Coupled Receptor. Neuron 18, 925–937. https://doi.org/10.1016/S0896-6273(00)80332-3

Krishnan, A., Nijmeijer, S., de Graaf, C., Schiöth, H.B., 2016. Classification, Nomenclature, and Structural Aspects of Adhesion GPCRs, in: Langenhan, T., Schöneberg, T. (Eds.), Adhesion G Protein-Coupled Receptors. Springer International Publishing, Cham, pp. 15–41. https://doi.org/10.1007/978-3-319-41523-9_2

Kwakkenbos, M.J., Kop, E.N., Stacey, M., Matmati, M., Gordon, S., Lin, H.-H., Hamann, J., 2004. The EGF-TM7 family: a postgenomic view. Immunogenetics 55, 655–666. https://doi.org/10.1007/s00251-003-0625-2

Kwakkenbos, M.J., Pouwels, W., Matmati, M., Stacey, M., Lin, H.-H., Gordon, S., Lier, R.A.W.V., Hamann, J., 2005. Expression of the largest CD97 and EMR2 isoforms on leukocytes facilitates a specific interaction with chondroitin sulfate on B cells. Journal of Leukocyte Biology 77, 112–119. https://doi.org/10.1189/jlb.0704402

Lagerström, M.C., Schiöth, H.B., 2008. Structural diversity of G protein-coupled receptors and significance for drug discovery. Nat Rev Drug Discov 7, 339–357. https://doi.org/10.1038/nrd2518

Langenhan, T., 2019. Adhesion G protein–coupled receptors—Candidate metabotropic mechanosensors and novel drug targets. Basic & Clinical Pharmacology & Toxicology 0, 1–12. https://doi.org/10.1111/bcpt.13223

Langenhan, T., Aust, G., Hamann, J., 2013. Sticky signaling--adhesion class G protein-coupled receptors take the stage. Sci Signal 6, re3. https://doi.org/10.1126/scisignal.2003825

Latorraca, N.R., Venkatakrishnan, A.J., Dror, R.O., 2017. GPCR Dynamics: Structures in Motion. Chem. Rev. 117, 139–155. https://doi.org/10.1021/acs.chemrev.6b00177

Leemans, J.C., te Velde, A.A., Florquin, S., Bennink, R.J., de Bruin, K., van Lier, R.A.W., van der Poll, T., Hamann, J., 2004. The Epidermal Growth Factor-Seven Transmembrane (EGF-TM7) Receptor CD97 Is Required for Neutrophil Migration and Host Defense. J Immunol 172, 1125–1131. https://doi.org/10.4049/jimmunol.172.2.1125

Levitin, F., Stern, O., Weiss, M., Gil-Henn, C., Ziv, R., Prokocimer, Z., Smorodinsky, N.I., Rubinstein, D.B., Wreschner, D.H., 2005. The MUC1 SEA Module Is a Self-cleaving Domain. J. Biol. Chem. 280, 33374–33386. https://doi.org/10.1074/jbc.M506047200

Li, M.Z., Elledge, S.J., 2012. SLIC: A Method for Sequence- and Ligation-Independent Cloning, in: Peccoud, J. (Ed.), Gene Synthesis: Methods and Protocols, Methods in Molecular Biology. Humana Press, Totowa, NJ, pp. 51–59. https://doi.org/10.1007/978-1-61779-564-0_5

Liebscher, I., Schön, J., Petersen, S.C., Fischer, L., Auerbach, N., Demberg, L.M., Mogha, A., Cöster, M., Simon, K.-U., Rothemund, S., Monk, K.R., Schöneberg, T., 2014. A tethered agonist within the ectodomain activates the adhesion G protein-coupled receptors GPR126 and GPR133. Cell Rep 9, 2018–2026. https://doi.org/10.1016/j.celrep.2014.11.036

Liebscher, I., Schöneberg, T., 2016. Tethered Agonism: A Common Activation Mechanism of Adhesion GPCRs. Handb Exp Pharmacol 234, 111–125. https://doi.org/10.1007/978-3-319-41523-9_6

Lin, H.-H., Chang, G.-W., Davies, J.Q., Stacey, M., Harris, J., Gordon, S., 2004. Autocatalytic Cleavage of the EMR2 Receptor Occurs at a Conserved G Protein-coupled Receptor Proteolytic Site Motif. J. Biol. Chem. 279, 31823–31832. https://doi.org/10.1074/jbc.M402974200

Lin, H.-H., Hsiao, C.-C., Pabst, C., Hébert, J., Schöneberg, T., Hamann, J., 2017.

Adhesion GPCRs in Regulating Immune Responses and Inflammation, in: Advances in Immunology. Elsevier, pp. 163–201. https://doi.org/10.1016/bs.ai.2017.05.005

Lin, H.H., Stacey, M., Hamann, J., Gordon, S., McKnight, A.J., 2000. Human EMR2, a novel EGF-TM7 molecule on chromosome 19p13.1, is closely related to CD97. Genomics 67, 188–200. https://doi.org/10.1006/geno.2000.6238

Lin, H.-H., Stacey, M., Saxby, C., Knott, V., Chaudhry, Y., Evans, D., Gordon, S., McKnight, A.J., Handford, P., Lea, S., 2001. Molecular Analysis of the Epidermal Growth Factor-like Short Consensus Repeat Domain-mediated Protein-Protein Interactions DISSECTION OF THE CD97-CD55 COMPLEX. J. Biol. Chem. 276, 24160–24169. https://doi.org/10.1074/jbc.M101770200

Lin, H.-H., Stacey, M., Yona, S., Chang, G.-W., 2010. GPS Proteolytic Cleavage of Adhesion-GPCRs, in: Yona, S., Stacey, M. (Eds.), Adhesion-GPCRs. Springer US, Boston, MA, pp. 49–58. https://doi.org/10.1007/978-1-4419-7913-1_4

Lohse, M.J., 2010. Dimerization in GPCR mobility and signaling. Current Opinion in Pharmacology 10, 53–58. https://doi.org/10.1016/j.coph.2009.10.007

Lohse, M.J., Hoffmann, C., 2014. Arrestin Interactions with G Protein-Coupled Receptors, in: Gurevich, V.V. (Ed.), Arrestins - Pharmacology and Therapeutic Potential. Springer Berlin Heidelberg, Berlin, Heidelberg, pp. 15–56. https://doi.org/10.1007/978-3-642-41199-1_2

Low, S.H., Vasanth, S., Larson, C.H., Mukherjee, S., Sharma, N., Kinter, M.T., Kane, M.E., Obara, T., Weimbs, T., 2006. Polycystin-1, STAT6, and P100 Function in a Pathway that Transduces Ciliary Mechanosensation and Is Activated in Polycystic Kidney Disease. Developmental Cell 10, 57–69. https://doi.org/10.1016/j.devcel.2005.12.005

Lum, A.M., Wang, B.B., Beck-Engeser, G.B., Li, L., Channa, N., Wabl, M., 2010. Orphan receptor GPR110, an oncogene overexpressed in lung and prostate cancer. BMC Cancer 10, 40. https://doi.org/10.1186/1471-2407-10-40

Manglik, A., Kim, T.H., Masureel, M., Altenbach, C., Yang, Z., Hilger, D., Lerch, M.T., Kobilka, T.S., Thian, F.S., Hubbell, W.L., Prosser, R.S., Kobilka, B.K., 2015. Structural Insights into the Dynamic Process of β 2 -Adrenergic Receptor Signaling. Cell 161, 1101–1111. https://doi.org/10.1016/j.cell.2015.04.043

Martin, B.R., Giepmans, B.N.G., Adams, S.R., Tsien, R.Y., 2005. Mammalian cell–based optimization of the biarsenical-binding tetracysteine motif for improved fluorescence and affinity. Nat Biotechnol 23, 1308–1314. https://doi.org/10.1038/nbt1136

McKnight, A.J., Gordon, S., 1996. EGF-TM7: a novel subfamily of seven-transmembrane-region leukocyte cell-surface molecules. Immunol. Today 17, 283–

287.

McMahon, H.T., Missler, M., Li, C., Südhof, T.C., 1995. Complexins: Cytosolic proteins that regulate SNAP receptor function. Cell 83, 111–119. https://doi.org/10.1016/0092-8674(95)90239-2

Merrick, D., Bertuccio, C.A., Chapin, H.C., Lal, M., Chauvet, V., Caplan, M.J., 2014. Polycystin-1 cleavage and the regulation of transcriptional pathways. Pediatr Nephrol 29, 505–511. https://doi.org/10.1007/s00467-013-2548-y

Merrick, D., Chapin, H., Baggs, J.E., Yu, Z., Somlo, S., Sun, Z., Hogenesch, J.B., Caplan, M.J., 2012. The γ-Secretase Cleavage Product of Polycystin-1 Regulates TCF and CHOP-Mediated Transcriptional Activation through a p300-Dependent Mechanism. Developmental Cell 22, 197–210. https://doi.org/10.1016/j.devcel.2011.10.028

Miller, W.E., Lefkowitz, R.J., 2001. Expanding roles for β-arrestins as scaffolds and adapters in GPCR signaling and trafficking. Current Opinion in Cell Biology 13, 139–145. https://doi.org/10.1016/S0955-0674(00)00190-3

Miserey-Lenkei, S., Parnot, C., Bardin, S., Corvol, P., Clauser, E., 2002. Constitutive Internalization of Constitutively Active Angiotensin II AT $_{1A}$ Receptor Mutants Is Blocked by Inverse Agonists. J. Biol. Chem. 277, 5891–5901. https://doi.org/10.1074/jbc.M108398200

Mitchell, L.S., Colwell, L.J., 2018. Comparative analysis of nanobody sequence and structure data. Proteins 86, 697–706. https://doi.org/10.1002/prot.25497

Mogha, A., Benesh, A.E., Patra, C., Engel, F.B., Schoneberg, T., Liebscher, I., Monk, K.R., 2013. Gpr126 Functions in Schwann Cells to Control Differentiation and Myelination via G-Protein Activation. Journal of Neuroscience 33, 17976–17985. https://doi.org/10.1523/JNEUROSCI.1809-13.2013

Mohammad, S., Baldini, Giovanna, Granell, S., Narducci, P., Martelli, A.M., Baldini, Giulia, 2007. Constitutive Traffic of Melanocortin-4 Receptor in Neuro2A Cells and Immortalized Hypothalamic Neurons. J. Biol. Chem. 282, 4963–4974. https://doi.org/10.1074/jbc.M608283200

Moriguchi, T., Haraguchi, K., Ueda, N., Okada, M., Furuya, T., Akiyama, T., 2004. DREG, a developmentally regulated G protein-coupled receptor containing two conserved proteolytic cleavage sites. Genes Cells 9, 549–560. https://doi.org/10.1111/j.1356-9597.2004.00743.x

Morris, D.P., Price, R.R., Smith, M.P., Lei, B., Schwinn, D.A., 2004. Cellular Trafficking of Human α $_{1a}$ -Adrenergic Receptors Is Continuous and Primarily Agonist-Independent. Mol Pharmacol 66, 843–854. https://doi.org/10.1124/mol.104.000430

Müller, A., Winkler, J., Fiedler, F., Sastradihardja, T., Binder, C., Schnabel, R., Kungel,

J., Rothemund, S., Hennig, C., Schöneberg, T., Prömel, S., 2015. Oriented Cell Division in the C. elegans Embryo Is Coordinated by G-Protein Signaling Dependent on the Adhesion GPCR LAT-1. PLoS Genet. 11, e1005624. https://doi.org/10.1371/journal.pgen.1005624

Mumm, J.S., Schroeter, E.H., Saxena, M.T., Griesemer, A., Tian, X., Pan, D.J., Ray, W.J., Kopan, R., 2000. A Ligand-Induced Extracellular Cleavage Regulates γ-Secretase-like Proteolytic Activation of Notch1. Molecular Cell 5, 197–206. https://doi.org/10.1016/S1097-2765(00)80416-5

Nakanishi, J., Takarada, T., Yunoki, S., Kikuchi, Y., Maeda, M., 2006. FRET-based monitoring of conformational change of the β2 adrenergic receptor in living cells. Biochemical and Biophysical Research Communications 343, 1191–1196. https://doi.org/10.1016/j.bbrc.2006.03.064

Nazarko, O., Kibrom, A., Winkler, J., Leon, K., Stoveken, H., Salzman, G., Merdas, K., Lu, Y., Narkhede, P., Tall, G., Prömel, S., Araç, D., 2018. A Comprehensive Mutagenesis Screen of the Adhesion GPCR Latrophilin-1/ADGRL1. iScience 3, 264–278. https://doi.org/10.1016/j.isci.2018.04.019

Nieberler, M., Kittel, R.J., Petrenko, A.G., Lin, H.-H., Langenhan, T., 2016. Control of Adhesion GPCR Function Through Proteolytic Processing, in: Langenhan, T., Schöneberg, T. (Eds.), Adhesion G Protein-Coupled Receptors. Springer International Publishing, Cham, pp. 83–109. https://doi.org/10.1007/978-3-319-41523-9_5

Nijmeijer, S., Wolf, S., Ernst, O.P., de Graaf, C., 2016. 7TM Domain Structure of Adhesion GPCRs, in: Langenhan, T., Schöneberg, T. (Eds.), Adhesion G Protein-Coupled Receptors. Springer International Publishing, Cham, pp. 43–66. https://doi.org/10.1007/978-3-319-41523-9_3

Nikić, I., Estrada Girona, G., Kang, J.H., Paci, G., Mikhaleva, S., Koehler, C., Shymanska, N.V., Ventura Santos, C., Spitz, D., Lemke, E.A., 2016. Debugging Eukaryotic Genetic Code Expansion for Site-Specific Click-PAINT Super-Resolution Microscopy. Angew. Chem. Int. Ed. Engl. 55, 16172–16176. https://doi.org/10.1002/anie.201608284

Nikić, I., Kang, J.H., Girona, G.E., Aramburu, I.V., Lemke, E.A., 2015. Labeling proteins on live mammalian cells using click chemistry. Nat Protoc 10, 780–791. https://doi.org/10.1038/nprot.2015.045

Nirthanan, S., Gwee, M.C.E., 2004. Three-Finger α-Neurotoxins and the Nicotinic Acetylcholine Receptor, Forty Years On. J Pharmacol Sci 94, 1–17. https://doi.org/10.1254/jphs.94.1

Nuber, S., Zabel, U., Lorenz, K., Nuber, A., Milligan, G., Tobin, A.B., Lohse, M.J., Hoffmann, C., 2016. β-Arrestin biosensors reveal a rapid, receptor-dependent activation/deactivation cycle. Nature 531, 661–664.

https://doi.org/10.1038/nature17198

Okajima, D., Kudo, G., Yokota, H., 2010. Brain-specific angiogenesis inhibitor 2 (BAI2) may be activated by proteolytic processing. Journal of Receptors and Signal Transduction 30, 143–153. https://doi.org/10.3109/10799891003671139

Ormö, M., Cubitt, A.B., Kallio, K., Gross, L.A., Tsien, R.Y., Remington, S.J., 1996. Crystal structure of the Aequorea victoria green fluorescent protein. Science 273, 1392–1395. https://doi.org/10.1126/science.273.5280.1392

Paavola, K.J., Stephenson, J.R., Ritter, S.L., Alter, S.P., Hall, R.A., 2011. The N Terminus of the Adhesion G Protein-coupled Receptor GPR56 Controls Receptor Signaling Activity. J. Biol. Chem. 286, 28914–28921. https://doi.org/10.1074/jbc.M111.247973

Pennington, M.W., Czerwinski, A., Norton, R.S., 2018. Peptide therapeutics from venom: Current status and potential. Bioorganic & Medicinal Chemistry 26, 2738–2758. https://doi.org/10.1016/j.bmc.2017.09.029

Petersen, S.C., Luo, R., Liebscher, I., Giera, S., Jeong, S.-J., Mogha, A., Ghidinelli, M., Feltri, M.L., Schöneberg, T., Piao, X., Monk, K.R., 2015. The Adhesion GPCR GPR126 Has Distinct, Domain-Dependent Functions in Schwann Cell Development Mediated by Interaction with Laminin-211. Neuron 85, 755–769. https://doi.org/10.1016/j.neuron.2014.12.057

Piao, X., Hill, R.S., Bodell, A., Chang, B.S., Basel-Vanagaite, L., Straussberg, R., Dobyns, W.B., Qasrawi, B., Winter, R.M., Innes, A.M., Voit, T., Ross, M.E., Michaud, J.L., Déscarie, J.-C., Barkovich, A.J., Walsh, C.A., 2004. G protein-coupled receptor-dependent development of human frontal cortex. Science 303, 2033–2036. https://doi.org/10.1126/science.1092780

Prasher, D.C., Eckenrode, V.K., Ward, W.W., Prendergast, F.G., Cormier, M.J., 1992. Primary structure of the Aequorea victoria green-fluorescent protein. Gene 111, 229–233. https://doi.org/10.1016/0378-1119(92)90691-H

Prömel, S., Frickenhaus, M., Hughes, S., Mestek, L., Staunton, D., Woollard, A., Vakonakis, I., Schöneberg, T., Schnabel, R., Russ, A.P., Langenhan, T., 2012. The GPS motif is a molecular switch for bimodal activities of adhesion class G protein-coupled receptors. Cell Rep 2, 321–331. https://doi.org/10.1016/j.celrep.2012.06.015

Reiners, J., van Wijk, E., Märker, T., Zimmermann, U., Jürgens, K., te Brinke, H., Overlack, N., Roepman, R., Knipper, M., Kremer, H., Wolfrum, U., 2005. Scaffold protein harmonin (USH1C) provides molecular links between Usher syndrome type 1 and type 2. Hum. Mol. Genet. 14, 3933–3943. https://doi.org/10.1093/hmg/ddi417

Robinson, A., Escuin, S., Doudney, K., Vekemans, M., Stevenson, R.E., Greene, N.D.E., Copp, A.J., Stanier, P., 2012. Mutations in the planar cell polarity genes

CELSR1 and SCRIB are associated with the severe neural tube defect craniorachischisis. Hum. Mutat. 33, 440–447. https://doi.org/10.1002/humu.21662

Salzman, G.S., Ackerman, S.D., Ding, C., Koide, A., Leon, K., Luo, R., Stoveken, H.M., Fernandez, C.G., Tall, G.G., Piao, X., Monk, K.R., Koide, S., Araç, D., 2016. Structural Basis for Regulation of GPR56/ADGRG1 by Its Alternatively Spliced Extracellular Domains. Neuron 91, 1292–1304. https://doi.org/10.1016/j.neuron.2016.08.022

Salzman, G.S., Zhang, S., Gupta, A., Koide, A., Koide, S., Araç, D., 2017. *Stachel* -independent modulation of GPR56/ADGRG1 signaling by synthetic ligands directed to its extracellular region. Proc Natl Acad Sci USA 114, 10095–10100. https://doi.org/10.1073/pnas.1708810114

Scarselli, M., Donaldson, J.G., 2009. Constitutive Internalization of G Protein-coupled Receptors and G Proteins via Clathrin-independent Endocytosis. J. Biol. Chem. 284, 3577–3585. https://doi.org/10.1074/jbc.M806819200

Scholz, N., Ehmann, N., Sachidanandan, D., Imig, C., Cooper, B.H., Jahn, O., Reim, K., Brose, N., Meyer, J., Lamberty, M., Altrichter, S., Bormann, A., Hallermann, S., Pauli, M., Heckmann, M., Stigloher, C., Langenhan, T., Kittel, R.J., 2019. Complexin cooperates with Bruchpilot to tether synaptic vesicles to the active zone cytomatrix. J Cell Biol 218, 1011–1026. https://doi.org/10.1083/jcb.201806155

Scholz, N., Gehring, J., Guan, C., Ljaschenko, D., Fischer, R., Lakshmanan, V., Kittel, R.J., Langenhan, T., 2015. The adhesion GPCR latrophilin/CIRL shapes mechanosensation. Cell Rep 11, 866–874. https://doi.org/10.1016/j.celrep.2015.04.008

Scholz, N., Guan, C., Nieberler, M., Grotemeyer, A., Maiellaro, I., Gao, S., Beck, S., Pawlak, M., Sauer, M., Asan, E., Rothemund, S., Winkler, J., Prömel, S., Nagel, G., Langenhan, T., Kittel, R.J., 2017. Mechano-dependent signaling by Latrophilin/CIRL quenches cAMP in proprioceptive neurons. Elife 6. https://doi.org/10.7554/eLife.28360

Scholz, N., Monk, K.R., Kittel, R.J., Langenhan, T., 2016. Adhesion GPCRs as a Putative Class of Metabotropic Mechanosensors, in: Langenhan, T., Schöneberg, T. (Eds.), Adhesion G Protein-Coupled Receptors. Springer International Publishing, Cham, pp. 221–247. https://doi.org/10.1007/978-3-319-41523-9_10

Serfling, R., Lorenz, C., Etzel, M., Schicht, G., Böttke, T., Mörl, M., Coin, I., 2018. Designer tRNAs for efficient incorporation of non-canonical amino acids by the pyrrolysine system in mammalian cells. Nucleic Acids Res. 46, 1–10. https://doi.org/10.1093/nar/gkx1156

Sergin, I., Jong, Y.-J.I., Harmon, S.K., Kumar, V., O'Malley, K.L., 2017. Sequences within the C Terminus of the Metabotropic Glutamate Receptor 5 (mGluR5) Are Responsible for Inner Nuclear Membrane Localization. J. Biol. Chem. 292, 3637–3655. https://doi.org/10.1074/jbc.M116.757724

Shimomura, O., Johnson, F.H., Saiga, Y., 1962. Extraction, Purification and Properties of Aequorin, a Bioluminescent Protein from the Luminous Hydromedusan,Aequorea. J. Cell. Comp. Physiol. 59, 223–239. https://doi.org/10.1002/jcp.1030590302

Söderberg, O., Gullberg, M., Jarvius, M., Ridderstråle, K., Leuchowius, K.-J., Jarvius, J., Wester, K., Hydbring, P., Bahram, F., Larsson, L.-G., Landegren, U., 2006. Direct observation of individual endogenous protein complexes in situ by proximity ligation. Nat Methods 3, 995–1000. https://doi.org/10.1038/nmeth947

Southern, C., Cook, J.M., Neetoo-Isseljee, Z., Taylor, D.L., Kettleborough, C.A., Merritt, A., Bassoni, D.L., Raab, W.J., Quinn, E., Wehrman, T.S., Davenport, A.P., Brown, A.J., Green, A., Wigglesworth, M.J., Rees, S., 2013. Screening β-Arrestin Recruitment for the Identification of Natural Ligands for Orphan G-Protein–Coupled Receptors. J Biomol Screen 18, 599–609. https://doi.org/10.1177/1087057113475480

Stewart, B.A., Atwood, H.L., Renger, J.J., Wang, J., Wu, C.F., 1994. Improved stability of Drosophila larval neuromuscular preparations in haemolymph-like physiological solutions. J. Comp. Physiol. A 175, 179–191.

Stoveken, H.M., Hajduczok, A.G., Xu, L., Tall, G.G., 2015. Adhesion G protein-coupled receptors are activated by exposure of a cryptic tethered agonist. Proc. Natl. Acad. Sci. U.S.A. 112, 6194–6199. https://doi.org/10.1073/pnas.1421785112

Stryer, L., 1978. Fluorescence Energy Transfer as a Spectroscopic Ruler. Annu. Rev. Biochem. 47, 819–846. https://doi.org/10.1146/annurev.bi.47.070178.004131

Stumpf, A.D., Hoffmann, C., 2016. Optical probes based on G protein-coupled receptors - added work or added value?: GPCR sensors. British Journal of Pharmacology 173, 255–266. https://doi.org/10.1111/bph.13382

Toseland, C.P., 2013. Fluorescent labeling and modification of proteins. J Chem Biol 6, 85–95. https://doi.org/10.1007/s12154-013-0094-5

Trivedi, R.R., Bhattacharyya, S., 2012. Constitutive internalization and recycling of metabotropic glutamate receptor 5 (mGluR5). Biochemical and Biophysical Research Communications 427, 185–190. https://doi.org/10.1016/j.bbrc.2012.09.040

Trudel, M., Yao, Q., Qian, F., 2016. The Role of G-Protein-Coupled Receptor Proteolysis Site Cleavage of Polycystin-1 in Renal Physiology and Polycystic Kidney Disease. Cells 5, 3. https://doi.org/10.3390/cells5010003

van Ooij, C., 2009. Recipe for fluorescent antibodies: Immunofluorescence. Nat Cell Biol 11, S10–S11. https://doi.org/10.1038/ncb1932

van Tetering, G., Vooijs, M., 2011. Proteolytic cleavage of Notch: “HIT and RUN.” Curr. Mol. Med. 11, 255–269.

Vilardaga, J.-P., Bünemann, M., Krasel, C., Castro, M., Lohse, M.J., 2003.

Measurement of the millisecond activation switch of G protein–coupled receptors in living cells. Nat Biotechnol 21, 807–812. https://doi.org/10.1038/nbt838

Vilardaga, J.-P., Steinmeyer, R., Harms, G.S., Lohse, M.J., 2005. Molecular basis of inverse agonism in a G protein–coupled receptor. Nat Chem Biol 1, 25–28. https://doi.org/10.1038/nchembio705

Visser, L., de Vos, A.F., Hamann, J., Melief, M.-J., van Meurs, M., van Lier, R.A.W., Laman, J.D., Hintzen, R.Q., 2002. Expression of the EGF-TM7 receptor CD97 and its ligand CD55 (DAF) in multiple sclerosis. Journal of Neuroimmunology 132, 156–163. https://doi.org/10.1016/S0165-5728(02)00306-5

Volynski, K.E., Silva, J.-P., Lelianova, V.G., Atiqur Rahman, M., Hopkins, C., Ushkaryov, Y.A., 2004. Latrophilin fragments behave as independent proteins that associate and signal on binding of LTX(N4C). EMBO J. 23, 4423–4433. https://doi.org/10.1038/sj.emboj.7600443

Vu, T.-K.H., Hung, D.T., Wheaton, V.I., Coughlin, S.R., 1991. Molecular cloning of a functional thrombin receptor reveals a novel proteolytic mechanism of receptor activation. Cell 64, 1057–1068. https://doi.org/10.1016/0092-8674(91)90261-V

Wagh, D.A., Rasse, T.M., Asan, E., Hofbauer, A., Schwenkert, I., Dürrbeck, H., Buchner, S., Dabauvalle, M.-C., Schmidt, M., Qin, G., Wichmann, C., Kittel, R., Sigrist, S.J., Buchner, E., 2006. Bruchpilot, a Protein with Homology to ELKS/CAST, Is Required for Structural Integrity and Function of Synaptic Active Zones in Drosophila. Neuron 49, 833–844. https://doi.org/10.1016/j.neuron.2006.02.008

Wandel, E., Saalbach, A., Sittig, D., Gebhardt, C., Aust, G., 2012. Thy-1 (CD90) Is an Interacting Partner for CD97 on Activated Endothelial Cells. The Journal of Immunology 188, 1442–1450. https://doi.org/10.4049/jimmunol.1003944

Wang, S., Yoo, S., Kim, H., Wang, M., Zheng, C., Parkhouse, W., Krieger, C., Harden, N., 2015. Detection of In Situ Protein-protein Complexes at the Drosophila Larval Neuromuscular Junction Using Proximity Ligation Assay. J Vis Exp. https://doi.org/10.3791/52139

Wang, T., Ward, Y., Tian, L., Lake, R., Guedez, L., Stetler-Stevenson, W.G., Kelly, K., 2005. CD97, an adhesion receptor on inflammatory cells, stimulates angiogenesis through binding integrin counterreceptors on endothelial cells. Blood 105, 2836–2844. https://doi.org/10.1182/blood-2004-07-2878

Ward, Y., Lake, R., Yin, J.J., Heger, C.D., Raffeld, M., Goldsmith, P.K., Merino, M., Kelly, K., 2011. LPA receptor heterodimerizes with CD97 to amplify LPA-initiated RHO-dependent signaling and invasion in prostate cancer cells. Cancer Res. 71, 7301–7311. https://doi.org/10.1158/0008-5472.CAN-11-2381

Weis, W.I., Kobilka, B.K., 2018. The Molecular Basis of G Protein-Coupled Receptor

Activation. Annu. Rev. Biochem. 87, 897–919. https://doi.org/10.1146/annurev-biochem-060614-033910

Weston, M.D., Luijendijk, M.W.J., Humphrey, K.D., Möller, C., Kimberling, W.J., 2004. Mutations in the VLGR1 gene implicate G-protein signaling in the pathogenesis of Usher syndrome type II. Am. J. Hum. Genet. 74, 357–366. https://doi.org/10.1086/381685

Wilde, C., Fischer, L., Lede, V., Kirchberger, J., Rothemund, S., Schöneberg, T., Liebscher, I., 2016. The constitutive activity of the adhesion GPCR GPR114/ADGRG5 is mediated by its tethered agonist. FASEB J. 30, 666–673. https://doi.org/10.1096/fj.15-276220

Wilkins, M.E., Li, X., Smart, T.G., 2008. Tracking Cell Surface GABA $_B$ Receptors Using an α-Bungarotoxin Tag. J. Biol. Chem. 283, 34745–34752. https://doi.org/10.1074/jbc.M803197200

Woodward, O.M., Li, Y., Yu, S., Greenwell, P., Wodarczyk, C., Boletta, A., Guggino, W.B., Qian, F., 2010. Identification of a Polycystin-1 Cleavage Product, P100, That Regulates Store Operated Ca2+ Entry through Interactions with STIM1. PLoS ONE 5, e12305. https://doi.org/10.1371/journal.pone.0012305

Wu, J., Lei, L., Wang, S., Gu, D., Zhang, J., 2012. Immunohistochemical Expression and Prognostic Value of CD97 and Its Ligand CD55 in Primary Gallbladder Carcinoma. Journal of Biomedicine and Biotechnology 2012, 1–7. https://doi.org/10.1155/2012/587672

Yang, Li-yun, Liu, X., Yang, Y., Yang, Lin-lin, Liu, K., Tang, Y., Zhang, M., Tan, M., Cheng, S., Xu, Y., Yang, H., Liu, Z., Song, G., Huang, W., 2017. Biochemical features of the adhesion G protein-coupled receptor CD97 related to its auto-proteolysis and HeLa cell attachment activities. Acta Pharmacol Sin 38, 56–68. https://doi.org/10.1038/aps.2016.89

Yin, Y., Xu, X., Tang, J., Zhang, W., Zhangyuan, G., Ji, J., Deng, L., Lu, S., Zhuo, H., Sun, B., 2018. CD97 Promotes Tumor Aggressiveness Through the Traditional G Protein-Coupled Receptor-Mediated Signaling in Hepatocellular Carcinoma. Hepatology 68, 1865–1878. https://doi.org/10.1002/hep.30068

Zhang, C., Srinivasan, Y., Arlow, D.H., Fung, J.J., Palmer, D., Zheng, Y., Green, H.F., Pandey, A., Dror, R.O., Shaw, D.E., Weis, W.I., Coughlin, S.R., Kobilka, B.K., 2012. High-resolution crystal structure of human protease-activated receptor 1. Nature 492, 387–392. https://doi.org/10.1038/nature11701

Zhang, D.-L., Sun, Y.-J., Ma, M.-L., Wang, Y., Lin, H., Li, R.-R., Liang, Z.-L., Gao, Y., Yang, Z., He, D.-F., Lin, A., Mo, H., Lu, Y.-J., Li, M.-J., Kong, W., Chung, K.Y., Yi, F., Li, J.-Y., Qin, Y.-Y., Li, J., Thomsen, A.R.B., Kahsai, A.W., Chen, Z.-J., Xu, Z.-G., Liu, M., Li, D., Yu, X., Sun, J.-P., 2018. Gq activity- and β-arrestin-1 scaffolding-mediated

ADGRG2/CFTR coupling are required for male fertility. eLife 7, e33432. https://doi.org/10.7554/eLife.33432

Zhao, H.L., Yao, X.Q., Xue, C., Wang, Y., Xiong, X.H., Liu, Z.M., 2008. Increasing the homogeneity, stability and activity of human serum albumin and interferon-α2b fusion protein by linker engineering. Protein Expression and Purification 61, 73–77. https://doi.org/10.1016/j.pep.2008.04.013

Ziegler, N., Bätz, J., Zabel, U., Lohse, M.J., Hoffmann, C., 2011. FRET-based sensors for the human M1-, M3-, and M5-acetylcholine receptors. Bioorganic & Medicinal Chemistry 19, 1048–1054. https://doi.org/10.1016/j.bmc.2010.07.060

9 Appendix

9.1 Supplementary tables

Supp. Tab. 1: Plasmids provided by internal and external sources.

Receptor construct	Plasmid ID	Description	Vector backbone	Tags	Reference
Subclone	pTL444	Mouse G1	pcDps	HA/FLAG	Ines Liebscher
CIRL	pTL512	*Drosophila* CIRL with N-terminally fused SP of G1	pcDps	HA	Tobias Langenhan
F5-mVenus	pTL647	Mouse F5 with C-terminally fused mVenus	pHL-sec	-	Elena Seiradake
F5-mVenus	pTL654	Mouse F5 with C-terminally fused mVenus	pHL-sec	HA	Tobias Langenhan
CIRL-mVenus	pTL665	*Drosophila* CIRL with C-terminally fused mVenus	pHL-sec	HA/FLAG	Tobias Langenhan
EV	pTL671	Empty pHL-sec vector	pHL-sec	-	Tobias Langenhan
E5-EGFP	pTL675	Human E5 with C-terminally fused EGFP	pcDNA4	-	Tobias Langenhan
E5	pTL676	Human E5	pcDps	HA/V5	Gabriela Aust
Subclone	pTL685	Cleavage-deficient human $E5^{S>A}$ with C-terminally fused EGFP	pcDNA4	-	Tobias Langenhan
Subclone	pTL695	Cleavage-deficient human $E5^{H>A}$ with C-terminally fused EGFP	pcDNA4	-	Tobias Langenhan
$P2Y_{12}$-CIRL	pTL696	Fusion protein between *Drosophila* CIRL CTF and ECR of human $P2Y_{12}$ receptor	pcDps	HA/FLAG	Tobias Langenhan
$P2Y_{12}$-$CIRL^{\Delta TA}$	pTL697	Fusion protein between *Drosophila* CIRL CTF without TA and ECR of human $P2Y_{12}$ receptor	pcDps	HA/FLAG	Tobias Langenhan
Subclone	pTL720	Human E5 with TAG codon between EGF5 and GAIN	pcDps	HA/V5	Gerti Beliu
RS^{Lemke}	pTL781	$tRNA^{Pyl}$/$NESPylRS^{AF}$	pcDNA3.1	-	Nikić et al., 2016
Subclone	pTL840	Rat L1	pcDps	HA/FLAG	Simone Prömel

Receptor construct	Plasmid ID	Description	Vector backbone	Tags	Reference
Subclone	pMN17	Cleavage-deficient *Drosophila* CIRL$^{T>A}$ with N-terminally fused SP of G1	pcDps	HA	Matthias Nieberler
Subclone	pMH18	Cleavage-deficient *Drosophila* CIRL$^{H>A}$ with N-terminally fused SP of G1	pcDps	HA	Matthias Nieberler
EV	pSA2	Empty pcDps vector	pcDps	-	Tobias Langenhan
P2Y$_{12}$	pSA3	Human P2Y$_{12}$	pcDps	HA/FLAG	Ines Liebscher
α_{2A}AR-FlAsH-mTurq	pSA18	Mouse α_{2A}AR with FlAsH tag within the ICL3 and C-terminally fused mTurq	pcDNA3.1	-	Isabella Maiellaro
EV	pSA25	Empty pcDNA3.1 vector	pcDNA3.1	-	Isabella Maiellaro
mRFP	pSA75	mRFP under CMV promotor	unknown	-	Gerti Beliu
RS^{Coin}	pSA81	*Mb*PylRS^{F}/tRNA^{M15}	pcDNA3.1	-	Serfling et al., 2018
Subclone	pNH104	Cleavage-deficient *Drosophila* CIRL$^{T>A}$ with N-terminally mTurquoise and FlAsH tag within the ICL3	pcDps	-	Nicole Scholz
B3	pNH221	Human B3	pcDNA3.1	HA	Nicole Scholz
B3-TAG^{GPS+3}	pNH235	Human B3 with TAG codon within the GPS at position +3	pcDNA3.1	HA	Nicole Scholz
B3-TAG^{GPS+6}	pNH236	Human B3 with TAG codon within the GPS at position +6	pcDNA3.1	HA	Nicole Scholz
B3-TAG^{GPS+15}	pNH237	Human B3 with TAG codon within the GPS at position +15	pcDNA3.1	HA	Nicole Scholz
Subclone	pIB8	Human E2	pcDNA3.1	HA	Ina Brauer
CIRL	pJT2	*Drosophila* CIRL with N-terminally fused SP of G1	pcDNA3.1	HA	Johanna Irmer

Supp. Tab. 2: Plasmids generated and used in this thesis.

Receptor construct	Plasmid ID	Description	Tags	Construction	Primers used
Constructs listed below were cloned into pcDps vector backbone					
mTurq^{a}-E5	pSA6	Human E5 with mTurq (+ AAAA linkers) between EGF5 and GAIN (DMTF…STWT)	HA/V5	SLIC of pTL676 (B) and pNH104 (I)	sa_12F, sa_13R (B) sa_14F, sa_15R (I)
mTurq^{b}-E5	pSA7	Human E5 with mTurq (+ AAAA linkers) between EGF5 and GAIN (SLPK…GPFT)	HA/V5	SLIC of pTL676 (B) and pNH104 (I)	sa_16F, sa_17R (B) sa_18F, sa_19R (I)
mTurq^{a}-E5$^{H>A}$	pSA8	Cleavage-deficient human E5$^{H>A}$ with mTurq (+ AAAA linkers) between EGF5 and GAIN (DMTF…STWT)	HA/V5	Ligation: 0.2 kb fragment of pTL695 and 6 kb fragment of pSA6 (AarI)	
mTurq^{b}-E5$^{H>A}$	pSA9	Cleavage-deficient human E5$^{H>A}$ with mTurq (+ AAAA linkers) between EGF5 and GAIN (SLPK…GPFT)	HA/V5	Ligation: 0.2 kb fragment of pTL695 and 6 kb fragment of pSA7 (AarI)	
Subclone	pSA14	Cleavage-deficient human E5$^{S>A}$ with TAG codon within the NTF	HA/V5	Ligation: 4.2 kb fragment of pTL720 and 1.3 kb fragment from pTL685 (EvoRV/SbfI)	
Subclone	pSA15	Cleavage-deficient human E5$^{H>A}$ with TAG codon within the NTF	HA/V5	Ligation: 4.2 kb fragment of pTL720 and 1.3 kb fragment from pTL695 (EvoRV/SbfI)	
Subclone	pSA16	Fragment of E5 in pMSC5 backbone with FlAsH tag within the ICL3	V5	Ligation: 3.5 kb fragment of pSA11 (B) and annealed primers (I)	sa_47F, sa_48R (B) sa_49F, sa_50R (I)
E5-FlAsH	pSA19	Human E5 with FlAsH tag within the ICL3 (LTQK…KKLK)	HA/V5	Ligation: 0.45 kb fragment of pSA16 and 5.1 kb fragment of pTL676 (EcoRI/EagI)	
mTurq^{a}-E5-FlAsH	pSA20	Human E5 with mTurq (+ AAAA linkers) between EGF5 and GAIN (DMTF…STWT), and FlAsH tag within the ICL3 (LTQK…KKLK)	HA/V5	Ligation: 0.45 kb fragment of pSA16 and 5.1 kb fragment of pSA6 (EcoRI/EagI)	
mTurq^{a}-E5$^{H>A}$-FlAsH	pSA21	Cleavage-deficient human E5$^{H>A}$ with mTurq (+ AAAA linkers) between EGF5 and GAIN (DMTF…STWT), and FlAsH tag within the ICL3 (LTQK…KKLK)	HA/V5	Ligation: 0.45 kb fragment of pSA16 and 5.1 kb fragment of pSA8 (EcoRI & EagI)	

Receptor construct	Plasmid ID	Description	Tags	Construction	Primers used
Constructs listed below were cloned into pcDNA3.1 vector backbone (pages 134 – 140)					
E5	pSA26	Human E5	HA/V5	Ligation: 2.3 kb fragment of pTL676 (KpnI/SpeI) and 5.3 kb fragment of pSA25 (KpnI/XbaI)	
E5$^{S>A}$	pSA27	Cleavage-deficient human E5$^{S>A}$	HA/V5	Ligation: 1.3 kb fragment of pSA14 and 6.3 kb fragment of pSA26 (EcoRV/SbfI)	
E5$^{H>A}$	pSA28	Cleavage-deficient human E5$^{H>A}$	HA/V5	Ligation: 1.3 kb fragment of pSA15 and 6.3 kb fragment of pSA26 (EcoRV/SbfI)	
E5-TAG^{NTF}	pSA29	Human E5 with TAG codon within the NTF	HA/V5	Ligation: 2.3 kb fragment of pTL720 (KpnI/SpeI) and 5.3 kb fragment of pSA25 (KpnI/XbaI)	
CIRL$^{T>A}$	pSA30	Cleavage-deficient *Drosophila* CIRL$^{T>A}$ with N-terminally fused SP of G1	HA	Ligation: 2.6 kb fragment of pMN17 and 5.7 kb fragment of pTL512 (KpnI/NheI)	
CIRL$^{H>A}$	pSA31	Cleavage-deficient *Drosophila* CIRL$^{H>A}$ with N-terminally fused SP of G1	HA	Ligation: 2.6 kb fragment of pMN18 and 5.7 kb fragment of pTL512 (KpnI/NheI)	
E5-TAG^{ECL1}	pSA32	Human E5 with TAG codon within the ECL1 (GGQV…GLRC)	HA/V5	Insertion of TAG via SDM in pSA26	sa_51F, sa_52R
E5-TAG^{ECL2}	pSA33	Human E5 with TAG codon within the ECL2 (GRPR…YCWL)	HA/V5	Insertion of TAG via SDM in pSA26	sa_53F, sa_54R
E5-TAG^{ECL3}	pSA34	Human E5 with TAG codon within the ECL3 (FIFD…DRSL)	HA/V5	Insertion of TAG via SDM in pSA26	sa_55F, sa_56R
mTurq-E5	pSA35	Human E5 with mTurq instead of EGF5 (NTCQ…DMTF)	HA/V5	SLIC of pSA26 (B) and pSA6 (I)	sa_57F, sa_58R (B) sa_59F, sa_60R (I)
mTurq-E5-TAG^{ECL1}	pSA36	Human E5 with mTurq instead of EGF5 (NTCQ…DMTF) and TAG codon within the ECL1 (GGQV…GLRC)	HA/V5	Ligation: 1.3 kb fragment of pSA35 and 6.9 kb fragment of pSA32 (KpnI/EcoRV)	

Receptor construct	Plasmid ID	Description	Tags	Construction	Primers used
mTurq-E5-TAG^{ECL2}	pSA37	Human E5 with mTurq instead of EGF5 (NTCQ…DMTF) and TAG codon within the ECL2 (GRPR…YCWL)	HA/V5	Ligation: 1.3 kb fragment of pSA35 and 6.9 kb fragment of pSA33 (KpnI/EcoRV)	
mTurq-E5-TAG^{ECL3}	pSA38	Human E5 with mTurq instead of EGF5 (NTCQ…DMTF) and with TAG codon within the ECL3 (FIFD…DRSL)	HA/V5	Ligation: 1.3 kb fragment of pSA35 and 6.9 kb fragment of pSA34 (KpnI/EcoRV)	
E5$^{S>A}$-TAG^{ECL1}	pSA39	Cleavage-deficient human E5$^{S>A}$ with TAG codon within the ECL1 (GGQV…GLRC)	HA/V5	Insertion of TAG via SDM in pSA27	sa_51F, sa_52R
E5$^{S>A}$-TAG^{ECL2}	pSA40	Cleavage-deficient human E5$^{S>A}$ with TAG codon within the ECL2 (GRPR…YCWL)	HA/V5	Insertion of TAG via SDM in pSA27	sa_53F, sa_54R
E5$^{S>A}$-TAG^{ECL3}	pSA41	Cleavage-deficient human E5$^{S>A}$ with TAG codon within the ECL3 (FIFD…DRSL)	HA/V5	Insertion of TAG via SDM in pSA27	sa_55F, sa_56R
E5$^{H>A}$-TAG^{ECL1}	pSA42	Cleavage-deficient human E5$^{H>A}$ with TAG codon within the ECL1 (GGQV…GLRC)	HA/V5	Insertion of TAG via SDM in pSA28	sa_51F, sa_52R
E5$^{H>A}$-TAG^{ECL2}	pSA43	Cleavage-deficient human E5$^{H>A}$ with TAG codon within the ECL2 (GRPR…YCWL)	HA/V5	Insertion of TAG via SDM in pSA28	sa_53F, sa_54R
E5$^{H>A}$-TAG^{ECL3}	pSA44	Cleavage-deficient human E5$^{H>A}$ with TAG codon within the ECL3 (FIFD…DRSL)	HA/V5	Insertion of TAG via SDM in pSA28	sa_55F, sa_56R
E5$^{\Delta HA}$	pSA45	Human E5 without N-terminal HA tag	V5	Self-ligation of the inverse PCR product of pSA26	sa_61F, sa_62R
E5	pSA46	Human E5	HA/V5	Ligation: 0.16 kb fragment of pSA27 and 7.5 kb fragment of pSA26 (BamHI)	
E5$^{\Delta HA}$-TAG^{NTF}	pSA49	Human E5 with TAG codon within the NTF, and without N-terminal HA tag	V5	Self-ligation of the inverse PCR product of pSA29	sa_61F, sa_62R
E5-TAG^{GPS+6}	pSA50	Human E5 with TAG codon within the GPS at position +6	HA/V5	Substitution of L to TAG codon at GPS+6 via SDM in pSA46	sa_67F, sa_68R

Receptor construct	Plasmid ID	Description	Tags	Construction	Primers used
E5-TAG^{GPS+15}	pSA51	Human E5 with TAG codon within the GPS at position +15	HA/V5	Substitution of W to TAG codon at GPS+15 via SDM in pSA46	sa_69F, sa_70R
E5-TAG^{GPS+3}	pSA52	Human E5 with TAG codon within the GPS at position +3	HA/V5	Substitution of F to TAG codon at GPS+3 via SDM in pSA46	sa_65F, sa_66R
E5$^{S>A}$-TAG^{NTF}	pSA58	Cleavage-deficient human E5$^{S>A}$ with TAG codon within the NTF	HA/V5	Ligation: 1.5 kb fragment of pSA27 and 6.2 kb fragment of pSA29 (EcoRI/EcoRV)	
E5$^{H>A}$-TAG^{NTF}	pSA59	Cleavage-deficient human E5$^{H>A}$ with TAG codon within the NTF	HA/V5	Ligation: 1.5 kb fragment of pSA28 and 6.2 kb fragment of pSA29 (EcoRI/EcoRV)	
E5-mTurq	pSA78	Human E5 with mTurq within the ICL3 (KFSE…INPD)	HA/V5	SLIC of pSA46 (B) and pSA35 (I)	sa_108F, sa_109R (B) sa_110F, sa_111R (I)
Subclone	pSA82	Human E5 with mTurq within the ICL3 (KFSE…INPD) and Cit instead of V5 tag in the ICR (EYRK…WACL)	HA	SLIC of pSA78 (B) and pNH178 (I)	sa_112F, sa_113R (B) sa_114F, sa_115R (I)
E5-mTurq-mCit	pSA91	Human E5 with mTurq within the ICL3 (KFSE…INPD) and mCit instead of V5 tag in the ICR (EYRK…WACL)	HA	Exchange of A > K (mCit) via SDM of pSA82	sa_124F, sa_125R
CIRL-TAG^{NTF}	pSA92	*Drosophila* CIRL with N-terminally fused SP of G1 and TAG codon within the NTF	HA	Insertion of TAG via SDM in pJT2	sa_126F, sa_127R
Subclone	pSA95	CTF of human E5	HA/V5	Self-ligation of the inverse PCR product of pSA26	sa_131F, sa_133R
E5$^{\Delta NTF}$-mTurq-mCit	pSA103	E5 CTF with mTurq within the ICL3 (KFSE…INPD) and mCit instead of V5 tag in the ICR (EYRK…WACL)	HA	Ligation: 3.1 kb fragment of pSA91 and 4.7 kb fragment of pSA95 Fragment (EagI)	
E5-mCit	pSA104	Human E5 with mCit instead of V5 tag in the ICR (EYRK…WACL)	HA	Self-ligation of the inverse PCR product of pSA91	sa_134F, sa_135R

Receptor construct	Plasmid ID	Description	Tags	Construction	Primers used
E5-BBS$^{ECL1/I+R-L}$	pSA105	Human E5 with BBS within the ECL1 (LAGI…VAGL) via substitution	HA/V5	Synthesized by GenScript based on pSA46	
E5-BBS$^{ECL1/I+R+L}$	pSA106	Human E5 with BBS (+ GGGGS linkers) within the ECL1 (LAGI…VAGL) via substitution	HA/V5	Synthesized by GenScript based on pSA46	
E5-BBS$^{ECL1/I-R-L}$	pSA107	Human E5 with BBS within the ECL1 (GGQV…GLRC) via insertion	HA/V5	Synthesized by GenScript based on pSA46	
E5-BBS$^{ECL1/I-R+L}$	pSA108	Human E5 with BBS (+ GGGGS linkers) within the ECL1 (GGQV…GLRC) via insertion	HA/V5	Synthesized by GenScript based on pSA46	
E5-BBS$^{ECL2/I+R-L}$	pSA109	Human E5 with BBS within the ECL2 (IYSK…QGFL) via substitution	HA/V5	Synthesized by GenScript based on pSA46	
E5-BBS$^{ECL2/I+R+L}$	pSA110	Human E5 with BBS (+ GGGGS linkers) within the ECL2 (IYSK…QGFL) via substitution	HA/V5	Synthesized by GenScript based on pSA46	
E5-BBS$^{ECL2/I-R-L}$	pSA111	Human E5 with BBS within the ECL2 (GRPR…YCWL) via insertion	HA/V5	Synthesized by GenScript based on pSA46	
E5-BBS$^{ECL2/I-R+L}$	pSA112	Human E5 with BBS (+ GGGGS linkers) within the ECL2 (GRPR…YCWL) via insertion	HA/V5	Synthesized by GenScript based on pSA46	
E5-BBS$^{ECL3/I+R-L}$	pSA113	Human E5 with BBS within the ECL3 (VFGL…LTYF) via substitution	HA/V5	Synthesized by GenScript based on pSA46	
E5-BBS$^{ECL3/I+R+L}$	pSA114	Human E5 with BBS (+ GGGGS linkers) within the ECL3 (VFGL…LTYF) via substitution	HA/V5	Synthesized by GenScript based on pSA46	
E5-BBS$^{ECL3/I-R-L}$	pSA115	Human E5 with BBS within the ECL3 (FIFD…DRSL) via insertion	HA/V5	Synthesized by GenScript based on pSA46	
E5-BBS$^{ECL3/I-R+L}$	pSA116	Human E5 with BBS (+ GGGGS linkers) within the ECL3 (FIFD…DRSL) via insertion	HA/V5	Synthesized by GenScript based on pSA46	
G1	pSA117	Mouse G1	HA/FLAG	Ligation: 2.1 kb fragment of pTL444 (SpeI) and 5.4 kb fragment of pSA25 (XbaI)	
E5$^{H>A}$-TAG^{NTF}-TCS	pSA119	Cleavage-deficient human E5$^{H>A}$ with TAG codon within the NTF and TCS between TA and TM1	HA/V5	Synthesized by GenScript based on pSA59	
mTurq- E5-BBS$^{ECL1/I-R+L}$	pSA125	Human E5 with BBS (+ GGGGS linkers) within the ECL1 (GGQV…GLRC) via insertion	HA/V5	Ligation: 1.3 kb fragment of pSA35 and 7 kb fragment of pSA108 (KpnI/EcoRV)	

Receptor construct	Plasmid ID	Description	Tags	Construction	Primers used
mTurq- E5-BBS$^{ECL2/I-R+L}$	pSA126	Human E5 with BBS (+ GGGGS linkers) within the ECL2 (GRPR…YCWL) via insertion	HA/V5	Ligation: 1.3 kb fragment of pSA35 and 7 kb fragment of pSA112 (KpnI/EcoRV)	
mTurq- E5-BBS$^{ECL3/I-R+L}$	pSA127	Human E5 with BBS (+ GGGGS linkers) within the ECL3 (FIFD…DRSL) via insertion	HA/V5	Ligation: 1.3 kb fragment of pSA35 and 7 kb fragment of pSA116 (KpnI/EcoRV)	
E5$^{F>A}$-mTurq-mCit	pSA128	Human E5 with mTurq within the ICL3 (KFSE…INPD) and mCit instead of V5 tag in the ICR (EYRK…WACL), mutated TA	HA	Substitution of F to A at GPS+3 via SDM in pSA91	sa_153F, sa_154R
E5$^{M>A}$-mTurq-mCit	pSA129	Human E5 with mTurq within the ICL3 (KFSE…INPD) and mCit instead of V5 tag in the ICR (EYRK…WACL), mutated TA	HA	Substitution of M to A at GPS+7 via SDM in pSA91	sa_155F, sa_156R
E5$^{\Delta NTF\ F>A}$-mTurq-mCit	pSA130	Human E5 CTF with mTurq within the ICL3 (KFSE…INPD) and mCit instead of V5 tag in the ICR (EYRK…WACL), mutated TA	HA	Substitution of F to A at GPS+3 via SDM in pSA103	sa_157F, sa_158R
E5$^{\Delta NTF\ M>A}$-mTurq-mCit	pSA131	Human E5 CTF with mTurq within the ICL3 (KFSE…INPD) and mCit instead of V5 tag in the ICR (EYRK…WACL), mutated TA	HA	Substitution of M to A at GPS+7 via SDM in pSA103	sa_155F, sa_156R
L1	pSA132	Rat L1	HA/FLAG	SLIC of pSA25 (B) and pTL840 (I)	sa_163F, sa_164R (B) sa_165F, sa_166R (I)
G1-TAG^{NTF}	pSA133	Mouse G1 with a TAG codon within the NTF	HA/FLAG	Synthesized by GenScript based on pSA117	
G1-TAG^{GPS+3}	pSA134	Mouse G1 with a TAG codon within the GPS at position +3	HA/FLAG	Synthesized by GenScript based on pSA117	
G1-TAG^{GPS+6}	pSA135	Mouse G1 with a TAG codon within the GPS at position +6	HA/FLAG	Synthesized by GenScript based on pSA117	
G1-TAG^{GPS+18}	pSA136	Mouse G1 with a TAG codon within the GPS at position +18	HA/FLAG	Synthesized by GenScript based on pSA117	
E5$^{\Delta ECR}$-mTurq-mCit	pSA143	Human E5 CTF without TA, with mTurq within the ICL3 (KFSE…INPD) and mCit instead of V5 tag in the ICR (EYRK…WACL)	HA	Synthesized by GenScript based on pSA103	
Subclone	pSA147	Cleavage-deficient human E5$^{H>A}$ with TAG codon within the NTF and TEV cleavage site (+ GGGGS linker) between TA and TM1	HA/V5	Synthesized by GenScript based on pSA59	
L1-TAG^{GPS+3}	pSA160	Rat L1 with TAG codon within the GPS at position +3	HA/FLAG	Synthesized by GenScript based on pSA132	

Receptor construct	Plasmid ID	Description	Tags	Construction	Primers used
L1-TAG^{GPS+6}	pSA161	Rat L1 with TAG codon within the GPS at position +6	HA/FLAG	Synthesized by GenScript based on pSA132	
L1-TAG^{GPS+15}	pSA162	Rat L1 with TAG codon within the GPS at position +15	HA/FLAG	Synthesized by GenScript based on pSA132	
E2	pSA168	Human E2	HA	Synthesized by GenScript based on pIB8	
E2-TAG^{GPS+3}	pSA170	Human E2 with TAG codon within the GPS at position +3	HA	Synthesized by GenScript based on pIB8	
E2-TAG^{GPS+6}	pSA171	Human E2 with TAG codon within the GPS at position +6	HA	Synthesized by GenScript based on pIB8	
E2-TAG^{GPS+17}	pSA172	Human E2 with TAG codon within the GPS at position +17	HA	Synthesized by GenScript based on pIB8	
E2^{C492Y}	pSA173	Human E2 with VBU mutation	HA	Synthesized by GenScript based on pIB8	
E2 ^{C492Y}-TAG^{GPS+3}	pSA175	Human E2 with TAG codon within the GPS at position +3	HA	Synthesized by GenScript based on pIB8	
E2 ^{C492Y}-TAG^{GPS+6}	pSA176	Human E2 with TAG codon within the GPS at position +6	HA	Synthesized by GenScript based on pIB8	
E2 ^{C492Y}-TAG^{GPS+17}	pSA177	Human E2 with TAG codon within the GPS at position +17	HA	Synthesized by GenScript based on pIB8	
E5$^{H>A}$-TEV^{Linker}	pSA181	Cleavage-deficient human E5$^{H>A}$ with TEV cleavage site (+ GGGGS linkers) between TA and TM1	HA/V5	Ligation: 0.8 kb fragment of pSA26 and 7 kb fragment of pSA147 (EcoRV/KpnI)	
E5$^{S>A}$-mTurq-mCit	pSA184	Cleveage-deficient human E5$^{S>A}$ with mTurq within the ICL3 (KFSE…INPD) and mCit instead of V5 tag in the ICR (EYRK…WACL)	HA	Ligation: 3.1 kb fragment of pSA91 and 5.9 kDa fragment of pSA27 (EagI)	
E5$^{H>A}$-mTurq-mCit	pSA185	Cleveage-deficient human E5$^{H>A}$ with mTurq within the ICL3 (KFSE…INPD) and mCit instead of V5 tag in the ICR (EYRK…WACL)	HA	Ligation: 3.1 kb fragment of pSA91 and 5.9 kDa fragment of pSA28 (EagI)	
E5$^{\Delta NTF}$-mTurq	pSA188	Human E5 CTF with mTurq within the ICL3 (KFSE…INPD)	HA/V5	Ligation: 4.7 kb fragment of pSA103 and 2.4 kb fragment of pSA78 (EagI)	

Receptor construct	Plasmid ID	Description	Tags	Construction	Primers used
E5$^{\Delta NTF}$-mCit	pSA189	Human E5 CTF with mCit instead of V5 tag in the ICR (EYRK…WACL)	HA	Ligation: 4.7 kb fragment of pSA103 and 2.4 kb fragment of pSA104 (EagI)	
E5$^{\Delta ECR}$-mTurq	pSA190	Human E5 CTF without TA, with mTurq within the ICL3 (KFSE…INPD)	HA/V5	Ligation: 4.7 kb fragment of pSA143 and 2.4 kb fragment of pSA78 (EagI)	
E5$^{\Delta ECR}$-mCit	pSA191	Human E5 CTF without TA, with mCit instead of V5 tag in the ICR (EYRK…WACL)	HA	Ligation: 4.7 kb fragment of pSA143 and 2.4 kb fragment of pSA104 (EagI)	

Supp. Tab. 3: Primers used for cloning and their nucleotide sequence.

Primer ID	Sequence (5' > 3')
sa_12F	TCCACCTGGACCCCGCCCCC
sa_13R	GAAAGTCATATCTTCACAGA
sa_14F	CACTGTCTGTGAAGATATGACTTTCGCTGCTGCAGCTATGGTGAG
sa_15R	CTCCAGGGGGCGGGGTCCAGGTGGAAGCCGCTGCAGCCTTGTACA
sa_16F	GGCCCCTTCACCTACATTTC
sa_17R	TTTAGGCAGGCTCTTGGCCA
sa_18F	GATCCTGGCCAAGAGCCTGCCTAAAGCTGCTGCAGCTATGGTGAG
sa_19R	AAGGGGAAATGTAGGTGAAGGGGCCAGCCGCTGCAGCCTTGTACA
sa_47F	AAGAAATTAAAGAAGGCGAGGGCGC
sa_48R	CTTCTGAGTGAGCTTCCAGACGGTA
sa_49F	GAGAGCCAGTGTTGTCCGGGGTGTTGTGCACGGTCC
sa_50R	GGACCGTGCACAACACCCCGGACAACACTGGCTCTC
sa_51F	GCGGCCAGGTGTAGGGGCTGCGCTG
sa_52R	CAGCGCAGCCCCTACACCTGGCCGC
sa_53F	CGGCCGCCCCAGATAGTACTGCTGGTTGG
sa_54R	CCAACCAGCAGTACTATCTGGGGCGGCCG
sa_55F	CCTGTTCATCTTCGACTAGGATCGGAGCTTGGTGC
sa_56R	GCACCAAGCTCCGATCCTAGTCGAAGATGAACAGG
sa_57F	GATATGACTTTCTCCACCTG
sa_58R	TTGACAGGTGTTCTCGCTCT
sa_59F	GAATGAGAGCGAGAACACCTGTCAAGTGAGCAAGGGCGAGGAGCT
sa_60R	GGGTCCAGGTGGAGAAAGTCATATCCTTGTACAGCTCGTCCATGC
sa_61F	CAGGACTCCAGGGGCTGTGC
sa_62R	GGTTTCAGCTCCCGGCAGAG
sa_65F	CACCTGAGCAGCTAGGCGATCCTTATGGC
sa_66R	GCCATAAGGATCGCCTAGCTGCTCAGGTG
sa_67F	CTGAGCAGCTTTGCGATCTAGATGGCTCATTATGACGTG
sa_68R	CACGTCATAATGAGCCATCTAGATCGCAAAGCTGCTCAG
sa_69F	GACGTGGAGGACTAGAAGCTGACCCTG
sa_70R	CAGGGTCAGCTTCTAGTCCTCCACGTC
sa_108F	ATCAATCCAGACATGAAGAAATTAAAGAAGGCGAGGG

Primer ID	Sequence (5’ > 3’)
sa_109R	TTCAGAAAACTTCTGAGTGAGCTTCCAGACGG
sa_110F	GAAGCTCACTCAGAAGTTTTCTGAAGTGAGCAAGGGCGAGGAGCT
sa_111R	TTAATTTCTTCATGTCTGGATTGATCTTGTACAGCTCGTCCATGC
sa_112F	TGGGCCTGCCTAGTTGCTG
sa_113R	CTTCCGGTATTCTTCCCGAACCTTC
sa_114F	GAAGGTTCGGGAAGAATACCGGAAGGTGAGCAAGGGCGAGGAGCT
sa_115R	TCCCCCCAGCAACTAGGCAGGCCCACTTGTACAGCTCGTCCATGC
sa_124F	CTGAGCTACCAGTCCAAGCTGAGCAAAGACCCC
sa_125R	GGGGTCTTTGCTCAGCTTGGACTGGTAGCTCAG
sa_126F	CCAGTCCGCCGTAGCCATGGGTGCTG
sa_127R	CAGCACCCATGGCTACGGCGGACTGG
sa_131F	AGCAGCTTTGCGATCCTTATGGC
sa_133R	GGCGTAGTCGGGGACGTC
sa_134F	ATCAATCCAGACATGAAGAAATTAAAGAAG
sa_135R	TTCAGAAAACTTCTGAGTGAGCTTC
sa_153F	CACCTGAGCAGCGCTGCGATCCTTATG
sa_154R	CATAAGGATCGCAGCGCTGCTCAGGTG
sa_155F	GCAGCTTTGCGATCCTTGCTGCTCATTATGACGTGG
sa_156R	CCACGTCATAATGAGCAGCAAGGATCGCAAAGCTGC
sa_157F	CTACGCCAGCAGCGCTGCGATCCTTATG
sa_158R	CATAAGGATCGCAGCGCTGCTGGCGTAG
sa_163F	GAATTCTGCAGATATCCATCACACTGGCGG
sa_164R	AAGCTTGGGTCTCCCTATAGTGAGTCG
sa_165F	ACTCACTATAGGGAGACCCAAGCTTGCCACCATGGCCCGCTTG
sa_166R	AGTGTGATGGATATCTGCAGAATTCTTACTTATCGTCGTCATCCTTGTAATCACC

9.2 Supplementary figures

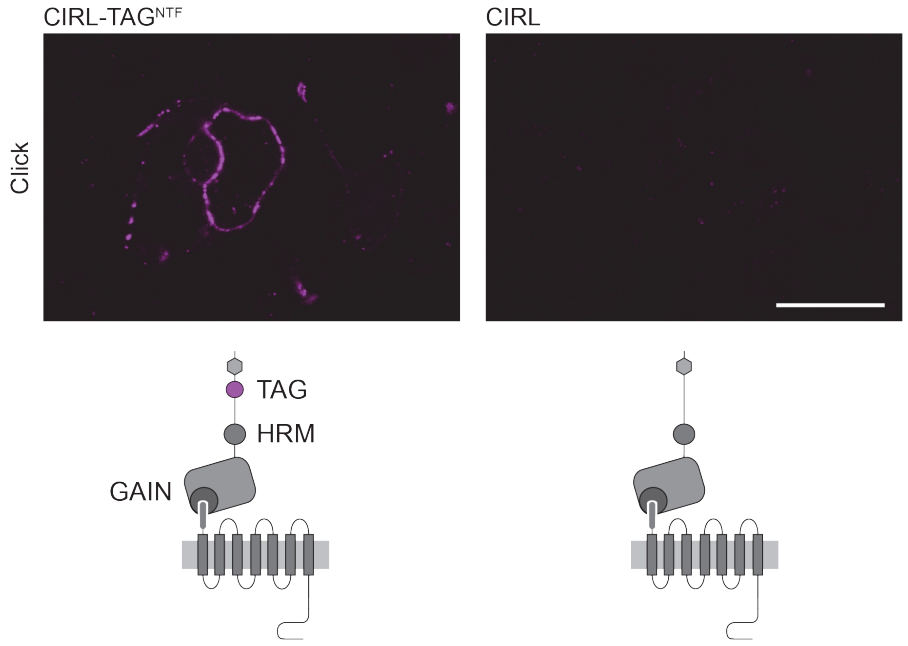

Supp. Fig. 1: Bioorthogonal labeling confirms the surface expression of CIRL in HEK-293T cells.

Confocal images of HEK-293T cells expressing CIRL-TAG^{NTF}. Untagged CIRL serves as labeling control. Cells were labeled using H-Tet-Cy5. Used Pyl$^{RS/}$tRNA^{Pyl} system: RS$_{Coin}$. Scale bar 20 µm.

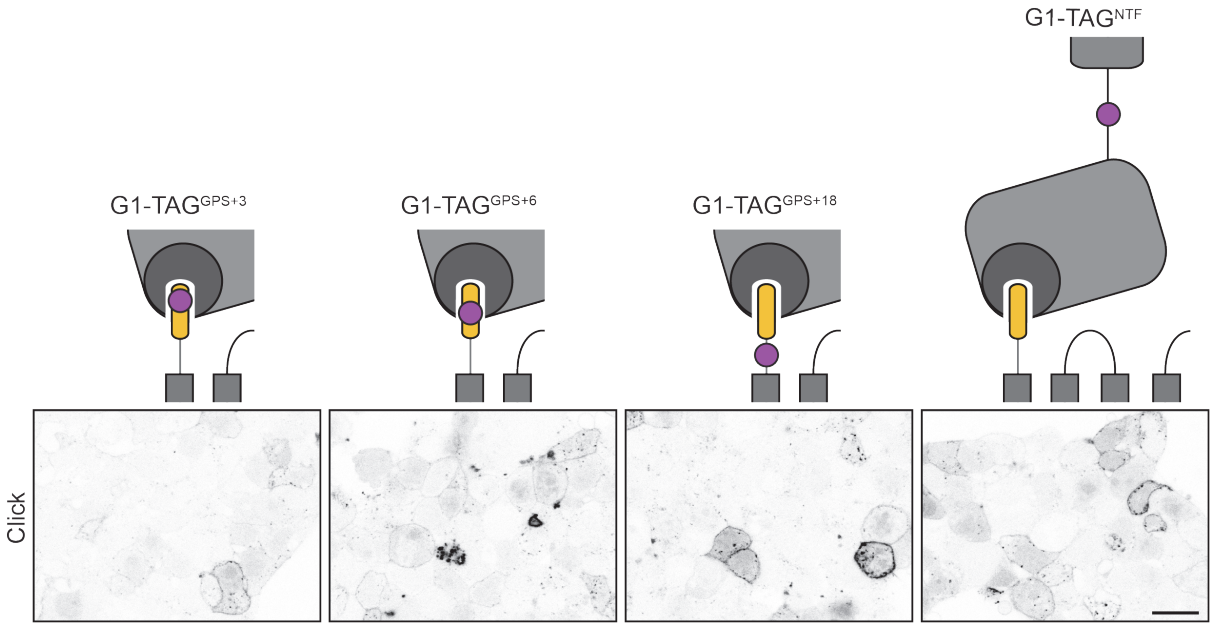

Supp. Fig. 2: Bioorthogonal labeling confirms the TA accessibility of G1.

Confocal images of HEK-293T cells expressing G1 variants (indicated above). Untagged G1 serves as labeling control. Cells were labeled using H-Tet-Cy5. Used Pyl$^{RS/}$tRNA^{Pyl} system: RS$_{Coin}$. Scale bar 20 µm.

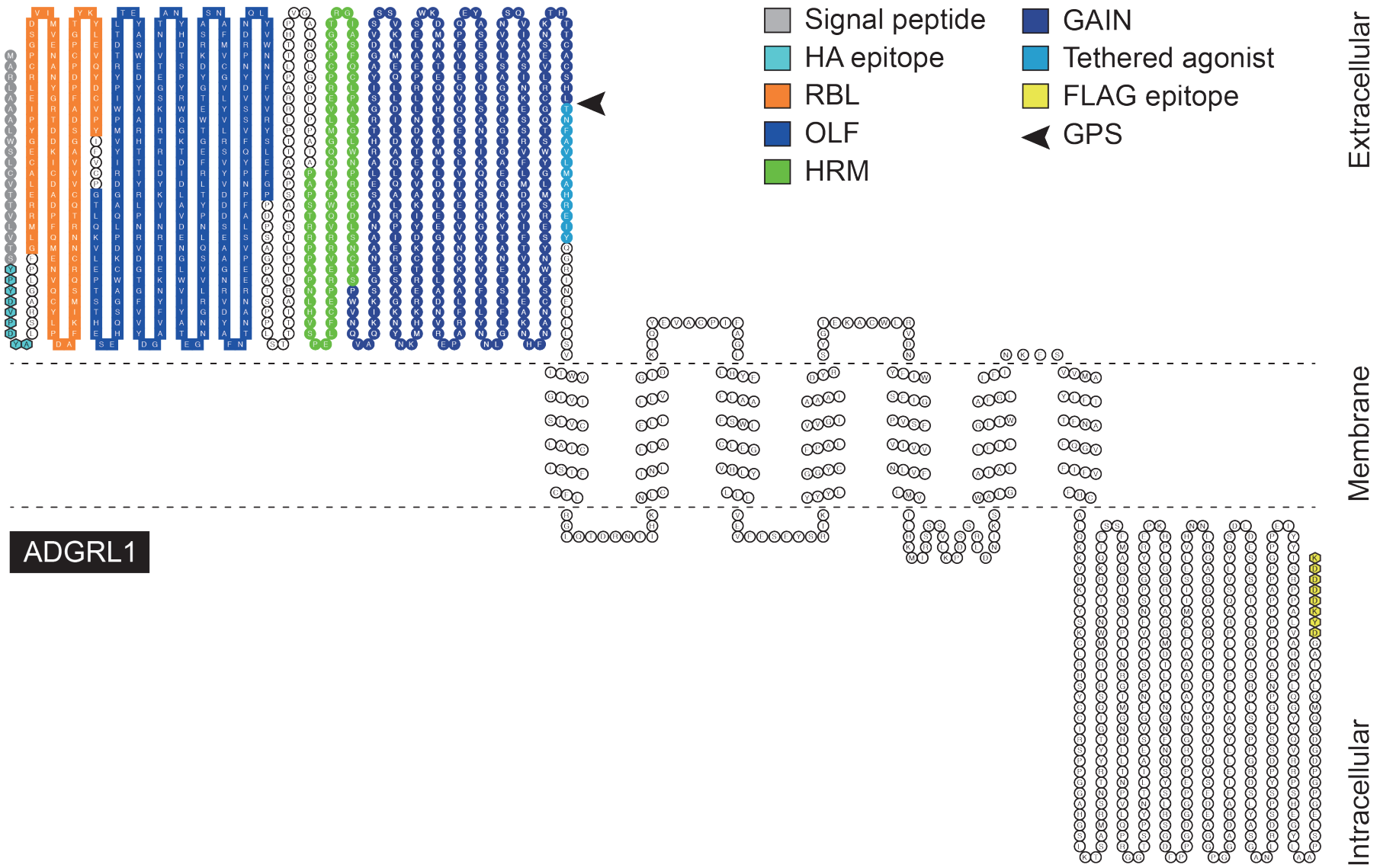

Supp. Fig. 3: Schematic structure and amino acid sequence of the rat L1 receptor used in this thesis.

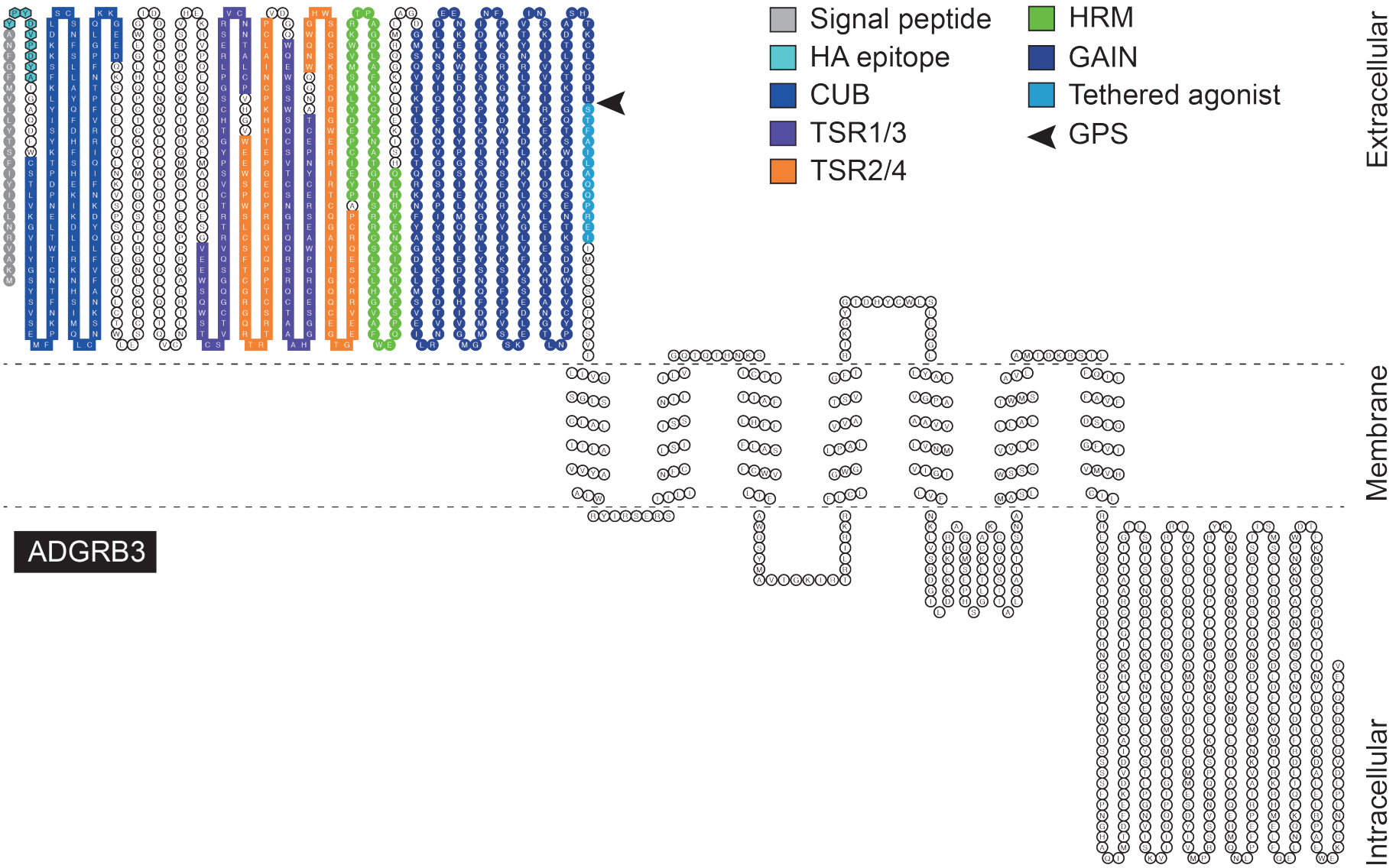

Supp. Fig. 4: Schematic structure and amino acid sequence of the human B3 receptor used in this thesis.

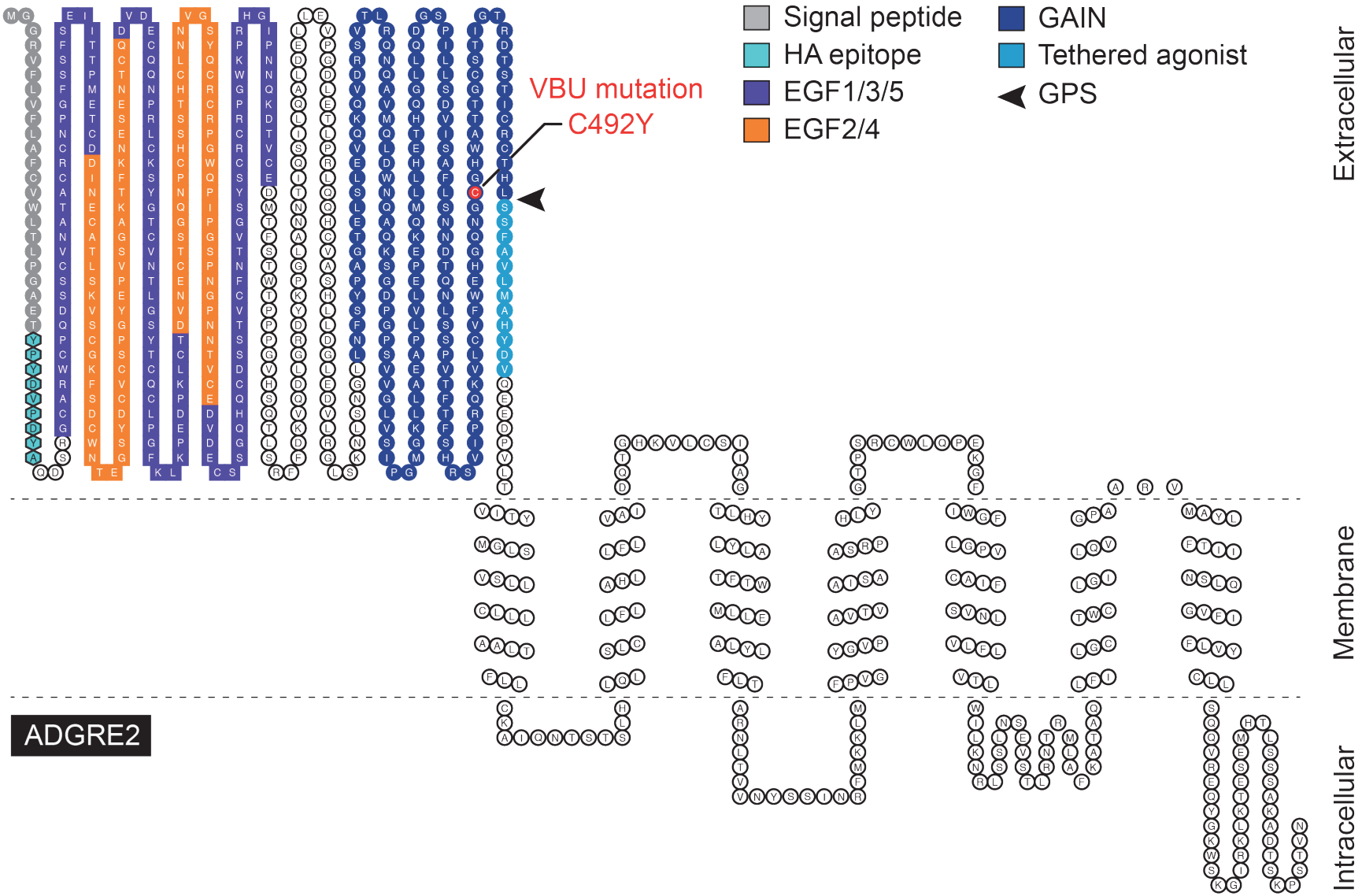

Supp. Fig. 5: Schematic structure and amino acid sequence of the human E2 receptor used in this thesis.

9.3 List of figures

9.4 List of tables